

FRACTURE OF ASPHALT CONCRETE:
A COHESIVE ZONE MODELING APPROACH
CONSIDERING VISCOELASTIC EFFECTS

BY

SEONG HYEOK SONG

B.E., University of Seoul, 2000

M.S., University of Illinois at Urbana-Champaign, 2003

THESIS

Submitted in partial fulfillment of the requirements
for the degree of Doctor of Philosophy in Civil and Environmental Engineering
in the Graduate College of the
University of Illinois at Urbana-Champaign, 2006

Urbana, Illinois

UMI Number: 3243000

INFORMATION TO USERS

The quality of this reproduction is dependent upon the quality of the copy submitted. Broken or indistinct print, colored or poor quality illustrations and photographs, print bleed-through, substandard margins, and improper alignment can adversely affect reproduction.

In the unlikely event that the author did not send a complete manuscript and there are missing pages, these will be noted. Also, if unauthorized copyright material had to be removed, a note will indicate the deletion.

UMI[®]

UMI Microform 3243000

Copyright 2007 by ProQuest Information and Learning Company.

All rights reserved. This microform edition is protected against unauthorized copying under Title 17, United States Code.

ProQuest Information and Learning Company
300 North Zeeb Road
P.O. Box 1346
Ann Arbor, MI 48106-1346

© Copyright by Seong Hyeok Song, 2006

CERTIFICATE OF COMMITTEE APPROVAL

*University of Illinois at Urbana-Champaign
Graduate College*

July 25, 2006

We hereby recommend that the thesis by:

SEONG HYEOK SONG


Entitled:

**FRACTURE OF ASPHALT CONCRETE: A COHESIVE ZONE MODELING
APPROACH CONSIDERING VISCOELASTIC EFFECTS**

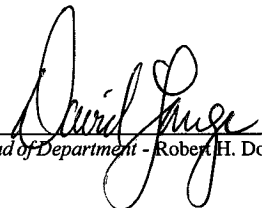
Be accepted in partial fulfillment of the requirements for the degree of:

Doctor of Philosophy

Signatures:

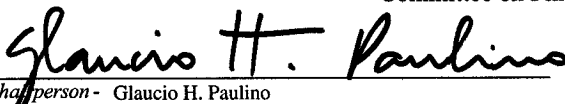


Director of Research - Glaucio H. Paulino

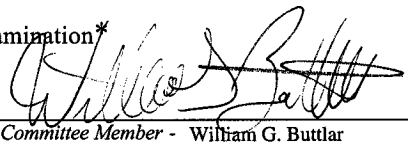


Head of Department - Robert H. Dodds Jr.

Committee on Final Examination*



Chairperson - Glaucio H. Paulino




Committee Member - William G. Buttlar



Committee Member - C. Armando Duarte



Committee Member - Jeffery R. Roesler



Committee Member - Philip B. Blenkinship

Committee Member -

* Required for doctoral degree but not for master's degree

Abstract

Asphalt concrete is a quasi-brittle material that exhibits time and temperature dependent fracture behavior. Softening of the material can be associated to interlocking and sliding between aggregates, while the asphalt mastic displays cohesion and viscoelastic properties. To properly account for both progressive softening and viscoelastic effects occurring in a relatively large fracture process zone, a cohesive zone model (CZM) is employed. Finite element implementation of the CZM is accomplished via user subroutines that can be used in conjunction with general-purpose software. The bulk properties (e.g. relaxation modulus) and fracture parameters (e.g. cohesive fracture energy) are obtained from experiments. In this study, artificial compliance and numerical convergence (which are associated with the intrinsic CZM and the implicit finite element scheme, respectively) are addressed in detail. New rate-independent and rate-dependent CZMs, e.g. a power-law CZM, tailored for fracture of asphalt concrete are proposed. A new operational definition of crack tip opening displacement (CTOD), called δ_{25} , is employed to considerably minimize the contribution of bulk material in measuring fracture energy. Predicted numerical results match well with experimental results without calibration. Simulations of various two- and three-dimensional mode I fracture tests, e.g. disk-shaped compact tension (DC(T)), are performed considering viscoelastic effects. The ability to simulate mixed-mode fracture and crack competition phenomenon is demonstrated in conjunction with single-edge notched beam (SE(B)) test simulation. The predicted mixed-mode fracture behaviors are found to be in close agreement with experimental results. Fracture behavior of pavement under tire and temperature loadings is explored.

For the Glory of God

Acknowledgments

The author would like to express his profound gratitude to his advisor Professor Glaucio H. Paulino who has been a continuous source of motivation, encouragement, direction, and support. His comments and suggestions helped to improve the content and clarity of this thesis. The author is also deeply indebted to Professor William G. Buttler for his friendly guidance and advice. To committee members Professors C. Armando Duarte and Jeffery R. Roesler, and Mr. Philip B. Blankenship, the author owes many thanks for their time, invaluable suggestions, and interactions. The author would like to express his appreciation to Professor Robert H. Dodds Jr. and Harry H. Hilton for their advice in this work.

The author is grateful to his colleagues: Jeong-Ho Kim, Matthew C. Walters, Alok Sutradhar, Zhengyu Zhang, Eshan Dave, Michael P. Wagoner, Huiming Yin, Kyungsoo Park, Bin Shen, Chau Le, Tam Nguyen, Maribel Gozalez, Jun-Ho Shin, Shun Wang, Andrew Braham, Fernando Stump, and Cameron Talischi.

The author heartily appreciates his parents (Seunghoo Song and Minsuk Kim), brother (Sungwoo), and sisters (Minjung and Suyun) for their love and support. To my wife, Seong Im Jin, I owe the most, for her endless love, patience, support, and encouragement. To my son, David Song, returning homes to your hugs and smiles has been the happiest time.

Table of Contents

List of Tables	ix
List of Figures	x
Chapter 1 Introduction	1
1.1 Overview	1
1.2 Bulk material behavior	3
1.2.1 Graded finite elements	4
1.2.2 Viscoelasticity	5
1.3 Fracture characterization	7
1.3.1 Quasi-brittle behavior	9
1.3.2 Viscoelastic fracture	10
1.3.3 Cohesive zone model	12
1.3.4 Fracture energy	12
1.3.5 Convergence and artificial compliance issues	14
1.4 Research objectives	17
1.5 Thesis organization	19
Chapter 2 Application of graded finite elements for asphalt pavements	21
2.1 Introduction	21
2.2 Spectral analysis of graded finite elements	23
2.3 Verification of UMAT	24
2.4 Application of UMAT for a pavement system	28
2.4.1 Input parameters and assumptions	29
2.4.2 Two-dimensional pavement model	32
2.4.3 Pavement modeling results	33
2.5 Concluding remarks	37
Chapter 3 Cohesive zone models	38
3.1 Various cohesive zone models	38
3.1.1 Potential based exponential model	38
3.1.2 Bilinear cohesive zone model	41
3.1.3 Power-law cohesive zone model	43
3.1.4 Remarks	46
3.2 Computational framework	47

3.2.1	CZM formulation	47
3.2.2	Finite element implementation	49
3.3	Determination of bulk and cohesive properties	51
3.3.1	Complex modulus	51
3.3.2	Relaxation modulus	52
3.3.3	Cohesive parameters	52
3.4	Concluding remarks	53
Chapter 4	Fracture modeling using the exponential CZM	55
4.1	Introduction	55
4.2	Verification of CZM	57
4.3	Mode-I single-edge notched beam (SE(B)) test simulation	58
4.3.1	Selection of a cohesive element size	59
4.3.2	Sensitivity analysis with respect to cohesive fracture energy and material strength	62
4.3.3	Calibration of cohesive parameters	64
4.4	Mixed-mode SE(B) test simulation	64
4.5	Concluding remarks	68
Chapter 5	A bilinear cohesive zone model tailored for fracture of asphalt concrete	70
5.1	Introduction	71
5.2	CZM compliance issues	73
5.3	Computational results considering viscoelastic bulk material	77
5.3.1	Energy balance	77
5.3.2	Calibration of cohesive parameters in the DC(T)	79
5.3.3	Mixed-mode crack propagation in the SE(B)	81
5.4	Discussion on numerical convergence	82
5.5	Crack competition phenomenon: nucleation versus initiation and propagation	87
5.5.1	Experimental investigations	89
5.5.2	Numerical studies	90
5.6	Concluding remarks	93
Chapter 6	Three-dimensional power-law cohesive zone modeling in conjunction with the δ_{25} concept	98
6.1	Introduction	99
6.2	Power-law cohesive zone modeling	101
6.3	The δ_{25} approach	104
6.3.1	Experimental set-up	104
6.3.2	Validation	105
6.4	Computational results	109
6.5	Concluding remarks	111

Chapter 7	Rate-dependent cohesive zone modeling for asphalt concrete fracture: exploratory investigation	113
7.1	Motivation	113
7.2	Related work	116
7.3	Challenges	119
7.4	Development of a rate-dependent CZM	119
7.4.1	Approach	121
7.4.2	On the theory of rate processes	121
7.4.3	Rate-dependent CZM	123
7.4.4	Summary	126
7.5	Sensitivity analysis	128
7.6	Proposed procedure	130
7.7	Computational results	133
7.7.1	Case I: IOWA-MAT-A	133
7.7.2	Case II: IOWA-MAT-B	137
7.8	Concluding remarks	139
Chapter 8	Pavement fracture using cohesive zone modeling	143
8.1	Field description	144
8.2	Numerical results	148
8.3	Discussion	148
Chapter 9	Concluding remarks	152
9.1	Summary	153
9.2	Conclusions	155
9.3	Suggestions for future work	158
Appendix A	ABAQUS user subroutine for the three-dimensional power-law CZM	161
Appendix B	ABAQUS user subroutine for the two-dimensional power-law CZM	178
References	187
Author's biography	205

List of Tables

1.1	Various cases for fracture modeling in asphalt concrete using a CZM.	11
2.1	Input Parameters for Global Aging Model Runs to compute asphalt Concrete Modulus Gradient with Depth. T denotes temperature.	30
5.1	Prony series parameters for the master relaxation modulus using the generalized Maxwell model [131].	78
5.2	Temperature shift factors [131].	79
5.3	Comparison of γ_{cr} between numerical and experimental results.	93
6.1	Prony series parameters for the master relaxation modulus using the generalized Maxwell model [131].	102
6.2	Temperature shift factors [131].	103
6.3	Fracture energy of the two replicates at $-20^{\circ}C$ [131].	106
7.1	Fracture energy and material strength [131].	114
7.2	Prony series parameters for the master relaxation modulus using the generalized Maxwell model [131].	114
7.3	Temperature shift factors [131].	114
7.4	Fracture energy of the two replicates and material strength at $-10^{\circ}C$, $-20^{\circ}C$ and $-30^{\circ}C$ [131].	134
7.5	Magnitudes of parameters of the viscoelastic CZM under $-20^{\circ}C$ and $1mm/min$ CMOD rate condition.	135
7.6	Fracture energy of the two replicates and material strength at $-10^{\circ}C$, $-20^{\circ}C$ and $-30^{\circ}C$	138
7.7	Magnitudes of parameters of the viscoelastic CZM for three temperatures with $1mm/min$ CMOD rate.	139
8.1	Model parameters for three different layers [131].	145
8.2	Temperature shift factors ($\log(1/a_T)$) [131].	147
8.3	Poisson's ratio for each layer [131].	147
8.4	Fracture energy and material strength for the three layers ($1mm/min$. CMOD rate and $-20^{\circ}C$) [131].	147

List of Figures

1.1	Illustration of STRATA ductility [94].	2
1.2	Asphalt concrete characterization.	3
1.3	Homogeneous versus graded finite elements: (a) property variation along one coordinate axis (z); (b) homogeneous elements; (c) graded elements. Notice that the property of the homogeneous elements corresponds to the property at the centroids of the graded elements. Also notice that $E(z)$ is Young's modulus, which is a function of z	4
1.4	Graded element with direct sampling of properties at the Gauss points. The notation $P(x,y)$ denotes a generic material property such as Young's modulus ($E(x,y)$) and Poisson's ratio ($\nu(x,y)$) in isotropic elasticity analysis.	5
1.5	Viscoelasticity in asphalt concrete: Generalized Maxwell model (10 parameters) for viscoelastic characterization.	7
1.6	Three types of fracture behavior [13]: (a) brittle; (b) ductile and; (c) quasi-brittle.	10
1.7	Time dependent behavior of the zones: (a) rate-dependent hardening; (b) rate-dependent softening.	11
1.8	Schematic representation of (a) the cohesive zone concept and (b) the normal opening displacement (δ_n) and the normal traction (t_n) along a cohesive surface. Notice that σ_c and δ_c are the material strength and the critical displacement, respectively, which are cohesive parameters.	13
1.9	Schematic illustration of the SE(B) test. Note that the deformed shape of the SE(B) indicates a rigid body mode.	14
1.10	A schematic drawing of a cohesive law in terms of normal opening displacement (δ_n) and normal traction (t_n).	15
1.11	One dimensional problem with bulk and cohesive elements.	16
1.12	Effective modulus as a function of h , δ_{ce} , and σ_c	17
2.1	Eigen-analysis for Q4 (2×2 Gauss quadrature) and $\beta = 0$ (homogeneous material). The numbers indicate the eigenvalues (λ_i).	24
2.2	Eigen-analysis for Q4 (2×2 Gauss quadrature) and $\beta = 1$ (FGM). The numbers indicate the eigenvalues (λ_i).	25
2.3	Functionally graded plate: (a) geometry - the domain covered by dotted line indicates the geometry used in the FEA; (b) a finite plate used in FEA with boundary conditions and material properties.	26

2.4	Stress distribution (σ_y) using Q8 elements for tension loading perpendicular to the exponential material gradation along the x direction. The inserts show the specimen before and after deformation.	28
2.5	Typical pavement cross-section for Illinois I-155.	29
2.6	Predicted pavement temperature versus depth for I-155, near Lincoln, Illinois, at 5 A.M. on July 4, 1997.	31
2.7	Dynamic modulus versus depth computed from aging, climatic, and modulus models with fitted function.	32
2.8	Poisson's ratio versus depth computed from aging, climatic, and modulus models with fitted function.	33
2.9	2D graded model versus 2D layered model: Normalized unaveraged horizontal stress (σ_x) with depth (d) at the location where maximum tensile stresses occur.	34
2.10	2D graded model versus 2D layered model : Normalized unaveraged horizontal stress (σ_x) with depth (d) along the center of the tire loads.	35
2.11	2D graded model versus 2D layered model : Normalized unaveraged vertical stress (σ_z) with depth (d) along the center of the tire loads.	35
2.12	2D graded model versus 2D layered model : Normalized unaveraged horizontal strain (ϵ_x) with depth (d) along the center of the tire loads.	36
3.1	The exponential cohesive law in terms of (a) the normalized effective displacement and the normalized effective traction and (b) the non-dimensional normal opening displacement and non-dimensional normal traction for different ratios of non-dimensional shear sliding displacements.	40
3.2	A bilinear cohesive law in terms of (a) non-dimensional effective displacement and non-dimensional effective traction and (b) non-dimensional normal opening displacement and non-dimensional normal traction.	42
3.3	The power-law cohesive zone model in terms of (a) the normalized effective displacement and the normalized effective traction and (b) the non-dimensional normal opening displacement and non-dimensional normal traction for different ratios of non-dimensional shear sliding displacement.	45
3.4	Normal traction (t_n) versus normal opening displacement (δ_n) curves of various cohesive laws.	47
3.5	Schematic drawing of a 4-noded linear cohesive element. Variables δ_s and δ_n represent shear sliding and normal displacement jump, respectively. Variables u_X^2 and u_Y^2 denote global displacements of node 2 along X and Y directions, respectively. The variable $\delta_Y^{(1,4)}$ represents the opening displacement along Y direction, while θ indicates the angle between global and local coordinates. Notice that X and Y denote global coordinates, whereas s and n denote local coordinates.	50
3.6	Experimental setting of (a) IDT test and (b) SE(B) test.	53
4.1	Schematic drawing of the double cantilever beam (DCB) test in which H is the thickness, 2Δ is crack mouth opening displacement, L is the total length, and a is the distance from the crack mouth to the assumed crack tip location.	58
4.2	Comparison between numerical and analytical solutions for the DCB specimen.	59

4.3	Geometry and mesh for analysis of the SE(B) test: (a) geometry and boundary condition; (b) mesh configuration for whole geometry; (c) mesh detail along the middle of the specimen. Notice that cohesive elements are inserted along the middle line of the specimen. Notice that cohesive element size $0.1mm$ is used.	61
4.4	Comparison of (a) the P versus CMOD and δ_{25} and (b) the CMOD versus the total dissipated fracture energy for different cohesive element sizes: $\ell_1=0.1mm$, $\ell_2=0.2mm$ and $\ell_3=1.0mm$. Notice that ℓ_i introduces a length-scale in the problem.	63
4.5	Sensitivity of P versus CMOD curve to (a) different cohesive fracture energy and (b) different material strength. Notice that $\sigma_c = 3.56MPa$ and $G_c = 344J/m^2$	65
4.6	Comparison between experimental result and numerical result with calibrated parameters.	66
4.7	Mixed-mode SE(B) test: (a) geometry and boundary condition; (b) mesh configuration for whole geometry; (c) mesh detail where cohesive elements are inserted. Notice that dashed line indicates an area where cohesive elements are inserted.	67
4.8	Simulation of mixed-mode SE(B) test: (a) deformed shape showing crack trajectory (scale factor is three); (b) comparison of crack trajectory between numerical and experimental results. Red line indicates the crack trajectory obtained from the 2D CZM, while blue line and green lines denote the crack trajectory from the experiment (front and back faces, respectively).	68
5.1	Effective modulus as a function of h and δ_c using bilinear and exponential cohesive zone models [144, 39] for asphalt concrete material properties. . . .	74
5.2	SE(B) test simulation: (a) geometry and boundary condition; (b) mesh configuration for the whole geometry; (c) mesh details for the regions where cohesive elements are inserted.	75
5.3	Comparison of P versus CMOD curves: (a) using cohesive zone models [144, 39] for the case I; and (b) using the bilinear model [39] for the three cases. . .	76
5.4	DC(T) test simulation; (a) geometry and boundary condition; (b) mesh configurations for the whole geometry.	78
5.5	DC(T) simulation: (a) energy balance with $1.0mm/min$. CMOD loading rate at $-10^\circ C$; (b) a load versus time curve.	80
5.6	Comparison of P versus CMOD curves between numerical and experimental results [135].	81
5.7	Mixed-mode SE(B) test: (a) geometry and boundary condition; (b) mesh configuration for the whole geometry; (c) mesh details of the shaded region of (123,19) and (150,95) where cohesive elements are inserted.	83

5.8	Simulation of the mixed-mode SE(B) test: (a) deformed shape showing crack trajectory (scale factor is 30); (b) comparison of the crack trajectory between numerical and experimental results. Red line indicates the crack trajectory obtained from the present numerical simulation, and green and blue lines denote the crack trajectories from the experiment.	84
5.9	Final crack trajectory: (a), (d) and (g) show mesh details for (b) and (c), (e) and (f), and (h) and (i), respectively. The Newton-Raphson is used for (b), (e) and (h), and the Riks method is adopted for (c), (f) and (i). Notice that the bottom left point of each deformed figure corresponds to the original crack tip and the top right point corresponds to the location of applied loading. Magnification factor 50 is used for (b), (c), (e) and (f), and the magnification factor 10 is employed for (h) and (i) to make crack trajectory visible.	86
5.10	Three different fracture behaviors: (a) mode I; (b) initiation and propagation; and (c) nucleation and propagation.	88
5.11	Dimensions of the beams tested by: (a) John and Shah [57]; (b) Guo et al. [45]; and (c) Wagoner et al. [132].	89
5.12	Experimental results with various notch offsets [132, 133]: (a) the actual beam with mixed-mode fracture; (b) crack trajectories for $\gamma = 0.5$; and (c) crack paths for $\gamma = 0.55$. Solid and dotted lines denote crack trajectories of front and back faces, respectively.	90
5.13	SE(B) test simulation considering crack competition phenomenon: (a) geometry and boundary conditions; (b) mesh discretization for the whole geometry; (c) mesh details for the notch tip region in which a crack initiates and propagates; and (d) mesh details for the central cross section where crack nucleation and propagation occur.	92
5.14	Numerical results: (a) initiation and propagation when $\gamma = 0.48$ and (b) nucleation and propagation when $\gamma = 0.56$. Magnification factor 30 is used to make crack trajectories visible.	94
5.15	Numerical results demonstrating crack initiation and propagation when $\gamma = 0.48$. Crack propagates from the crack tip location.	95
5.16	Numerical results illustrating crack nucleation and propagation when $\gamma = 0.56$. Crack propagates at the middle region of the specimen.	96
6.1	Typical asphalt concrete microstructure.	101
6.2	DC(T) test simulation: (a) geometry and boundary conditions; (b) mesh configurations for the whole geometry.	103
6.3	Comparison of a P versus CMOD curve between the numerical and experimental results.	105
6.4	The parameter δ_{25} : (a) experimental setting [131]; (b) schematic drawing. Note that Δa denotes a distance between the original crack tip and the current crack tip.	106
6.5	Load versus displacement of CMOD and δ_{25} (experimental results) [131]. . .	107
6.6	Displacement versus time for the CMOD and δ_{25} (experimental results) [131].	108



6.7	Comparison of fracture energy in context of the δ_{25} and CMOD for different temperatures [131].	108
6.8	Comparison of the numerical results with the experimental results.	110
6.9	Time versus CMOD and δ_{25} . Notice that in this simulation, the power-law CZM with $\alpha = 10$ is employed and the fracture energy evaluated in conjunction with the δ_{25} is adopted.	110
6.10	Stresses σ_y and deformed shapes. Note that magnification factor 500 is employed to make crack propagation visible.	111
7.1	DC(T) test simulation: (a) geometry and boundary conditions; (b) mesh configuration for the whole geometry.	115
7.2	Comparison of P versus CMOD curves between numerical and experimental results for different temperatures. In this case, rate independent CZM has been employed.	116
7.3	P versus CMOD curves: (a) IOWA-MAT-A (PG64-22); and (b) IOWA-MAT-B (PG58-34).	120
7.4	The energy barrier when both bond-breaking and bond-healing occur [70].	123
7.5	asinh function.	125
7.6	Viscoelastic cohesive laws for different values of f_v	127
7.7	Illustration of rate-dependent cohesive laws: (a) for different normal opening rates $\dot{\delta}_n$ with $\eta = 1$ and $\gamma = 1$; (b) for different magnitudes of the parameter γ with $\dot{\delta}_n = 0.575$ and $\eta = 1$; and (c) for different magnitudes of the parameter η with $\dot{\delta}_n = 0.575$ and $\gamma = 1$	129
7.8	Viscoelastic cohesive laws for different magnitudes of the parameter η and $\dot{\delta}_n$ with $\gamma = 1$	130
7.9	Comparison of P versus CMOD curves between numerical and experimental results at $T = T_0 = -20^\circ C$	134
7.10	Comparison of P versus CMOD curves between numerical and experimental results at $T = -30^\circ C$ and $1mm/min$ CMOD rate.	136
7.11	Comparison of P versus CMOD curves between numerical and experimental results at $T = -10^\circ C$ and $1mm/min$ CMOD rate.	136
7.12	Comparison of P versus CMOD curves between numerical and experimental results.	137
7.13	Comparison of P versus CMOD curves between numerical and experimental results at: (a) $T = T_0 = -20^\circ C$; (b) $T = -30^\circ C$; and (c) $T = -10^\circ C$	140
7.14	Comparison of P versus CMOD curves between numerical and experimental results [135].	141
8.1	Actual pavement section in IOWA.	143
8.2	Schematic drawing of the pavement section in IOWA.	144
8.3	Pavement modeling: (a) geometry and boundary conditions; (b) mesh configuration for the whole geometry; and (c) mesh details for the regions where cohesive elements are inserted.	146
8.4	Temperature profile along the depth of the pavement.	147

8.5 Deformed shape of the pavement structure under the temperature loading:
(a) whole geometry; and (b) regions where cohesive element are inserted. . . 149

8.6 Deformed shape of the pavement structure under the tire loading: (a) whole
geometry; and (b) regions right above the PCC joint where cohesive element
are inserted. 150

8.7 Integrated approach involving experiment, modeling and field. 151

9.1 Pavement with crack offset. 159

Chapter 1

Introduction

Asphalt concrete has various features which distinguish it from other materials. Bulk (background or volumetric) material of asphalt concrete shows viscoelastic effects and material gradients due to asphalt binders and oxidative hardening, respectively. Asphalt concrete shows quasi-brittle behavior and time and temperature dependence with respect to fracture behavior. These aspects have been quite difficult for researchers and engineers to examine and classify. This thesis addresses how to properly account for these issues in order to increase understanding of asphalt concrete fracture behavior and to reasonably predict experimentally-derived responses.

This chapter presents an overview of the project. Crucial aspects in modeling asphalt concrete and pavement in context of bulk material and fracture characterizations are introduced. Then, research objectives of this study are provided, followed by a brief presentation of the thesis organization.

1.1 Overview

Reflective cracking has occurred in nearly all types of asphalt overlays, whether placed on existing asphalt or concrete pavements. Due to mechanical and environmental loadings, movements take place at its joints or pre-existing notches, and as a result, cracks start to grow from existing joints or cracks. Reflective cracking in overlays causes water penetration thereby weakening the foundation of the pavement structure and contributing to increased

roughness and joint deterioration. A number of studies have been conducted in an effort to minimize or delay the occurrence of reflective cracking. However, earlier attempts were not successful in mitigating reflective crack nor did they provide a significant economic benefit [18, 76, 82].

Recently, SemMaterials (previously Koch Materials) has developed a promising reflective crack control treatment, called STRATA reflective crack relief system (RCRS) (see Figure 1.1). The STRATA RCRS is a highly strain-tolerant interlayer, which protects the more brittle asphalt overlay from stress intensities caused by existing joints or cracks. The STRATA is composed of a premium polymer modified asphalt binder at a high asphalt content in a dense fine aggregate mixture. Based on a performance-based specification, the mix is designed and certified using the flexural beam fatigue test. This system has been placed in the field and most treated sections have shown relatively better performance compared to untreated control sections. However, the fracture mechanisms in the system are not well understood. This problem needs to be investigated from a fundamental, systematic and in-depth point of view. Thus, the goal of the GOALI¹ project [94] is to address this problem by means of an integrated approach involving experiments, numerical and theoretical analysis, computational modeling and simulation, parametric study and field validation.



Figure 1.1: Illustration of STRATA ductility [94].

The author's role in this project is to recognize important factors affecting asphalt concrete fracture and pavement responses in context of bulk (background) and fracture char-

¹GOALI: Grant Opportunities for Academic Liaison with Industry

acterizations and to properly address the relevant factors in the analysis (see Figure 1.2) including

- Material gradient due to oxidative hardening of the asphalt surface course [79].
- Time and temperature dependence in bulk and fracture.
- Quasi-brittle behavior (laboratory tests and pavement system).

These aspects will be covered throughout the thesis in detail.

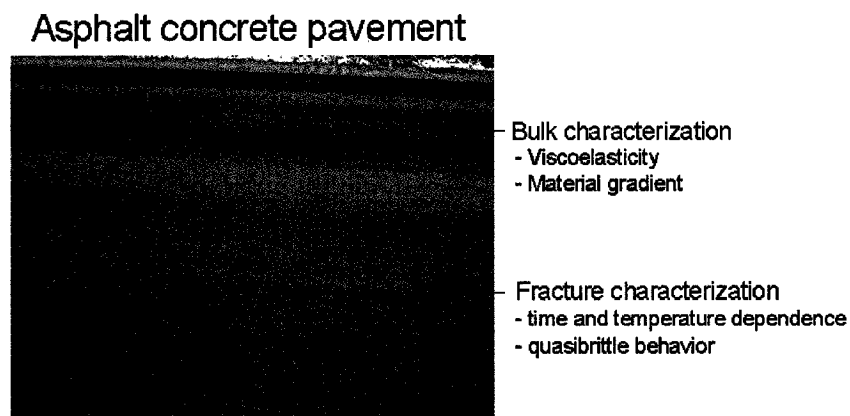


Figure 1.2: Asphalt concrete characterization.

1.2 Bulk material behavior

Time and temperature dependence as well as material gradient of asphalt concrete bulk material are regarded as crucial aspects and, as a result, need to be properly taken into account in order to have a better understanding of asphalt concrete and pavement responses. Material gradient can be treated using graded finite elements, which initially were developed and applied to functionally graded materials or FGMs. Viscoelastic effects are considered by means of the use of hereditary integral formulation.

1.2.1 Graded finite elements

The graded element incorporates the material property gradient at the size scale of the element, while the homogeneous element, which has been used in traditional layered analysis of pavement [85], produces a stepwise constant approximation to a continuous material property field such as the one shown in Figure 1.3. Graded elements are implemented by means of direct sampling properties at the Gauss points of the element [63, 112], as illustrated by Figure 1.4. The finite element stiffness matrix relations can be written as [52]

$$\mathbf{K}\mathbf{u} = \mathbf{f} \quad (1.1)$$

with

$$\mathbf{K} = \int_{\Omega} \mathbf{B}^T \mathbf{D}(\mathbf{x}) \mathbf{B} d\Omega \quad (1.2)$$

where \mathbf{u} is nodal displacement vector, \mathbf{f} is the load vector, \mathbf{B} is the strain-displacement matrix which contains gradients of the interpolating functions, $\mathbf{D}(\mathbf{x})$ is the constitutive matrix (variable), and Ω is the domain of element. In the present work, the elasticity matrix $\mathbf{D}(\mathbf{x}) = \mathbf{D}(x, y)$ is assumed to be a function of spatial co-ordinates.

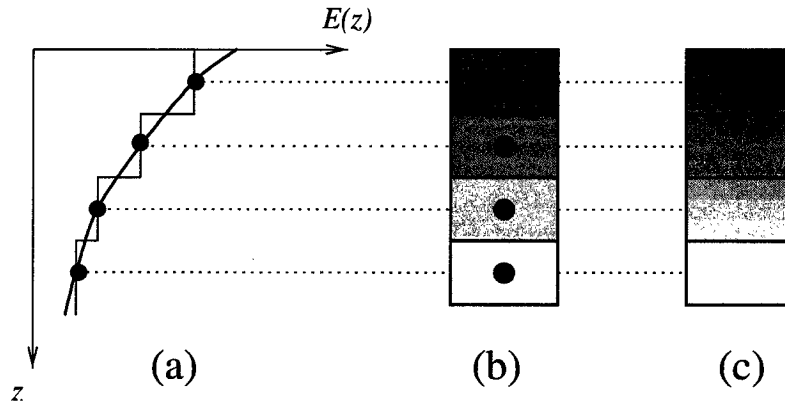


Figure 1.3: Homogeneous versus graded finite elements: (a) property variation along one coordinate axis (z); (b) homogeneous elements; (c) graded elements. Notice that the property of the homogeneous elements corresponds to the property at the centroids of the graded elements. Also notice that $E(z)$ is Young's modulus, which is a function of z .

The integral in Eq. (1.2) is evaluated by Gauss quadrature, and the matrix $\mathbf{D}(\mathbf{x})$ is spec-

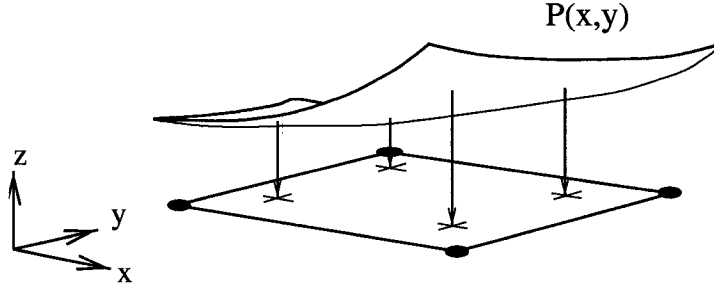


Figure 1.4: Graded element with direct sampling of properties at the Gauss points. The notation $P(x,y)$ denotes a generic material property such as Young's modulus ($E(x,y)$) and Poisson's ratio ($\nu(x,y)$) in isotropic elasticity analysis.

ified at each Gaussian integration point. Thus for two-dimensional problems, the resulting integral becomes:

$$\mathbf{K} = \sum_{i=1}^N \sum_{j=1}^N \mathbf{B}_{ij}^T \mathbf{D}_{ij} \mathbf{B}_{ij} J_{ij} w_i w_j \quad (1.3)$$

where the subscripts i and j refer to the Gaussian integration points, J_{ij} is the determinant of the Jacobian matrix, and w_i and w_j are the Gaussian weights.

1.2.2 Viscoelasticity

The constitutive law for isotropic viscoelasticity in the form of a hereditary integral formulation is [2, 26, 128]

$$\sigma_{ij}(t) = \int_0^t 2G(\xi - t') \dot{e}_{ij} dt' + \delta_{ij} \int_0^t K(\xi - t') \dot{\epsilon}_{kk} dt', \quad (1.4)$$

where K and G are bulk and shear relaxation moduli, respectively, and are functions of the reduced time ξ . The superscripted dots denote differentiation with respect to time t' . The symbol δ_{ij} is the Kronecker delta, and ϵ_{kk} and e_{ij} are components of the mechanical volumetric and deviatoric strains, respectively. The bulk (K) and shear (G) relaxation moduli can be defined individually using Prony series representation

$$K(\xi) = K_\infty + \sum_{i=1}^{n_k} K_i \exp(-\xi/\tau_i^K) \quad G(\xi) = G_\infty + \sum_{i=1}^{n_G} G_i \exp(-\xi/\tau_i^G), \quad (1.5)$$

where K_∞ and G_∞ are the long term bulk and shear moduli, respectively. In general, the material has a different relaxation time of τ_i^K and τ_i^G , and different moduli of K_i and G_i , and a variable number of Prony series parameters ending in n_K and n_G . In this study, all relaxation is assumed to occur in the shear mode [99].

Two approaches are generally considered in order to obtain the relaxation modulus. The first is to conduct a relaxation test, where constant strain is imposed and a generalized Maxwell model is used to describe the resulting material response. The second is to conduct a creep test, where constant stress is imposed and a Voight-Kelvin model is used to describe creep compliance behavior, which is then used to obtain the relaxation modulus using inter-conversion schemes [48, 93]. The second approach is preferable when working with asphalt concrete due to several reasons (e.g. a constant stress creep test is easier to perform than the constant strain relaxation test) [93].

The creep compliance function using a Voight-Kelvin model is given as

$$D(\xi) = D(0) + \sum_{i=1}^N D_i(1 - e^{-\xi/\tau_i}) + \frac{\xi}{\eta_v}, \quad (1.6)$$

where ξ is reduced time, $D(\xi)$ is creep compliance at the reduced time, and $D(0)$, D_i , τ_i and η_v are model constants. The reduced time ξ is obtained from t/a_T where t is a real time and a_T is a temperature shift factor. Model constants are obtained from creep tests conducted at multiple temperatures, and shift factors are evaluated from shifting the compliance versus time curve at different temperatures in a log scale to establish a smooth, continuous curve.

Interconversion of the time dependent creep compliance function of Eq. (1.6) yields a relaxation modulus given as

$$E(\xi) = \sum_{i=1}^{N+1} E_i e^{-\xi/\tau_i}, \quad (1.7)$$

where $E(\xi)$ is a relaxation modulus at the reduced time of ξ , and E_i and τ_i are model constants for the master relaxation modulus curve. Figure 1.5 shows a generalized Maxwell model, which is a widely used constitutive model to describe the linear viscoelastic behavior

of asphalt concrete.

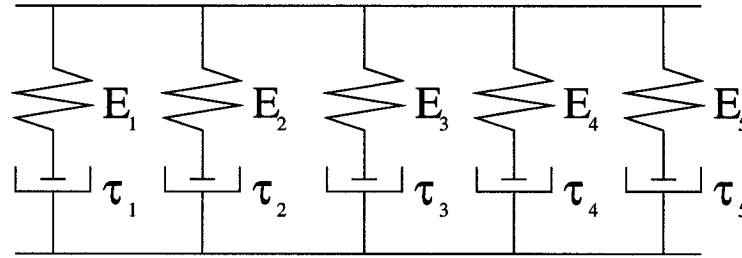


Figure 1.5: Viscoelasticity in asphalt concrete: Generalized Maxwell model (10 parameters) for viscoelastic characterization.

1.3 Fracture characterization

A number of studies have been conducted to obtain better understanding of cracking mechanisms and to tackle the cracking problem in asphalt concrete. Majidzadeh et al. [78] made an early attempt to study crack propagation using fracture testing. Abdulshafi and Majidzadh [3] applied the J-integral concept to fatigue and fracture of asphalt mixtures in conjunction with the disk-shaped specimen. Kim and El Hussein [65] used three point bending tests to explore fracture behavior of asphalt concrete and evaluate fracture toughness of asphalt concrete at low temperatures. Jacobs et al. [54] employed Paris' law to analyze cracking in asphalt concrete and to obtain more insight into the crack propagation and resistance of asphalt mixes. Bhurke et al. [14] developed a test protocol to calculate fracture toughness of asphalt concrete at low temperatures. Castell et al. [20] investigated fatigue crack growth in laboratory beam specimen and layered pavements using the code Franc2D/L. Additionally, several other researchers [90, 111, 119] have applied fracture mechanics principles in the study of cracking in asphalt concrete laboratory specimens and pavements.

However, a number of studies conducted thus far do not account for both quasi-brittle behavior and viscoelastic effects inherent in asphalt concrete properly. Asphalt concrete is considered a quasi-brittle material due to the relatively large fracture process zone size with respect to the structure size. This aspect makes it very difficult to apply linear elastic

fracture mechanics (LEFM) to asphalt concrete fracture study, because the fracture process zone in which progressive softening occurs is no longer inside of the K-dominance region where stress is proportional to $1/\sqrt{r}$. Section 1.3.1 will provide detailed explanation on quasi-brittle behavior. Furthermore, asphalt concrete exhibits time and temperature dependent fracture behavior. Unfortunately, this behavior is not well understood due to limited experimental data and understanding. Detailed issues on viscoelasticity will be presented in Section 1.3.2.

This work employs a powerful numerical scheme, a cohesive zone model (CZM), to investigate fracture behavior of asphalt concrete because both progressive softening effects and viscoelastic effects occurring in a relatively large fracture process zone can be taken into account properly by means of a suitable constitutive model between displacement jump and the corresponding traction. The early conceptual works related to the cohesive zone model (CZM) date back to the early 60s and were carried out by Barenblatt [7, 8], who proposed the CZM to study perfectly brittle materials and Dugdale [36], who adopted a fracture process zone concept to investigate ductile materials exhibiting plasticity. During the 90s, leaps were made as a result of the pioneering works by Needleman and his co-workers [86, 144], and Camacho and Ortiz [19]. Xu and Needleman [144] proposed a potential-based cohesive zone model in which cohesive elements are inserted into a finite element mesh in advance, which follow an exponential cohesive law. In such a scheme, as displacement between cohesive elements increases, the traction initially increases, reaches a maximum, and then decays monotonically. However, the model by Xu and Needleman induces artificial compliance due to the elasticity of the intrinsic cohesive law. To alleviate such problems, Geubelle and Baylor [41] and Espinosa and Zavattieri [39] adopted bilinear CZMs, and Song et al. [124] proposed a power-law CZM to reduce the compliance by providing an adjustable initial slope in the cohesive law. Another noteworthy CZM is the extrinsic cohesive law proposed by Camacho and Ortiz [19] where a new surface is adaptively created by duplicating nodes which were previously bonded. The extrinsic CZM eliminates the artificial compliance inherent in the intrinsic CZM. Recently, Paulino and his co-workers developed a new data

structure to facilitate the insertion of cohesive elements in conjunction with the extrinsic CZM [22, 23]. Subsequent investigations have been carried out to address issues of ductility fracture [34, 74, 108], brittle fracture [43, 145], concrete fracture [10, 37], asphalt concrete fracture [122], fracture in functionally graded materials [55, 56, 96], dynamic crack propagation [109, 120, 146], time discontinuity [91], fatigue [77, 136], interfacial fracture [24, 41, 100], thermomechanical behavior [15, 29] and mixed-mode fracture [130].

A relatively small number of studies have been performed investigating viscoelastic fracture. Early works in this area include the important contributions of Knauss [67] and Schapery [113], who developed theories for macroscopic cracks in viscoelastic media. More recently, a number of different attempts have been made to consider rate effects in a material separation model. Knauss and Losi [68] combined a viscoelastic constitutive model with a damage function. Rahul Kumar et al. [100] and Allen and Searcy [4] adopted a hereditary integral approach, which is identical to the formulation for the bulk material, in conjunction with a traction-separation function. Additionally, Bazant and Li [12] formulated a rate-dependent cohesive crack model. Finally, Xu et al. [141] has also proposed a rate-dependent CZM, having both rate-independent and rate-dependent material parameters which are determined from experiments and numerical analysis.

1.3.1 Quasi-brittle behavior

Fracture behavior of asphalt concrete deviates from LEFM considerably due to the relatively large fracture process zone in which progressive nonlinear softening behavior, e.g. microcracking and void formation, occurs. This zone is surrounded by a non-softening nonlinear zone characterized by hardening or perfect plasticity. In general, fracture behavior of all materials can be categorized as brittle, ductile and quasi-brittle, depending upon the relative sizes of the softening and hardening zones with respect to the size of the structures [13] (see Figure 1.6).

In the first material type (see Figure 1.6 (a)), the size of the fracture process zone is

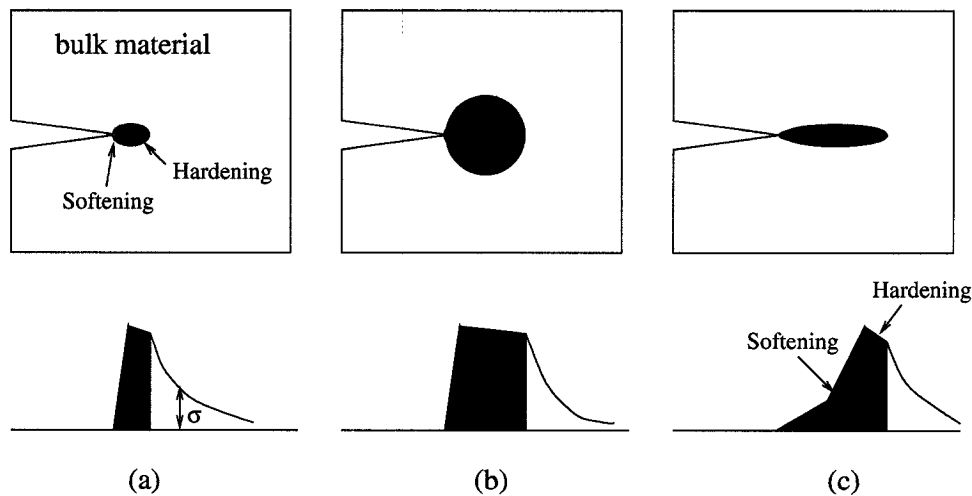


Figure 1.6: Three types of fracture behavior [13]: (a) brittle; (b) ductile and; (c) quasi-brittle.

relatively small compared to the structure size. With brittle materials, the entire fracture takes place in very small region so that LEFM can be generally applied. Plexiglass, glass and brittle ceramics are considered brittle materials. In the second type (see Figure 1.6 (b)), ductile material, the size of the fracture process zone where material separation occurs is still small, although hardening zone is not small. This kind of behavior is effectively treated by the elasto-plastic fracture mechanics. Many ductile metals fall into this category. The behavior of quasi-brittle materials (see Figure 1.6 (c)) shows the relatively large fracture process zone size compared to the structure size. A major part of the nonlinear fracture process zone experiences progressive softening due to microcracking and crack initiation and propagation. Various approaches, such as a CZM, are undertaken to handle this behavior properly. Concrete, rocks, fiber composites and asphalt concrete are all of this type.

1.3.2 Viscoelastic fracture

Figure 1.7 illustrates viscoelastic behavior including bulk and fracture. The outermost zone is assumed to be viscoelastic, while the intermediate zone is viscoelastic hardening. The innermost zone is the viscoelastic fracture process zone in which the softening of material differs at different rates and temperatures. The relative contribution of each zone to fracture

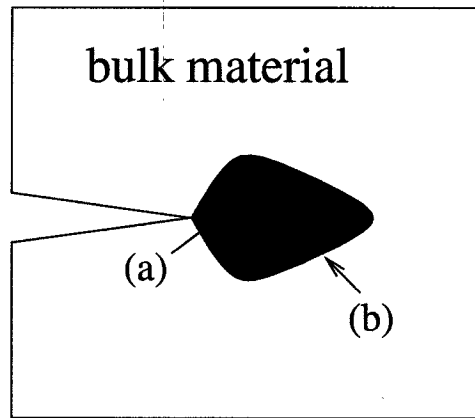


Figure 1.7: Time dependent behavior of the zones: (a) rate-dependent hardening; (b) rate-dependent softening.

behavior is not well understood. Moreover, the contribution of time and temperature to material separation is not well known either. As a result, relatively a few studies have been carried out to investigate time and temperature dependent fracture behavior in viscoelastic materials. In addition, assumptions and calibrations played a considerable role in their studies with varying degrees of success under particular conditions.

For quasi-brittle material, two possibilities must be examined, excepting case 1 in which time and temperature dependence is neglected in both bulk and fracture materials (see Chapter 4). In case 2, the outer zone is linear viscoelastic and the fracture process zone is time and temperature independent, as presented in Chapters 5 and 6. In case 3, both the outer zone and the fracture process zone are time and temperature dependent, which is addressed in Chapter 7.

Table 1.1: Various cases for fracture modeling in asphalt concrete using a CZM.

CASES	Bulk (background)	Cohesive (fracture)
Case 1	No viscoelastic effects	No viscoelastic effects
Case 2	Viscoelastic effects	No viscoelastic effects
Case 3	Viscoelastic effects	Viscoelastic effects

1.3.3 Cohesive zone model

The cohesive zone model provides a computationally efficient way to simulate damage occurring in a process zone located ahead of a crack tip (see Figure 1.8). This approach, which involves nonlinear constitutive laws described by displacement jump and the corresponding traction along the interfaces, provides a phenomenological model to simulate fracture behavior such as crack nucleation, initiation and propagation.

Figure 1.8 illustrates the CZM concept in the opening mode (pure mode I) where t_n and δ_n , respectively, denote normal traction and normal opening displacement, σ_c is material strength, and δ_c denotes displacement corresponding to zero traction. The true (material) crack tip indicates a point where traction is zero and the cohesive (fictitious) crack tip is a point where the traction reaches a maximum. The cohesive zone (or fracture process zone) is defined as the region between the true crack tip and the cohesive crack tip where complicated fracture behaviors, including inelasticity, occur. The cohesive surfaces are joined together by a cohesive traction, which depends upon the displacement jump across crack faces. As the displacement jump increases due to an increase of external force or compliance in structure, the traction first increases, reaches a maximum, and then decays monotonically to zero. The material-separation response depends on the critical traction, critical displacement, and fracture energy, which represent the cohesive parameters, and cohesive law softening shapes.

1.3.4 Fracture energy

A very important material property that is required for the CZM is the cohesive fracture energy (or the energy required to fully separate the material). For concrete, which is quasi-brittle material like asphalt concrete, the 1985 RILEM committee on fracture mechanics of concrete has recommended a three-point bend specimen in order to measure the fracture energy [27]. The recommendation is based on the fictitious crack model by Hillerborg et al. [47]. The fracture energy absorbed by the beam is represented by the area under the load and the load line displacement (LLD). Note that, in this case, the load and the displacement

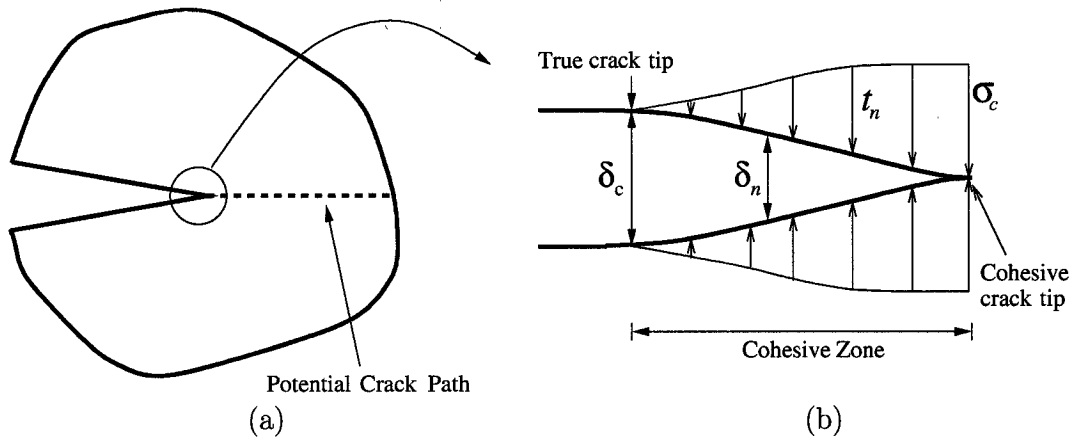


Figure 1.8: Schematic representation of (a) the cohesive zone concept and (b) the normal opening displacement (δ_n) and the normal traction (t_n) along a cohesive surface. Notice that σ_c and δ_c are the material strength and the critical displacement, respectively, which are cohesive parameters.

are both downward. For asphalt concrete, Wagoner et al. [133, 134] proposed two laboratory fracture tests, i.e. single-edge notched beam (SE(B)) test and disk-shaped compact tension (DC(T)) test, in order to evaluate fracture energy. Wagoner et al. [133, 134] utilized the crack mouth opening displacement (CMOD) to evaluate fracture energy, because the CMOD is a measurement required to perform the experiment. The fracture energy is estimated as the area under the load versus CMOD curve. In the SE(B) test, the loading is imposed downward (i.e. vertically), while the CMOD opens horizontally. However, the CMOD in the SE(B) test can be seen as an alternative measurement to the load line displacement for particular dimensions of the beam. Figure 1.9 illustrates schematic drawings of the undeformed shapes, and deformed shapes of a potential SE(B) test when the crack reaches the boundary of the beam specimen. Note that recoverable strain energy is minimal when crack reaches the top edge of the beam specimen. Using the geometrical information and considering rigid body motion, one obtains the following relationship between the CMOD and the load line displacement as

$$L : 2L = CMOD/2 : \text{Load line displacement} \quad (1.8)$$

$$\Leftrightarrow \text{CMOD} = \text{Load line displacement}$$

Thus, the fracture energy represented by the area under the load versus the CMOD curve can be considered as a candidate fracture energy.

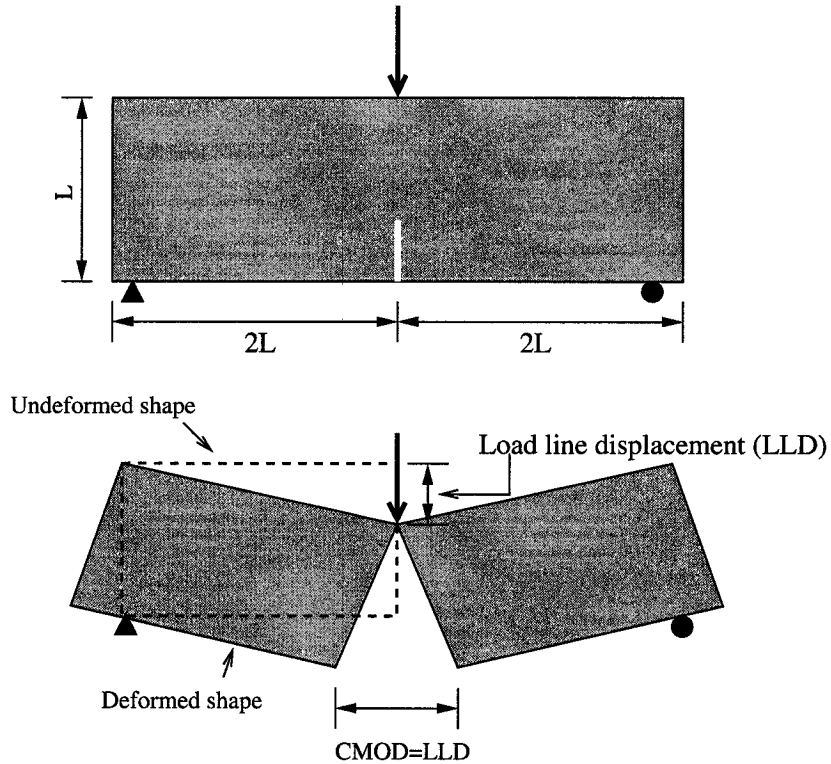


Figure 1.9: Schematic illustration of the SE(B) test. Note that the deformed shape of the SE(B) indicates a rigid body mode.

1.3.5 Convergence and artificial compliance issues

In spite of the great successes of a CZM, numerical convergence problems and artificial compliance are unavoidable when an implicit finite element method and an intrinsic CZM, respectively, are employed. Unlike an explicit finite element method where the evaluation of the tangent stiffness matrix is not necessary in solving a boundary value problem, when an implicit finite element scheme is adopted, numerical convergence problems occur because a cohesive law slope (i.e. $\partial t_n / \partial \delta_n$), which is used for the evaluation of the tangent stiffness

matrix, changes from positive to negative, as normal opening displacement (δ_n) increases (see Figure 1.10). This problem is rarely observed when cohesive elements are inserted along a predefined line. Numerical convergence problems, however, are more pronounced when a number of cohesive elements are inserted over an area in absence of known crack paths [122, 127]. Section 5.4 provides a discussion of numerical convergence.



Figure 1.10: A schematic drawing of a cohesive law in terms of normal opening displacement (δ_n) and normal traction (t_n).

Unlike an extrinsic CZM in which cohesive elements are inserted adaptively [19, 22, 23], artificial compliance is inherent in the intrinsic CZM due to a pre-peak slope. To address CZM compliance, the simple one-dimensional problem with bulk and cohesive elements is adopted (see Figure 1.11). F denotes the force, h is the length of the bulk material, u is the stretch of the bulk material, δ_n is the displacement jump between the cohesive surfaces, and A is the area of the block upon which F is applied. Imposing an equilibrium condition between bulk and cohesive elements with unit area A [66], one obtains

$$E\varepsilon = k\delta_n \quad (1.9)$$

where E is Young's modulus, ε is strain of the bulk material and k is a constant of proportionality between displacement jump and the corresponding traction, i.e. stiffness. Combining $\varepsilon = u/h$ and $E_e = \sigma/\varepsilon_{tot} = \sigma h/(u + \delta_n)$ with Eq. (1.9), one obtains the effective modulus

(E_e) under mode I condition as follows

$$E_e = E\varepsilon \frac{h}{u + \delta_n} = E \frac{h}{h + E/k} = E \left[1 - \frac{1}{1 + \frac{kh}{E}} \right] = E \left[1 - \frac{1}{1 + \frac{\sigma_c}{E} \frac{h}{\delta_{cc}}} \right], \quad (1.10)$$

where σ_c and δ_{cc} denote the maximum traction (finite material strength) and the displacement at the peak traction, respectively. σ_c/δ_{cc} represents the pre-peak slope. It is important to note that in order to avoid confusion between δ_c and δ_{cc} , δ_{cc} is defined as displacement corresponding to the peak traction, while δ_c is displacement at zero traction in this thesis.

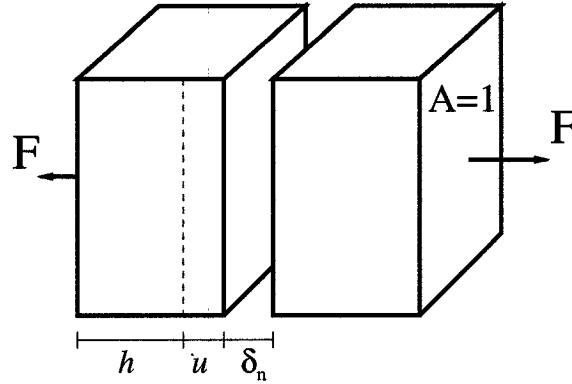


Figure 1.11: One dimensional problem with bulk and cohesive elements.

Figure 1.12 shows the effective modulus of a one-dimensional specimen as a function of h , δ_{cc} , and σ_c . From this result, we observe that as the ratios σ_c/E and h/δ_{cc} increase, the compliance due to the pre-peak slope of the cohesive law is negligible, indicating that the effective modulus (E_e) of the specimen approaches the properties of the continuum (E). This is intuitive because as the ratio of σ_c/E and h/δ_{cc} increases, the relative contribution of cohesive elements to global responses decreases, and as a result, the amount of artificially induced compliance becomes small. Section 5.2 will discuss compliance inherent in an intrinsic CZM in detail.

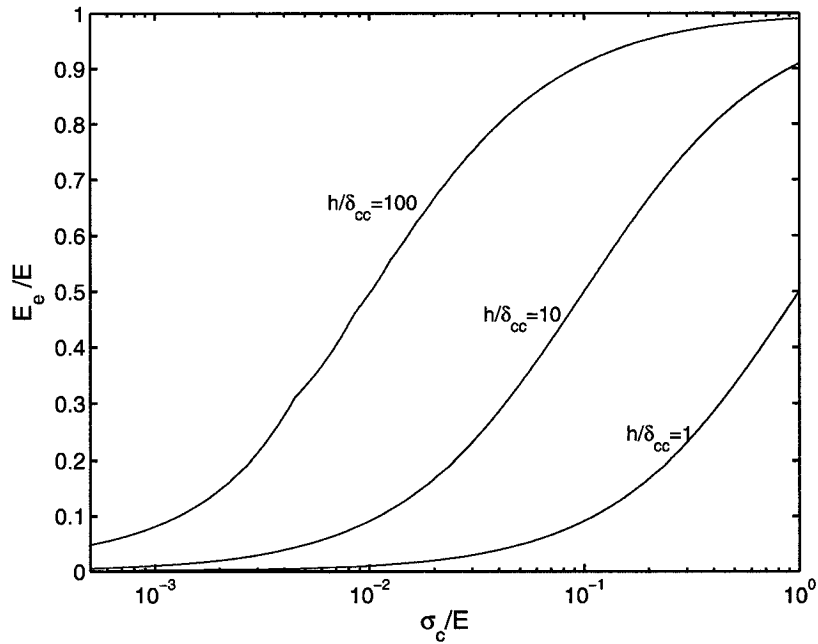


Figure 1.12: Effective modulus as a function of h , δ_{cc} , and σ_c .

1.4 Research objectives

This thesis investigates various crucial aspects in modeling asphalt concrete and pavement in terms of bulk (background) material and fracture characterizations. The procedures examined herein include an application of graded elements to pavement, an improvement of current rate-independent and viscoelastic CZMs, two and three-dimensional crack propagation simulations, and a comparison of numerical results with experimental results. The detailed research objectives of each chapter in this study are summarized as follows:

- To implement graded elements into the ABAQUS user material (UMAT) subroutine and to verify the implementation. To apply graded elements for pavement analysis considering aging related stiffness gradients due to oxidative hardening of the asphalt surface course.
- To implement a cohesive zone model by means of ABAQUS user element (UEL) capability. To verify the implementation using a double cantilever beam (DCB) test.

To perform sensitivity analysis to cohesive parameters. To numerically demonstrate that cohesive element sizes chosen in this study are small enough to capture nonlinear behavior properly. To compare a force (P) versus crack mouth opening displacement (CMOD) curve of numerical results with that of experimental results.

- To investigate compliance due to a pre-peak slope of intrinsic CZMs in conjunction with asphalt concrete material. To check energy balance using disk-shaped compact tension (DC(T)) test simulation. To perform a mixed-mode single-edge notched beam (SE(B)) test simulation, in which cohesive elements with a regular pattern are inserted over an area to allow cracks to propagate in any general direction, considering viscoelastic bulk (background) material. To compare the predicted mixed-mode crack trajectory with experimental results. To explore the influence of finite element discretizations on numerical convergence. To explore crack competition phenomenon between nucleation and initiation.
- To improve the present power-law CZM to 1) reduce artificial compliance, 2) model general cases, e.g. mixed-mode and three-dimensional, and 3) have various choices in terms of CZM softening shapes. To introduce δ_{25} as an operational definition of CTOD and employ it when evaluating cohesive fracture energy. To perform three-dimensional DC(T) test simulation. To propose a suitable CZM softening shape for asphalt concrete fracture modeling. To examine the influence of CZM softening shapes.
- To illustrate motivations and challenges in developing a viscoelastic CZM. To develop a viscoelastic CZM from the activation energy theory of the rate process of bond rupture in conjunction with reasonable assumptions and simplifications. To propose appropriate procedures to evaluate several parameters accounting for time and temperature effects. To perform sensitivity analysis to several parameters of the viscoelastic CZM. To validate the proposed viscoelastic CZM and procedures by comparing predicted numerical results with experimental results.



- To demonstrate the ability of a cohesive zone modeling technique to perform pavement crack propagation simulation and to investigate pavement fracture behavior subjected to various tire and temperature loadings.

1.5 Thesis organization

This thesis is organized as follows: Chapter 2 addresses the application of graded elements to pavement in which Young's modulus is graded due to oxidative hardening. Chapter 3 provides theoretical and numerical aspects of three cohesive zone models adopted in this study. Chapter 4 describes fracture modeling using the exponential model without consideration for viscoelastic effects in both bulk and fracture. Chapter 5 investigates asphalt concrete fracture behavior considering viscoelastic bulk material in conjunction with the bilinear CZM. Chapter 6 improves the previous power-law CZM and examines the usage of δ_{25} for asphalt concrete fracture modeling. Chapter 7 develops a novel viscoelastic CZM from the activation energy theory of the rate process of bond rupture in conjunction with reasonable assumptions and simplifications. Chapter 8 demonstrates fracture modeling in pavement subjected to tire and temperature loading using a CZM. Chapter 9 presents summary, conclusions and suggestions for future work.

Each of these chapters is a self-contained, stand-alone study. At the same time, as the number of chapter increases, one sees overall research progress. For example, we explore asphalt concrete pavement responses without fracture (see Chapter 2), then investigate fracture behavior in asphalt concrete using a CZM (see Chapters 4-7), and finally apply a CZM to pavement fracture study (see Chapter 8). With respect to a CZM employed for fracture modeling, first we use the potential based exponential CZM (see Chapter 4), then the bilinear CZM (see Chapter 5) and the power-law CZM we improved in this study (see Chapters 6-8). First, two dimensional analysis is performed (see Chapters 4, 5, and 7) and then three-dimensional analysis is carried out (see Chapter 6). Regarding viscoelastic effects, we perform fracture analysis without consideration of viscoelastic effects in both bulk and frac-

ture (see Chapter 4). Then, we consider viscoelastic bulk materials only (see Chapters 5 and 6) and finally viscoelastic effects in both bulk and fracture (see Chapter 7).

Chapter 2

Application of graded finite elements for asphalt pavements

Asphalt paving layers, particularly the surface course, exhibit vertically graded material properties. This grading is caused primarily by temperature gradients and aging related stiffness gradients. Most conventional existing analysis models do not directly account for the continuous grading of properties in flexible pavement layers. As a result, conventional analysis methods may lead to inaccurate prediction of pavement responses and distress under traffic and environmental loading. In this chapter, the graded element implementation using the user material subroutine (UMAT) capability of the finite element software ABAQUS [2] is verified using benchmark problems. Numerical examples using the UMAT are provided to illustrate the benefits of using graded elements in pavement analysis.

2.1 Introduction

Modern pavement design procedures involve structural modeling of the layered pavement system, as a tool to select and optimize materials and layer thickness to satisfy the design criteria for pavement serviceability under anticipated traffic loads and environmental conditions. Ideally, the structural model used for design will accurately estimate the critical responses in the pavement system and predict, as a function of time, distress development such as fatigue, fracture and permanent deformation. There are many complexities to con-

sider in properly modeling flexible pavement systems, including: non-linear material behavior, variable interface conditions, complex tire load patterns, and temperature and asphalt aging effects. Most of these complexities can be adequately addressed by using finite element modeling approaches [16, 60]. It can be argued that the most important aspect of flexible pavement modeling is the proper treatment of near-surface materials, since this region is in direct contact with vehicular loads and environment. Proper analysis is critical in the design of layer thickness and selection of surface materials to avoid premature failure.

One shortcoming of commercially available finite element codes at the present time is the inability to properly handle severe material property gradients within elements. In particular, oxidative hardening of the asphalt surface course is known to create a severe modulus gradient with depth [79]. Of course, one benefit of the finite element method is the ability to assign different material properties to elements in the mesh and as a result, one can approximate a material property gradient by assigning different properties to successive layers in the model. In pavement, this layered approach has been quite common [85, 60, 111]. The following quotation extracted from the mechanistic-empirical pavement design guide [85] is a good example illustrating the prevalence of the layered approach in the analysis of pavements. “The original pavement structure defined by the user usually has 4 to 6 layers. However, the Design Guide software may subdivide the pavement structure into 12 to 15 sublayers for the modeling of temperature and moisture variations. The Design Guide software performs the sublayering internally based on the material type, layer thickness and the location of the layer within the pavement structure.” However, this approach requires a very fine mesh to achieve accuracy, which can lead to excessive solution times. This is particularly critical in pavements, where three dimensional modeling is generally required, due to geometric asymmetries [59].

Thus, it is desirable to model the material property variation at the element level so that coarser meshes can be used, while maintaining accuracy. Recently such elements (called graded finite elements) have been developed and applied to *functionally graded materials* or



FGMs [63, 112]. Significant advances have been made in the analysis of FGMs using graded finite elements including fracture mechanics investigations involving stress intensity factors and T-stress evaluation [62, 64]. Unlike traditional laminated composites, in FGMs the material grading is continuous. This has the benefit of avoiding stress concentration and delamination, leading to a more durable material. Although the initial emphasis in FGM development was for thermal barrier coating for spacecraft [49], many other applications have followed. These include: nuclear breeder reactors [53], high density magnetic recording media [126], and biomaterials, such as dental and other implants [88, 137]. *Although an aged asphalt pavement is graded by environmental causes rather than by design, many of the analysis tools used to analyze FGMs can be applied or modified for use in flexible pavement analysis and design.* Such is the motivation for the current work.

Thus, the graded finite elements are advantageous for two main reasons: 1) to model material gradient in a single pavement layer such as the stiffening effect induced by aging of the top asphalt layer; 2) to model material gradient between two adjoining layers by means of a smooth transition of material properties (rather than a sharp transition as in the traditional approach). The graded interlayer simulates the actual merit of materials that may occur in engineering practice. The graded interlayer leads to smoother and more reliable interfacial stress.

2.2 Spectral analysis of graded finite elements

A brief introduction on graded finite elements is presented in Section 1.2.1. A comparison between homogeneous and graded elements by means of a simple element using spectral analysis reveals further differences between elements. Consider a square element of unit length with the origin at the left-bottom-corner. The Young's modulus is given by

$$E(x) = E_1 e^{\beta x} \tag{2.1}$$

where $E_1 = 1.0$ and $\beta = 0.0$ for the homogeneous material case and $\beta = 1.0$ for the nonhomogeneous material case. Figures 2.1 and 2.2 illustrate a comparison between the two cases for the Q4 element. The following observations can be made

- As expected, the number of rigid modes (3) and spurious deformation (zero energy) modes (e.g. 2 spurious modes for Q4 with 1×1 Gauss integration) is the same for both cases (homogeneous and graded elements).
- Symmetry, as expressed by the deformation modes (eigenvectors) is broken for graded elements, i.e. there are no repeated eigenvalues.
- The total energy ($U_i = \lambda_i/2, i = 1 \dots NDOFs$) increases for the FGM with $\beta > 0$. Here NDOFs indicates the number of degree of freedom in the element and λ_i indicates the i -th eigenvalue.

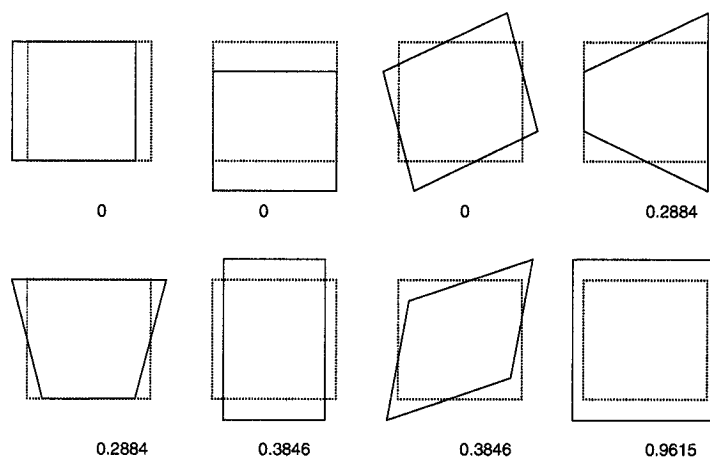


Figure 2.1: Eigen-analysis for Q4 (2×2 Gauss quadrature) and $\beta = 0$ (homogeneous material). The numbers indicate the eigenvalues (λ_i).

2.3 Verification of UMAT

Analytical solutions [38] for isotropic FGMs where material properties vary exponentially along the x direction are used as a reference to verify the implementation of the UMAT.

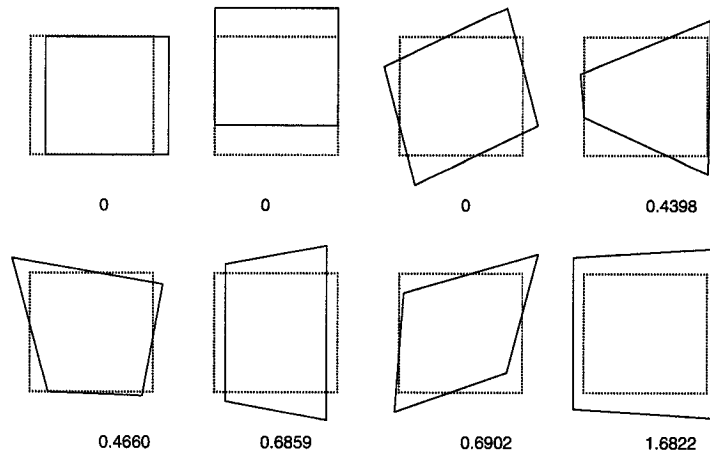


Figure 2.2: Eigen-analysis for Q4 (2x2 Gauss quadrature) and $\beta = 1$ (FGM). The numbers indicate the eigenvalues (λ_i).

Moreover, by means of this example, the benefit of using the graded element approach is illustrated by comparing unaveraged nodal stresses obtained with graded elements with those obtained from the layered approach.

Consider a rectangular finite plate of width $W = 9$ and height $H = 9$ as illustrated in Figure 2.3. A constant traction of $\sigma_t = 1$ perpendicular to the material gradation is applied to the top edge and displacement boundary conditions, $u_2 = 0$ for the bottom edge and $u_1 = 0$ for the left bottom node, are prescribed (see Figure 2.3 (b)). Consistent units are employed. The finite element mesh consists of 81 Q8 elements, which are either graded or homogeneous elements. The elastic modulus varies exponentially along the x direction

$$E(x) = E(0)e^{\beta x}, \quad \beta = \frac{1}{W} \log \left[\frac{E(W)}{E(0)} \right] \quad (2.2)$$

where $E(0) = 1$, $E(W) = 8$, and β is an independent material nonhomogeneity parameter which has units $[length]^{-1}$. Therefore $1/\beta$ is the length scale of nonhomogeneity. A constant Poisson's ration of 0.3 is employed. Plane stress condition and 3×3 Gauss quadrature are adopted.

For tension loading, the compatibility condition, $\partial \varepsilon_{yy}^2 / \partial x^2 = 0$, yields strain and stress

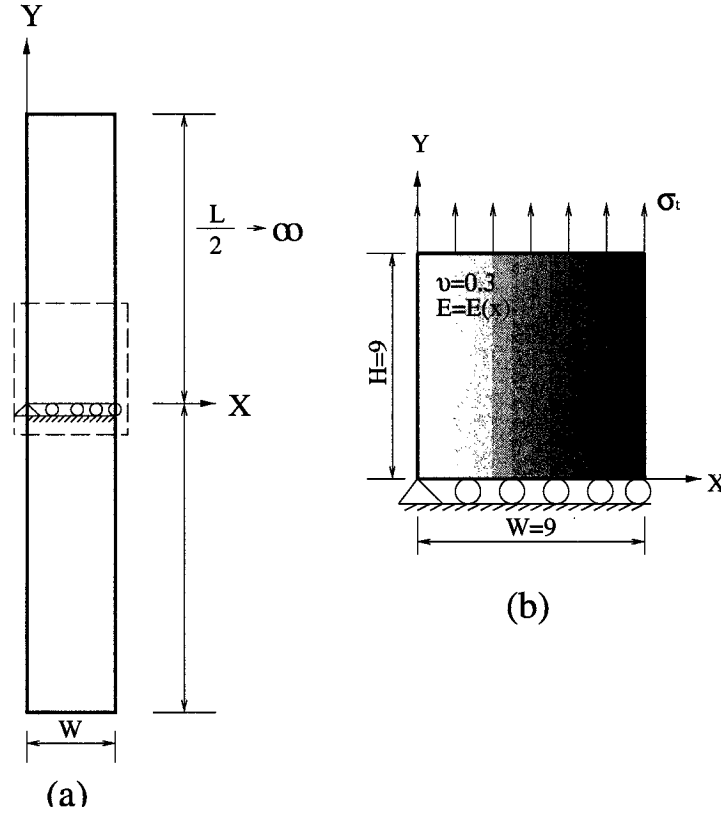


Figure 2.3: Functionally graded plate: (a) geometry - the domain covered by dotted line indicates the geometry used in the FEA; (b) a finite plate used in FEA with boundary conditions and material properties.

fields given by [38]

$$\varepsilon_{yy} = Ax + B, \quad (2.3)$$

$$\sigma_{yy}(x) = E'(0)e^{\beta x}(Ax + B), \quad (2.4)$$

where $E'(0)$ is $E(0)$ for plane stress and $E(0)/(1 - \nu^2)$ for plane strain. The coefficients A and B are determined from the following equilibrium conditions for the tension loading

$$\int_0^W \sigma_{yy}(x) dx = N \text{ and } \int_0^W \sigma_{yy}(x)x dx = M, \quad (2.5)$$

where N is $\sigma_t W$ and M is assumed to be zero. Therefore, the stress distribution is [38]

$$\sigma_{yy}(x) = \frac{\beta N}{2} e^{\beta x} \left\{ \left(\frac{W\beta^2 e^{\beta W} - 2\beta e^{\beta W} + W\beta^2 + 2\beta}{e^{\beta W} \beta^2 W^2 - e^{2\beta W} + 2e^{\beta W} - 1} \right) x + \frac{e^{\beta W} [e^{\beta W} (-W^2 \beta^2 + 3\beta W - 4) + W^2 \beta^2 - 2\beta W + 8] - \beta W - 4}{(e^{\beta W} - 1)(e^{\beta W} \beta^2 W^2 - e^{2\beta W} + 2e^{\beta W} - 1)} \right\}. \quad (2.6)$$

Figure 2.4 compares unaveraged nodal stresses interpolated from stresses at Gauss points using graded and homogeneous Q8 elements. The abscissa indicates the horizontal distance from the zero coordinate. The ordinate indicates σ_y . Bending effects due to both the exponential material gradation and the constant traction perpendicular to the material gradation lead to the trend that the exact solution first increases and then decreases with the increase of x (see Figure 2.4). The homogeneous Q8 elements show piecewise variation due to the stepwise approximation of the continuous material property. However, the graded Q8 elements show remarkably smooth stress variation and match with the analytical solution quite well demonstrating the verification of the UMAT implementation. The relatively small differences observed between the analytical solutions and the numerical results using the graded Q8 elements may be attributed to the fact that the analytical solution is derived based on an infinite plate length, while the numerical results are determined based on a finite length. Regarding performance of both graded and homogeneous elements, the graded elements are superior to homogeneous elements due to the following reasons: 1) unaveraged stresses using layered elements show large differences between the boundary where material property is not continuous, while graded elements predict almost identical unaveraged stresses at the same boundary; 2) unaveraged stresses using graded elements show much better approximation to the exact solution in every element than those using homogeneous elements. Nodal averaging schemes and refined meshes can improve the performance of the layered approach. However, averaging of nodal stresses may lead to inaccurate responses especially in the vicinity of corners, cracks or other discontinuities. Furthermore, refined meshes can increase computational expense, particularly for three dimensional analysis which is generally required in



pavement analysis due to geometric asymmetries. Notice that the use of graded elements leads to averaging or approximation process in the material properties (by adopting a variable D matrix - see Eq. (2)) rather than averaging at the end, i.e. after discretization and solution of the boundary value problem.

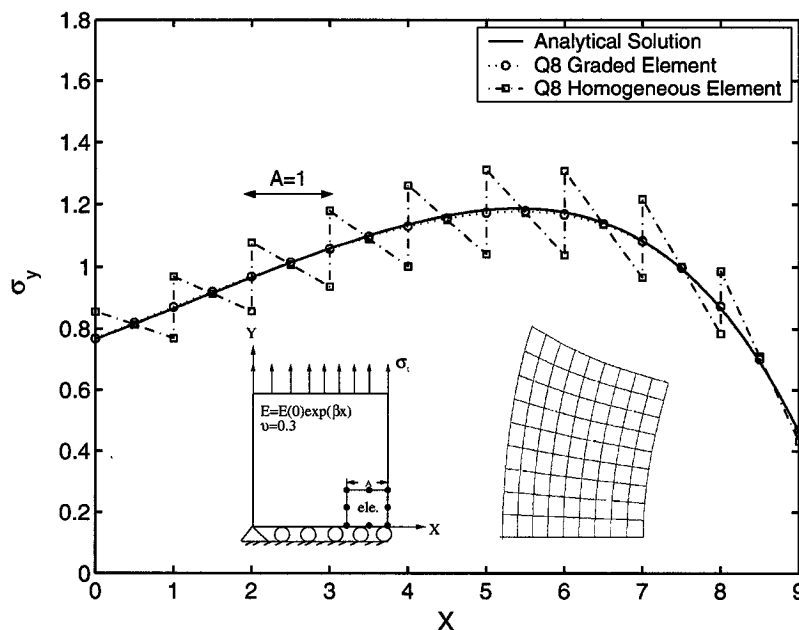


Figure 2.4: Stress distribution (σ_y) using Q8 elements for tension loading perpendicular to the exponential material gradation along the x direction. The inserts show the specimen before and after deformation.

2.4 Application of UMAT for a pavement system

A numerical example was chosen to coincide with a pavement case study previously conducted at the University of Illinois involving highway I-155, a four-lane divided interstate pavement in central Illinois near the town of Lincoln (see Figure 2.5). This pavement section has received considerable attention because it has shown several surface related problems, such as block cracking, thermal cracking, and longitudinal surface cracking [51, 75]. I-155 is a full-depth asphalt pavement, with 375 mm of hot-mix asphalt on a lime-stabilized clay subgrade.

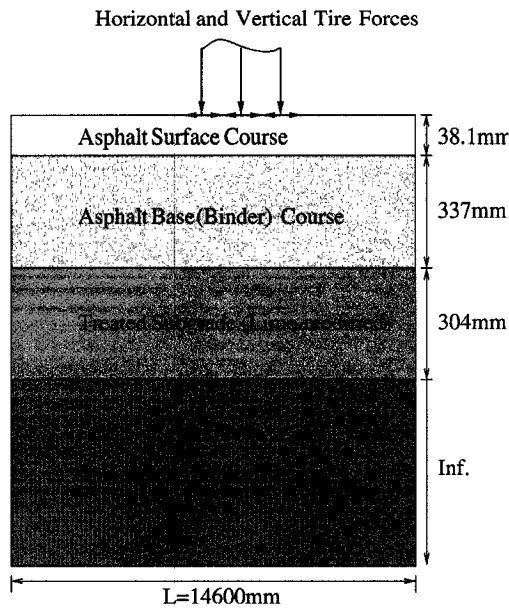


Figure 2.5: Typical pavement cross-section for Illinois I-155.

Although a detailed case study of I-155 is beyond the scope of this paper, it is hoped that the theoretical framework and preliminary analysis conducted herein will be of future benefit for forensic investigations of I-155 and other pavements showing premature distress development. Early testing of recovered binder from I-155 indicated very severe aging of the surface. For example, the binder viscosity at $60^{\circ}C$ which was approximately 4000 Poise just after construction, had increased to over 100,000 Poise near the surface after three years in service.

2.4.1 Input parameters and assumptions

To evaluate the response of the I-155 pavement structure using the graded finite element approach, a description of the asphalt mixture property gradients as a function of depth was needed, particularly near the pavement surface where gradients are most severe. Gradients in material properties within a given pavement asphalt arise due to two main effects: 1) oxidative hardening (aging) of the asphalt layer, particularly near the surface and ; 2) temperature gradients within the pavement, giving rise to material gradients due to the

extreme sensitivity of asphalt modulus and Poisson's ratio to temperature. Unfortunately, insufficient mixture testing of materials obtained at multiple depth in the pavement was available at the time of this study to completely describe the material property gradients on I-155. Fortunately, empirical models have been developed by Mirza and Witczak [79] and Witczak [138]. Thus, they were used to approximate the asphalt concrete material property gradients based upon asphalt viscosity, pavement age, depth below the pavement surface, air void content, asphalt content, etc. The severe aging gradients obtained with these models were found to be consistent with those reported in the experimental field investigations of Huber and Scherocman [51] and Lippert [75]. Table 2.1 summarizes the inputs used in the global aging model and modulus prediction model.

Table 2.1: Input Parameters for Global Aging Model Runs to compute asphalt Concrete Modulus Gradient with Depth. T denotes temperature.

Input Parameters	Value
Cumulative Percent Retained on 3/4" Sieve	0
Cumulative Percent Retained on 3/8" Sieve	8.0
Cumulative Percent Retained on 4 Sieve	42.0
Percent passing 200 Sieve	4.6
Volume of Effective Asphalt Content	10.0
Loading Time(sec)	0.1
Mean Average Air Temperature	51.4
Pavement Age in Months	96
In-Place Air Voids(percent)	7
$A=(\log \text{ Penetration at } T_1 - \log \text{ Penetration at } T_2) / (T_1 - T_2)$	11.0248
$VTS=(\log \log \text{ viscosity at } T_2 - \log \log \text{ viscosity at } T_1) / (\log T_1 - \log T_2)$	-3.7053

In order to obtain pavement moduli under a realistic temperature gradient, it was necessary to predict pavement temperatures versus depth at I-155. To accomplish this, the Enhanced Integrated Climatic Model [71], or EICM, was employed along with measured air temperature at Lincoln, IL at tracked by the Illinois State Water Survey at the University of Illinois at Urbana-Champaign. The EICM program is a one-dimensional coupled heat and moisture flow model, which was used in the current study to predict pavement temperature profiles as a function of measured air temperature, latitude, percent sunshine, emissivity, surface short wave absorptivity, maximum convection coefficient, wind speed, and several

other factors. The predicted pavement temperature versus depth for I-155, at 5 AM on July 4, 1997 is given in Figure 2.6. Although the selection process of this specific temperature event was somewhat arbitrary for the purposes of this analysis, the selected temperature profile appeared to create a fairly high stiffness gradient (which was desirable from the standpoint of illustrating differences between the graded element approach and the layered approach). Temperature profiles from cooler months were found to produce higher overall pavement stiffness, but much lower stiffness gradients. This is because the mixture stiffness, as obtained from Witzak [138] modulus prediction model, tends to approach a plateau at approximately $21GPa$. Since all other model coefficients were held constant, this mixture plateau is caused primarily by a plateau in the binder stiffness master curve as the glassy modulus is approached. In the case of an aged pavement such as I-155, a very low stiffness gradient was predicted during the winter months and even portions of the spring months.

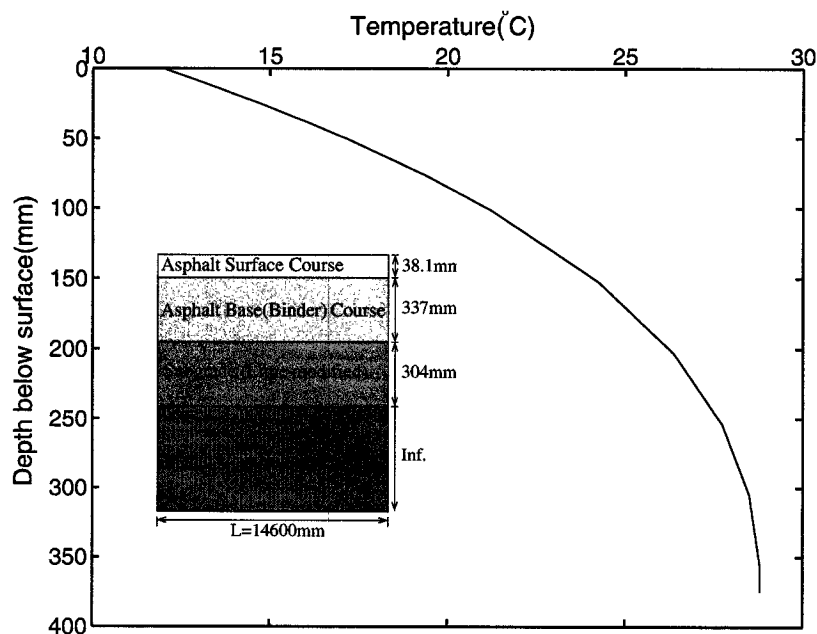


Figure 2.6: Predicted pavement temperature versus depth for I-155, near Lincoln, Illinois, at 5 A.M. on July 4, 1997.

Figures 2.7 and 2.8 present the dynamic modulus and Poisson's ratio versus depth based upon the empirical prediction models of Mirza and Witzak [79]. Clearly, the combination of

temperature and aging gradients creates a large gradient of predicted E^* with depth for the selected conditions, particularly in the first 100mm of depth. Poisson's ratio is predicted to increase with depth in pavement. Simple polynomial models were fit, as shown on Figures 2.7 and 2.8, to facilitate input of these parameters into the graded and layered FE models.

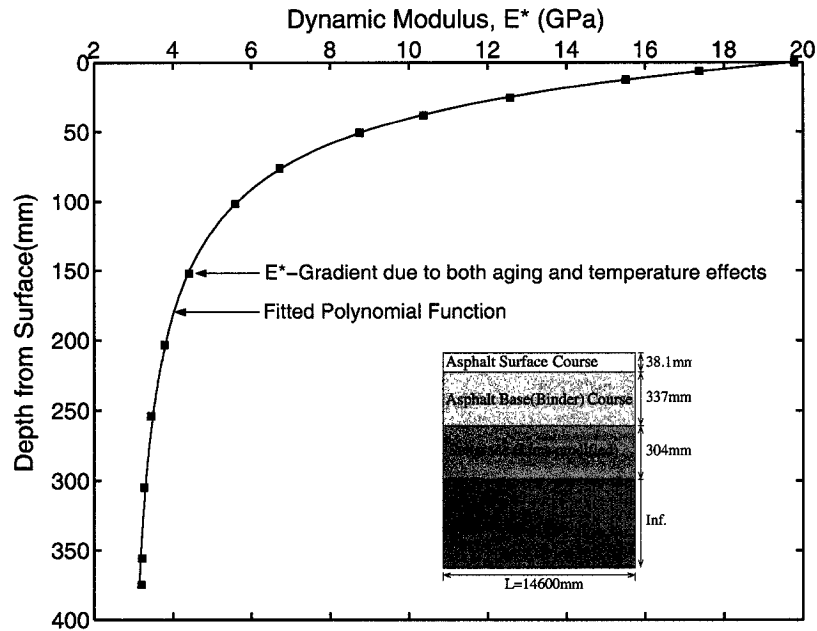


Figure 2.7: Dynamic modulus versus depth computed from aging, climatic, and modulus models with fitted function.

2.4.2 Two-dimensional pavement model

A four-lane pavement structure of length $2L = 14600mm$ with thickness of surface and binder $374.7mm$, thickness of subgrade $304.1mm$ and thickness of soil $9144mm$ was analyzed in conjunction with the UMAT where graded and homogeneous elements were implemented. To reduce the model size, a symmetry condition was adopted. Displacement boundary conditions of $u_2 = 0$ for the bottom edge were prescribed. Normal and shear stresses induced by a truck tire, based upon measured contact stresses by Myers et al. [84] for a radial tire, were used. For simplicity, a single radial truck tire was applied to the pavement surface because the purpose of this analysis is primarily focused on making a relative comparison

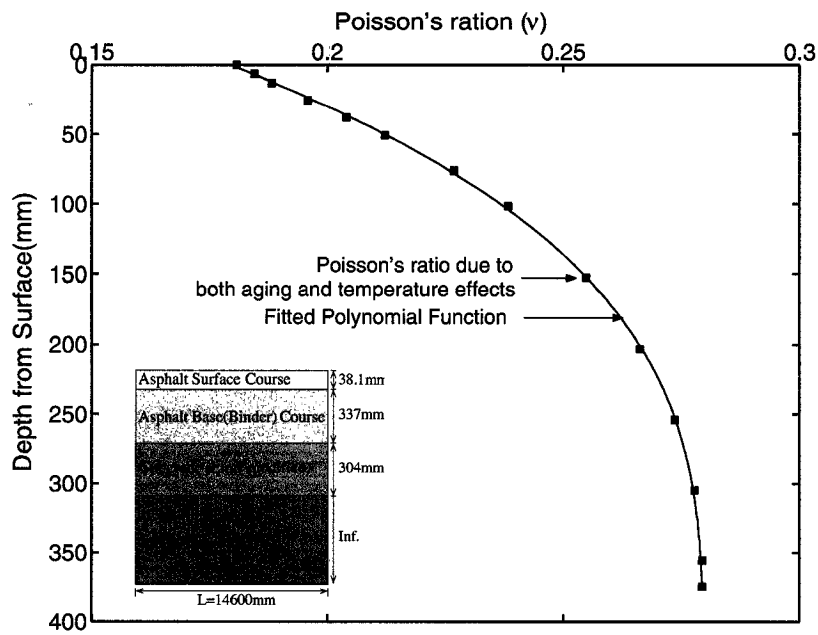


Figure 2.8: Poisson's ratio versus depth computed from aging, climatic, and modulus models with fitted function.

between the graded element and layered element approaches. The material properties where aging and temperature are taken into account were applied to surface and binder courses (see Figures 2.7 and 2.8). Young's modulus was taken as $E = 138MPa$ in the lime-cemented subgrade and $E = 35MPa$ in the soil. Four layered pavement systems were constructed using 23840 Q8 elements. Plane strain condition was adopted with 3×3 Gauss quadrature.

2.4.3 Pavement modeling results

Three strategic evaluation regions within the pavement model were examined to quantify the difference between graded elements and the traditional layered approach as shown in Figures 2.9 through 2.12. Figure 2.9 illustrates normalized unaveraged horizontal stress profiles for graded and homogeneous elements along the depth at the location where maximum surface tension occurs. The range of stresses in the plot is between 0.2 and 0.52MPa. It is located at 2400 mm away from the center of the applied load. The abscissa indicates the vertical evaluation depth to 40 mm below the surface and the ordinate indicates unaveraged

horizontal stresses, i.e. σ_x . Along the boundaries where material properties are not continuous, layered elements predict a large difference in unaveraged stress, while graded elements predict almost identical unaveraged stresses, illustrating the superiority of graded elements. Moreover, surface tensile stresses, which are important in thermal cracking problems, are underestimated when homogeneous elements are used, as shown in Figure 2.9.

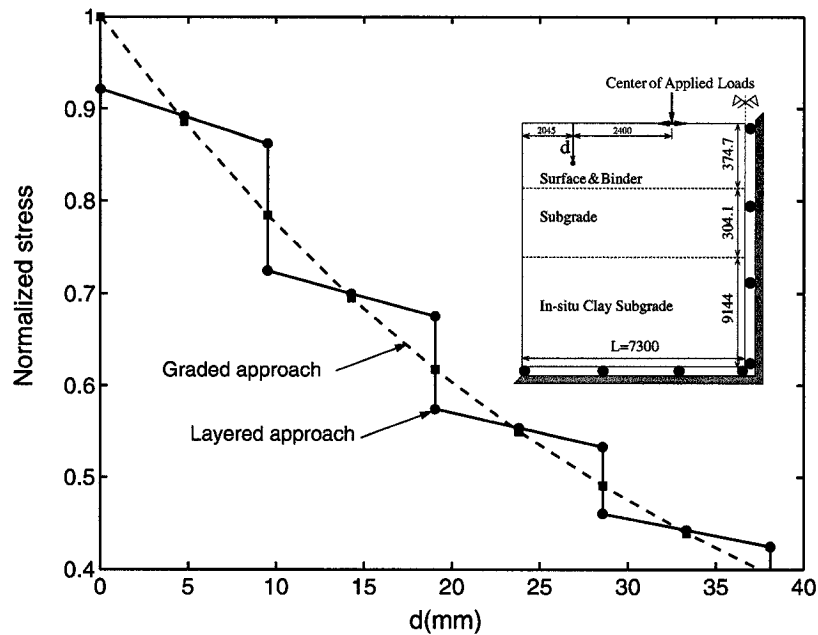


Figure 2.9: 2D graded model versus 2D layered model: Normalized unaveraged horizontal stress (σ_x) with depth (d) at the location where maximum tensile stresses occur.

Figure 2.10 shows the comparison of compressive stresses between graded and layered approaches. The abscissa indicates the vertical evaluation depth up to 40mm below the surface, starting just below the center of the applied loads. The ordinate indicates the normalized unaveraged horizontal stresses, i.e. σ_x . The range of stresses is between -6.6 and -2.1MPa. As expected, homogeneous Q8 elements show piecewise variation. However, this does not occur with the graded elements. Moreover, the surface stresses are underestimated when homogeneous elements are adopted. A benefit of graded elements is pronounced when the stiffness gradient is severe (see Figure 2.7) for this problem. Notice that although the realistic tire loads [84] consisting of the normal and shear traction are applied, surface tension

under the tire loads are not observed in this simulation.

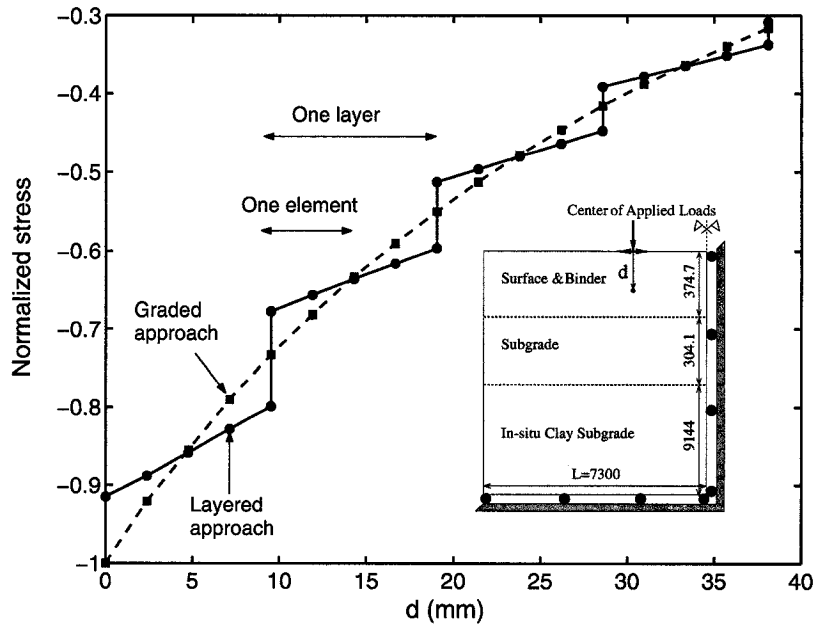


Figure 2.10: 2D graded model versus 2D layered model : Normalized unaveraged horizontal stress (σ_x) with depth (d) along the center of the tire loads.

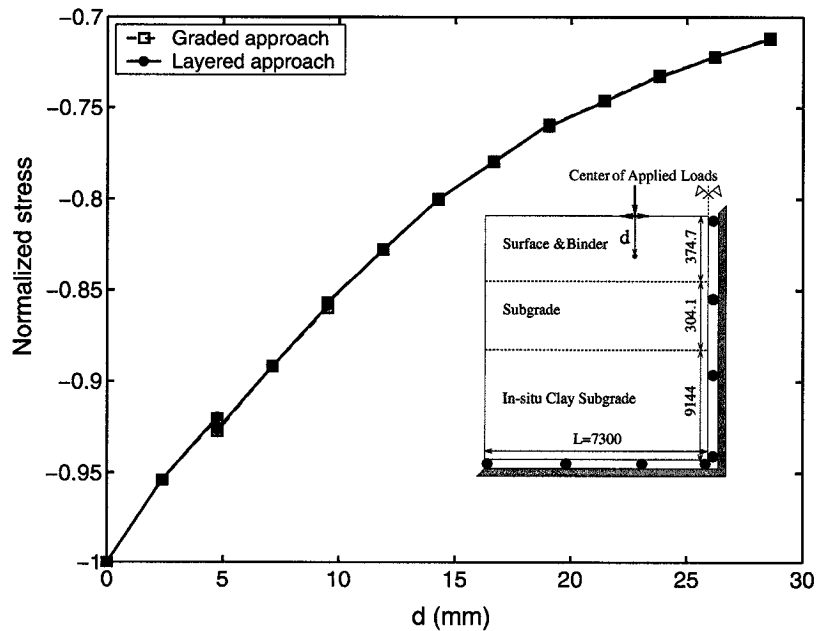


Figure 2.11: 2D graded model versus 2D layered model : Normalized unaveraged vertical stress (σ_z) with depth (d) along the center of the tire loads.

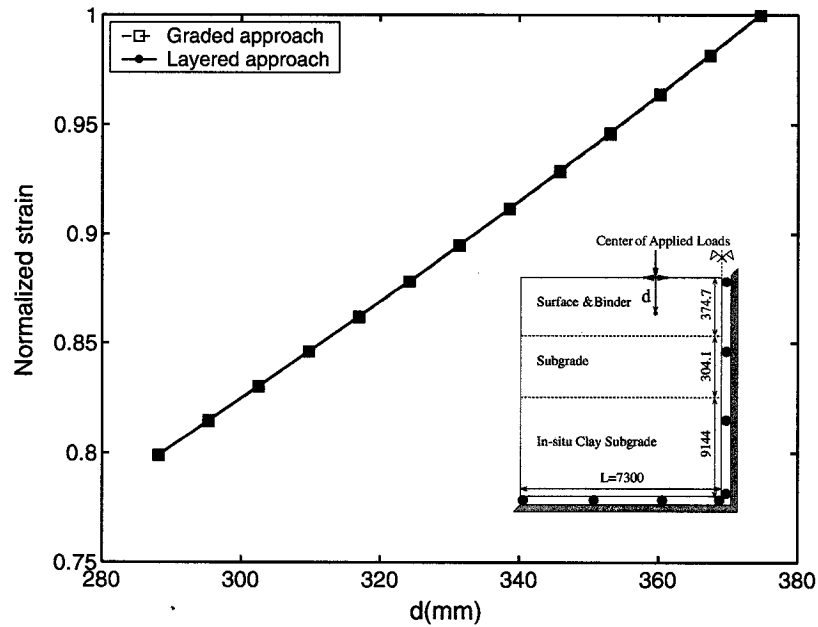


Figure 2.12: 2D graded model versus 2D layered model : Normalized unaveraged horizontal strain (ϵ_x) with depth (d) along the center of the tire loads.

Normalized unaveraged σ_z versus vertical depth is plotted for two different approaches in Figure 2.11. The range of stresses in the plot is between -1.15 and $-0.84 MPa$. The absolute magnitude of σ_z decreases as the vertical distance increases. However, for σ_z , which is an important stress component in evaluating rutting potential in pavements, the two approaches yield almost identical results. Normalized unaveraged tensile strains for graded and layered approaches are illustrated in Figure 2.12. The range of strains in the plot is between 0.37 and 0.46×10^{-3} . The abscissa indicates the vertical distance from the bottom of the surface to 85 mm above this point, directly beneath the center of the applied loads. The absolute magnitude of ϵ_x decreases almost linearly with position. As expected, the difference between graded and layered approaches are insignificant in this case, where material gradations are small. Thus, for the purpose of a traditional fatigue analysis (bottom-up cracking due to bending induced tensile stresses), the traditional layered approach may suffice.

2.5 Concluding remarks

This chapter presents the development and application of graded finite elements for pavement analysis. The implementation of the UMAT was verified by comparing the numerical results with the analytical solutions by means of the isotropic graded materials where Young's modulus varies perpendicular to the loading direction. Numerical examples illustrate the benefits of using graded elements.

The combination of temperature and aging gradients led to the prediction of a large E^* gradient with depth for the selected conditions on Interstate pavement I-155 in Illinois. The stiffness gradient was found to be severe as far down as 100mm of depth.

In general, the graded finite element method used here provides better results over the conventional finite element solution, which involves assigning mixture properties in layers. As expected, the differences were most pronounced when evaluating near-surface pavement responses, where severe material gradients are present due to environmental exposure. The use of fine meshes and stress averaging techniques can be used to minimize errors in the layered approach. However, both of these techniques can have significant drawbacks. For instance, very fine meshes are computationally expensive, particularly when conducting three-dimensional analyses. Furthermore, averaging of nodal stresses was shown to lead to inaccuracies at layer interfaces of different materials, and may lead to inaccuracies in areas of high stress gradients, such as in the vicinity of cracks or other discontinuities.

Chapter 3

Cohesive zone models

This chapter provides theoretical and numerical aspects of three cohesive zone models adopted in this study. For each model, both traction vector and tangent modulus matrix are evaluated. A description on how the cohesive element is incorporated into a finite element framework follows. Experimental procedures to evaluate bulk properties and cohesive parameters, e.g. relaxation modulus, fracture energy and material strength, are presented.

3.1 Various cohesive zone models

In this section, three cohesive laws, i.e. exponential, bilinear and power-law CZMs, are presented in detail. Both traction vector and tangent modulus matrix (cohesive material Jacobian) are evaluated.

3.1.1 Potential based exponential model

An exponential form for the free energy potential proposed by Xu and Needleman [144] between the displacement jump and the corresponding traction provides a computationally convenient description of the decohesion process represented by a shape of constitutive model, material strength and cohesive fracture energy. The present formulation and notation are fairly based on the work by Needleman, Ortiz, Dodds and co-workers [86, 89, 108].

The exponential form for the free energy potential is given by [144]:

$$\phi = \exp(1)\sigma_c\delta_{cc} \left[1 - \left(1 + \frac{\delta_e}{\delta_{cc}} \right) \exp \left(-\frac{\delta_e}{\delta_{cc}} \right) \right] \quad (3.1)$$

where σ_c is the material strength (critical traction), and δ_{cc} is the critical displacement in which traction becomes a maximum. The effective displacement (δ_e) and the corresponding effective traction (t_e) for two-dimensional (2D) analysis become:

$$\delta_e = \sqrt{\delta_n^2 + \beta^2\delta_s^2}, \quad t_e = \sqrt{t_n^2 + \beta^{-2}t_s^2}, \quad (3.2)$$

in which subscript e denotes effective, δ_n and δ_s represent normal opening and shear sliding displacements, respectively, and t_n and t_s stand for the corresponding normal and shear tractions, respectively. The parameter β , which is defined as the ratio between maximum normal traction and shear traction, is introduced to express the formulation with single effective displacement by assigning different weights for displacements and tractions along normal and shear directions.

As illustrated in Figure 3.1 (a), the relationship between the effective displacement and the corresponding traction, upon loading, follows the form:

$$t_e = \frac{\partial\phi}{\partial\delta_e} = \exp(1)\sigma_c\frac{\delta_e}{\delta_{cc}} \exp\left(-\frac{\delta_e}{\delta_{cc}}\right), \quad (3.3)$$

and for unloading and reloading, the traction can be obtained with the following expression:

$$t_e = \left(\frac{t_u}{\delta_u} \right) \delta_e, \quad (3.4)$$

where subscript u indicates a point where unloading starts to occur in the cohesive law (see Figure 3.1 (a)). The unloading path follows toward the origin of the cohesive law. The cohesive fracture energy is defined by:

$$G_c = \int_0^{\infty} t_e d\delta_e = e\sigma_c\delta_{cc}. \quad (3.5)$$

The shear and normal tractions are obtained from differentiating energy potential, ϕ ,

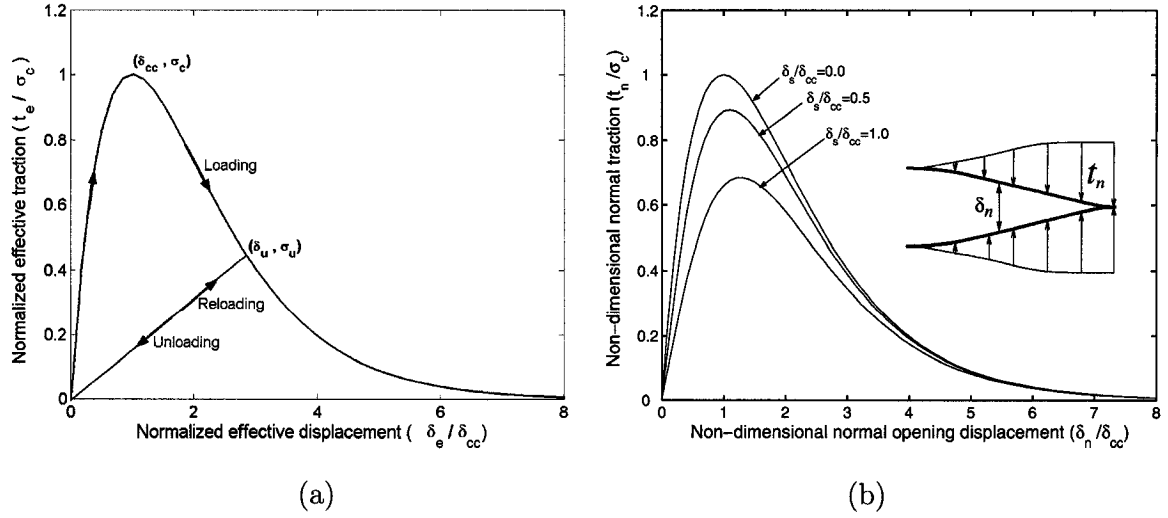


Figure 3.1: The exponential cohesive law in terms of (a) the normalized effective displacement and the normalized effective traction and (b) the non-dimensional normal opening displacement and non-dimensional normal traction for different ratios of non-dimensional shear sliding displacements.

with respect to shear sliding and normal opening displacements, respectively:

$$t_s = \frac{\partial \phi}{\partial \delta_s} = \frac{\partial \phi}{\partial \delta_e} \frac{\partial \delta_e}{\partial \delta_s} = t_e \frac{\delta_s}{\delta_e} = e \sigma_c \frac{\delta_e}{\delta_{cc}} \exp\left(\frac{-\delta_e}{\delta_{cc}}\right) \frac{\delta_s}{\delta_e} \beta^2 \quad (3.6)$$

$$t_n = \frac{\partial \phi}{\partial \delta_n} = \frac{\partial \phi}{\partial \delta_e} \frac{\partial \delta_e}{\partial \delta_n} = t_e \frac{\delta_n}{\delta_e} = e \sigma_c \frac{\delta_e}{\delta_{cc}} \exp\left(\frac{-\delta_e}{\delta_{cc}}\right) \frac{\delta_n}{\delta_e} \quad (3.7)$$

Figure 3.1 (b) shows the cohesive law in terms of non-dimensional normal opening displacement and non-dimensional normal traction for several different ratios of normalized shear sliding displacements.

The tangent modulus matrix, \mathbf{C} , is obtained from differentiating tractions, i.e. t_s and t_n , with respect to shear sliding and normal opening displacements, i.e. δ_s and δ_n . The components of the tangent modulus matrix are given as

$$C_{ss} = \frac{\partial t_s}{\partial \delta_s} = \frac{t_e \beta^2}{\delta_e} + \frac{\beta^4 \delta_s^2}{\delta_e^2} \left[A - \frac{t_e}{\delta_e} \right] \quad (3.8)$$

$$C_{sn} = \frac{\partial t_s}{\partial \delta_n} = C_{ns} = \frac{\partial t_n}{\partial \delta_s} = \frac{\beta^2 \delta_n \delta_s}{\delta_e^2} \left[A - \frac{t_e}{\delta_e} \right] \quad (3.9)$$

$$C_{nn} = \frac{\partial t_n}{\partial \delta_n} = \frac{t_e}{\delta_e} + \frac{\delta_n^2}{\delta_e^2} \left[A - \frac{t_e}{\delta_e} \right], \quad (3.10)$$

in which t_e is given by Eq. (3.3) and A is given as

$$A = \frac{t_e}{\delta_e} \left[1 - \frac{\delta_e}{\delta_{cc}} \right] \quad (3.11)$$

3.1.2 Bilinear cohesive zone model

Despite the many successful applications of the potential based exponential cohesive law reported in the literature, the model inherently produces artificial compliance due to a pre-peak slope described in this cohesive law. Recently, Espinosa and Zavattieri [39] formulated a bilinear model to reduce CZM compliance by providing an adjustable initial slope in the cohesive law.

Non-dimensional effective displacement and effective traction are defined as

$$\lambda_e = \sqrt{\left(\frac{\delta_n}{\delta_c}\right)^2 + \left(\frac{\delta_s}{\delta_c}\right)^2} \quad \text{and} \quad (3.12)$$

$$t_e = \sqrt{t_n^2 + t_s^2}, \quad (3.13)$$

respectively. δ_c is a critical displacement where complete separation, i.e. zero traction, occurs.

As illustrated in Figure 3.2 (a), the cohesive law in terms of non-dimensional effective displacement and effective traction has the following expression

$$t_e = \begin{cases} \sigma_c \frac{\lambda_e}{\lambda_{cr}} & \lambda_e < \lambda_{cr} \\ \sigma_c \frac{1-\lambda_e}{1-\lambda_{cr}} & \lambda_e > \lambda_{cr} \end{cases} \quad (3.14)$$

For unloading and reloading, the traction can be obtained from

$$t_e = \left(\frac{t_u}{\lambda_u} \right) \lambda_e. \quad (3.15)$$

The pre-peak region represents the elastic part of the intrinsic cohesive law whereas the softening portion after the peak load accounts for damages occurring in the fracture process

zone (see Figure 3.2 (a)). Notice that the parameter λ_{cr} is non-dimensional displacement in which the traction is a maximum, and is incorporated to reduce the elastic compliance by adjusting the pre-peak slope of the cohesive law. In other words, as the value of λ_{cr} decreases, the pre-peak slope of the cohesive law increases and as a result, artificial compliance is reduced. The cohesive fracture energy is given as

$$G_c = \frac{1}{2} \delta_c \sigma_c \quad (3.16)$$

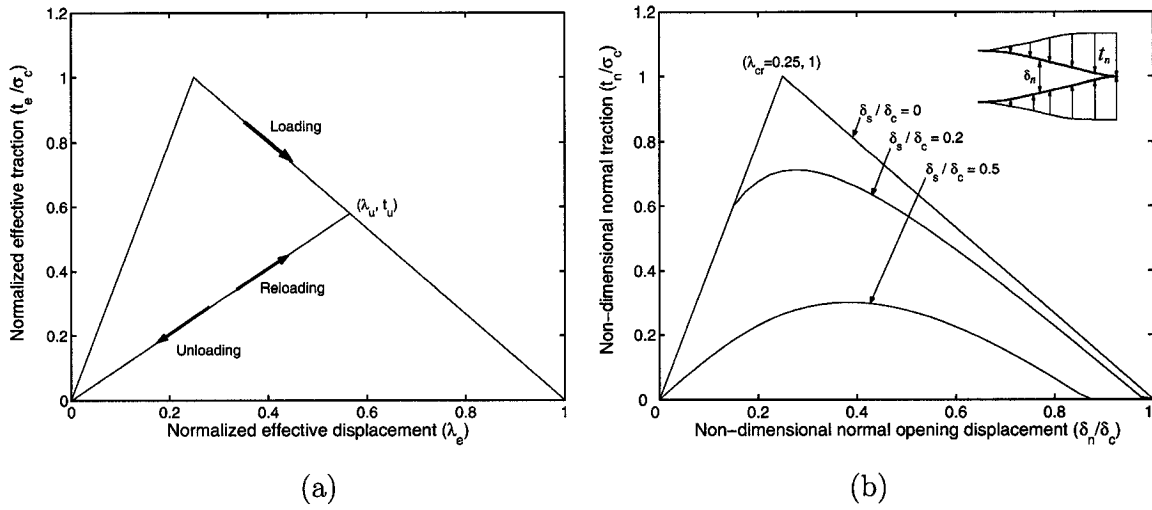


Figure 3.2: A bilinear cohesive law in terms of (a) non-dimensional effective displacement and non-dimensional effective traction and (b) non-dimensional normal opening displacement and non-dimensional normal traction.

For $\lambda_e < \lambda_{cr}$, the components of the traction vector are given as

$$t_s = \sigma_c \frac{1}{\lambda_{cr}} \left(\frac{\delta_s}{\delta_c} \right) \quad \text{and} \quad t_n = \sigma_c \frac{1}{\lambda_{cr}} \left(\frac{\delta_n}{\delta_c} \right), \quad (3.17)$$

and for $\lambda_e > \lambda_{cr}$, the shear and normal tractions are described by

$$t_s = \sigma_c \frac{1 - \lambda_e}{1 - \lambda_{cr}} \frac{1}{\lambda_e} \left(\frac{\delta_s}{\delta_c} \right) \quad \text{and} \quad t_n = \sigma_c \frac{1 - \lambda_e}{1 - \lambda_{cr}} \frac{1}{\lambda_e} \left(\frac{\delta_n}{\delta_c} \right). \quad (3.18)$$

Figure 3.2 (b) shows the bilinear cohesive law in terms of non-dimensional normal opening displacement and non-dimensional normal traction for several different ratios of non-

dimensional shear sliding displacements.

The tangent modulus matrix is obtained from differentiating tractions, i.e. t_s and t_n , with respect to relative displacements, i.e. δ_s and δ_n . For $\lambda_e < \lambda_{cr}$, the tangent modulus matrix components are given as

$$C_{ss} = \frac{\partial t_s}{\partial \delta_s} = C_{nn} = \frac{\partial t_n}{\partial \delta_n} = \frac{\sigma_c}{\lambda_{cr} \delta_c} \quad (3.19)$$

$$C_{sn} = \frac{\partial t_s}{\partial \delta_n} = C_{ns} = \frac{\partial t_n}{\partial \delta_s} = 0 \quad (3.20)$$

and for $\lambda_e > \lambda_{cr}$, they are given as

$$C_{ss} = \frac{\partial t_s}{\partial \delta_s} = -\frac{\delta_c \sigma_c}{1 - \lambda_{cr}} \left(\frac{\delta_s}{\lambda_e \delta_c^2} \right)^2 + (1 - \lambda_e) \frac{\delta_c \sigma_c}{1 - \lambda_{cr}} \left(\frac{1}{\lambda_e \delta_c^2} - \frac{1}{\lambda_e^3 \delta_c^4} \right) \quad (3.21)$$

$$C_{sn} = \frac{\partial t_s}{\partial \delta_n} = C_{ns} = \frac{\partial t_n}{\partial \delta_s} = -\frac{\delta_c \sigma_c}{1 - \lambda_{cr}} \left(\frac{\delta_s}{\lambda_e \delta_c^2} \right) \left(\frac{\delta_n}{\lambda_e \delta_c^2} \right) + (1 - \lambda_e) \frac{\delta_c \sigma_c}{1 - \lambda_{cr}} \left(-\frac{1}{\lambda_e^3} \frac{\delta_s \delta_n}{\delta_c^4} \right) \quad (3.22)$$

$$C_{nn} = \frac{\partial t_n}{\partial \delta_n} = -\frac{\delta_c \sigma_c}{1 - \lambda_{cr}} \left(\frac{\delta_n}{\lambda_e \delta_c^2} \right)^2 + (1 - \lambda_e) \frac{\delta_c \sigma_c}{1 - \lambda_{cr}} \left(\frac{1}{\lambda_e \delta_c^2} - \frac{1}{\lambda_e^3} \frac{\delta_n^2}{\delta_c^4} \right). \quad (3.23)$$

3.1.3 Power-law cohesive zone model

A CZM softening shape for asphalt concrete and other quasi-brittle materials is as important as the cohesive parameters, i.e. fracture energy and material strength, due to the relatively large size of the fracture process zone compared to the structure size. However, most CZMs including the models presented in Sections 3.1.1 and 3.1.2 do not have an variable to control a CZM softening shape, which represents progressive softening phenomena occurring along the fracture process zone. In this study, a power-law cohesive zone model [35] is revisited and improved 1) to reduce artificial compliance, 2) to model general cases, e.g. mixed-mode and three-dimensional, and 3) to have various choices in terms of CZM softening shapes.

The effective displacement, δ_e , and the effective traction, t_e , for three-dimensional (3D) analysis become

$$\delta_e = \sqrt{\delta_n^2 + \delta_s^2} = \sqrt{\delta_n^2 + \delta_{s1}^2 + \delta_{s2}^2} \quad (3.24)$$

$$t_e = \sqrt{t_n^2 + t_s^2} = \sqrt{t_n^2 + t_{s1}^2 + t_{s2}^2} \quad (3.25)$$

in which δ_{s1} and δ_{s2} denote components of shear sliding displacement (δ_s), and t_{s1} and t_{s2} are components of shear traction (t_s).

The power-law cohesive zone model can be expressed as

$$t_e = \begin{cases} \sigma_c \delta_e / \delta_{cc} & \delta_e < \delta_{cc} \\ \sigma_c (1 - \delta_e / \delta_c)^\alpha \frac{1}{(1 - \delta_{cc} / \delta_c)^\alpha} & \delta_e > \delta_{cc} \end{cases} \quad (3.26)$$

where δ_{cc} is displacement where traction becomes a maximum, δ_c is critical displacement in which a complete separation (i.e. zero traction) occurs, α is an internal variable affecting a CZM softening shape. Notice that δ_{cc} is a user defined variable to control a pre-peak slope which influences artificial compliance. The parameter δ_c is obtained by equating the area of the displacement and traction curve to the cohesive fracture energy which is given as

$$G_c = \frac{\sigma_c \delta_{cc}}{2} + \int_{\delta_{cc}}^{\delta_c} t_e d\delta_e \quad (3.27)$$

Figure 3.3 (a) illustrates various shapes of the power-law CZM. The ordinate is normalized effective traction. The abscissa is effective displacement which is normalized with respect to critical displacement evaluated when $\alpha = 1$, say $\delta_c^{\alpha=1.0}$. Notice that $\delta_{cc} / \delta_c^{\alpha=1.0} = 0.1$. When α is equal to zero, it is a rectangular shape. As α increases, the shape of the power-law CZM softening curves changes from the linear to nonlinearly decaying shapes. Notice that when $\alpha = 1$, this model is equivalent to the bilinear model [39] explained in Section 3.1.2. The bilinear model refers to the model in which slopes of both pre-peak and post-peak curves are linear, and is different from the bilinear softening curve, which is commonly used in concrete literature [13].

For $\delta_e < \delta_{cc}$, the components of the traction are expressed as

$$t_{s1} = \sigma_c \frac{\delta_{s1}}{\delta_{cc}}, \quad t_{s2} = \sigma_c \frac{\delta_{s2}}{\delta_{cc}}, \quad t_n = \sigma_c \frac{\delta_n}{\delta_{cc}}, \quad (3.28)$$

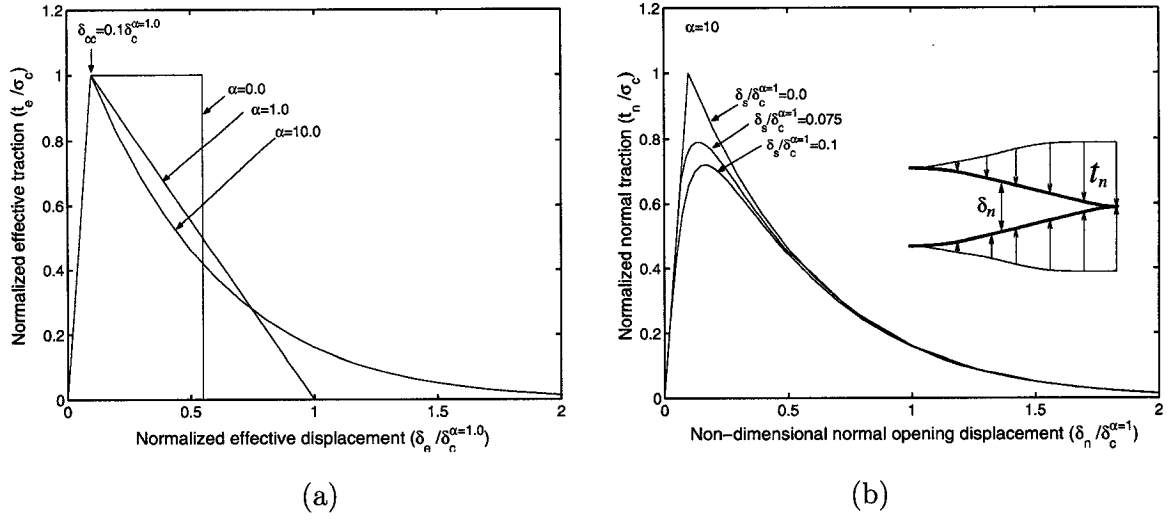


Figure 3.3: The power-law cohesive zone model in terms of (a) the normalized effective displacement and the normalized effective traction and (b) the non-dimensional normal opening displacement and non-dimensional normal traction for different ratios of non-dimensional shear sliding displacement.

and for $\delta_e > \delta_{cc}$, they are governed by

$$\begin{aligned}
 t_{s1} &= \sigma_c \left(1 - \frac{\delta_e}{\delta_c}\right)^\alpha \frac{1}{(1 - \delta_{cc}/\delta_c)^\alpha} \frac{\delta_{s1}}{\delta_e}, \\
 t_{s2} &= \sigma_c \left(1 - \frac{\delta_e}{\delta_c}\right)^\alpha \frac{1}{(1 - \delta_{cc}/\delta_c)^\alpha} \frac{\delta_{s2}}{\delta_e}, \\
 t_n &= \sigma_c \left(1 - \frac{\delta_e}{\delta_c}\right)^\alpha \frac{1}{(1 - \delta_{cc}/\delta_c)^\alpha} \frac{\delta_n}{\delta_e}.
 \end{aligned} \tag{3.29}$$

The components of tangent modulus matrix are give as

$$\begin{aligned}
 C_{s1s1} &= \frac{\partial t_{s1}}{\partial \delta_{s1}}, \quad C_{s1s2} = \frac{\partial t_{s1}}{\partial \delta_{s2}} = C_{s2s1} = \frac{\partial t_{s2}}{\partial \delta_{s1}}, \\
 C_{s1n} &= \frac{\partial t_{s1}}{\partial \delta_n} = C_{ns1} = \frac{\partial t_n}{\partial \delta_{s1}}, \quad C_{s2s2} = \frac{\partial t_{s2}}{\partial \delta_{s2}}, \\
 C_{s2n} &= \frac{\partial t_{s2}}{\partial \delta_n} = C_{ns2} = \frac{\partial t_n}{\partial \delta_{s2}}, \quad C_{nn} = \frac{\partial t_n}{\partial \delta_n},
 \end{aligned} \tag{3.30}$$

where the traction components are given by Eq. (3.28) for $\delta_e < \delta_{cc}$, and by Eq. (3.29) for $\delta_e > \delta_{cc}$. Figure 3.3 (b) shows the power-law CZM with $\alpha = 10$ for various ratios of non-dimensional shear sliding displacement in terms of non-dimensional normal opening

displacement and non-dimensional normal traction.

3.1.4 Remarks

From Sections 3.1.1 through 3.1.3, various cohesive laws are presented. In this section, brief remarks on the CZMs are provided. Figure 3.4 illustrates a comparison of normal traction versus normal opening displacement among the exponential CZM, the bilinear CZM and the power-law CZM with $\alpha = 10$. Notice that the bilinear CZM is equivalent to the power-law CZM with $\alpha = 1$. Material strength (σ_c) and cohesive fracture energy (G_c) are assumed to be 1 for the illustration purpose. Consistent units are used.

Artificial compliance is not avoidable in an intrinsic CZM and the pre-peak slope of the CZM is a major source of the compliance. An attractive feature in the bilinear and power-law CZMs compared to the exponential model is that we can control the pre-peak slope to minimize compliance. In this section, δ_{cc} is defined as $0.01\alpha_c^{\alpha=1}$. As illustrated in Figure 3.4, the pre-peak slope of the bilinear and power-law CZMs is much stiffer than that of the exponential CZM so that undesirable compliance can be reduced. Discussion on artificial compliance is presented in Chapter 5.

For asphalt concrete and other quasibrittle materials, a CZM softening shape is as relevant as cohesive parameters due to the relatively large size of the fracture process zone compared to the structure size. A nice feature in the power-law CZM compared to the bilinear and exponential CZMs is that we can have various choices in CZM softening shapes which represents progressive softening behavior occurring along the fracture process zone. For instance, the bilinear model (see Figure 3.4) has the constant reduction of capacity with respect to displacement jump, which may not be relevant to asphalt concrete. This aspect is discussed in detail in Chapter 6.

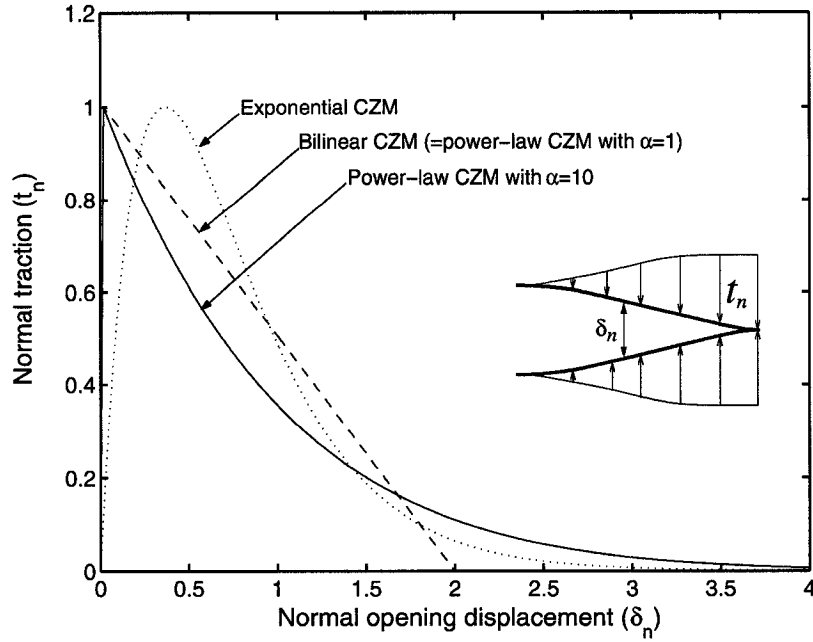


Figure 3.4: Normal traction (t_n) versus normal opening displacement (δ_n) curves of various cohesive laws.

3.2 Computational framework

The section describes how the cohesive element is incorporated into a finite element framework. A displacement-based formulation is adopted.

3.2.1 CZM formulation

The principle of virtual work considering the cohesive element contribution is given as:

$$\int_V (\boldsymbol{\varepsilon}^*)^T \boldsymbol{\sigma} dV - \int_S (\boldsymbol{\delta}^*)^T \boldsymbol{t} dS - \int_S (\boldsymbol{u}^*)^T \boldsymbol{t} dS = 0, \quad (3.31)$$

where superscript T denotes transpose, $\boldsymbol{\sigma}$ is the Cauchy stress tensor, $\boldsymbol{\varepsilon}^*$ is the virtual strain tensor, \boldsymbol{t} is the traction on the boundary, $\boldsymbol{\delta}^*$ is the virtual displacement jump across the cohesive element, \boldsymbol{u}^* is virtual displacement in the bulk (background) material, and S and V represent the current (deformed) surface and volume, respectively.

An implicit displacement-based finite element scheme requires evaluation of several terms such as a force vector and a tangent stiffness matrix based on different numerical schemes.

The evaluation of the tangent stiffness matrix and the force vector is necessary for the iteration of the Newton-Raphson method and the Riks method. An additional term, which is an incremental load vector, needs to be defined for the iteration of the Riks method [2]. The force vector and the tangent stiffness matrix of the cohesive elements are obtained from the second term of Eq.(3.31) and the first variation of the second term in Eq.(3.31), respectively. Notice that the incremental load vector of the cohesive elements to be defined for the Riks method is zero for the CZM because a cohesive force is independent of the Riks load parameter.

Due to the fact that the integration is carried out at Gauss points, we need to interpolate displacement at nodal points to relative displacement at Gauss points using \mathbf{B} matrix, which consists of shape function:

$$\boldsymbol{\delta}^* = \mathbf{B}\bar{\mathbf{u}}^*, \quad (3.32)$$

in which $\boldsymbol{\delta}^*$ and $\bar{\mathbf{u}}^*$ represent virtual relative displacement vector at the Gauss points and virtual displacement at the nodal points, respectively. Substituting Eq.(3.32) into the second term of Eq.(3.31), one obtains the virtual cohesive element work, which is given as

$$W^* = \int_S ((\bar{\mathbf{u}}^*)^T \mathbf{B}^T \mathbf{t}) dS = (\bar{\mathbf{u}}^*)^T \int_S \mathbf{B}^T \mathbf{t} dS \quad (3.33)$$

Thus, the force vector due to cohesive elements can be obtained as follows:

$$\mathbf{f} = \int_S \mathbf{B}^T \mathbf{t} dS \quad (3.34)$$

The first variation of the virtual work, dW^* , is obtained from differentiation of Eq. (3.33) with respect to relative displacements, i.e. δ_n and δ_s , and is given as

$$dW^* = (\bar{\mathbf{u}}^*)^T \int_S (\mathbf{B}^T d\mathbf{t}) dS. \quad (3.35)$$

Notice that \mathbf{t} is a function of δ_n and δ_s such that $d\mathbf{t}$ can not be zero. The relationship between traction and displacement jump is given by the tangent modulus matrix, \mathbf{C} , which

is obtained as

$$\begin{Bmatrix} dt_n \\ dt_s \end{Bmatrix} = \mathbf{C} \begin{Bmatrix} d\delta_n \\ d\delta_s \end{Bmatrix} \quad (3.36)$$

where \mathbf{C} is given by

$$\mathbf{C} = \begin{bmatrix} \partial t_n / \partial \delta_n & \partial t_n / \partial \delta_s \\ \partial t_s / \partial \delta_n & \partial t_s / \partial \delta_s \end{bmatrix}$$

Thus, the tangent stiffness matrix is given by the usual expression

$$\mathbf{K} = \int_S \mathbf{B}^T \mathbf{C} \mathbf{B} dS. \quad (3.37)$$

Notice that Eqs. (3.34) and (3.37) are formulated based on the updated Lagrangian formulation.

3.2.2 Finite element implementation

This section describes how the CZMs presented in Section 3.1 are incorporated into the ABAQUS user element (UEL) [2]. In the UEL, the contribution of cohesive elements to the force vector and the tangent stiffness matrix, which are functions of displacements, cohesive parameters and internal variables, should be defined. Because the force vector and the tangent stiffness matrix need to be defined globally, while the cohesive law represents a local separation and traction relationship, transformation between global and local coordinates is necessary. Consider the 4-noded cohesive element shown in Figure 3.5. The parameter θ represents the angle between global and local coordinates. X and Y denote global coordinates, while s and n indicate local coordinates. Nodes 1 and 2 are located on the bottom of the element whereas nodes 3 and 4 are located on the top of the element. Each node has two degrees of freedom. The global displacement vector of the nodes belonging to the cohesive element can be expressed as follows:

$$\mathbf{u} = [u_X^1 \ u_Y^1 \ u_X^2 \ u_Y^2 \ u_X^3 \ u_Y^3 \ u_X^4 \ u_Y^4]^T \quad (3.38)$$

where superscripts indicate node numbers.

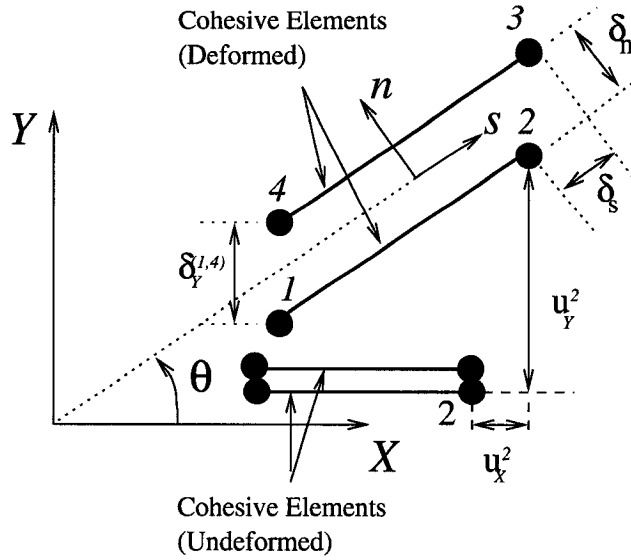


Figure 3.5: Schematic drawing of a 4-noded linear cohesive element. Variables δ_s and δ_n represent shear sliding and normal displacement jump, respectively. Variables u_x^2 and u_y^2 denote global displacements of node 2 along X and Y directions, respectively. The variable $\delta_Y^{(1,4)}$ represents the opening displacement along Y direction, while θ indicates the angle between global and local coordinates. Notice that X and Y denote global coordinates, whereas s and n denote local coordinates.

Based on the global coordinate system, the relative displacements (i.e. δ_X and δ_Y) between top and bottom nodes can be obtained as

$$\begin{Bmatrix} \delta_X^{(1,4)} \\ \delta_Y^{(1,4)} \\ \delta_X^{(2,3)} \\ \delta_Y^{(2,3)} \end{Bmatrix} = \mathbf{L}\mathbf{u}, \quad \mathbf{L} = \begin{bmatrix} 1 & 0 & 0 & 0 & 0 & 0 & -1 & 0 \\ 0 & 1 & 0 & 0 & 0 & 0 & 0 & -1 \\ 0 & 0 & 1 & 0 & -1 & 0 & 0 & 0 \\ 0 & 0 & 0 & 1 & 0 & -1 & 0 & 0 \end{bmatrix} \quad (3.39)$$

where \mathbf{L} is the operator matrix, and superscripts denote corresponding nodes of the interface element for which cohesive separation will be enforced (see Figure 3.5). The relative global displacement at Gauss points can be obtained as follows

$$\begin{Bmatrix} \delta_X \\ \delta_Y \end{Bmatrix} = \begin{bmatrix} N_1 & 0 & N_2 & 0 \\ 0 & N_1 & 0 & N_2 \end{bmatrix} \begin{Bmatrix} \delta_X^{(1,4)} \\ \delta_Y^{(1,4)} \\ \delta_X^{(2,3)} \\ \delta_Y^{(2,3)} \end{Bmatrix} = \mathbf{N} \begin{Bmatrix} \delta_X^{(1,4)} \\ \delta_Y^{(1,4)} \\ \delta_X^{(2,3)} \\ \delta_Y^{(2,3)} \end{Bmatrix} = \mathbf{N}\mathbf{L}\mathbf{u} \quad (3.40)$$

Note that δ_X and δ_Y require transformation from global coordinates to a local coordinate system for the cohesive element. Let matrix \mathbf{R} define the orthogonal transformation from global reference frame (X, Y) to the element specific, local coordinate system (s, n) , where the direction n lies normal to the cohesive element. Finally, the relative local displacement vector, δ_s and δ_n , is obtained as follows

$$\begin{Bmatrix} \delta_s \\ \delta_n \end{Bmatrix} = \mathbf{B}\mathbf{u} = \mathbf{R}\mathbf{N}\mathbf{L}\mathbf{u}. \quad (3.41)$$

The global nodal force vector and global tangent stiffness matrix for a 4-noded cohesive element can be evaluated as:

$$\mathbf{f} = \int_{-1}^1 \mathbf{B}^T \mathbf{t} J_0 d\zeta, \quad \mathbf{K} = \int_{-1}^1 \mathbf{B}^T \mathbf{C} \mathbf{B} J_0 d\zeta \quad (3.42)$$

where J_0 denotes the Jacobian between reference and original coordinates. Notice that the evaluation of the traction vector (\mathbf{t}) and the tangent modulus matrix (\mathbf{C}) are presented for each cohesive law in Section 3.1, e.g. Eqs. (3.6) through (3.10).

3.3 Determination of bulk and cohesive properties

In this section, experimental procedures to obtain bulk and cohesive parameters, i.e. complex modulus, relaxation modulus, fracture energy and material strength, are presented briefly.

3.3.1 Complex modulus

The complex (dynamic) modulus is often used to characterize the time-temperature modulus of asphalt concrete, and is used as a material property for the design of asphalt pavement layers (NCHRP 1-37a). The essence of the test is to apply a sinusoidal compressive loading on the specimen and measure the strain response. The complex modulus is simply the amplitude of the stress wave divided by the amplitude of the strain wave. In order to capture the time-temperature dependency, the complex modulus is measured over a range of frequencies (25, 10, 5, 1, 0.5, and 0.1 Hz) and temperatures (-10 to 60 $^{\circ}C$).

3.3.2 Relaxation modulus

In order to obtain relaxation modulus in asphalt concrete, first a creep test, where constant stress is imposed, is performed and a Voight-Kelvin model is used to describe creep compliance behavior. Then, interconversion schemes are adopted to obtain relaxation modulus.

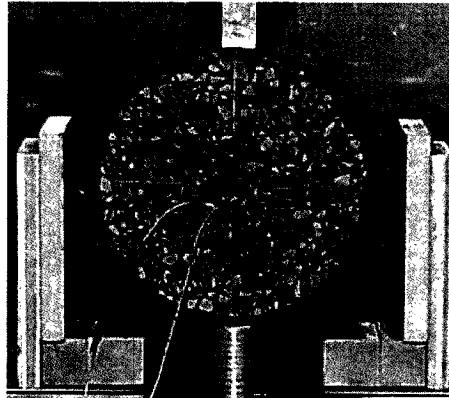
The creep compliance, $D(t)$, is usually the primary quantity to be obtained for the creep test for which the Superpave IDT test is employed. For typical asphalt mixtures, creep test in which a fixed load that produces a horizontal deformation of 0.00125 mm to 0.0190 mm for 150-mm diameter specimens are employed is performed for multiple temperatures, e.g. -20, -10, and 0°C. Model constants are obtained from creep tests and shift factors are evaluated from shifting compliance versus time curve at different temperatures in log scale to establish a smooth and continuous curve. Various schemes are employed to obtain relaxation modulus from creep compliance. Detailed creep test procedures and interconversion schemes are found in references [1, 17, 48, 93].

3.3.3 Cohesive parameters

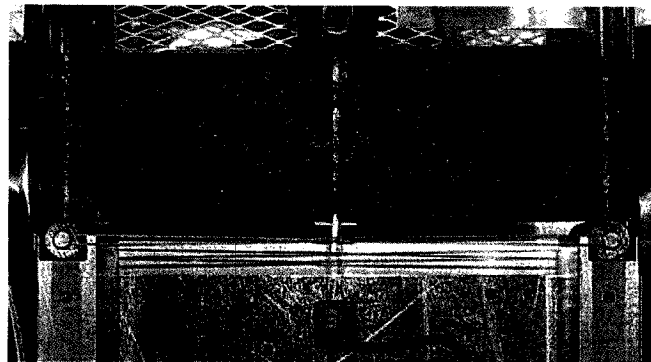
Two experimental fracture properties of material strength and fracture energy are evaluated as material inputs into the CZM. The first-failure tensile strength determined from the IDT test is defined as the material strength. The procedure for determining the first-failure tensile strength is outlined in the AASHTO specification [1]. Figure 3.6 (a) illustrates IDT test setting.

The fracture energy of asphalt concrete is the other fracture property required as an input into the CZM. Either the single-edge notched beam (SE(B)) and the disk-shaped compact tension (DC(T)) test was used for determining the fracture energy. The crack-mouth opening displacement (CMOD) was increased at a linear rate to produce a stable post-peak fracture. The CMOD rate was determined by trial and error to produce a peak load at approximately five seconds into the test. Five seconds was selected as the time to peak load based on the AASHTO procedure [1] for determining the tensile strength. The fracture energy was

determined by calculating the area under either the load-CMOD curve or the load- δ_{25} and normalizing by the cross-sectional area of the specimen. A detailed procedure for specimen preparation and test controls of the SE(B) and DC(T) test are outlined [133, 134]. For illustration purpose, the SE(B) test apparatus is shown in Figure 3.6 (b).



(a)



(b)

Figure 3.6: Experimental setting of (a) IDT test and (b) SE(B) test.

3.4 Concluding remarks

In this chapter, various aspects of three cohesive zone models are presented. Both traction vector and tangent stiffness matrix are evaluated for each cohesive law. Computational framework is presented in conjunction with ABAQUS user element (UEL) subroutine. Experimental procedures to compute bulk properties and cohesive parameters are presented.

Among the various CZMs investigated, the power-law CZM appears to be the most suited for investigating fracture of asphalt concrete due to the capability to control a pre-peak slope, which influences artificial compliance, and to have various softening shapes, which affect progressive softening behavior. It includes the bilinear model as a special case when $\alpha = 1$.

Chapter 4

Fracture modeling using the exponential CZM

This chapter explores fracture behavior in asphalt concrete using an intrinsic cohesive zone model (CZM). The separation and traction response along the cohesive zone ahead of a crack tip is governed by an exponential cohesive law [144] specifically tailored to describe cracking in asphalt pavement materials by means of softening associated to the cohesive law. Finite element implementation of the CZM is accomplished by means of a user-subroutine using the user element (UEL) capability of the ABAQUS software, which is verified by simulation of the double cantilever beam test and by comparison to closed-form solutions. The cohesive parameters of finite material strength and cohesive fracture energy are calibrated in conjunction with the single-edge notched beam (SE(B)) test. The CZM is then extended to simulate mixed-mode crack propagation in the SE(B) test in which cohesive elements are inserted over an area. It is shown that the simulated crack trajectory compares favorably with that of experimental results.

4.1 Introduction

In order to better understand cracking in pavement systems, many experimental investigations have been conducted. Majidzadeh [78] first attempted to study crack propagation using fracture testing. Since then, several researchers [54, 80, 101] have developed fracture

testing programs, with varying degrees of success, to measure and describe crack initiation and propagation in asphalt concrete. Cohesive zone models (CZMs) have been used in the analysis and simulation of crack propagation for both homogeneous and nonhomogeneous material systems. Dugdale [36] and Barenblatt [7, 8] proposed cohesive models to investigate ductile and brittle material fracture behavior, respectively. Xu and Needleman [144] and Camacho and Ortiz [19] presented a potential based cohesive model and stress-based cohesive model, respectively, with a corresponding implementation by means of the finite element method. These models have been extended to explore crack propagation in concrete [109], ductile metals [108] and functionally graded materials (FGMs) [96]. Recently, an improved description of the exponential cohesive zone model by Xu and Needleman [144] was developed by van den Bosch et al. [130]. Cohesive zone modeling involves the placement of interface elements in a finite element model, where the separation law used at the interface describes a typical softening curve. Cohesive zone models are particularly useful for computational modeling of fracture processes for a number of reasons, including: 1) computational efficiency; 2) ability to simulate complex global fracture behavior with a relative simple, local (intrinsic) damage function; 3) ability to simulate crack nucleation, crack initiation, and non-prescribed, mixed-mode crack propagation. For asphalt concrete, Soares et al. [121] used a cohesive zone modeling approach to investigate crack propagation in indirect tension (IDT) specimens using the cohesive law proposed by Tvergaard [129]. However, they performed only pure-mode I crack propagation simulations in conjunction with IDT and they did not address important issues clearly, e.g. selection of a cohesive element size.

Therefore, the following important aspects of cohesive zone modeling of asphalt concrete are presented and discussed in this chapter thoroughly:

- Verification of the CZM implementation into ABAQUS user element (UEL) using double cantilever beam (DCB) test simulation.
- Sensitivity analysis of cohesive parameters to fracture response.

- Justification of selecting cohesive element sizes for asphalt concrete fracture modeling.
- Simulation of mixed-mode crack propagation in conjunction with SE(B) test in which mesh discretizations of cohesive elements are tailored to the crack trajectory predicted by I-Franc2D [61].
- Comparison of complete crack trajectory of the present numerical simulation using the Riks method [103, 30] and the user element (UEL) of ABAQUS [2] with that of experimental results.

4.2 Verification of CZM

In order to verify the numerical implementation of the exponential CZM explained in Section 3.1.1 into the UEL of ABAQUS, a DCB test simulation is performed, because the DCB is well accepted by the fracture community and an analytical solution exists. Using linear elastic beam theory, the analytical solution for crack length in terms of Young's modulus (E), the end displacement (Δ), the beam height (H) and the cohesive fracture energy (G_c) is obtained as [5]

$$a = \sqrt[4]{\frac{3EH^3\Delta^2}{4G_c}}. \quad (4.1)$$

Figure 4.1 illustrates a schematic of the DCB geometry. To avoid shear effects in the beam, a relatively slender DCB of length $L = 200mm$ and width $H = 10mm$ is adopted. External displacement is applied to the node located at $x = 0$ and $y = 0$ upward and downward. Cohesive elements are inserted along the middle of specimen. Two-dimensional plane strain elements and linear four node cohesive elements are employed for the bulk material and cohesive material, respectively. To obtain material and cohesive parameters, a 9.5-mm nominal maximum sized aggregate surface mixture is selected, which is used at the Greater Peoria Regional Airport. Young's modulus is taken as $14.2 GPa$, based upon the aforementioned modulus tests. A Poisson's ratio value of 0.35 is assumed, based upon previous experience with similar materials. The cohesive fracture energy and material strength for

this mixture are $344J/m^2$ and $3.56MPa$, respectively. For the exponential model, $0.1\delta_c$ is defined as the crack tip location.

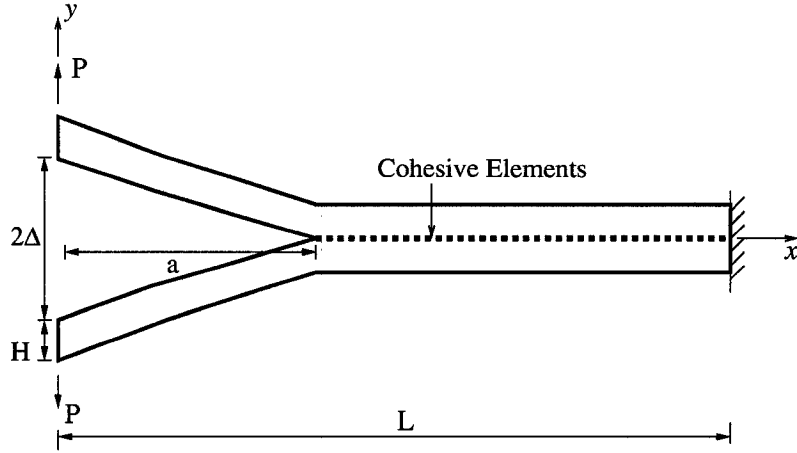


Figure 4.1: Schematic drawing of the double cantilever beam (DCB) test in which H is the thickness, 2Δ is crack mouth opening displacement, L is the total length, and a is the distance from the crack mouth to the assumed crack tip location.

Figure 4.2 illustrates a comparison between numerical and analytical solutions. The abscissa indicates normalized crack length, a/L , and the ordinate indicates the normalized crack opening displacement, Δ/δ_c . The numerical results show excellent agreement with the analytical solution. Notice that even for both initial stage and final stage of crack propagation, which are influenced by boundary conditions, both numerical and analytical results agree reasonably well.

4.3 Mode-I single-edge notched beam (SE(B)) test simulation

In this section, utilizing mode I SE(B) test, various important aspects of CZM are presented. First, justification of cohesive elements size is provided. Three different cohesive element sizes are chosen and numerical results for each cohesive element size are compared to make sure that element sizes chosen in the simulation are small enough to capture the nonlinear behavior occurring along the cohesive zone [66]. Second, sensitivity analysis to cohesive

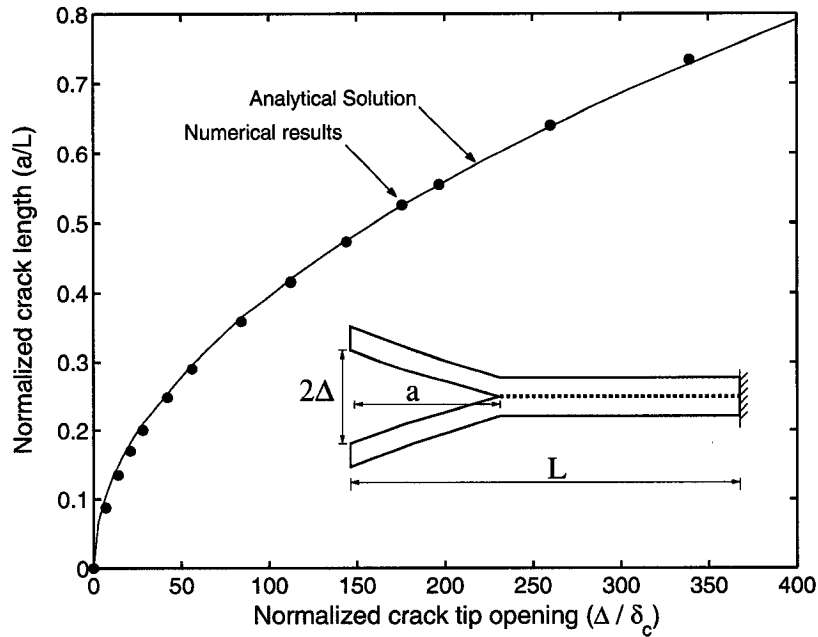


Figure 4.2: Comparison between numerical and analytical solutions for the DCB specimen.

parameters of material strength and cohesive fracture energy is performed. Finally, cohesive parameters of material strength and cohesive fracture energy are calibrated by comparing numerical result with experimental results of SE(B) test.

4.3.1 Selection of a cohesive element size

When the concept of the cohesive zone model is combined with the discrete finite element method, a numerical issue on the sensitivity of the size of cohesive element to the numerical solution arises. It is due to the fact that the cohesive zone is represented by a highly nonlinear relation between traction and displacement jump such that enough cohesive elements need to be inserted along the cohesive zone in order to capture nonlinearly softening behavior properly. Camacho and Ortiz [19] showed that, as cohesive element size increases, considerable accuracy is lost under dynamic loading. Furthermore, they reported that some of fragmentation and branching is suppressed when the coarse mesh is adopted. Recently, Klein et al. [66] explored the influence of cohesive element sizes in conjunction with the

double cantilever beam, and illustrated that coarse meshes yield accelerated crack growth, i.e. larger discrepancy between numerical and analytical solutions. Ruiz et al. [109] studied mesh size sensitivity to computational results, e.g. reaction versus time curve, simulating SE(B) tests with and without pre-notch under dynamic loading. They observed that for the cracked SE(B), the reaction histories and energy consumption are almost identical for different cohesive element sizes; while for the uncracked SE(B), the cohesive energy consumption is larger for the finer mesh and as time increases, the discrepancy of the reaction increases for different cohesive element sizes. A general rule in choosing the element size is that there should be at least 3 elements or so along the fracture process zone. For some specific brittle materials, the fracture process zone can be estimated theoretically as [102]

$$\ell_c = \frac{\pi}{8} \frac{E}{1 - \nu^2} \frac{G_c}{\sigma_{ave}^2} \quad (4.2)$$

where G_c is the cohesive fracture energy and σ_{ave} is a measure of material strength in an average sense. However, this estimation may not be valid for materials such as asphalt concrete which is quasi-brittle and viscoelastic, because Eq. (4.2) is evaluated based on the assumption that energy is absorbed in a very thin cohesive zone without any consideration of viscoelastic effects. Thus, from numerical point of view, although viscoelastic effects are not directly considered, it is crucial to make sure that the cohesive element size chosen is not sensitive to artifacts of the numerical solution. In this study, three different cohesive element sizes, i.e. $0.1mm$, $0.2mm$ and $1.0mm$, are employed.

Figure 4.3 (a) illustrates a simply supported SE(B) with length of $376mm$, height of $100mm$ and thickness of $75mm$. A mechanical notch is simulated, which extends $19mm$ upward from the bottom edge of the beam. Displacement boundary conditions are imposed at the center of the top edge of the model. Figures 4.3 (b) and (c) show a finite element configuration for the whole geometry and the center region of the specimen where cohesive elements are inserted, respectively. Notice that cohesive element size $1.0mm$ is used in Figure 4.3. Two-dimensional, four-noded cohesive elements are inserted along the center

of the specimen. The bulk material is modeled as elastic, homogeneous, isotropic, and rate-independent. Given the low test temperature and short test duration, it is assumed that the bulk material can be adequately simulated with elastic materials. In this analysis, $E = 14.2\text{GPa}$, $\nu = 0.35$, $G_c = 344\text{J/m}^2$ and $\sigma_c = 3.56\text{MPa}$. The Newton-Raphson method and plane strain conditions are adopted.

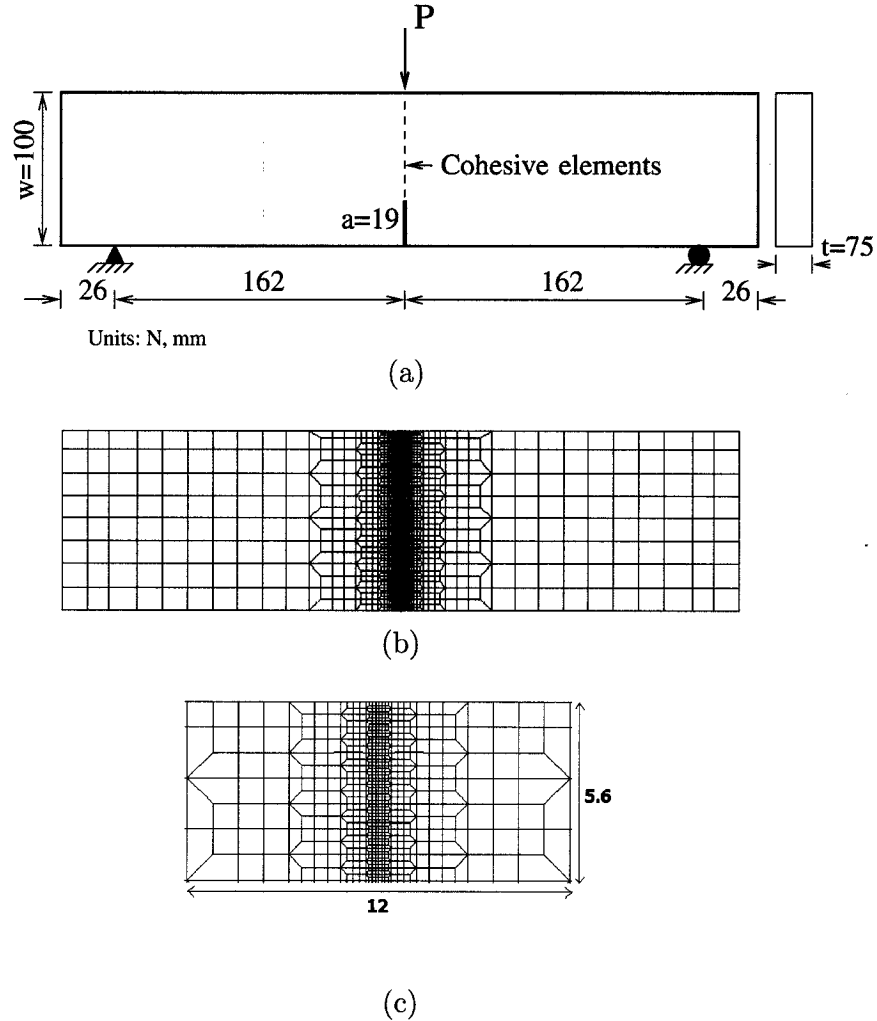


Figure 4.3: Geometry and mesh for analysis of the SE(B) test: (a) geometry and boundary condition; (b) mesh configuration for whole geometry; (c) mesh detail along the middle of the specimen. Notice that cohesive elements are inserted along the middle line of the specimen. Notice that cohesive element size 0.1mm is used.

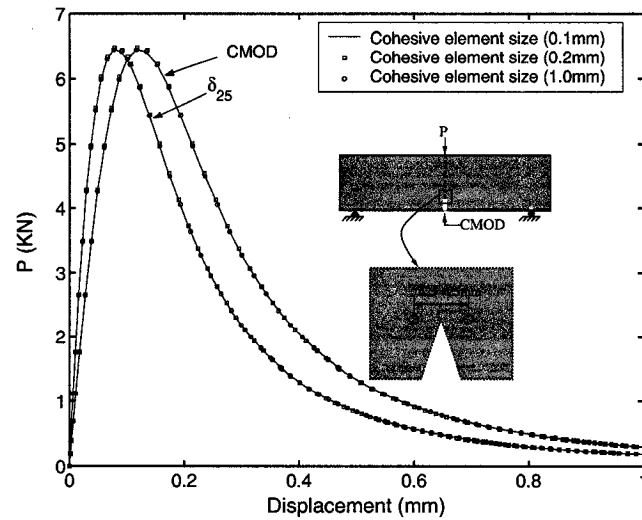
To illustrate that the cohesive element size chosen in this study is objective (i.e. some-

how independent of a particular numerical solution), a local quantity, e.g. δ_{25} , and global quantities, i.e. CMOD and total dissipated energy due to fracture, are evaluated and compared. The δ_{25} , which is measured from gage length of 25mm spanning the original crack tip, is introduced for operational definition of crack tip opening displacement (CTOD) with the following advantages: it is a local quantity near crack tip; and it can be applied to any cracked specimen due to direct and easy measurement of CTOD. The proposed δ_{25} measurement is inspired by the work by Schwalbe and his coworkers [116, 114] who proposed the insightful δ_5 concept. Notice that the original concept of δ_5 was developed and has been applied for fine grain sized materials like steel [21]. However, due to the coarse microstructure of asphalt concrete (e.g. aggregate sizes ranging from 4.75mm to 19mm in this study), the δ -type evaluation in the order of 25mm is more appropriate, leading, for instance, to the δ_{25} definition. Notice that a schematic is provided in Figure 4.4 (a).

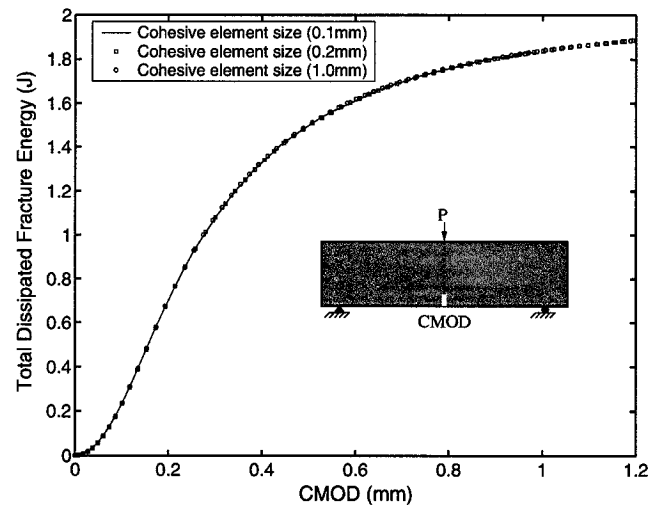
Figure 4.4 (a) illustrates P (applied force) versus displacement curves in which both CMOD and δ_{25} are plotted together. Figure 4.4 (b) shows the consumption of the cohesive fracture energy as the crack propagates. The abscissa indicates the CMOD and the ordinate indicates the total dissipated fracture energy. Due to accumulation of the cohesive fracture energy, it shows an increasing trend of the total dissipated fracture energy with an increase of the CMOD. Both the global and local responses as a function of different cohesive element sizes are nearly identical demonstrating that the cohesive elements chosen in this particular investigation are small enough to be insensitive to numerical artifacts.

4.3.2 Sensitivity analysis with respect to cohesive fracture energy and material strength

In this section, the sensitivity analysis to cohesive parameters of material strength and fracture energy is carried out to explore the influence of cohesive parameters, i.e. $\sigma_c = 3.56\text{MPa}$ and $G_c = 344\text{J/m}^2$ [133]. The geometry, boundary conditions and material properties used here are the same as those used in Section 4.3.1.



(a)



(b)

Figure 4.4: Comparison of (a) the P versus $CMOD$ and δ_{25} and (b) the $CMOD$ versus the total dissipated fracture energy for different cohesive element sizes: $\ell_1=0.1\text{mm}$, $\ell_2=0.2\text{mm}$ and $\ell_3=1.0\text{mm}$. Notice that ℓ_i introduces a length-scale in the problem.

Figure 4.5 (a) illustrates the sensitivity of P versus $CMOD$ curve to different cohesive fracture energy. Three different fracture energies, i.e. $1.2G_c$, G_c and $0.8G_c$, are employed with a constant value of critical strength. As the cohesive fracture energy is increased, the area of P versus $CMOD$ curve is increased and the maximum load is increased as well. This

result is intuitive because as the intrinsic fracture energy used in the CZM is increased, more fracture energy is dissipated, which is indicated by an increased area under the P versus CMOD curve. The softening trend, however, seems insensitive to the magnitude of fracture energy. Figure 4.5 (b) shows the sensitivity of P versus CMOD curve to different critical strength, $1.2\sigma_c$, σ_c and $0.8\sigma_c$. As the critical strength is increased, the maximum load is increased, while the area of the curve remains almost constant.

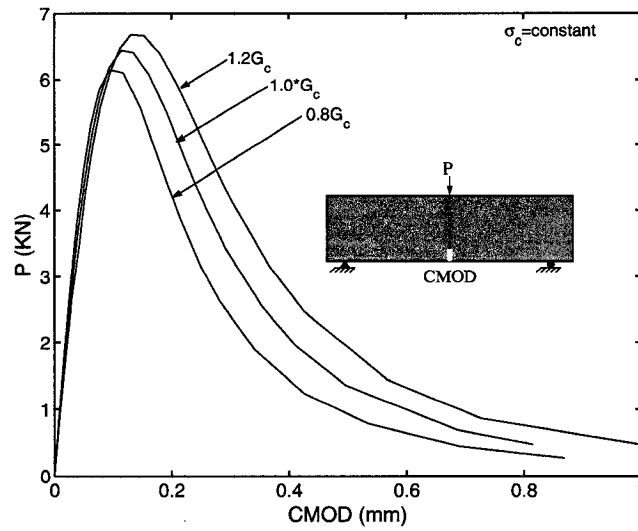
4.3.3 Calibration of cohesive parameters

In the nonlinear cohesive constitutive model, cohesive fracture energy and material strength are two important parameters. These parameters are measured directly from the experiments, and reflect the actual viscoelastic heterogeneous material. However, in the present numerical modeling, bulk material is assumed as elastic, homogeneous and rate-independent, while cohesive material is assumed as inelastic and rate-independent. So, the parameters of the CZM model are calibrated by fitting present numerical results into experimental results in order to take into account these differences between the actual and numerical models. The same geometry, boundary conditions and material properties, which are used in Section 4.3.1, are employed in this section.

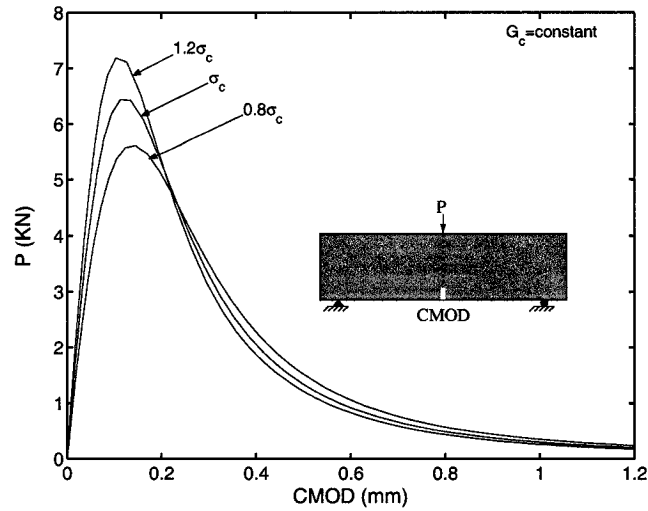
A first order calibration of material strength and cohesive fracture energy was accomplished by matching present numerical results with experimental SE(B) test results (see Figure 4.6). Relatively small calibration shifts of cohesive parameters, i.e. $0.7G_c = 0.7 \times 344J/m^2$ and $1.1\sigma_c = 1.1 \times 3.56MPa$, are required to bring simulated results into reasonable comparison with measured results. The calibrated cohesive parameters are employed in the following simulations.

4.4 Mixed-mode SE(B) test simulation

Using the calibrated cohesive parameters and the cohesive element size $1.0mm$, a simulation of mixed-mode crack propagation in the SE(B) test is carried out. The cohesive elements are



(a)



(b)

Figure 4.5: Sensitivity of P versus $CMOD$ curve to (a) different cohesive fracture energy and (b) different material strength. Notice that $\sigma_c = 3.56 MPa$ and $G_c = 344 J/m^2$.

inserted over an area. Figure 4.7 (a) shows the geometry, boundary condition, and region enclosed by the dashed lines. The length, height and thickness are 376 mm, 100mm and 75mm, respectively. The crack tip is located at 65mm left and 19mm above from the center of bottom edge. Displacement boundary condition is applied at the center of the top edge

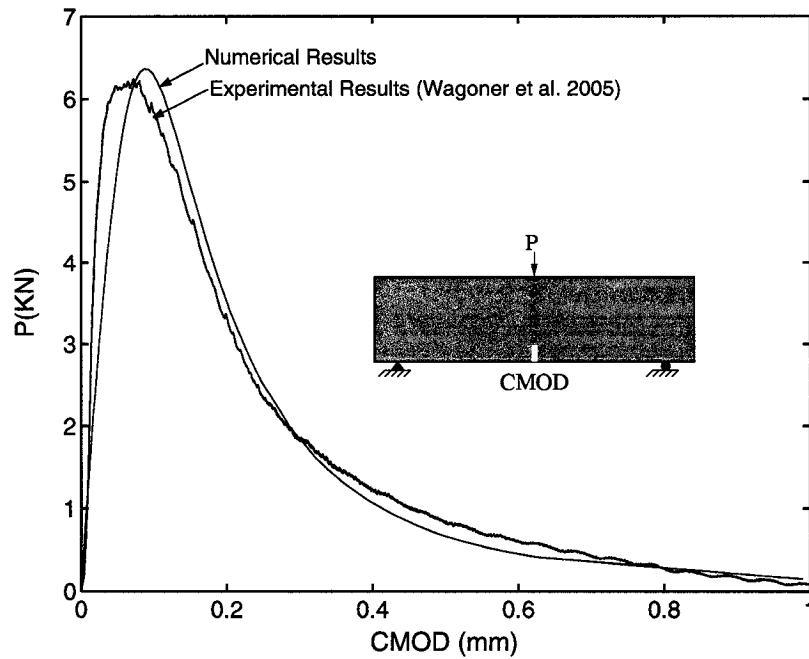
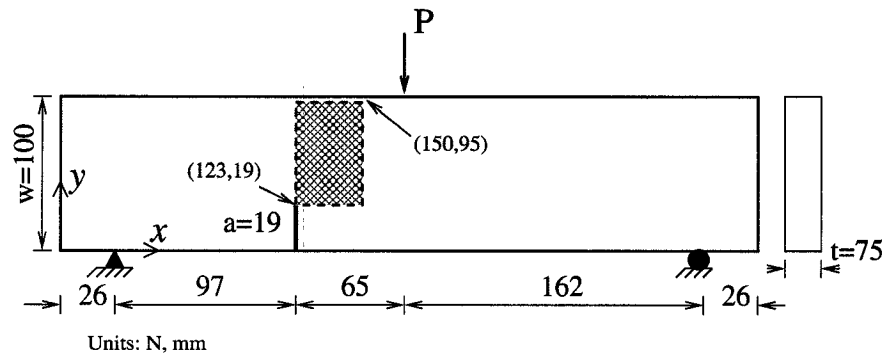


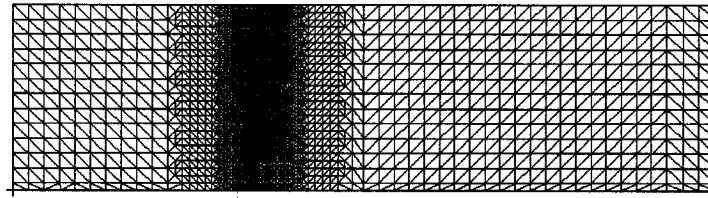
Figure 4.6: Comparison between experimental result and numerical result with calibrated parameters.

of the model. The cohesive elements are inserted over an area enclosed by the dashed lines. Figure 4.7 (b) illustrates finite element discretization for the whole geometry and Figure 4.7 (c) shows finite element mesh details of the region where cohesive elements are inserted. The SE(B) structure is constructed by 5810 3-noded triangular elements for bulk materials, and by 1010 4-noded linear elements for cohesive materials. Notice that in order to avoid numerical convergence problems, the mesh of Figure 4.7 (c) is tailored to the crack trajectory predicted by I-Franc2D [61], and the Riks method [30, 103] is employed for this simulation.

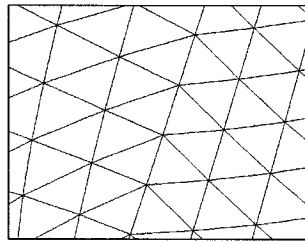
Figure 4.8 (a) shows the final deformed shapes which can be obtained with convergent solutions using the Riks method. A magnification factor of 10 is used to make the crack trajectory visible. We observed that when the Newton-Raphson method is adopted, the cracks begin to grow but eventually the solution diverges when a crack tip reaches around 40 percent of the height of the SE(B) specimen. The main reason of the numerical convergence problem in the CZM is that during the quasi-static calculation, we often reach a point where



(a)



(b)



(c)

Figure 4.7: Mixed-mode SE(B) test: (a) geometry and boundary condition; (b) mesh configuration for whole geometry; (c) mesh detail where cohesive elements are inserted. Notice that dashed line indicates an area where cohesive elements are inserted.

the incremental solution jumps back and forth between two near equilibrium states [127]. However, in this study, this numerical problem is not observed when the Riks method is employed indicating its superior performance compared to the Newton-Raphson method in this particular problem. Detailed discussion on numerical convergence will be presented in Chapter 5. Figure 4.8 (b) illustrates the comparison of the crack trajectory between experiment and numerical results obtained using the Riks method. Green and blue lines indicate the crack trajectory of the front and back side of the specimen based on the experimental

results, respectively. The red line indicates the numerical result, which is in good agreement with the experimental results.

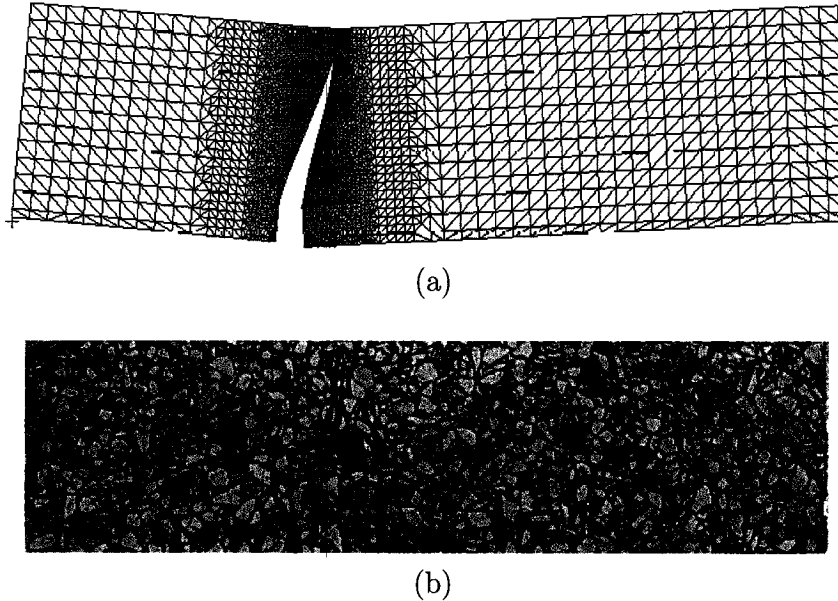


Figure 4.8: Simulation of mixed-mode SE(B) test: (a) deformed shape showing crack trajectory (scale factor is three); (b) comparison of crack trajectory between numerical and experimental results. Red line indicates the crack trajectory obtained from the 2D CZM, while blue line and green lines denote the crack trajectory from the experiment (front and back faces, respectively).

4.5 Concluding remarks

A potential-based cohesive zone model was implemented using a ABAQUS user-specified element (UEL) and employed to simulate crack propagation in asphalt concrete laboratory fracture test of SE(B). To verify the CZM implementation into the UEL of ABAQUS, the slender double cantilever beam is chosen and analyzed. The numerical results from this simulation matched the analytical solution remarkably well even for small crack extensions, which included boundary effects. Using the cohesive parameters obtained from the experiment, i.e. the material strength from the IDT and the fracture energy from the SE(B), a simulation of the SE(B) fracture test was performed to calibrate cohesive parameters.

Overall, the trend, peak load and corresponding CMOD of present numerical results with the calibrated cohesive parameters matched well with experimental results. Moreover, using the same SE(B) test, sensitivity analysis to cohesive element sizes, and cohesive parameters of material strength and fracture energy was performed. The cohesive element sizes chosen here, i.e. $0.1mm$, $0.2mm$ and $1.0mm$, were shown to be insensitive to the numerical solutions. As fracture energy increases, the peak load and the area of the curve increases. Moreover, as the critical strength increases, the peak load increases. Mixed-mode crack propagation simulation of SE(B) test was performed using the calibrated cohesive parameters. In this analysis, the cohesive elements were inserted over an area to allow crack propagation along an arbitrary direction. To avoid numerical convergence problems, the Riks method was employed. The complete crack trajectory of present numerical results matched well with that of experimental results.

Chapter 5

A bilinear cohesive zone model tailored for fracture of asphalt concrete

A bilinear cohesive zone model (CZM) is employed in conjunction with a viscoelastic bulk (background) material to investigate fracture behavior of asphalt concrete. An attractive feature of the bilinear CZM is a potential reduction of artificial compliance inherent in the intrinsic CZM. In this study, finite material strength and cohesive fracture energy, which are cohesive parameters, are obtained from laboratory experiments. Finite element implementation of the CZM is accomplished by means of a user-subroutine which is employed in a commercial finite element code (e.g., UEL in ABAQUS). The cohesive parameters are calibrated by simulation of mode I disk-shaped compact tension results. The ability to simulate mixed-mode fracture is demonstrated. The single-edge notched beam test is simulated where cohesive elements are inserted over an area to allow cracks to propagate in any general direction. The predicted mixed-mode crack trajectory is found to be in close agreement with experimental results. Furthermore, various aspects of CZMs and fracture behavior in asphalt concrete are discussed including: compliance, numerical convergence problems, and energy balance.

5.1 Introduction

Cohesive zone modeling has gained considerable attention over the past decade, as it represents a powerful yet efficient technique for computational fracture studies. During the 90s, leaps were made as a result of the pioneering works by Needleman and his co-workers [86, 144], and Camacho and Ortiz [19]. Xu and Needleman [144] proposed a potential-based cohesive zone model in which cohesive elements are inserted into a finite element mesh in advance, which follow an exponential cohesive law. In such a scheme, as displacement between cohesive elements increases, the traction initially increases, reaches a maximum, and then decays monotonically. On the contrary, Camacho and Ortiz [19] presented a stress-based extrinsic cohesive law where a new surface is adaptively created by duplicating nodes which were previously bonded. Recently, the CZM by Xu and Needleman [144] has been widely used over the model by Camacho and Ortiz [19], because it is relatively easier to implement into the finite element method (FEM). For the study of fracture in asphalt concrete, most efforts to obtain a better understanding of cracking mechanisms in this particulate viscoelastic materials have taken an experimental approach [3, 14, 65, 78]. Recently, Soares et al. [121] applied a cohesive zone model to investigate mode I crack propagation in the Superpave Indirect Tension Test (IDT) using the cohesive law proposed by Tvergaard [129]. Song et al. [123] simulated mode I and mixed-mode crack propagation of laboratory fracture tests, e.g. the single-edge notched beam (SE(B)) test, using a potential based cohesive zone model [144] and investigated various aspects of fracture behavior in conjunction with experiments. However, the models used [129, 144] in asphalt concrete fracture modeling thus far are found to induce considerable artificial compliance due to the pre-peak slope of the intrinsic cohesive law. To diminish artificial compliance inherent in an intrinsic CZM, Geubelle and Baylor [41] and Espinosa and Zavattieri [39] adopted bilinear cohesive zone models to reduce the compliance by providing an adjustable initial slope in the cohesive law. In this study, the bilinear model [39] is employed to reduce artificial compliance.

A relatively fewer number of studies have been carried out which address fracture in viscoelastic materials. Early works in this area include the important contributions of Knauss [67] and Schapery [113], who developed theories for macroscopic cracks in viscoelastic media. More recently, a number of different attempts have been made to consider rate effects in a material separation model. Knauss and Losi [68] combined a viscoelastic constitutive model with a damage function. Rahul Kumar et al. [100] and Allen and Searcy [4] adopted a hereditary integral approach, which is identical with the formulation for the bulk material, in conjunction with a traction-separation function. Bazant and Li [12] formulated a rate-dependent cohesive crack model. Xu et al. [141] has also proposed a rate-dependent CZM, having both rate-independent and rate-dependent material parameters which are determined from experiments and numerical analysis. However, the literature is currently devoid of numerical simulations of fracture in asphalt concrete which consider viscoelastic effects.

Thus, the scope of this chapter is as follows:

- To numerically quantify the effects of CZM compliance with respect to fracture in asphalt concrete.
- To present a bilinear CZM, which has been implemented as UEL in ABAQUS, to effectively reduce artificial compliance in asphalt concrete fracture simulations.
- To investigate the fracture behavior of asphalt concrete considering bulk (background) material viscoelasticity.
- To simulate mixed-mode crack propagation in a SE(B) test in which cohesive elements with a regular pattern are inserted over an area to allow cracks to grow in any general direction and to minimize influence of mesh discretization on crack trajectory.
- To compare the mixed-mode crack trajectory obtained from CZM simulation with that of experimental results.

- To study numerical convergence problems in mixed-mode CZM fracture simulation (including influence of finite element discretization).
- To explore crack competition phenomenon between nucleation and initiation, and predict the exchange of stability between crack initiation and propagation at a critical pre-notch offset.

5.2 CZM compliance issues

CZM compliance is presented briefly in Section 1.3.5. In this section, it is discussed thoroughly. In order to correlate material properties of asphalt concrete and the compliance of the cohesive models, two cohesive models [39, 144] are employed. Identical material properties are used in the comparison of the two models, namely: $E = 14.2GPa$, $\nu = 0.35$, $\sigma_c = 3.56MPa$ and $G_c = 344J/m^2$. These properties were measured from samples of asphalt concrete tested as part of the design of a surface mixture for the rehabilitation of taxiway E at the Greater Peoria (Illinois) Regional Airport in 2001. The effective modulus of the exponential model [144] and bilinear model [39] as a function of h and δ_c is plotted in Figure 5.1. Significant compliance is induced due to the low ratio of σ_c/E , e.g. $\sigma_c/E=0.000276$, when the exponential model is adopted. A considerable reduction of compliance results when the bilinear model is employed. Moreover, the effective modulus (E_{eff}) approaches the properties of continuum (E) as λ_{cr} decreases.

To investigate further the compliance of the cohesive laws [39, 144] using asphalt concrete materials, a simulation of a recently developed SE(B) test for asphalt concrete is performed. Figure 5.2 (a) illustrates a simply supported SE(B) with a length of $376mm$, a height of $100mm$ and a thickness of $75mm$. The simulated mechanical notch extends $19mm$ from the bottom edge of the beam. External loading is imposed at the center of the top edge of the model. Figure 5.2 (b) shows the finite element configuration for the whole geometry, which is constructed using 28112 3-noded triangular plane strain elements. Figure 5.2 (c)

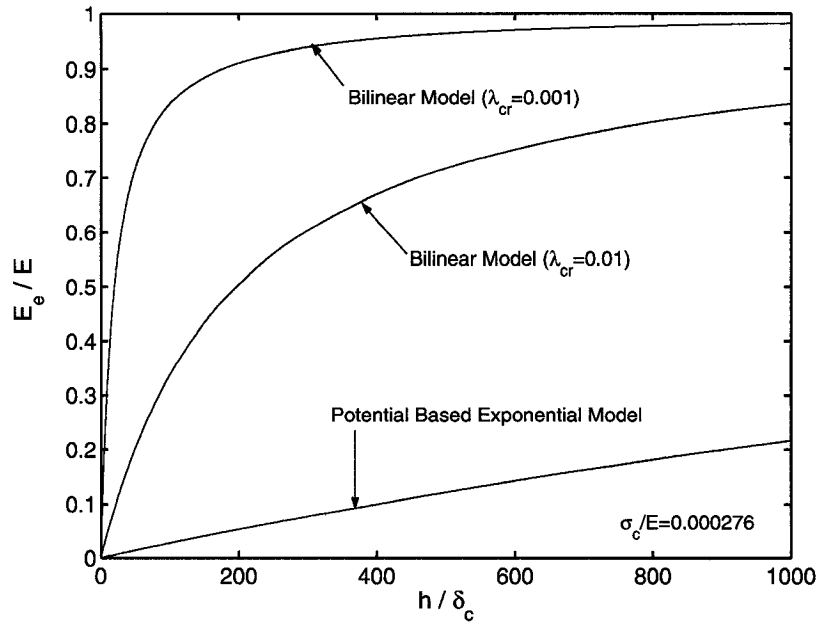
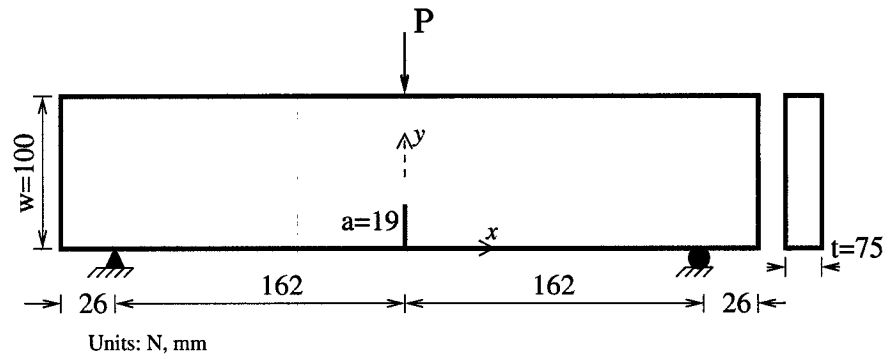


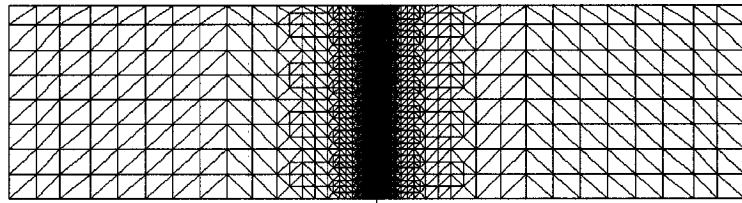
Figure 5.1: Effective modulus as a function of h and δ_c using bilinear and exponential cohesive zone models [144, 39] for asphalt concrete material properties.

illustrates mesh details for the regions where cohesive elements are inserted. Three different cases are considered. In the first case, cohesive elements are inserted only along the center of the specimen with 800 4-noded linear cohesive elements. In the second case, cohesive elements are inserted over central region of the specimen between $(-0.2, 19.0)$ and $(0.2, 99.2)$ with 13236 4-noded linear cohesive elements. Finally, in the third case cohesive elements are inserted between $(-9.2, 19.0)$ and $(9.2, 99.2)$ with 32186 4-noded linear cohesive elements. Notice that the number of cohesive elements used in cases II and III is approximately 15 and 40 times, respectively, larger than that of case I.

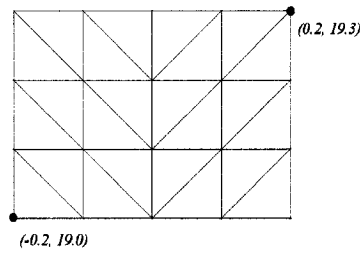
Force (P) versus crack mouth opening displacement (CMOD) curves using the exponential model and the bilinear model for case I are plotted in Figure 5.3 (a). For comparison purposes, the P versus CMOD curve obtained when cohesive elements are not used is plotted, which establishes a baseline corresponding to zero artificially-induced compliance. When the bilinear model is adopted, the compliance is reduced tremendously. Moreover, the influence of λ_{cr} in the bilinear model is noteworthy. To examine the relationship between number of



(a)



(b)

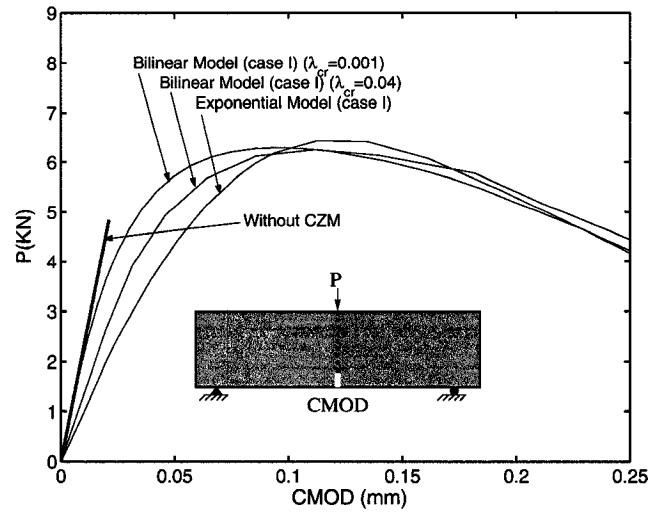


(c)

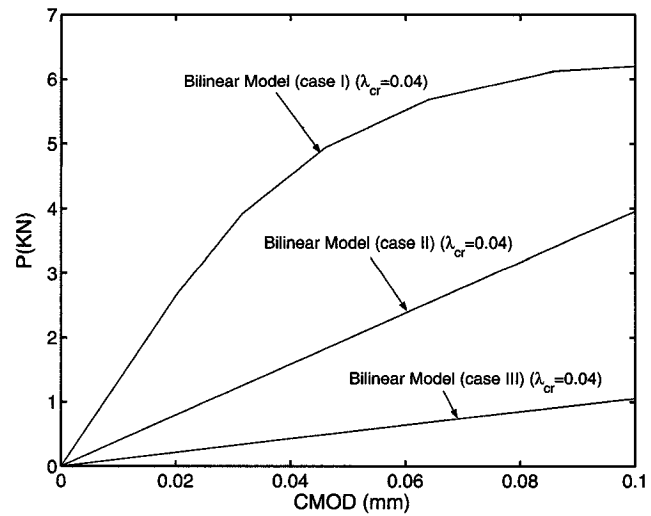
Figure 5.2: SE(B) test simulation: (a) geometry and boundary condition; (b) mesh configuration for the whole geometry; (c) mesh details for the regions where cohesive elements are inserted.

cohesive elements and compliance, P versus $CMOD$ curves using the bilinear model for the three cases are plotted in Figure 5.3 (b). It is clearly observed that as the number of cohesive elements increases, the compliance likewise increases. This is intuitive because as the number of cohesive elements increases, the contribution of the cohesive elements in terms of the compliance likewise increases. Thus, it is recommended to minimize the number of cohesive elements, if possible, and to adopt cohesive zone models which can control a pre-peak slope,

e.g. a bilinear CZM, when modeling fracture in asphalt concrete.



(a)



(b)

Figure 5.3: Comparison of P versus CMOD curves: (a) using cohesive zone models [144, 39] for the case I; and (b) using the bilinear model [39] for the three cases.

5.3 Computational results considering viscoelastic bulk material

In this section, energy balance is presented and simulation of crack propagation in the mode I DC(T) test and mixed-mode SE(B) test are carried out. Notice that brief explanation on viscoelasticity is presented in Section 1.2.2 so that it is not repeated here.

5.3.1 Energy balance

Wagoner et al. [134, 135] proposed the disk-shaped compact tension test, or DC(T), for asphalt concrete. Figure 5.4 (a) illustrates a DC(T) specimen which is 150mm high, 145mm long and 50mm thick. The length of the mechanical notch is 27.5mm, leading to $a/w = 0.25$. Loading pins are inserted in the holes and pulled apart with a closed-loop servohydraulic loading system to induce opening. Figure 5.4 (b) shows mesh discretizations for the whole geometry. The DC(T) test specimen is constructed using 2376 4-noded quadrilateral plane strain elements for the bulk elements and 88 4-noded linear elements for the cohesive elements. The cohesive elements are inserted along the middle of specimen to enable the simulation of pure mode-I crack propagation. Cohesive elements of 1.0mm size are employed, as these are found through parametric investigation to be small enough to capture nonlinear softening behavior occurring in the cohesive zone [123]. A constant Poisson's ratio is used: $\nu=0.35$. The cohesive fracture energy obtained at $-10^{\circ}C$ and 1mm/min. CMOD loading rate is $324J/m^2$ ($G_c = 324J/m^2$), and the material strength measured at $-10^{\circ}C$ is 3.58MPa ($\sigma_c = 3.58MPa$) [131]. Tables 5.1 and 5.2 contain the generalized Maxwell model parameters and shift factors, respectively. Notice that bulk and cohesive material properties employed in the remainder of simulations are based on a typical surface mixture used in central Illinois in which the binder grade is PG 64-22 and a nominal maximum aggregate size (NMAS) of 9.5mm is used [131]. The instantaneous modulus and the modulus at 60sec. and $-10^{\circ}C$ are 25.6GPa and 11.9GPa, respectively.

Figure 5.5 (a) shows energy components for a DC(T) test simulation with a controlled

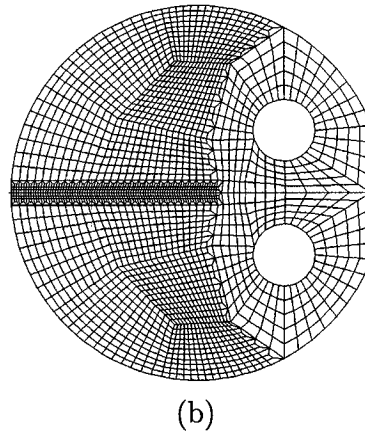
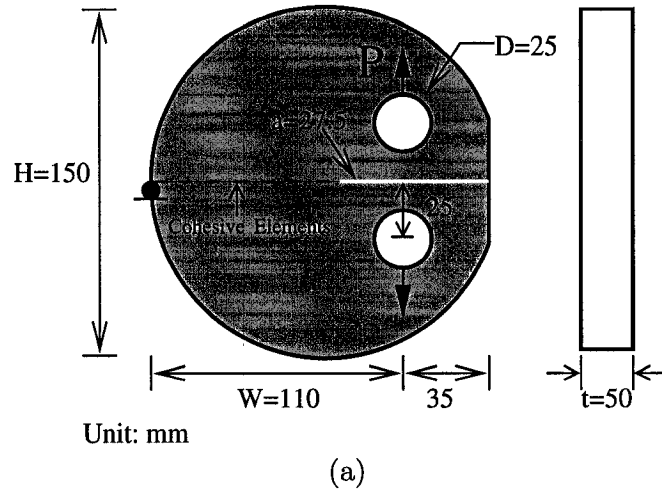


Figure 5.4: DC(T) test simulation; (a) geometry and boundary condition; (b) mesh configurations for the whole geometry.

Table 5.1: Prony series parameters for the master relaxation modulus using the generalized Maxwell model [131].

i	Relaxation Modulus Parameters	
	E_i (GPa)	τ_i (sec)
1	3.4	12
2	3.4	162
3	5.9	1852
4	6.8	17476
5	6.1	465460

CMOD rate of $1\text{mm}/\text{min}$. loading rate and material parameters associated with -10°C . The abscissa represents time and the ordinate denotes components of total energy. The

Table 5.2: Temperature shift factors [131].

Temperatures	$\log(1/a_T)$
$-20^\circ C$	0
$-10^\circ C$	1.34
$0^\circ C$	2.70

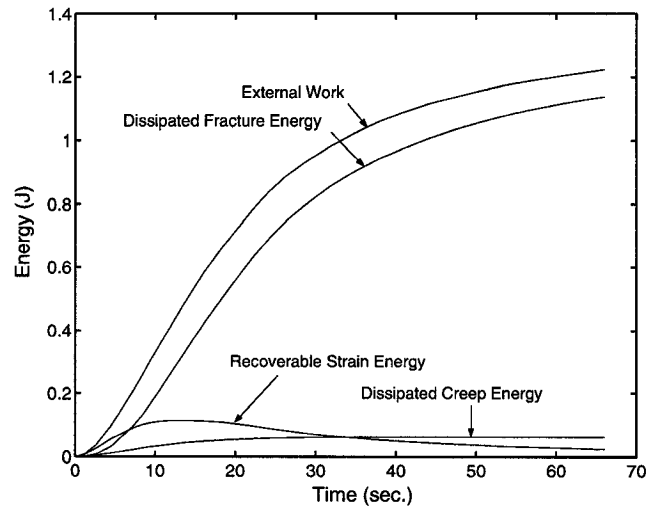
total dissipated fracture energy is computed as part of the UEL and is given as

$$E^f = \sum \int \int t_e d\delta_e dA \quad (5.1)$$

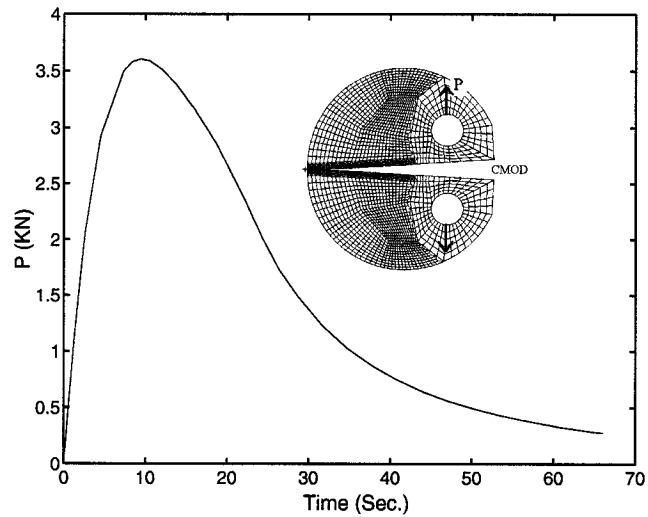
where superscript f denotes fracture, A represents area, and δ_e and t_e denote effective displacement and the corresponding traction between a cohesive element, respectively. As illustrated in Figure 5.5 (a), dissipated fracture energy increases as time increases, which is expected. However, recoverable strain energy and dissipated creep energy show different behavior. As time increases, recoverable strain energy increases, reaches peak point around 10 seconds and then decays as the crack extends through the specimen. This trend is almost identical with that of load versus time as illustrated in Figure 5.5 (b). On the other hand, the creep energy dissipation increases gradually before 40 seconds and shows a steady-state trend after 40 seconds. The contribution of recoverable strain energy, dissipated creep energy and dissipated fracture energy to the total work is 35, 10 and 55 percent, respectively at 10 seconds, and 2, 5 and 93 percent, respectively at 60 seconds.

5.3.2 Calibration of cohesive parameters in the DC(T)

In the nonlinear cohesive constitutive model, the cohesive fracture energy and material strength are the main parameters used in this study. While these parameters obtained from experiments reflect viscoelastic heterogeneous material, several assumptions are made in the current modeling: 1) the bulk element is assumed to be viscoelastic homogeneous; and 2) the cohesive element is assumed to be elastic homogeneous. Furthermore, a cohesive fracture energy obtained from equating to an area of a force versus CMOD curve [118] may



(a)



(b)

Figure 5.5: DC(T) simulation: (a) energy balance with $1.0\text{mm}/\text{min}$. CMOD loading rate at -10°C ; (b) a load versus time curve.

overestimate the local work of separation, because CMOD is contributed from both the bulk and fracture. As a result, model calibration is necessary. In this work, parameters of the CZM model are calibrated by fitting present numerical results to experimental results in order to account for the differences between experiments and numerical simulations.

Figure 5.6 compares the present numerical results with experimental results. The abscissa

indicates $CMOD(mm)$ and the ordinate indicates the load $P(KN)$. Three specimens are tested at $-10C$ and $1mm/min.$ loading rate. Detailed procedures for the $DC(T)$ test are described by Wagoner et al. [134]. The predicted P versus CMOD curve matches favorably with that of experimental results. Relatively small calibration shifts of cohesive parameters, i.e. $0.7G_c = 0.7 \times 324J/m^2$ and $0.95\sigma_c = 0.95 \times 3.58MPa$, are required to bring simulated results into reasonable comparison with measured results. For the rest of simulations, the calibrated cohesive parameters are adopted.

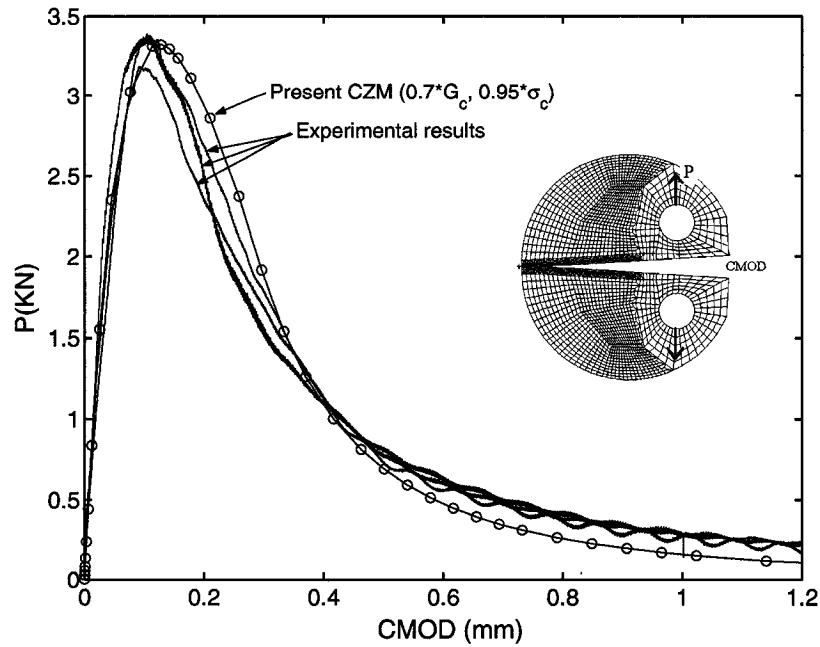


Figure 5.6: Comparison of P versus CMOD curves between numerical and experimental results [135].

5.3.3 Mixed-mode crack propagation in the SE(B)

Unlike the previous example (mode I) where a crack path is predefined, in the simulation of mixed-mode fracture in the SE(B) test cohesive elements are inserted over an area to allow cracks to propagate in any direction. Figure 5.7 (a) shows the geometry, boundary condition, and shaded region where cohesive elements have been inserted. The length, height

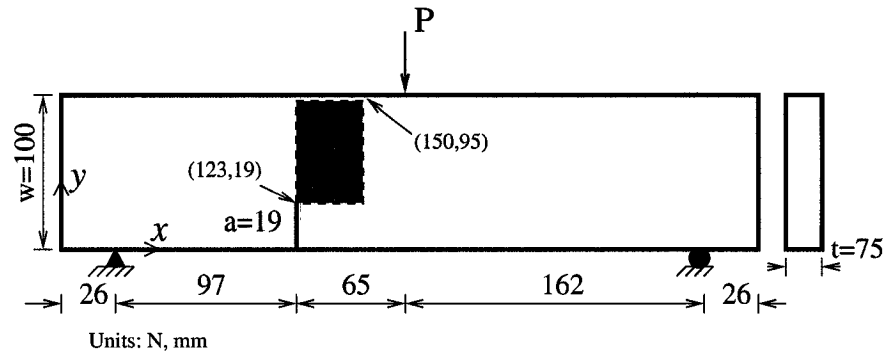
and thickness of the SE(B) specimen are 376mm , 100mm and 75mm , respectively. The notch tip is located at 65mm left and 19mm above the center of the bottom edge of the beam. External loading is imposed at the center of the top edge of the model for the mid-span loading configuration of the SE(B) test. Figures 5.7 (b) and (c) illustrate finite element discretization for the entire model along with mesh details in the shaded region where cohesive elements are inserted. The shaded region between (123, 19) and (150, 95) is constructed in a regular pattern with 3-noded triangular elements having an aspect ratio of 1:1.9 ($= x : y$). The SE(B) structure is constructed using 5398 3-node triangular elements for bulk material, and by 3066 4-node linear elements for cohesive interfaces. Viscoelastic analysis is performed. We assume the same cohesive fracture energy for mode-I and mode-II.

Figure 5.8 (a) illustrates the final deformed shapes and crack trajectories. A magnification factor of 30 is used to make crack trajectories visible. Figure 5.8 (b) shows a comparison of the crack trajectories of experimental and numerical results obtained from the viscoelastic analysis. Green and blue lines indicate the crack trajectory of the experimental results and a red line indicates the crack trajectory of the present numerical simulation, indicating favorable agreement.

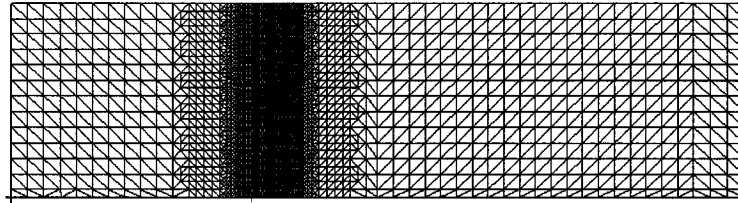
5.4 Discussion on numerical convergence

It has been reported that one of the challenges in cohesive zone modeling is a numerical convergence problem when an implicit displacement based finite element scheme is used. This problem is rarely observed when cohesive elements are inserted along a predefined line. Numerical convergence problems, however, are pronounced when a number of cohesive elements are inserted over an area in the absence of known crack paths. In this section, numerical convergence is presented and discussed in context of mesh discretization and nonlinear equation solvers. For simplicity, viscoelastic effects are not considered in this portion of study.

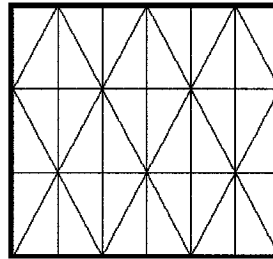
Several researchers [108, 46, 107] have explored integration schemes and/or nonlinear equation solvers to avoid convergence problems when using cohesive zone models. Regard-



(a)



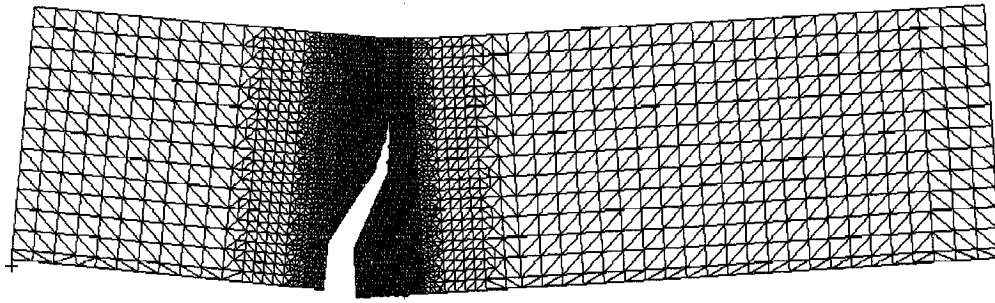
(b)



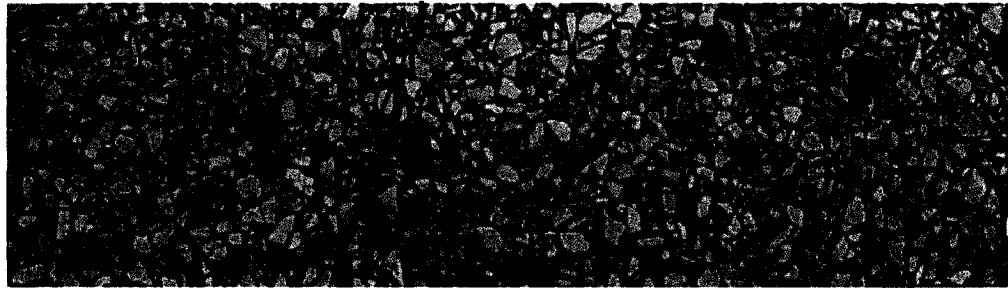
(c)

Figure 5.7: Mixed-mode SE(B) test: (a) geometry and boundary condition; (b) mesh configuration for the whole geometry; (c) mesh details of the shaded region of (123,19) and (150,95) where cohesive elements are inserted.

ing integration schemes, Roy and Dodds [108] reported that the Newton-Cotes integration rule leads to oscillatory opening profiles and induces numerical divergence, indicating that conventional Gauss Quadrature is superior to the Newton-Cotes. Han et al. [46] adopted a Lobatto 3×3 numerical integration for interface elements and a modified version of the arc-length control to avoid numerical divergence for three dimensional problems. Regarding nonlinear equation solvers, several researchers adopted arc-length methods to overcome



(a)



(b)

Figure 5.8: Simulation of the mixed-mode SE(B) test: (a) deformed shape showing crack trajectory (scale factor is 30); (b) comparison of the crack trajectory between numerical and experimental results. Red line indicates the crack trajectory obtained from the present numerical simulation, and green and blue lines denote the crack trajectories from the experiment.

numerical convergence problems in conjunction with cohesive elements [46, 107]. This arc-length method, initially proposed by Riks and modified by Crisfield [30] and others succeeded in tracing the limit point and post peak responses by a prescribed arc-length. However, it has often been reported that the arc-length method still fails to converge at or near the limiting points. Rots and de Borst [107] pointed out that “this instability should be attributed to the global constraints equations including all the degree of freedom, which was contradictory to the fact that the failure zone or fracture process zone is highly localized.”

To address and clarify these numerical issues associated with the CZM, crack propagation analysis of the mixed-mode SE(B) test is performed. The geometry, boundary conditions,

material properties and cohesive parameters of SE(B) test are identical with those of SE(B) test in Section 5.3.3 (see Figure 5.7 (a)). The three different mesh discretizations are adopted to study the influence of mesh discretization on the numerical convergence (see Figures 5.9 (a), (d) and (g)). Furthermore, two nonlinear solvers, i.e. the Newton-Raphson and the Riks methods, are employed to explore their influence on the convergence. Notice that the meshes of Figures 5.9 (a) and (d) are constructed in a regular pattern, while the mesh of Figure 5.9 (g) is tailored to the crack trajectory predicted using a discrete fracture approach with the program I-FRANC2D [61].

Figure 5.9 illustrates the final crack trajectory for different mesh discretizations using two nonlinear solvers before the solutions experience divergence. The bottom-left point in each deformed shape corresponds to the original crack tip and the top-right point corresponds to the location of external loading. Figures 5.9 (a), (d), and (g) illustrate mesh details for Figures 5.9 (b) and (c), (e) and (f), and (h) and (i), respectively. Several important observations from this analysis include: 1) for the meshes constructed in a regular pattern, the Riks method yields better performance than the Newton-Raphson method with a varying degree of success depending on the mesh discretization; 2) for the mesh tailored to the crack trajectory predicted from I-Franc2D, both nonlinear solvers perform very well demonstrating that the degree of numerical convergence highly depends upon the finite element discretizations; 3) once crack branching occurs, numerical solutions are rarely converged; and 4) if the crack propagation angle of finite element discretization is similar with that of either analytical or experimental results, say an optimal crack trajectory, numerical solution converges relatively well.

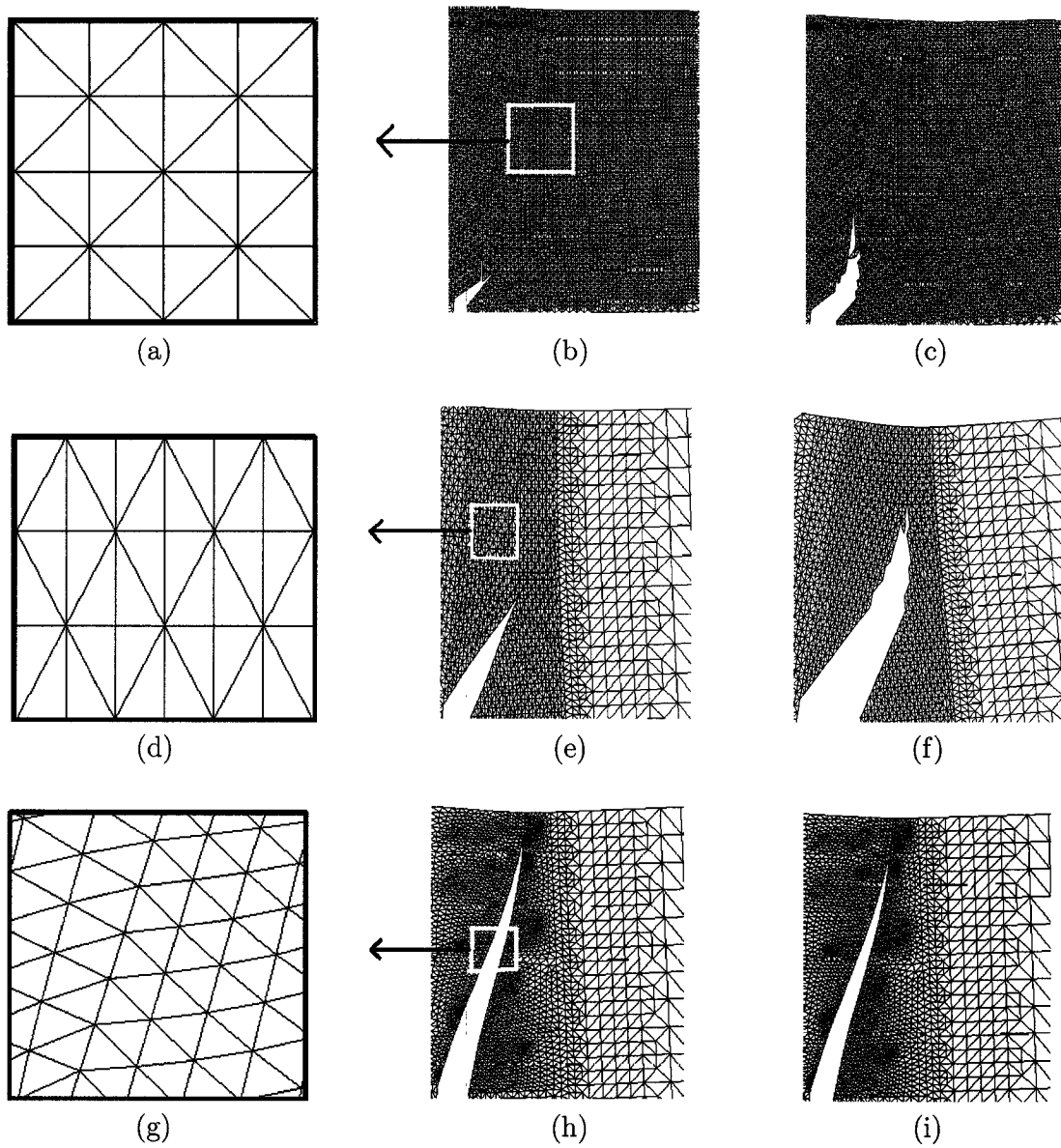


Figure 5.9: Final crack trajectory: (a), (d) and (g) show mesh details for (b) and (c), (e) and (f), and (h) and (i), respectively. The Newton-Raphson is used for (b), (e) and (h), and the Riks method is adopted for (c), (f) and (i). Notice that the bottom left point of each deformed figure corresponds to the original crack tip and the top right point corresponds to the location of applied loading. Magnification factor 50 is used for (b), (c), (e) and (f), and the magnification factor 10 is employed for (h) and (i) to make crack trajectory visible.

5.5 Crack competition phenomenon: nucleation versus initiation and propagation

This section investigates crack competition between nucleation and initiation. In actual roads, asphalt concrete pavement is loaded in both tension and shear, and as a result, understanding mixed-mode fracture events in asphalt concrete is crucial. The crack competition phenomenon was investigated by offsetting the mechanical notch from the centerline of the single-edge notched beam (SE(B)) [45, 57, 109, 132]. The SE(B) specimens, which are notched at an offset with respect to the central cross section, lead to asymmetric loading conditions, and thus, mixed-mode fracture. A benefit of a SE(B) test simulation is that mode-I and mixed-mode fractures can be easily induced with a different offset of the notch with respect to the central cross section, considering crack competition between initiation and nucleation mechanisms. Figure 5.10 illustrates schematic drawings of various fracture phenomena. The variable s denotes the clear span length of the beam, and the variable γ defines the crack offset, i.e.

$$\text{offset} = r s/2 \quad (5.2)$$

With the notch located along the middle of the specimen, mode-I crack propagation can be simulated (see Figure 5.10 (a)). As the notch moves from the central cross section to the boundary, crack competition between nucleation and initiation is induced. When γ is lower than the critical value γ_{cr} , which is defined as the exchange of fracture mechanisms from crack initiation to crack nucleation at a critical notch offset, crack initiates from the existing notch tip and propagates (see Figure 5.10 (b)). On the contrary, when $\gamma > \gamma_{cr}$, a crack nucleates at the bottom of the specimen and propagates (see Figure 5.10 (c)).

John and Shah [57] and Guo et al. [45] experimentally investigated crack competition phenomenon in plain concrete beams subjected to dynamic loading. John and Shan [57] observed that the transition from crack initiation to crack nucleation occurs at a critical offset of around 0.7, i.e. $\gamma_{cr} = 0.7$. Wagoner et al. [132] investigated the competition mechanisms

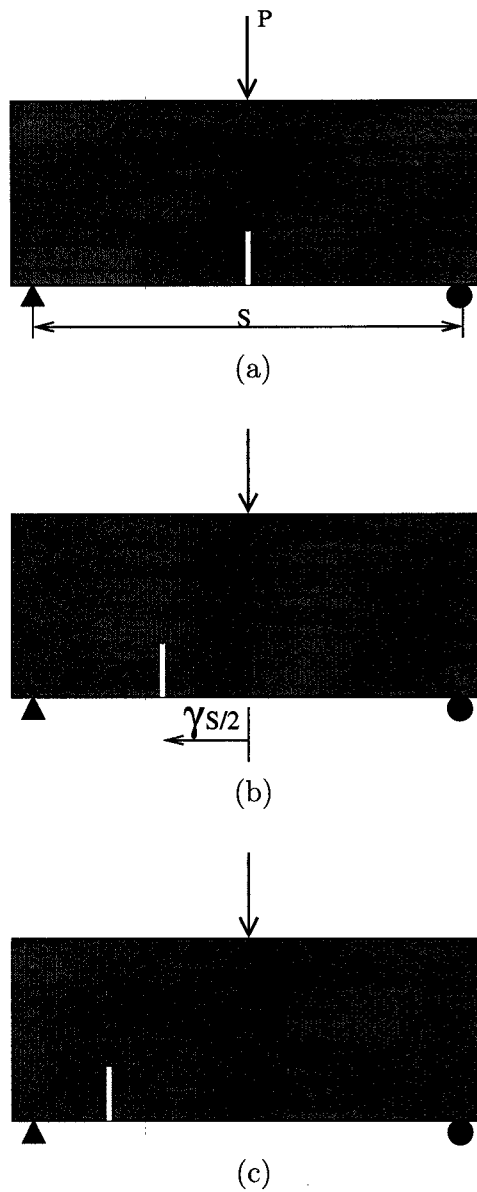


Figure 5.10: Three different fracture behaviors: (a) mode I; (b) initiation and propagation; and (c) nucleation and propagation.

employing an asphalt concrete beam subjected to quasi-static loading, and found that γ_{cr} is between 0.5 and 0.55. Geometry and dimensions of the beams tested by John and Shah [57], Guo et al. [45], and Wagoner et al. [132] are illustrated in Figure 5.11. Note that the dimensions of the tested beam by John and Shah [57] are fairly smaller than those of the beams by

Guo et al. [45] and Wagoner et al. [132]. Ruiz et al. [109] investigated these problems employing a three-dimensional extrinsic CZM. Sam et al. [110] used a two-dimensional cohesive zone modeling technique to investigate the experiment tested by John and Shah [57]. Ruiz et al. [109] and Sam et al. [110] reasonably predicted the exchange of stability between crack initiation and nucleation at a critical pre-notch offset. Chong and Kuruppu [25], and Khan and Al-Shayea [58] investigated mixed-mode fracture in geomaterials such as limestone rock, using the semi-circular specimen with an inclined crack at the central line.

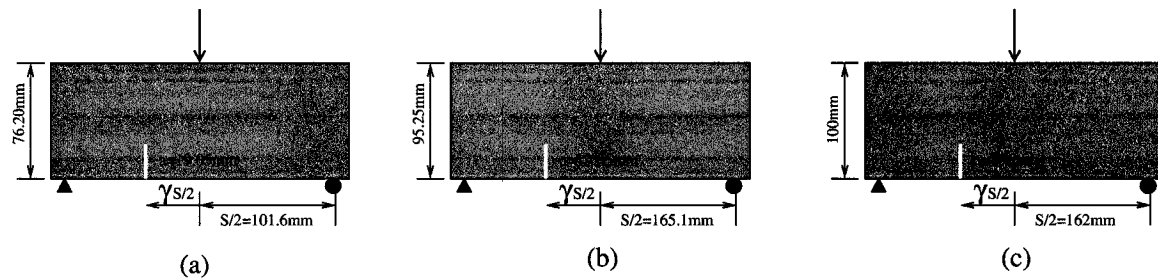


Figure 5.11: Dimensions of the beams tested by: (a) John and Shah [57]; (b) Guo et al. [45]; and (c) Wagoner et al. [132].

5.5.1 Experimental investigations

Wagoner et al. [132, 133] experimentally explored crack competition phenomenon in asphalt concrete. Experimental procedures and results are summarized briefly. The geometry and boundary conditions are already illustrated in the previous section (see Figure 5.11 (c)). In this test, a load-line displacement control is conducted to ensure that crack competition phenomenon between crack initiation and nucleation occurs. The load line displacement rate $5\text{mm}/\text{min}$. is adopted. A single 4.75mm NMAS mixture is used. Figure 5.12 (a) illustrates the actual beam with mixed-mode fracture, whereas Figures 5.12 (b) and (c) show crack paths for $\gamma = 0.5$ and $\gamma = 0.55$, respectively. Solid and dotted lines denote crack trajectories of front and back faces, respectively. As shown in Figure 5.12, the exchange of stability from crack initiation to crack nucleation occurs between 0.5 and 0.55.

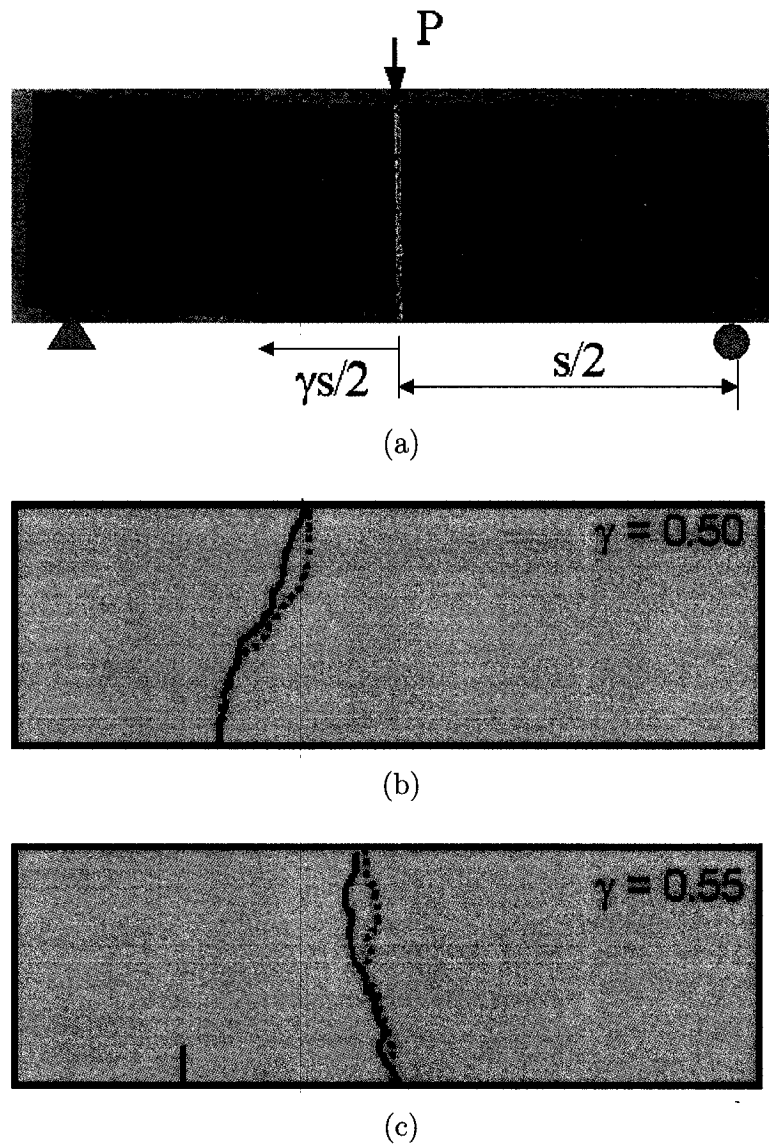


Figure 5.12: Experimental results with various notch offsets [132, 133]: (a) the actual beam with mixed-mode fracture; (b) crack trajectories for $\gamma = 0.5$; and (c) crack paths for $\gamma = 0.55$. Solid and dotted lines denote crack trajectories of front and back faces, respectively.

5.5.2 Numerical studies

Cohesive zone modeling technique is adopted to investigate the competition phenomenon between initiation and nucleation. Figure 5.13 (a) schematically shows the geometry, boundary conditions, and lines along which cohesive elements are inserted. The length, height and

thickness are 376 mm, 100mm and 75mm, respectively. The crack tip is located at 78mm left and 19mm above from the center of the bottom edge, leading to $\gamma = 0.48$. The displacement boundary condition, which increases linearly with respect to pseudo-time, is applied at the center of the top edge of the model. Cohesive elements are inserted in advance along the middle of the specimen to induce nucleation and propagation, and along the line, which is connected to the existing notch tip, to cause crack initiation and propagation. Figure 5.13 (b) illustrates a finite element configuration for the whole geometry when $\gamma = 0.48$. The SE(B) structure is constructed by 5748 3-noded triangular and 2065 four-noded quadrilateral elements for the bulk material and 181 four-noded linear elements for the cohesive material. Plane strain condition is adopted. Figures 5.13 (c) and (d) illustrate mesh details for the notch tip region and the central cross section, respectively. The cohesive element size 1.0mm is used to ensure that the size is small enough to properly capture nonlinear behavior occurring along the fracture process zone. The fracture energy and material strength calibrated in Section 5.3.2 are employed. $E = 14.2GPa$ and $\nu = 0.35$ are used.

Figure 5.14 shows the outcomes of the numerical simulations considering crack competition between nucleation and initiation. Deformed shapes with a magnification factor 30 are shown for both $\gamma = 0.48$ and $\gamma = 0.56$. A crack initiates from the existing crack tip and propagates when $\gamma = 0.48$, while a crack is nucleated at the bottom of the central cross section and propagates when $\gamma = 0.56$. The exchange of stability between crack initiation and nucleation at a critical pre-notch offset occurs between $\gamma = 0.48$ and $\gamma = 0.56$, demonstrating that the numerically predicted γ_{cr} is in excellent agreement with the experimental finding (see Table 5.3). Figures 5.15 and 5.16 illustrate σ_{xx} for $\gamma = 0.48$ and $\gamma = 0.56$, respectively, at different loading steps. These contour plots show crack competition and interaction phenomena between nucleation and initiation, and crack propagation clearly. Tensile stresses of the red-colored region are higher than those of other areas. For $\gamma = 0.48$, when external loading is imposed, energy starts to be accumulated around the existing notch tip and the bottom of the central cross section. As external loading increases, more energy is accumulated for

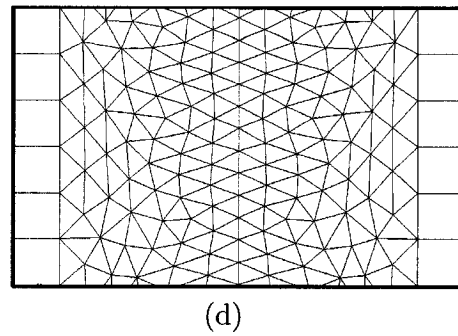
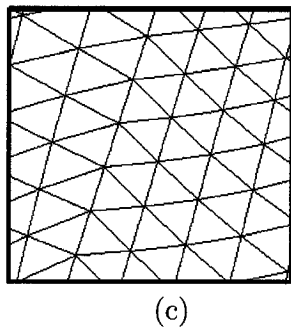
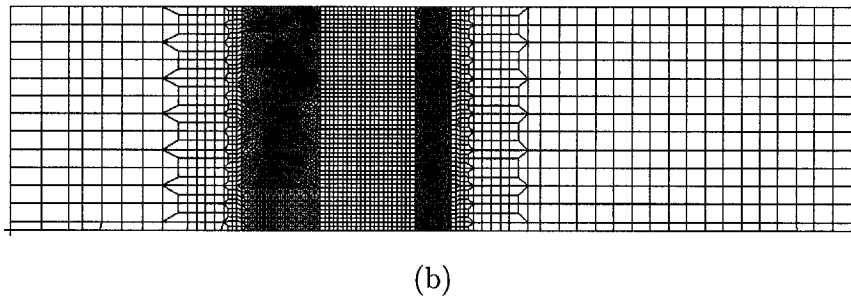
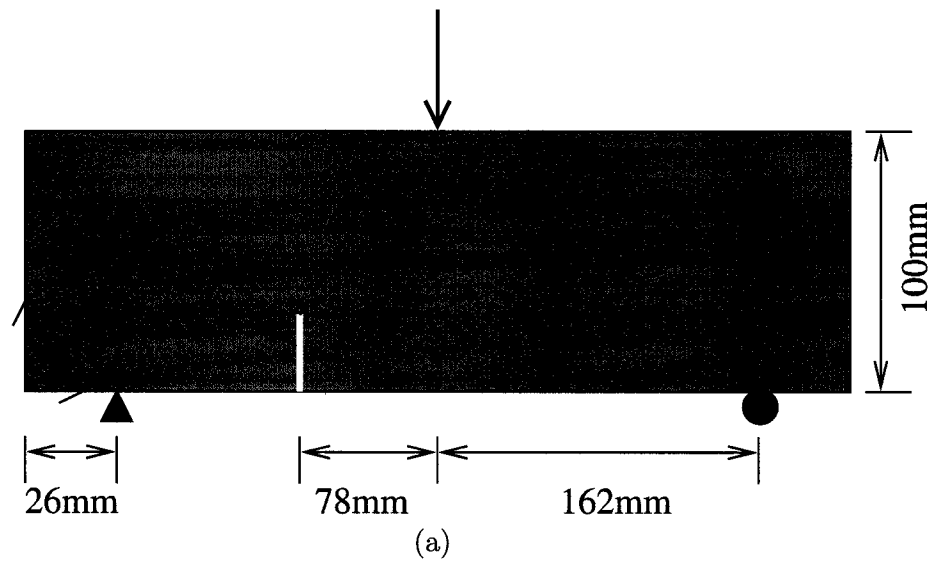


Figure 5.13: SE(B) test simulation considering crack competition phenomenon: (a) geometry and boundary conditions; (b) mesh discretization for the whole geometry; (c) mesh details for the notch tip region in which a crack initiates and propagates; and (d) mesh details for the central cross section where crack nucleation and propagation occur.

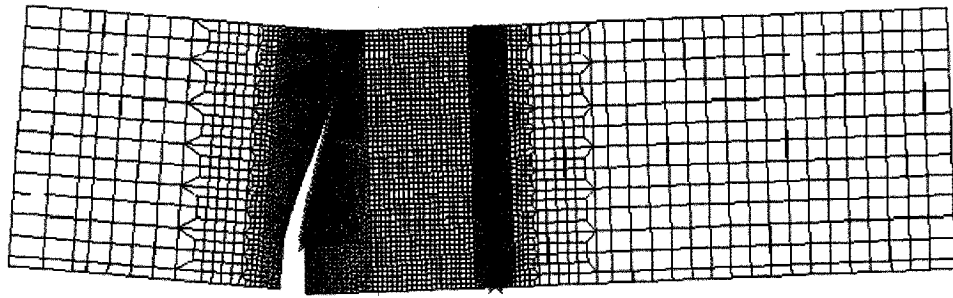
both areas, demonstrating crack competition between initiation and nucleation. Then, more energy is absorbed at the crack tip and crack starts to propagate from the existing notch tip, while energy decreases around the bottom of the middle of the specimen and crack arrests. Finally, most external works are transformed to make a crack propagate from the existing notch tip to the top of the specimen, illustrating mixed-mode fracture. For $\gamma = 0.56$, a similar observation is obtained at earlier steps of the analysis. However, more energy is built up around the middle of the specimen, indicating crack nucleation and propagation. On the contrary, cohesive elements inserted above the notch tip arrest the development of a material failure. Finally, most energies are used for crack propagation from the bottom of the specimen.

Table 5.3: Comparison of γ_{cr} between numerical and experimental results.

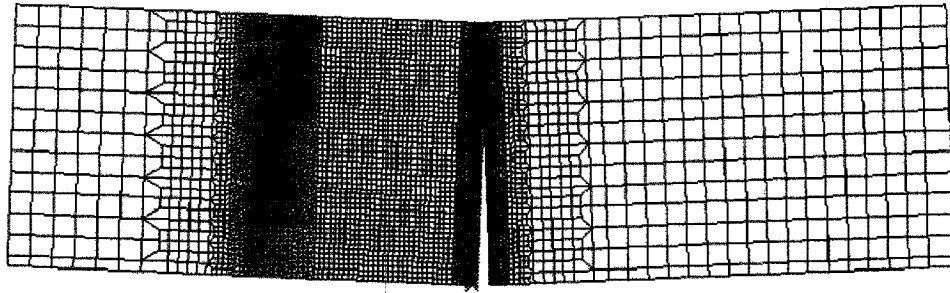
	γ_{cr}
Experiment	0.5~0.55
Modeling	0.48~0.56

5.6 Concluding remarks

In this study, a bilinear cohesive zone model is used for fracture modeling in asphalt concrete laboratory tests such as DC(T) and SE(B) considering viscoelastic effects in bulk materials. In Section 5.2, the issues regarding compliance of the cohesive laws, i.e. potential-based cohesive zone model [144] and bilinear model [39], are explored by simulating a one-dimensional problem [66] and a two-dimensional SE(B) test in asphalt concrete. It is demonstrated that the bilinear cohesive zone model [39] is more appropriate for asphalt concrete materials than the model by Xu and Needleman [144]. In Section 5.3, numerical results considering viscoelastic bulk material are presented. Simulation of the DC(T) fracture test is presented, in which the cohesive elements are inserted along the middle of the specimen to permit mode I crack propagation. This simulation is used to calibrate the cohesive zone model parameters to experimental results. Overall, the predicted load CMOD behavior is found to match well



(a)



(b)

Figure 5.14: Numerical results: (a) initiation and propagation when $\gamma = 0.48$ and (b) nucleation and propagation when $\gamma = 0.56$. Magnification factor 30 is used to make crack trajectories visible.

with experimental results. In the mixed-mode SE(B) test simulation, cohesive elements are inserted over an area to allow cracks to grow in any direction. Moreover, a regular finite element discretization is used to lower the influence of mesh discretization on crack trajectory. A mixed-mode crack propagation simulation is performed with good success. The mixed-mode crack trajectory from the present simulation is found to match remarkably well with experimental results. In Section 5.4, numerical convergence problems are discussed. In this study, it is observed that a numerical divergence is unavoidable for mixed-mode simulations, and highly depends upon the nature of the finite element discretization used. In Section 5.5, crack competition phenomenon between initiation and propagation is studied numerically in conjunction with the SE(B) test simulation in which cohesive elements are inserted in advance to simulate either crack initiation or nucleation, and propagation. The predicted

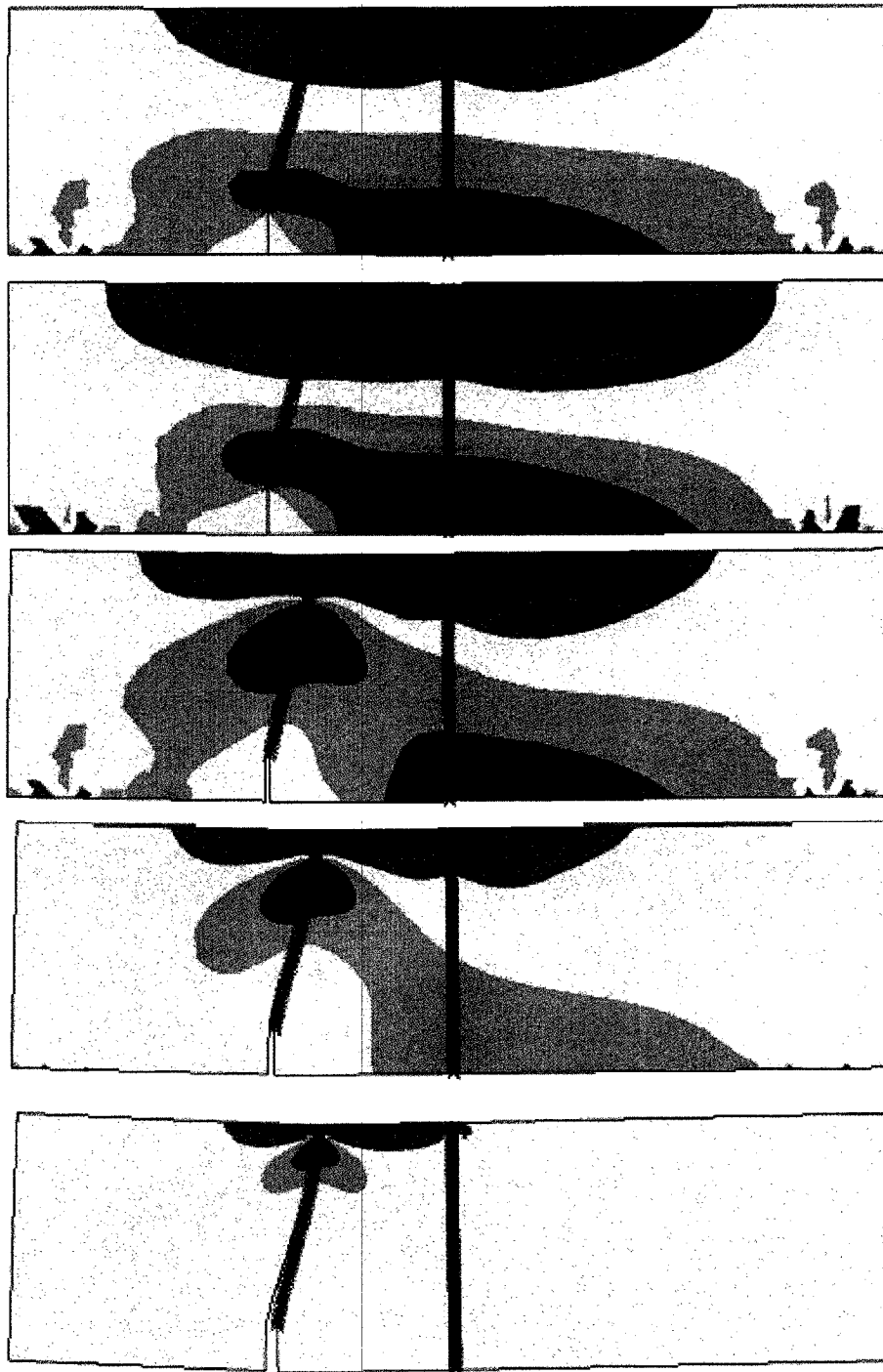


Figure 5.15: Numerical results demonstrating crack initiation and propagation when $\gamma = 0.48$. Crack propagates from the crack tip location.

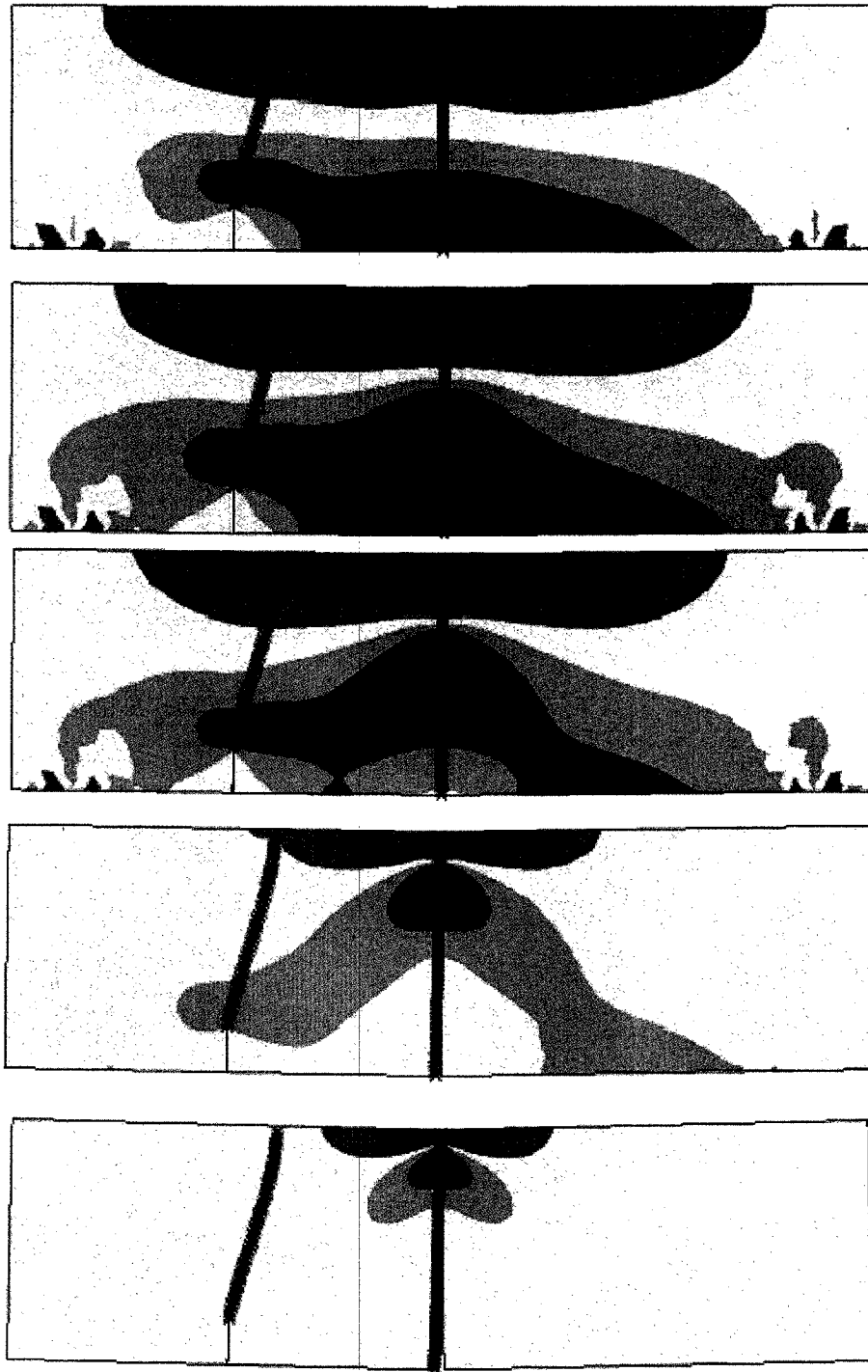


Figure 5.16: Numerical results illustrating crack nucleation and propagation when $\gamma = 0.56$. Crack propagates at the middle region of the specimen.

γ_{cr} is found to be in excellent agreement with the experimental results.

Chapter 6

Three-dimensional power-law cohesive zone modeling in conjunction with the δ_{25} concept

A cohesive zone model (CZM) has been effective in exploring fracture behavior in various materials. In general, the cohesive parameters associated to material strength and cohesive fracture energy are considered more important than a CZM softening shape. However, the influence of the CZM softening shape becomes significant as the relative size of the fracture process zone compared to the structure size increases, which is relevant for asphalt concrete and other quasi-brittle materials. In this study, the power-law CZM [35] is revisited and improved 1) to reduce artificial compliance by means of an internal variable controlling a pre-peak slope, 2) to model general cases (e.g. mixed-mode and three-dimensional), and 3) to have various softening shapes. Then, the improved power-law CZM is employed to investigate the influence of the CZM softening shape on asphalt concrete fracture behavior and to propose a suitable softening shape for asphalt concrete. Furthermore, a new parameter, δ_{25} , which was inspired by the insightful δ_5 concept of Schwalbe and co-workers, is proposed as an operational definition of a crack tip opening displacement (CTOD). The δ_{25} measurement is incorporated into experimental validation of its usefulness with asphalt concrete. Once the δ_{25} parameter is deemed relevant, the parameter is utilized to measure fracture energy. Three dimensional DC(T) test simulation is performed considering bulk (background) ma-

terial viscoelasticity. The integration of the δ_{25} parameter and the new power-law CZM has provided further insight into asphalt concrete fracture behavior with good agreement between the experimental results and numerical simulations.

6.1 Introduction

Asphalt concrete is used as a surfacing material for pavement structures throughout the world with large amounts of money being invested into the maintenance of these pavement structures. Although there are many distresses, or causes of deterioration, associated with asphalt concrete, a major concern is fracture of asphalt concrete, which decreases the serviceability of the structure. Until recently, empirical relationships are utilized to develop design approaches that reduce the likelihood of the pavement structure fracturing [50]. However, these empirical approaches are limited to specific pavement structures, since extrapolating the design approaches to different pavement designs (pavement thickness, materials, environmental effects, etc.) may not result in good performing pavements. The movement in recent years in the asphalt concrete pavement community has been to incorporate fundamental mechanics into the pavement designs that would allow for the prediction of pavement performance over a wide range of design variables. Specifically, fracture mechanics is being applied to characterize the mechanisms that initiate and propagate a crack through asphalt concrete by using experimental and computational techniques [72, 121, 122, 134].

Asphalt concrete has been shown to exhibit quasibrittle and time and temperature dependent fracture where the softening of the material can be attributed to the microstructure where the aggregates have the ability to interlock and slide, while the asphalt mastic displays cohesion and viscoelastic properties. Among several computational techniques, a cohesive zone model is considered as an attractive computational method, because we can define a suitable constitutive model in terms of displacement jump and traction. Due to the relatively large size of the fracture process zone compared to the structure size in asphalt concrete and other quasi-brittle materials, a CZM softening shape becomes as relevant as the cohesive

parameters associated to material strength and cohesive fracture energy, and as a result, it becomes crucial to adopt a proper CZM softening shape to obtain reasonable numerical results. Unfortunately, most CZMs including the models [39, 129, 144] used in asphalt concrete fracture studies can not control a CZM softening shape, which represents progressive softening phenomena occurring along the fracture process zone. For example, the bilinear CZM [129] has the constant reduction of traction with respect to displacement jump (see Figure 3.2). The bilinear model can be reasonable for a particular material, but may not be good for other materials. It can be costly to implement a CZM with a different softening shape, whenever needed. So, from a computational point of view, it can be very attractive to have a CZM which can have various softening shapes. In this study, a power-law cohesive zone model [35] is revisited and improved 1) to reduce artificial compliance, 2) to model general cases, e.g. mixed-mode and three-dimensional, and 3) to have various choices in terms of CZM softening shapes.

One of the material properties that are required for the CZMs is the cohesive fracture energy, or the energy required to fully separate the material. Work conducted by Wagoner et al. [134] suggests that the fracture energy of asphalt concrete can be obtained by using a disk-shaped compact tension specimen, DC(T), in which the fracture energy is obtained by using the CMOD of the specimen. This is utilized since the CMOD is a measurement required to perform the experiment. The main disadvantage of using the CMOD for obtaining fracture energy is that the CMOD is a quantity contributed by the specimen structure, i.e. the bulk material and fracture, not solely by fracture. In this work, a new displacement measurement, δ_{25} , is introduced to provide a local quantity of CTOD. The work of Schwalbe and his colleges provided the framework for the δ_{25} measurement with their work of the δ_5 quantity [114, 115, 117]. The δ_5 measurement was developed and applied to fine-grained materials with great success. The challenge with applying the δ -measurement to asphalt concrete is the coarse microstructure that has aggregates as large as 25 mm (see Figure 6.1 for typical asphalt concrete microstructure). For this current study, the maximum aggregate size in the asphalt

concrete mixture is 9.5 mm, therefore, the measurement at the notch tip is obtained over a 25 mm gage length to ensure that the influence of the aggregates are minimized from the measurements. As a general rule for heterogeneous mixtures, such as asphalt concrete, the gage length should be at least 3 times the maximum aggregate size [106]. The fracture energy obtained from the δ_{25} parameter may provide better estimation for asphalt concrete mixtures, since the compliance associated with the global response is reduced. The work herein will go on to describe the usefulness of the δ_{25} parameter.

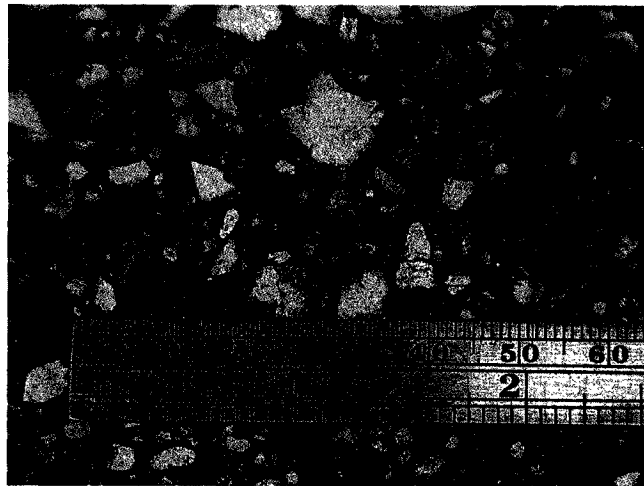


Figure 6.1: Typical asphalt concrete microstructure.

6.2 Power-law cohesive zone modeling

A CZM softening shape for fracture study in quasibrittle materials is as important as the cohesive parameters, i.e. fracture energy and material strength, due to the relatively large size of the fracture process zone compared to the structure size. To model fracture behavior in concrete, which is the best example among quasibrittle materials, the rectangular and linear softening curves were proposed initially. However, it turned out that these softening curves capture concrete fracture behavior poorly. Next shape was a bilinear softening curve by Peterson [97]. Reasonable numerical results were obtained using the bilinear shape. Since then, many research group have proposed various bilinear type softening curves such

as bilinear shapes [105, 139], exponential shapes [28, 44, 98] and power-law shapes [35]. However, the literature is currently devoid of study on a CZM softening shape in asphalt concrete fracture modeling. In this study, the improved power-law CZM [124] is used to explore the influence of CZM softening shapes and to propose a suitable one for an asphalt concrete fracture study.

Figure 6.2 (a) illustrates a DC(T) specimen which is 143 mm high, 139 mm long and 35mm thick. The length of the mechanical notch, say a , is 26.5mm, leading to $a/w=0.25$. A displacement control inducing a constant CMOD rate of 1.0mm/min. is adopted. Figure 6.2 (b) shows three dimensional mesh discretizations for the whole geometry. The DC(T) test specimen is constructed using 28094 8-node brick elements for the bulk material and 840 8-node elements for the cohesive material. The cohesive elements are inserted along the middle of specimen to enable the simulation of pure mode-I crack propagation. A symmetry condition along the thickness direction is employed to reduce a computational cost. A constant Poisson's ratio is used: $\nu=0.35$. The fracture energy obtained at $-20^{\circ}C$ and $1mm/min.$ CMOD rate is $190J/m^2$ in the context of CMOD, and the material strength measured at $-20^{\circ}C$ is $2.90MPa$. Model parameters (see Table 6.1) and shift factors (see Table 6.2) evaluated from the IDT test are adopted for viscoelastic analysis of bulk materials. The geometry, material properties, and cohesive parameters are based on the cored pavement material in northeast Iowa, in which PG64-22 binder is used.

Table 6.1: Prony series parameters for the master relaxation modulus using the generalized Maxwell model [131].

i	Relaxation Modulus Parameters	
	$E_i(GPa)$	$\tau_i(sec)$
1	3.54	15
2	3.43	249
3	1.75	4817
4	7.21	57378
5	11.92	2605452

Figure 6.3 shows a comparison of the present numerical results with the experimental

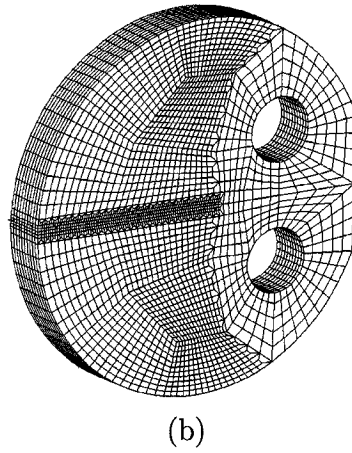
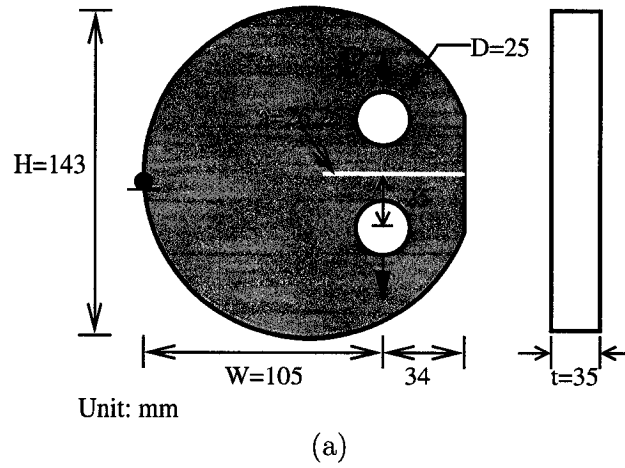


Figure 6.2: DC(T) test simulation: (a) geometry and boundary conditions; (b) mesh configurations for the whole geometry.

Table 6.2: Temperature shift factors [131].

Temperatures	$\log(1/a_T)$
$-30^{\circ}C$	0
$-20^{\circ}C$	1.95
$-10^{\circ}C$	3.2

results. In the present simulations, the power-law CZM with $\alpha = 1$ and $\alpha = 10$ is used. When the power-law CZM with $\alpha = 1$ is used, the numerical results overpredict both the peak load and the area under the curve, which is identical with observation by other research groups [13]. Furthermore, the discrepancy between the numerical and experimental results is

considerable around the peak load and becomes small as a crack approaches to the boundary. It is attributed to the fact that the linear softening curve of the bilinear CZM, which has the constant reduction of capacity with respect to displacement jump, does not properly represent softening phenomena. In fact, it is observed in asphalt concrete that the capacity to resist crack opening drops suddenly due to cracks along interfaces between aggregates and asphalt mastics, and then the cohesion occurs because of asphalt mastics and interlocking. When the power-law CZM with $\alpha = 10$ is employed, the peak load and the softening trend of the present numerical results are quite similar with those of the experiments. It can be inferred from the comparison that the softening shape represented by the power-law with $\alpha = 10$ is a reasonable approximation of softening phenomena occurring along the fracture process zone. However, the area under the curve of the numerical results is bigger than that of the experiments. This indicates that the energy evaluated in context of the CMOD is over-estimated. It is intuitive because when the CMOD is employed to compute fracture energy, both the bulk and fracture contribute to the evaluation of cohesive fracture energy. The issues related to the evaluation of fracture energy will be thoroughly discussed in next section.

6.3 The δ_{25} approach

In this section, experimental investigations are performed to illustrate that δ_{25} -measurement is more appropriate in evaluating cohesive fracture energy than *CMOD*-measurement in asphalt concrete.

6.3.1 Experimental set-up

The development of the δ_{25} measurement is conducted using a disk-shaped compact tension, DC(T), specimen. The DC(T) test has been successfully developed for estimating the fracture energy of asphalt concrete [134]. In addition to the typical measurements, the test set-up for the δ_{25} measurements require two extra clip gages to be attached to the specimen

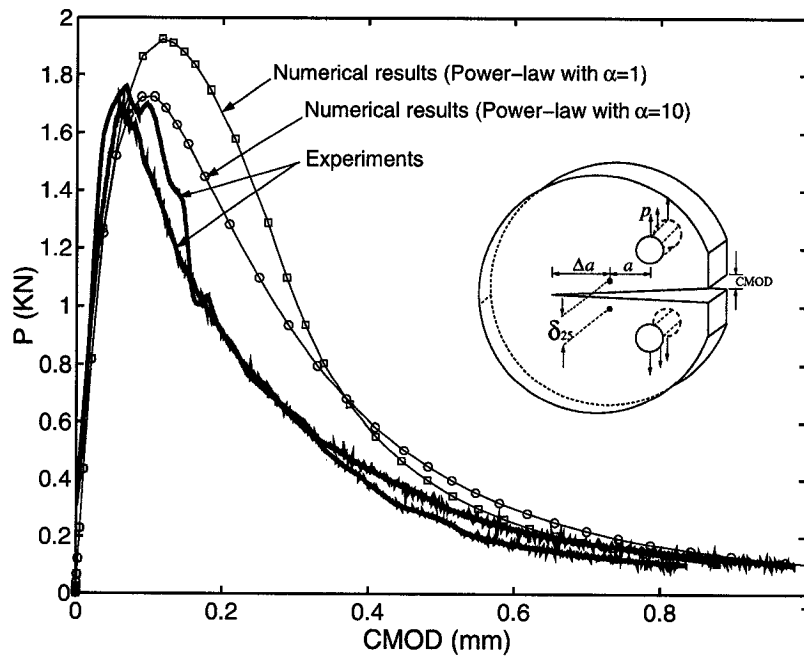


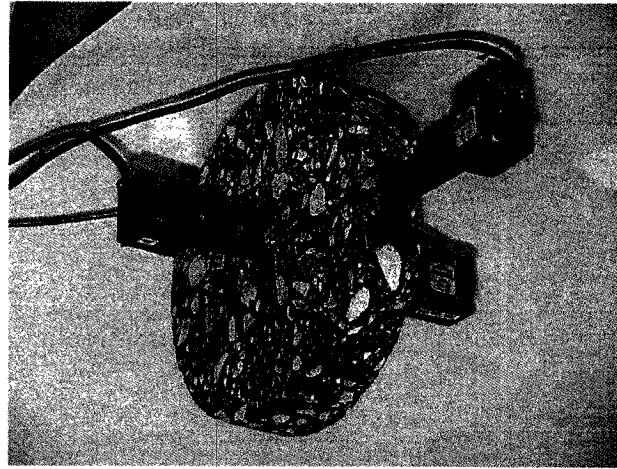
Figure 6.3: Comparison of a P versus CMOD curve between the numerical and experimental results.

at the notch tip. Gages are attached to the specimen at a gage length of 25 mm on both sides of the specimen (See Figure 6.4 (a)). The data presented herein is obtained at a single test temperature of $-20^{\circ}C$ and a constant CMOD rate of 1 mm/min.

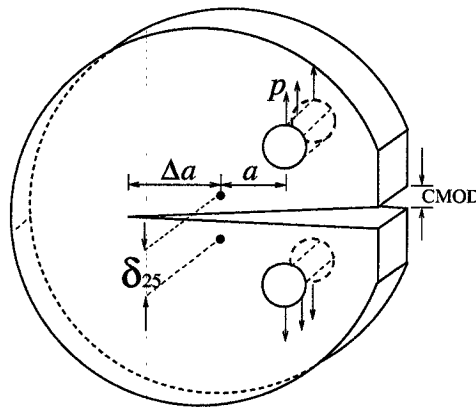
6.3.2 Validation

The fracture energy is estimated using the DC(T) specimen at $-20^{\circ}C$ and a CMOD rate of 1 mm/min. The energy is calculated using both the CMOD and δ_{25} measurements. Two replicates are tested and the results are shown in Table 6.3. The average fracture energy calculated using the CMOD is $190J/m^2$ while the fracture energy calculated from the δ_{25} measurement is $120J/m^2$. The difference between the CMOD and δ_{25} measurements can be seen in Figure 6.5. The initial slope of the load-CMOD curve up to the peak is greater for the δ_{25} measurements indicating that the δ_{25} measurement minimizes the extraneous bulk contribution that is associated with the CMOD measurement.

Another important experimental finding from the δ_{25} measurement is the difference in



(a)



(b)

Figure 6.4: The parameter δ_{25} : (a) experimental setting [131]; (b) schematic drawing. Note that Δa denotes a distance between the original crack tip and the current crack tip.

Table 6.3: Fracture energy of the two replicates at $-20^\circ C$ [131].

Replicate	fracture energy		
	CMOD	δ_{25} (face 1)	δ_{25} (face 2)
1	180	116	117
2	200	129	118
Average	190	120	

the shape and rate of the displacements. The CMOD is utilized as the test control and had a constant opening rate of 1 mm/min. The δ_{25} measurements do not show a constant

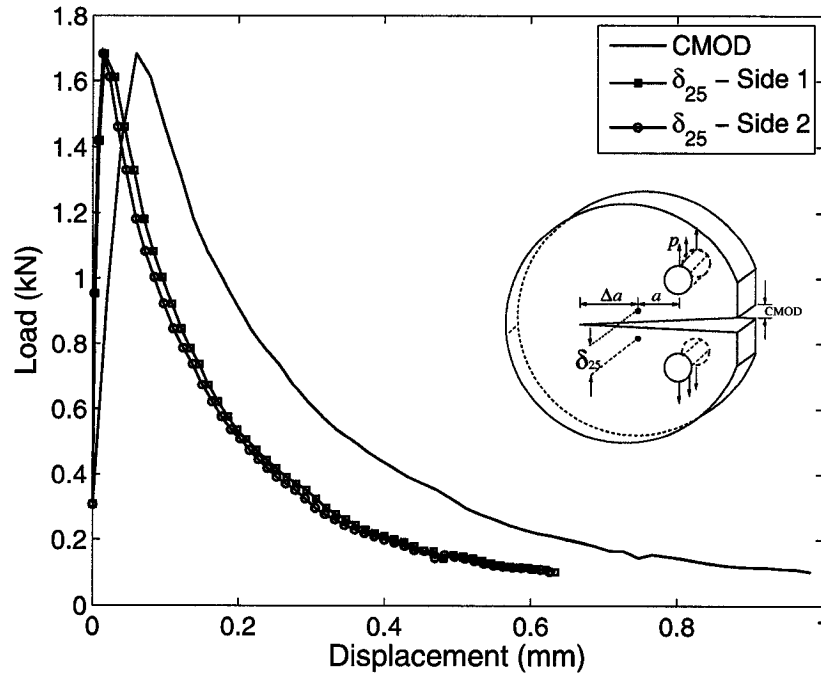


Figure 6.5: Load versus displacement of CMOD and δ_{25} (experimental results) [131].

opening rate. As shown in Figure 6.6, the δ_{25} measurement showed a nonlinear response up to a point, then a linear response. Typical results have shown that the time corresponding to the inflection point where the δ_{25} measurement rate becomes constant is close to the time at the peak load of a P versus CMOD curve (see Figure 6.5). Once the δ_{25} opening rate is constant, the rate is less than the CMOD rate by 30 percent. More importantly, as a temperature increases, the difference of fracture energy between using the δ_{25} and CMOD measurements becomes significant as illustrated in Figure 6.7. It is intuitive because as we increase temperatures, structures become more compliant and as a result, the contribution of bulk material to the CMOD increases. So, based on experimental investigation, we can conclude that for asphalt concrete, which shows time and temperature dependent behavior, the δ_{25} measurement is more suitable in evaluating fracture energy than the CMOD measurement.

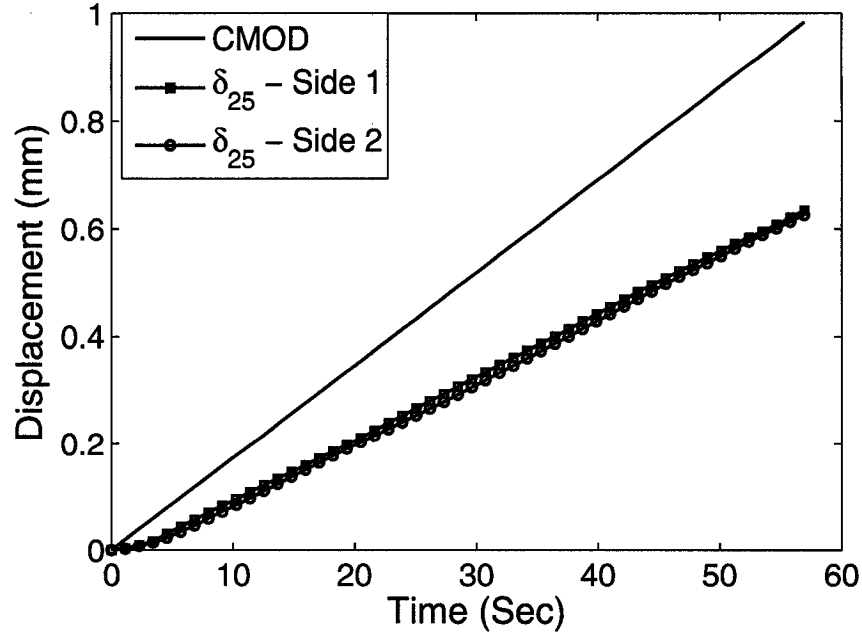


Figure 6.6: Displacement versus time for the CMOD and δ_{25} (experimental results) [131].

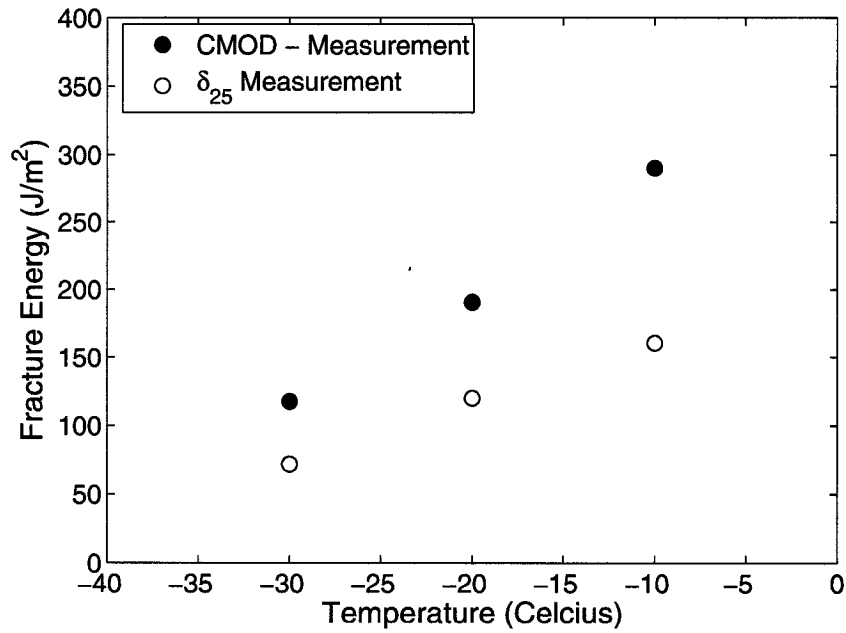


Figure 6.7: Comparison of fracture energy in context of the δ_{25} and CMOD for different temperatures [131].

6.4 Computational results

In this section, a three-dimensional DC(T) test simulation is performed to illustrate that the calibration procedure can be removed when we use 1) the power-law CZM with $\alpha = 10$ to represent progressive softening phenomena occurring along the fracture process zone and 2) the δ_{25} measurement to compute cohesive fracture energy. Figure 6.8 illustrates comparison between the experimental results and the numerical results in terms of P and CMOD. In the modeling, the power-law CZM with $\alpha = 10$ and $\alpha = 1$ is used. Cohesive fracture energy evaluated in context of the δ_{25} and CMOD are $120J/m^2$ and $190J/m^2$, respectively. Material strength σ_c is $2.90MPa$. When the conventional bilinear CZM, i.e. the power-law CZM with $\alpha = 1$, and $G_c = 190J/m^2$ are used, the considerable discrepancy of the softening trend between the numerical and experimental results is generated. In addition, the peak load of the numerical results is over-estimated. However, good agreement between the numerical and experimental results is obtained when the power-law CZM with $\alpha = 10$ and $G_c = 120J/m^2$ are adopted.

Figure 6.9 illustrates time versus displacements, i.e. the CMOD and the δ_{25} , of the experiments and numerical results. The CMOD of both numerical results and experiments are identical which is expected because of the boundary condition imposed. For the δ_{25} , the numerical results favorably match with experimental results. Both the numerical and experimental results have a very close deflection point. From the simulations, it is inferred that when we use the power-law CZM with $\alpha = 10$ and cohesive fracture energy evaluated in context of the δ_{25} , numerical results can be reasonably predicted without any calibration.

Figure 6.10 illustrates a deformed shape and σ_y corresponding to $P=1KN$ before the peak. When the imposed displacement increases, energy is accumulated at the initial crack tip, which is denoted by red color in the contour plot. Then, the crack tip propagates to the left boundary as red regions move from the original crack tip to the left boundary. Magnification factor 500 is employed to make crack propagation visible.

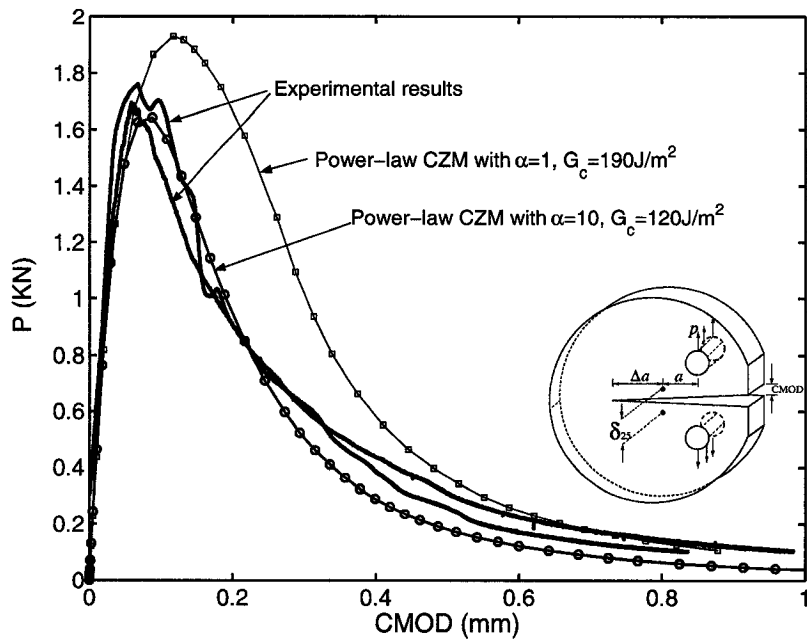


Figure 6.8: Comparison of the numerical results with the experimental results.

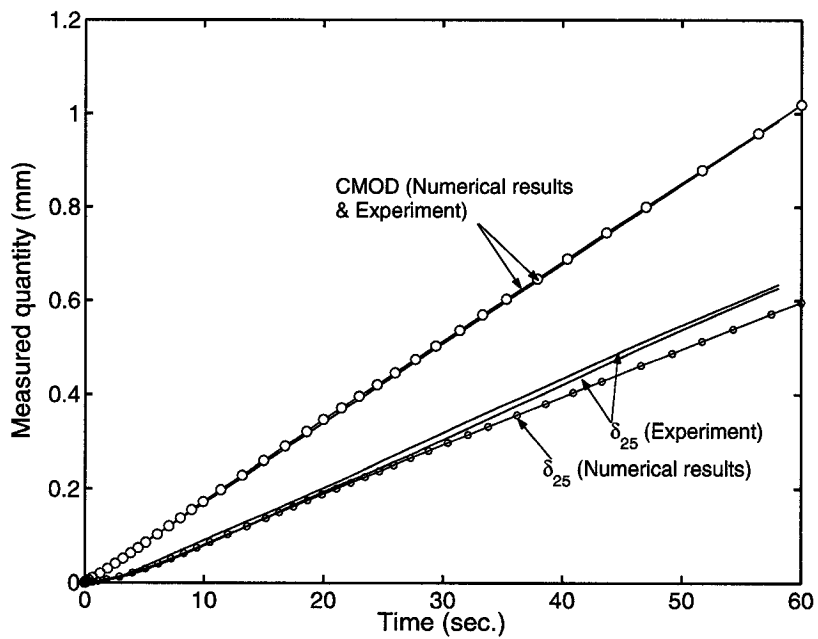


Figure 6.9: Time versus CMOD and δ_{25} . Notice that in this simulation, the power-law CZM with $\alpha = 10$ is employed and the fracture energy evaluated in conjunction with the δ_{25} is adopted.

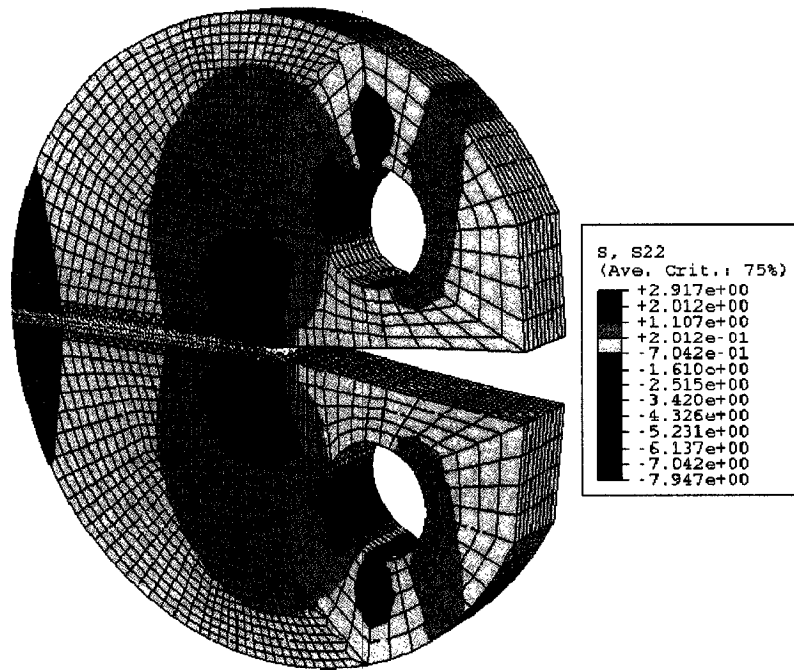


Figure 6.10: Stresses σ_y and deformed shapes. Note that magnification factor 500 is employed to make crack propagation visible.

6.5 Concluding remarks

A common approach to measure fracture energy in asphalt concrete is to utilize the CMOD since the CMOD is a measurement required to perform the experiment and easy to be measured. However, due to the contribution of the bulk and fracture to the computation of fracture energy, the fracture energy using the conventional approach is over-estimated and as a result, calibration procedures in numerical modeling are unavoidable [122, 123]. Therefore, the δ_{25} parameter is proposed as an operational definition of crack tip opening displacement (CTOD) in asphalt concrete. The use of the δ_{25} parameter in evaluating fracture energy leads to more reasonable numerical results due to the fact that the δ_{25} is more close to local quantity than the CMOD.

Due to the relatively large size of the fracture process zone compared to the structure size in asphalt concrete and other quasi-brittle materials, a CZM softening shape becomes

as relevant as the cohesive parameters associated to material strength and cohesive fracture energy. In this study, the improved power-law CZM model [124] is employed to investigate the influence of various CZM softening shapes and to propose a suitable one for asphalt concrete fracture study. When the power-law CZM with $\alpha = 1$, which is equivalent to the bilinear CZM, is adopted, it captures the peak load and the softening behavior poorly. There is a significant improvement in modeling when a nonlinearly decaying softening curve represented by the power-law CZM with $\alpha = 10$ is employed. The integration of the δ_{25} measurement in computing cohesive fracture energy and the improved power-law CZM with $\alpha = 10$ has provided further insight into asphalt concrete fracture with good agreement between the experimental and numerical results.

Chapter 7

Rate-dependent cohesive zone modeling for asphalt concrete fracture: exploratory investigation

This chapter develops a novel rate-dependent CZM from the activation energy theory of the rate process of bond rupture in conjunction with reasonable assumptions and simplifications, and proposes appropriate procedure to evaluate several parameters accounting for time and temperature effects. Additionally, sensitivity analysis to the new parameters introduced into the proposed CZM is carried out. The proposed rate-dependent CZM improves numerical results significantly, leading to a better comparison with experimental results, when viscoelastic effects are considerable. The predicted numerical results at $-30^{\circ}C$, $-20^{\circ}C$ and $-10^{\circ}C$ are found to be in close agreement with experimental results.

7.1 Motivation

A rate-independent CZM may not be sufficient to capture viscoelastic fracture behavior properly [100]. To demonstrate this point, the DC(T) test simulation is carried out. Figure 7.1 (a) illustrates a DC(T) specimen which is 143 mm high and 139 mm long and 30mm thick. The length of the mechanical notch is 26.5mm, leading to $a/w=0.25$. A displacement control inducing constant CMOD rate of 1.0mm/min is adopted. Figure 7.1 (b) shows a two-dimensional mesh discretization for the whole geometry. The cohesive elements are

inserted along the middle of the specimen to enable the simulation of pure mode-I crack propagation. Cohesive fracture energy and material strength at $-10^{\circ}C$ and $-30^{\circ}C$ are shown in Table 7.1, and cohesive fracture energy is evaluated based on the δ_{25} measurement. Note that the material strength at $-10^{\circ}C$ and $-30^{\circ}C$ is assumed to be 79 percent and 82 percent, respectively, of material strength obtained from experiment at $-20^{\circ}C$. Model parameters (see Table 7.2) and shift factors (see Table 7.3) evaluated from the IDT test are adopted for viscoelastic bulk materials. The material parameters are based on the cored pavement in northeast IOWA, in which PG58-34 performance graded asphalt binder is used. The power-law CZM with $\alpha = 10$ is used to account for progressive softening behavior occurring along the fracture process zone.

Table 7.1: Fracture energy and material strength [131].

	$-10^{\circ}C$	$-30^{\circ}C$
Fracture energy (G_c) (J/m^2)	410	162
Material strength (σ_c) (MPa)	2.85	2.95

Table 7.2: Prony series parameters for the master relaxation modulus using the generalized Maxwell model [131].

i	Relaxation Modulus Parameters.	
	E_i (GPa)	τ_i (sec)
1	4.7	15
2	6.4	259
3	6.0	4112
4	5.2	59041
5	4.9	2320938

Table 7.3: Temperature shift factors [131].

Temperatures	$\log(1/a_T)$
$-30^{\circ}C$	0
$-20^{\circ}C$	1.55
$-10^{\circ}C$	3.35

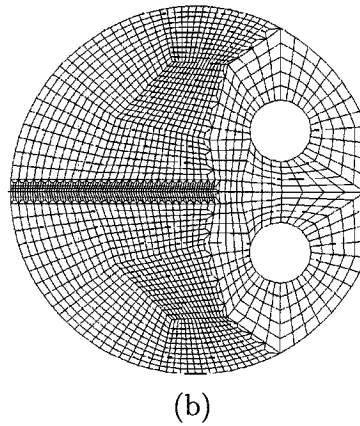
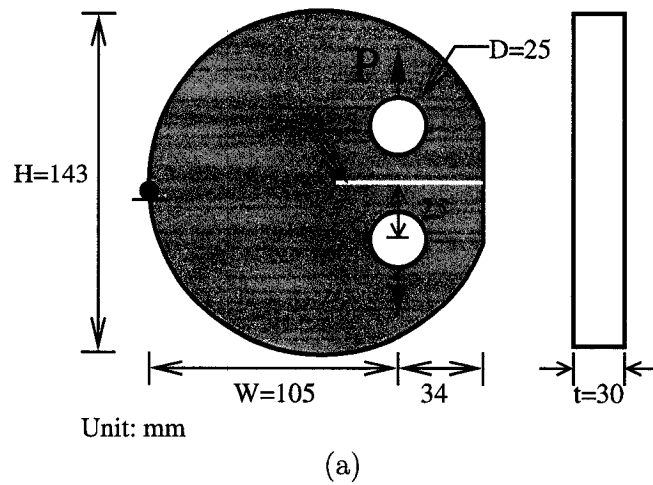


Figure 7.1: DC(T) test simulation: (a) geometry and boundary conditions; (b) mesh configuration for the whole geometry.

Figure 7.2 illustrates a comparison of P versus $CMOD$ curves between numerical and experimental results for different temperatures of $-30^{\circ}C$ and $-10^{\circ}C$. At $-30^{\circ}C$, the numerical results using the rate-independent power-law CZM with $\alpha = 10$ match favorably with the experimental results, which demonstrates that a rate-independent CZM can be used for asphalt concrete fracture at low temperatures, provided that viscoelastic effects are minimal. However, as temperature increases (e.g. $-10^{\circ}C$), the discrepancy between numerical and experimental results becomes significant. This comparison indicates that if rate effects are important, time and temperature effects occurring along the fracture process zone need to be

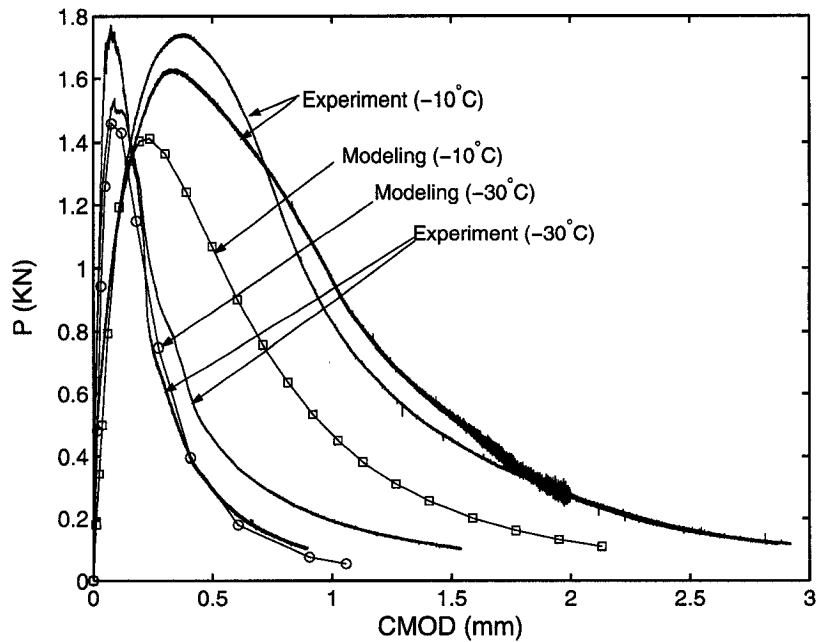


Figure 7.2: Comparison of P versus $CMOD$ curves between numerical and experimental results for different temperatures. In this case, rate independent CZM has been employed.

considered properly in order to obtain reasonable numerical results. Consequently, the rest of this chapter will be devoted to the development and the validation of a rate-dependent CZM.

7.2 Related work

In this section, a brief literature review on viscoelastic fracture modeling is provided. Knauss and Losi [68] investigated rate and temperature-dependent behavior of polymers by incorporating the effect of the nonlinear constitutive response of the failing material. They claimed that “Instead of prescribing these cohesive forces as a separate material function, it would seem fundamentally preferable to compute their rate-dependent evolution from the constitutive behavior for the disintegrating material so that their development is coupled mutually to the viscoelastic response of the surrounding bulk materials.” So, they proposed the following

expression:

$$\sigma(t) = \psi(\varepsilon) \int_0^t G(t-t') \frac{d\varepsilon}{dt'} dt', \quad (7.1)$$

in which $\sigma(t)$ denotes stress, which is function of time; $\psi(\varepsilon)$ is a damage parameter, which is extrapolated to zero at maximum strain; and G is the shear relaxation moduli. Notice that the above expression is a multiplication of the damage function, ψ , and the hereditary integral used to characterize viscoelastic bulk material. Rahul-Kumar et al. [100, 99] employed a cohesive zone model to investigate polymer interfacial fracture. Allen and Search [4] extended the works by Knauss and Losi [68] and Rahul-Kumar et al. [100, 99] by incorporating micromechanics.

Bazant and his coworkers [9, 12, 73, 140] developed a rate-dependent softening law based on the activation theory of the rate-process of bond rupture on the atomic scale [42] to investigate time-dependent fracture behavior in concrete. The final expression for the rate-dependent law becomes

$$\dot{\delta}_n = \dot{\delta}_0 \sinh \left(\frac{\sigma - f(\delta_n)}{\sigma_c} \right), \quad (7.2)$$

in which $\dot{\delta}_n$ is normal opening displacement rate occurring along the fracture process zone, $\dot{\delta}_0$ is reference normal opening displacement rate, and $f(\delta_n)$ is a unique softening stress-displacement law for infinitely slow loading. To deal with a large fracture process zone in typical of concrete and other quasi-brittle materials, a boundary integral formulation of the cohesive crack model in terms of the compliance functions for loads applied anywhere on the crack surface is introduced, which reads

$$\delta_n = f^{-1} \left[\sigma - \sigma_c \operatorname{asinh} \left(\frac{\dot{\delta}_n}{\dot{\delta}_0} \right) \right], \quad (7.3)$$

where asinh is an inverse function of \sinh .

Xu et al. [143] and Kogan et al [69] proposed a separate material function to handle

viscoelastic fracture, which is given by

$$t_{vn} = \sigma_c \left[1 + \left(\frac{\dot{\delta}_n}{\dot{\delta}_0} \right)^m \right], \quad (7.4)$$

in which m and $\dot{\delta}_0$ are parameters associated with viscoelastic fracture. The stress σ_c is assumed to be either constant for a Dugdale-like model [143], or a function of opening displacement [69]. Rahul-Kumar et al. [100] extended the above expression to

$$t_{vn} = t_n(\delta_n) \left[1 + \left(\frac{\dot{\delta}_n}{\dot{\delta}_0} \right)^m \right]. \quad (7.5)$$

Xu et al. [141, 142] investigated rate effects of failure in adhesive bonds where the source of time-dependency is the rate of the material separation in the fracture process zone. A rate-dependent CZM consisting of rate-independent and rate-dependent material separation parameters is given as

$$\mu \frac{dt_{vn}}{dt} + k_2 t_{vn} = \mu \left[\frac{dt_n}{d\delta_n} + k_2 \right] \frac{d\delta_n}{dt} + k_2 t_n \quad (7.6)$$

where μ is the cohesive zone viscosity with a unit force per velocity per area, and k_2 is a secondary cohesive zone stiffness with a unit of force per relative displacement per area. The rate-independent and rate-dependent material separation parameters are obtained with reasonable experimental and numerical analyses efforts. Double cantilever beam joints bonded with a high-density polyethylene based adhesive under constant loading rates were investigated [141, 142].

To account for particle interaction in a viscous medium, Nguyen et al. [87] developed a rate-dependent cohesive continuum model in which elastic bond breaking and viscous weakening are considered. The cohesive interactions are modeled using phenomenological bond force law, whereas the local resistance is described through a continuum viscosity function. Afterwards, they employed the model to analyze steady-state peeling and dynamic crack growth.

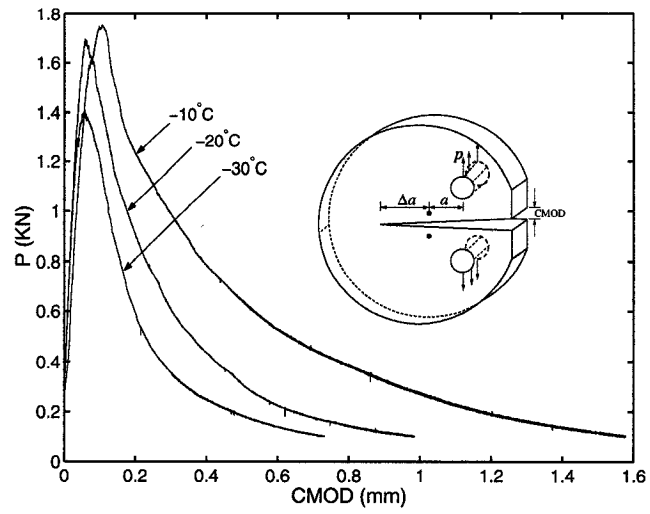


7.3 Challenges

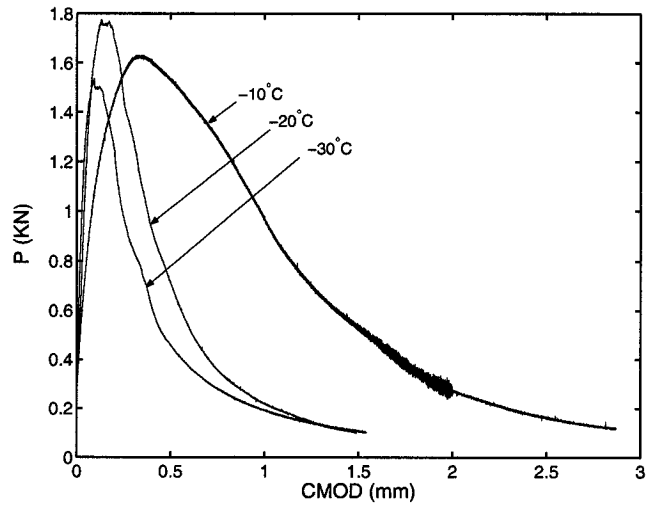
Asphalt concrete may show different fracture behavior for different temperatures and loading rates due to asphalt binders displaying viscoelastic properties. Furthermore, each binder may show different sensitivity to temperature and rate. This problem can be illustrated by the DC(T) test results performed on different asphalt concrete samples cored in northern Iowa. The performance graded asphalt binders PG64-22 and PG58-34 were used in the asphalt concrete samples. Asphalt concrete with a PG64-22 binder is referred to as IOWA-MAT-A and asphalt concrete with a PG58-34 binder is IOWA-MAT-B. Figures 7.3 (a) and (b) illustrate P versus CMOD curves for IOWA-MAT-A and IOWA-MAT-B, respectively, at three different temperatures, -30 , -20 and -10°C . Figure 7.3 (a) shows that as temperature increases, the peak load increases likewise. Similarly, the area of the curve increases, indicating that the energy dissipated due to fracture is proportional to the increase of temperature. The general trend of the three curves, e.g. post-peak trend, is quite identical. Fracture behavior of regular concrete is similar to that shown in Figure 7.3 (a) [11]. On the other hand, in Figure 7.3 (b), as temperature increases, the area of the curve increases, while the peak load first increases and then decreases. The pre-peak and post-peak trends of the curves for -30°C and -20°C are different from those for -10°C . The overall fracture behavior of IOWA-MAT-A is found to be different from that of IOWA-MAT-B. Each binder of asphalt concrete plays a considerable role in fracture behavior with different dependence on various temperatures and loading rates. Thus, prediction of time and temperature dependent fracture behavior in asphalt concrete poses a great challenge.

7.4 Development of a rate-dependent CZM

In this section, development of a rate-dependent CZM is presented. The approach taken in this study is briefly explained, and a rate theory from which a rate-dependent CZM is derived is provided. Additionally, a sensitivity analysis to several parameters introduced into



(a)



(b)

Figure 7.3: P versus CMOD curves: (a) IOWA-MAT-A (PG64-22); and (b) IOWA-MAT-B (PG58-34).

a new rate-dependent CZM is performed. Finally, summary and remarks on the proposed rate-dependent CZM are provided.

7.4.1 Approach

In this work, we employ the activation energy theory of the rate-process of bond rupture to derive a separate material function which can deal with time and temperature dependent fracture in asphalt concrete. In other words, we combine the work by Bazant and his coworkers [9, 12, 73, 140] with the ones by Kogan et al. [69] and Rahul-Kumar et al. [100]. The motivation for combining two different approaches to derive a rate-dependent CZM is that we can accomplish the following goals:

- utilize a well-known theory, the activation energy theory
- account for rate and temperature effects to the existing rate-independent CZMs, e.g. the power-law CZM (see Eq. (7.5))
- implement the CZM into a finite element framework easily, not only because we can simply multiply both rate and temperature effects to the existing rate-independent CZM implementation but also because we can avoid the burden in handling the hereditary integral appeared in the approaches [4, 68, 99].

7.4.2 On the theory of rate processes

Fracture results from rupture of bonds between atoms or molecules. The atoms or molecules in solids are in a random vibratory motion around their equilibrium positions representing the minimum potential of the bond forces [42, 70]. The potential energy surface of the bond force exhibits maxima representing energy barriers called activation energy, Q . If the maximum kinetic energy of the atom or molecules exceeds the activation energy, the atom or molecules can jump over the activation energy barrier, which signifies a rupture of the bond. The frequency of the jumps of atoms or molecules over their activation energy barrier controls the rate of the rupture process, which is the rate constant, κ , whose unit is $second^{-1}$. Arrhenius said that the rate of a chemical reaction with temperature should be expressed



by an expression of the form [42, 70]

$$\kappa = ce^{-Q/RT}, \quad (7.7)$$

where c is a frequency factor, R is the universal gas constant ($R = 8.3144 \text{ J/mol/K}$) and T is absolute temperature (K). The elementary rate constant, κ , is a fundamentally important quantity. Time and temperature-dependent crack growth processes are described as a function of κ , which is expressed in terms of well-defined physical quantities and represents all effects that control crack growth. The rate of fracture is assumed to be proportional to κ , which is equal to the number of particles whose kinetic energy exceeds a certain energy value within a unit time. When external work, W , is applied to the bond which will undergo fracturing, Eq. (7.7) is modified as follows

$$\kappa_b = ce^{-(Q-W)/RT}, \quad (7.8)$$

in which subscript b signifies that the quantity is associated with the atomic bond-breaking process. Similarly, the rate constant for the backward activation, i.e. healing, is given as

$$\kappa_h = ce^{-(Q+W)/RT}, \quad (7.9)$$

in which subscript h denotes healing. Figure 7.4 represents the breaking and healing energy concepts under the external work, W . The abscissa and ordinate indicate crack growth direction and activation energy, respectively.

The fracture constitutive equation is the resultant of the two steps regarding bond breaking and healing:

$$v = L\kappa_b - L\kappa_h = Lce^{-(Q-W)/RT} - Lce^{-(Q+W)/RT} = L\frac{c}{2}e^{-Q/RT} \sinh(W/RT) \quad (7.10)$$

where v is velocity and L is the distance over which the crack moves after each activation. The Arrhenius type equation, justified by the rate-process theory for bond rupture, was introduced into LEFM-type fracture modeling by Zhurkov [147] and was proposed for the

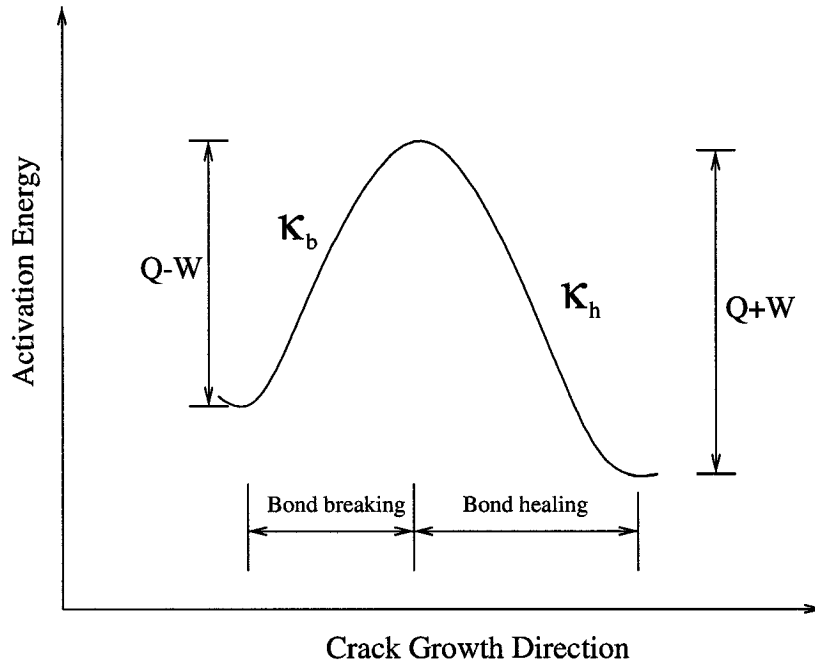


Figure 7.4: The energy barrier when both bond-breaking and bond-healing occur [70].

crack band and cohesive crack models by Bazant [9].

7.4.3 Rate-dependent CZM

To derive a rate-dependent CZM, it is important to introduce reference temperature, T_0 , and to denote that

$$C_0 = L \frac{c}{2} e^{-Q/RT_0} = \text{constant}. \quad (7.11)$$

Assuming W/RT_0 as σ/σ_c , one modifies Eq. (7.10) at any temperature T as follows [12]:

$$v = C_0 \sinh \left(\frac{T_0 \sigma}{T \sigma_c} \right) \exp \left(\frac{Q}{RT_0} - \frac{Q}{RT} \right), \quad (7.12)$$

where σ is assumed as overall crack bridging stress occurring along the fracture process zone and σ_c is tensile strength. Bazant and his coworkers [12, 73] pointed out that “Although at first it seems questionable to deduce Eq. (7.12) directly from the rate of rupture of atomic bonds, which represent a process on a far smaller scale, as far as the rates are concerned, such bridging of many scales is known to be admissible and has been successful

in many other applications of rate process theory [40, 42].” The basic assumption is that the macroscopic fracture growth is proportional to the process of atomic bond ruptures. With further modifications and assumptions, Bazant and his coworkers [12, 73] derived a rate dependent softening law for the cohesive crack model from the activation energy theory of the rate-process of bond ruptures on the atomic level (see Eq. (7.2)). The rate-dependent softening law [9] is modified to be used in a boundary integral formulation of the crack cohesive model in terms of the compliance functions (see Eq. (7.3)).

Replacing v and C_0 with $\dot{\delta}_n$ and $\dot{\delta}_0$, respectively, one obtains the following expression

$$\dot{\delta}_n = \dot{\delta}_0 \sinh\left(\frac{T_0 \sigma}{T \sigma_c}\right) \exp\left(\frac{Q}{RT_0} - \frac{Q}{RT}\right) \quad (7.13)$$

$$\Leftrightarrow \sigma = \sigma_c \frac{T}{T_0} \operatorname{asinh}\left(\exp\left(\frac{Q}{RT} - \frac{Q}{RT_0}\right) \frac{\dot{\delta}_n}{\dot{\delta}_0}\right) \quad (7.14)$$

in which $\dot{\delta}_0$ is reference normal opening displacement rate and $\dot{\delta}_n$ is normal opening displacement rate occurring along the fracture process zone. Substituting σ for t_{vn} and defining parameters γ and χ as

$$\gamma = \frac{T}{T_0}, \quad \chi = \exp\left(\frac{Q}{RT} - \frac{Q}{RT_0}\right), \quad (7.15)$$

one simplifies Eq. (7.14) to

$$t_{vn} = \sigma_c \gamma \operatorname{asinh}\left(\chi \frac{\dot{\delta}_n}{\dot{\delta}_0}\right), \quad (7.16)$$

in which t_{vn} stands for viscoelastic normal traction and the parameters γ and χ , which account for temperature effects, become 1 if $T = T_0$. Although temperature effects are taken into account outside and inside of the *asinh* function in Eq. (7.16), it is convenient to assume $\chi=1$ so that effects of temperature and rate to material strength are decoupled. The stress σ_c is assumed to be constant for a Dugdale-like model [143]. It is important to consider the following aspects in Eq. (7.16): 1) When $\dot{\delta}_n$ is very small, t_{vn} becomes almost zero as illustrated in Figure 7.5, which is not realistic such that a new parameter, ζ , is introduced to consider infinitely slow loading; and 2) Rate-dependent normal traction, t_{vn} , never reaches a peak and decays under constant normal opening displacement rate, $\dot{\delta}_n$, due to σ_c (see

Figure 7.5). Thus, one obtains

$$t_{vn} = t_n f_v = t_n \gamma \operatorname{asinh} \left(\frac{\dot{\delta}_n}{\dot{\delta}_0} + \zeta \right), \quad (7.17)$$

in which f_v is a function accounting for rate and temperature effects. Notice that Eq. (7.17) is similar to Eq. (7.5) except for functions accounting for viscoelastic effects, i.e. $\left[\gamma \operatorname{asinh} \left(\frac{\dot{\delta}_n}{\dot{\delta}_0} + \zeta \right) \right]$ and $\left[1 + \left(\frac{\dot{\delta}_n}{\dot{\delta}_0} \right)^m \right]$. It is implicit in the model that as loading rate decreases, material strength decreases likewise, which generally agrees with experimental observations.

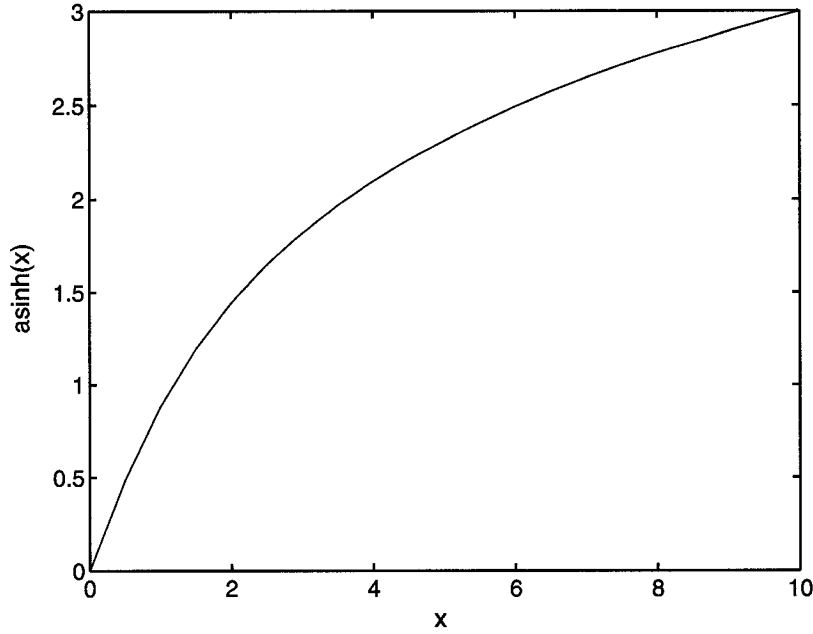


Figure 7.5: asinh function.

However, in Eq. (7.17), both material strength and the area of the displacement jump and traction curve representing cohesive fracture energy are proportional to f_v , which is not realistic for asphalt concrete. To illustrate this point, the power-law CZM with $\alpha = 1$ (i.e. bilinear model) is used so that Eq. (7.17) becomes

$$t_{vn} = \begin{cases} \sigma_c \frac{\delta_n}{\delta_{cc}} f_v = \sigma_c \frac{\delta_n}{\delta_{cc}} \gamma \operatorname{asinh} \left(\frac{\dot{\delta}_n}{\dot{\delta}_0} + \zeta \right) & \delta_n < \delta_{cc} \\ \sigma_c \left(1 - \frac{\delta_n}{\delta_c} \right) \frac{1}{(1 - \delta_{cc}/\delta_c)} f_v = \sigma_c \left(1 - \frac{\delta_n}{\delta_c} \right) \frac{1}{(1 - \delta_{cc}/\delta_c)} \gamma \operatorname{asinh} \left(\frac{\dot{\delta}_n}{\dot{\delta}_0} + \zeta \right) & \delta_n > \delta_{cc} \end{cases} \quad (7.18)$$

Figure 7.6 shows viscoelastic cohesive laws for different magnitudes of f_v . The parameter

δ_{cc} is defined as $0.1\delta_c^{\alpha=1}$ to show the pre-peak region clearly, which is for illustration purposes. The abscissa denotes non-dimensional normal opening displacement and the ordinate represents non-dimensional viscoelastic normal traction. As f_v , which includes effects of temperature and rate, duplicates, the peak traction and the area of the curve also duplicate. Furthermore, regardless of the magnitudes of f_v , the critical displacement, in which normal viscoelastic traction is zero, is the same. Since asphalt concrete with different binders is found to show various fracture behaviors (see Section 7.3), it is convenient to replace δ_c with δ_{vc} , which is viscoelastic critical displacement, as shown in Eq. (7.18), in order to consider different fracture energies for various temperatures and rates. Thus, Eq. (7.18) becomes

$$t_{vn} = \begin{cases} \sigma_c \frac{\delta_n}{\delta_{cc}} f_v = \sigma_c \frac{\delta_n}{\delta_{cc}} \gamma \operatorname{asinh} \left(\frac{\dot{\delta}_n}{\dot{\delta}_0} + \zeta \right) & \delta_n < \delta_{cc} \\ \sigma_c \left(1 - \frac{\delta_n}{\delta_{vc}}\right) \frac{1}{(1-\delta_{cc}/\delta_{vc})} f_v = \sigma_c \left(1 - \frac{\delta_n}{\delta_{vc}}\right) \frac{1}{(1-\delta_{cc}/\delta_{vc})} \gamma \operatorname{asinh} \left(\frac{\dot{\delta}_n}{\dot{\delta}_0} + \zeta \right) & \delta_n > \delta_{cc} \end{cases} \quad (7.19)$$

We propose the following relationship between δ_{vc} and δ_c

$$\delta_{vc} = \eta^{-1} f_v^{-1} \delta_c \quad (7.20)$$

to ensure that fracture energy and material strength for different temperatures and rates vary independently.

7.4.4 Summary

In this section, the proposed viscoelastic CZM is summarized. Although the model is explained in the previous sections, each term is clearly explained before this model is used for viscoelastic fracture modeling. If the power-law CZM is used, the final forms of the proposed viscoelastic CZM are

$$t_{vn} = \begin{cases} \sigma_{vc} \frac{\delta_n}{\delta_{cc}} & \delta_n < \delta_{cc} \\ \sigma_{vc} \left(1 - \frac{\delta_n}{\delta_{vc}}\right)^\alpha \frac{1}{(1-\delta_{cc}/\delta_{vc})^\alpha} & \delta_n > \delta_{cc} \end{cases} \quad (7.21)$$

in which

$$\delta_{vc} = \eta^{-1} f_v^{-1} \delta_c. \quad (7.22)$$

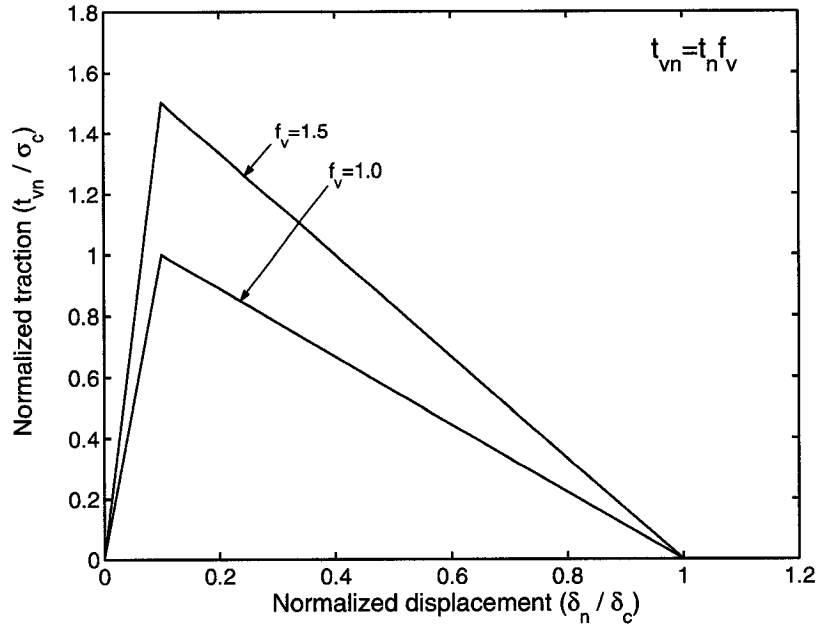


Figure 7.6: Viscoelastic cohesive laws for different values of f_v .

$$\sigma_{vc} = f_v \sigma_c, \quad (7.23)$$

$$f_v = \gamma \alpha \sinh \left(\frac{\dot{\delta}_n}{\dot{\delta}_0} + \zeta \right). \quad (7.24)$$

Viscoelastic cohesive fracture energy is obtained if we assume $\alpha = 1$ as follows:

$$G_{vc} = \frac{1}{2} \sigma_{vc} \delta_{vc} = \frac{1}{2} f_v \sigma_c \eta^{-1} f_v^{-1} \delta_c = \eta^{-1} G_c. \quad (7.25)$$

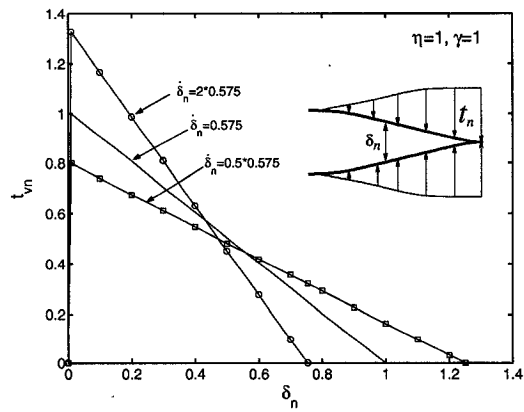
The notation is defined as such: t_{vn} is viscoelastic normal traction; σ_{vc} is viscoelastic material strength; δ_{cc} , which controls artificial compliance, is displacement corresponding to peak traction; δ_n is normal opening displacement; α is an internal variable affecting a CZM softening shape; δ_{vc} is viscoelastic critical displacement, in which viscoelastic traction becomes zero; $\dot{\delta}_n$ is normal opening displacement rate; $\dot{\delta}_0$ is reference opening displacement rate; γ is a parameter to account for temperature effects; ζ is introduced to consider slow loading rate case; and δ_c , σ_c and G_c are critical displacement, material strength, and cohesive fracture energy, respectively, evaluated at reference temperature and loading rate. Notice that Eq. (7.21) is identical with Eq. (3.26) except that σ_c and δ_c in Eq. (3.26) are replaced with σ_{vc}

and δ_{vc} , respectively. Rate and temperature effects on material strength are explicitly considered as expressed by Eqs. (7.23) and (7.24), while both effects to cohesive fracture energy are implicitly taken into account through the parameter η (because cohesive fracture energy obtained from experiments accounts for both effects already). More importantly, fracture energy and material strength vary independently for different temperatures and rates. In this study, δ_{cc} is defined as $0.01\delta_c^{\alpha=1}$ so that it is constant regardless of different rates and temperatures.

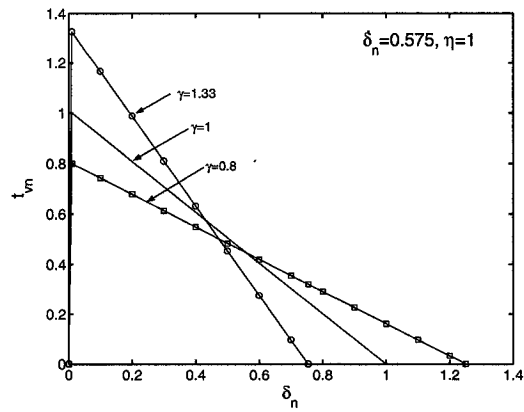
7.5 Sensitivity analysis

In this section, sensitivity analysis to $\dot{\delta}_n$, γ , and η is performed. The parameters $\dot{\delta}_n$ and γ affect peak traction, i.e. material strength, while η influences the area of the displacement jump and traction curve, i.e. cohesive fracture energy. For the sake of illustration, the following values are assumed: $\alpha = 1$, $\sigma_c = 1$, $\delta_c = 1$, $G_c = 0.5$, $\delta_{cc} = 0.01$, $\zeta = 0.6$ and $\dot{\delta}_0 = 1.0$. Consistent units are used. Figure 7.7 (a) compares viscoelastic cohesive laws for different normal opening displacement rates with fixed $\eta = 1$ and $\gamma = 1$. As $\dot{\delta}_n$ increases, the peak traction, i.e. material strength, increases. This trend is similar with experimental observation. However, the area under the curve remains constant due to the constraint established by Eq. (7.25). Figure 7.7 (b) shows various viscoelastic cohesive laws for different magnitudes of the parameter γ with fixed $\dot{\delta}_n=0.575$ and $\eta = 1$. As γ increases, the peak traction increases and vice-versa, with a constant area under the curve for all cases. Viscoelastic cohesive laws for different values of the parameter η with fixed $\dot{\delta}_n=0.575$ and $\gamma = 1$ are illustrated in Figure 7.7 (c). As η increases, the area of the curve increases, while the peak traction remains the same. Thus, as γ and δ_n increase, peak traction (i.e. material strength) increases. However, they do not influence fracture energy, which is only affected by the parameter η .

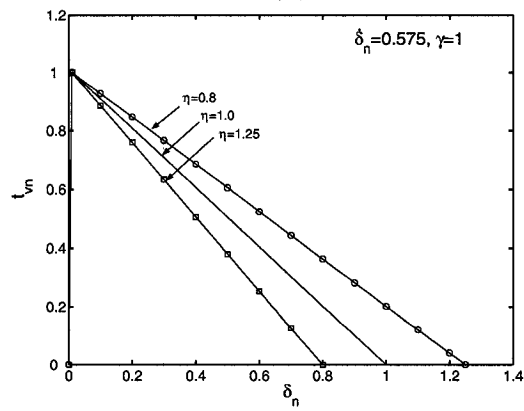
The combination of the two variables, which is $\dot{\delta}_n$ or γ and η , can generate rate-dependent cohesive laws with various fracture energies and material strengths. For example, Figure 7.8



(a)



(b)



(c)

Figure 7.7: Illustration of rate-dependent cohesive laws: (a) for different normal opening rates $\dot{\delta}_n$ with $\eta = 1$ and $\gamma = 1$; (b) for different magnitudes of the parameter γ with $\delta_n = 0.575$ and $\eta = 1$; and (c) for different magnitudes of the parameter η with $\delta_n = 0.575$ and $\gamma = 1$.

shows various viscoelastic cohesive laws considering various $\dot{\delta}_n$ and η with fixed $\gamma = 1$. The solid line denotes a cohesive law at reference temperature and rate. The solid line with circles represents a case in which as loading rate increases, both material strength and fracture energy increase. The solid line with crosses illustrates a case in which as loading rate increases, material strength increases, while fracture energy decreases. The solid line with squares stands for a case in which as loading rate decreases, material strength decreases, while fracture energy increases. Due to various and complicated viscoelastic fracture behaviors of asphalt concrete, we propose the idea of independently controlling two important parameters, material strength and fracture energy, to capture fracture behavior reasonably.

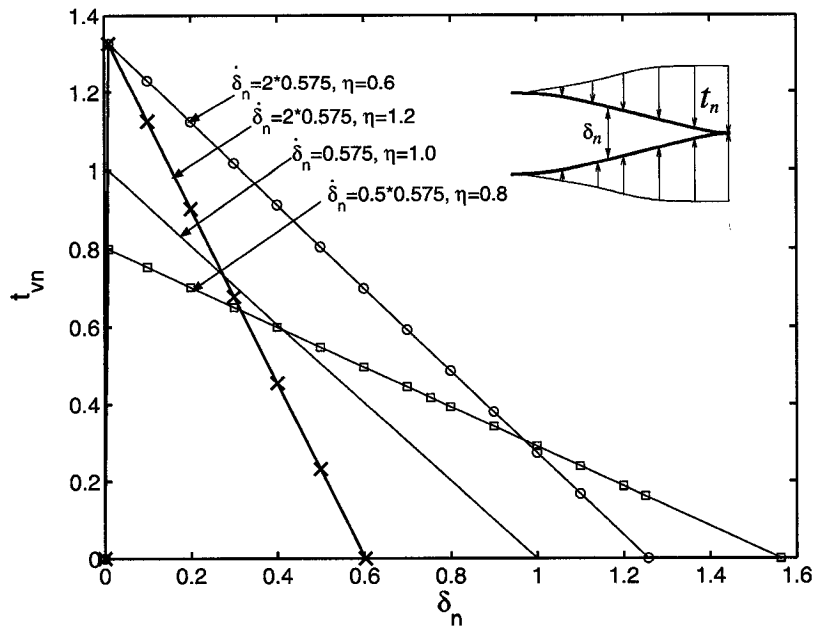


Figure 7.8: Viscoelastic cohesive laws for different magnitudes of the parameter η and $\dot{\delta}_n$ with $\gamma = 1$.

7.6 Proposed procedure

We proposed the novel rate-dependent CZM from the activation energy theory of the rate process of bond rupture in conjunction with reasonable assumptions and simplifications. This CZM, from Eqs. (7.21) to (7.24), can represent various situations, which may be

relevant to asphalt concrete. Before applying the proposed viscoelastic CZM to investigate time and temperature dependent fracture behavior in asphalt concrete, we need to adopt an acceptable procedure for various cases under different temperatures and rates. A general procedure is employed in order to:

- obtain cohesive parameters associated to material strength and cohesive fracture energy at reference temperature and loading rate
- simulate a fracture test using cohesive parameters at the reference conditions, and calibrate a parameter η
- determine η and γ , which are viscoelastic parameters, using the ratio of cohesive parameters between the reference temperature and loading rate, and current temperature and loading rate
- perform fracture test simulation subjected to the current temperature and loading rate condition using the parameters, which are evaluated at the reference condition, and the viscoelastic parameters, which are evaluated at the current condition

To illustrate the point, suppose we use the power-law CZM. The parameters to be evaluated are δ_c , σ_c , δ_{cc} , α , ζ , γ , η and $\dot{\delta}_0$. The cohesive parameter σ_c is obtained from the IDT test in asphalt concrete. The parameter δ_{cc} , which has a good effect on reducing artificial compliance, is assumed as $0.01\delta_c^{\alpha=1}$, in which $\delta_c^{\alpha=1}$ is obtained from $2G_c/\sigma_c$. The cohesive parameter G_c is obtained from the fracture tests, e.g. DC(T) test. The parameter α , which influences CZM softening shape, is assumed as 10, because we found that this softening shape captures fracture behavior in asphalt concrete reasonably well. The cohesive parameter δ_c can be obtained from Eq. (3.27). Notice that the cohesive parameters, σ_c and δ_c , are based on experimental tests at the reference temperature and reference loading rate.

The parameters ζ , γ , η and $\dot{\delta}_0$ are newly introduced variables of the proposed viscoelastic CZM. For concrete, it is assumed that for infinitely slow loading rate, there exists a unique



softening behavior, and material strength is around 80 percent of material strength obtained under normal loading rate fracture test [12, 140]. For asphalt concrete, we expect to have more pronounced viscoelastic effect so that ζ is taken as 0.6. Material strength at infinitely slow loading rate is assumed to be around 60 percent of material strength obtained at normal loading rate. The parameter $\dot{\delta}_0$, which is constant reference displacement rate, is taken as $\dot{\delta}_{25}$ which is normal opening displacement rate at the initial crack tip. the parameter γ expresses the relationship between referent and current temperatures, and any difference between the two affects the value of γ . Since the parameter γ is multiplied by material strength σ_c to generate viscoelastic material strength σ_{vc} , it is determined based on the ratio of material strength evaluated between the reference temperature and the current temperature. Suppose we have material strength at two different temperatures with the same loading rate, σ_1 and σ_2 . Using Eqs. (7.23) and (7.24), the following relationship can be obtained:

$$\sigma_{vc} = \sigma_1 = \gamma_1 \text{asinh}\left(\frac{\dot{\delta}_n}{\dot{\delta}_0} + \zeta\right) \sigma_c \quad (7.26)$$

$$\sigma_{vc} = \sigma_2 = \gamma_2 \text{asinh}\left(\frac{\dot{\delta}_n}{\dot{\delta}_0} + \zeta\right) \sigma_c. \quad (7.27)$$

Subscripts 1 and 2 denote temperature 1 and temperature 2, respectively, and σ_c is material strength evaluated at the reference loading rate and temperature. Since we evaluate σ_1 and σ_2 at the same loading condition, we speculate that the contribution of the rate term $\left[\text{asinh}\left(\frac{\dot{\delta}_n}{\dot{\delta}_0} + \zeta\right)\right]$ to material strength between Eqs. (7.26) and (7.27) is very close. So, one obtains

$$\gamma_2 = \gamma_1 \frac{\sigma_2}{\sigma_1}. \quad (7.28)$$

The parameter η , which considers various cohesive fracture energies for different temperatures and loading rates, is evaluated based on the ratio of cohesive fracture energy evaluated between the reference temperature and loading rate and the current temperature and loading rate. Similarly, one obtains

$$\eta_2 = \eta_1 \frac{G_1}{G_2}. \quad (7.29)$$

Two important viscoelastic parameters, η and γ , have physical meaning that η implicitly accounts for viscoelastic effects on cohesive fracture energy, whereas γ explicitly represents temperature effects on material strength.

7.7 Computational results

In this section, the proposed viscoelastic CZM is employed to investigate time and temperature dependent fracture behavior of asphalt concrete. Asphalt concretes IOWA-MAT-A and IOWA-MAT-B are used to validate the novel viscoelastic CZM and procedures proposed in this study.

7.7.1 Case I: IOWA-MAT-A

In this section, asphalt concrete IOWA-MAT-A is adopted. The same geometry and boundary condition used in Section 7.1 are employed, except for the difference in thickness. The thickness of the specimen is 35mm. The fracture energies and the material strengths for three different temperatures are shown in Table 7.4. The fracture energy is obtained using the δ_{25} -measurement. Constant $1.0\text{mm}/\text{min}$ CMOD rate is adopted for the DC(T) test for three temperatures. Material strength at -20°C is obtained from the experimental test, i.e. IDT test, and for the rest of the temperatures, we assume material strength. Model parameters (see Table 6.1) and shift factors (see Table 6.2) evaluated from experiments using the IDT test are adopted for viscoelastic analysis of bulk materials. The geometry and material and cohesive parameters are based on the cored pavement material, in which PG64-22 binder is used, located in northeast Iowa. In this analysis, -20°C and $1\text{mm}/\text{min}$ CMOD rate are chosen as reference temperature T_0 and reference loading rate, respectively. The power-law CZM with $\alpha = 10$ is used.

DC(T) test simulation subjected to the reference temperature and loading rate condition is carried out. The parameter γ equals 1 at the reference temperature (i.e. $T = T_0 = -20^\circ\text{C}$) (see Eq (7.15)). The purpose of this simulation is to find an appropriate value of

Table 7.4: Fracture energy of the two replicates and material strength at -10°C , -20°C and -30°C [131].

Temperature	Replicate	Fracture energy (J/m^2)		Material strength (MPa)
		face 1	face 2	
-10°C	1	180	175	2.45
	2	161	127	
	Average	160		
-20°C	1	116	117	2.9
	2	129	118	
	Average	120		
-30°C	1	73	61	2.6
	2	80	74	
	Average	72		

the parameter η . Figure 7.9 illustrates a comparison of P versus CMOD curves between numerical and experimental results. Two solid lines denote experimental results, while solid circles stand for numerical results. The predicted numerical results using $\eta = 0.8$ are in close agreement with the experimental results. Magnitudes of all parameters used in this simulation are shown in Table 7.5.

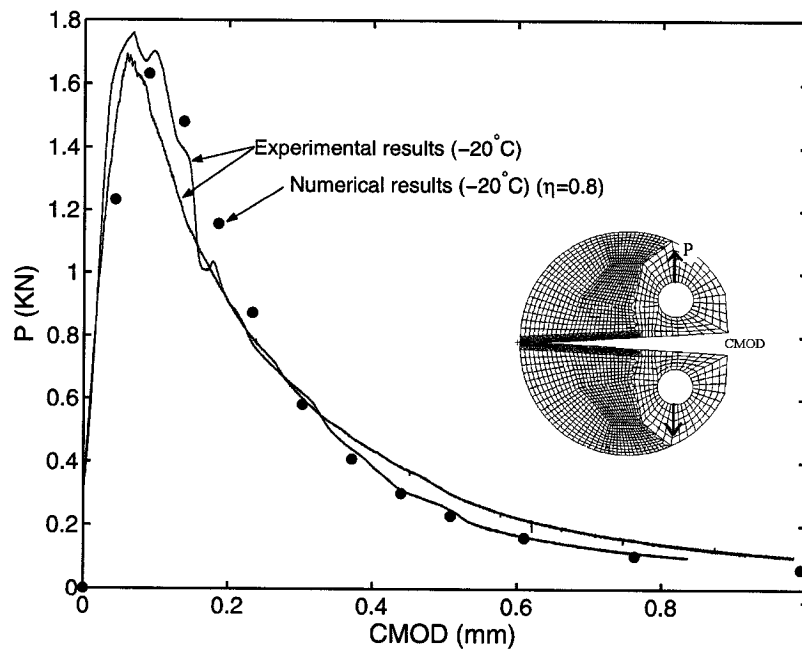


Figure 7.9: Comparison of P versus CMOD curves between numerical and experimental results at $T = T_0 = -20^{\circ}\text{C}$.

Table 7.5: Magnitudes of parameters of the viscoelastic CZM under $-20^\circ C$ and $1mm/min$ CMOD rate condition.

α	δ_{cc}	G_c	σ_c	δ_c	ζ	δ_0	η	γ
10	0.000828 mm	$120J/m^2$	$2.9MPa$	0.436	0.6	0.7mm/min	0.8	1

Before we perform DC(T) test simulation subjected to $-30^\circ C$ and $1mm/min$ CMOD rate, parameters γ and η at $-30^\circ C$ and $1mm/min$ CMOD rate need to be defined using the parameters $\gamma = 1$ and $\eta = 0.8$ obtained at the reference temperature ($-20^\circ C$) and CMOD rate ($1mm/min$). The parameter γ is obtained from the following relationship:

$$\gamma^{T=-30^\circ C} = \gamma^{T=T_0} \frac{\sigma_c^{T=-30^\circ C}}{\sigma_c^{T=T_0}} = 1 \frac{2.6}{2.9} = 0.89 \quad (7.30)$$

Similarly, the parameter η is obtained from

$$\eta^{T=-30^\circ C} = \eta^{T=T_0} \frac{G_c^{T=T_0}}{G_c^{T=-30^\circ C}} = 0.8 \frac{120}{72} = 1.34 \quad (7.31)$$

Using the parameters obtained, the present numerical results are compared with experimental results (see Figure 7.10). The abscissa and ordinate denote CMOD and P, respectively. The predicted pre-peak shape, peak load and post-peak shape match favorably with experimental results.

For DC(T) analysis at $-10^\circ C$ and $1mm/min$ CMOD rate, the parameters γ and η are obtained as follows, using the same approach described above:

$$\gamma^{T=-10^\circ C} = \gamma^{T=T_0} \frac{\sigma_c^{T=-10^\circ C}}{\sigma_c^{T=T_0}} = 1 \frac{2.45}{2.9} = 0.85 \quad (7.32)$$

$$\eta^{T=-10^\circ C} = \eta^{T=T_0} \frac{G_c^{T=T_0}}{G_c^{T=-10^\circ C}} = 0.8 \frac{120}{160} = 0.6 \quad (7.33)$$

Numerical results at $-10^\circ C$ and $1mm/min$ CMOD rate are plotted together with experimental results in terms of CMOD and P (see Figure 7.11). Two solid lines denote experimental results and solid circles stand for numerical results. The numerical results match reasonably well with experimental results.

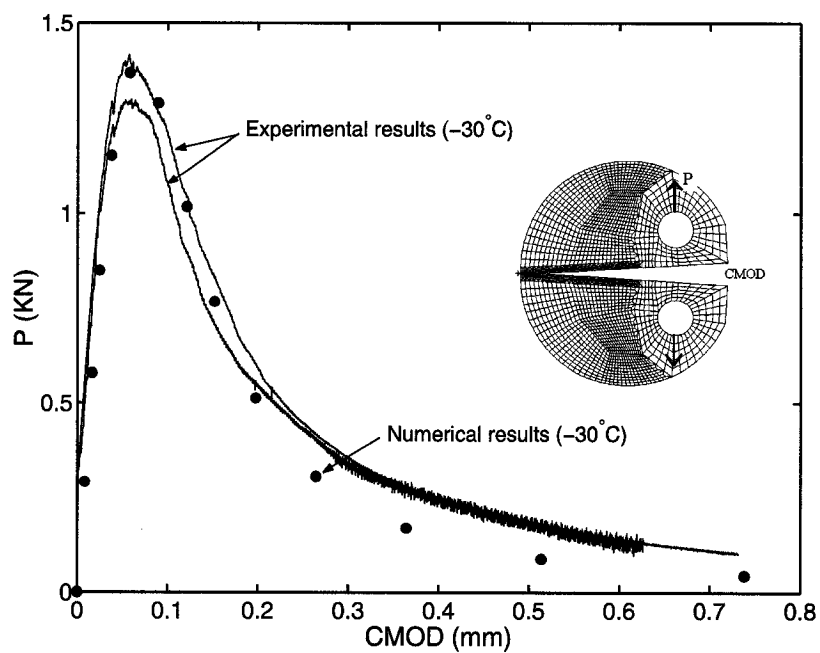


Figure 7.10: Comparison of P versus CMOD curves between numerical and experimental results at $T = -30^{\circ}\text{C}$ and $1\text{mm}/\text{min}$ CMOD rate.

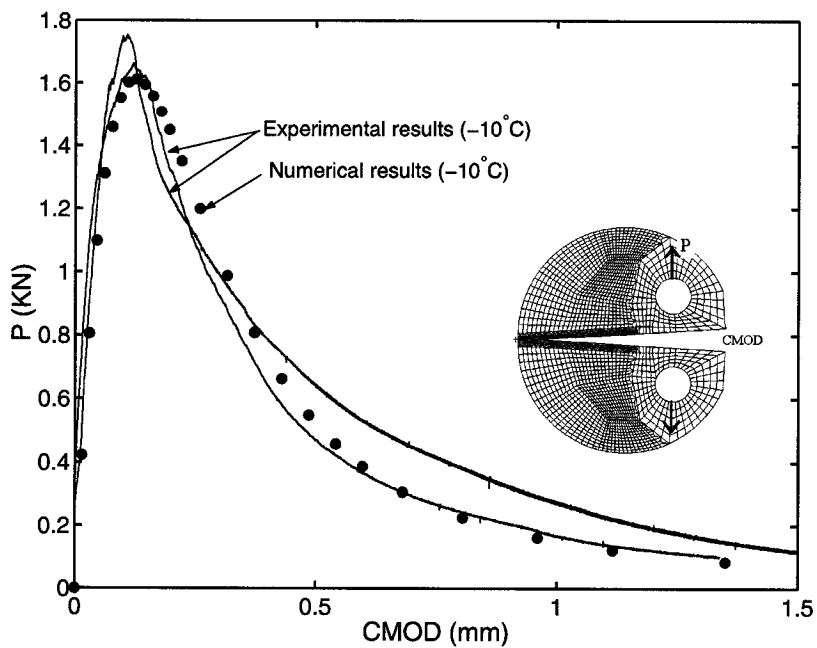


Figure 7.11: Comparison of P versus CMOD curves between numerical and experimental results at $T = -10^{\circ}\text{C}$ and $1\text{mm}/\text{min}$ CMOD rate.

It is demonstrated that the proposed viscoelastic CZM and procedures capture time and temperature dependent behavior in asphalt concrete well. It might be attributed to reasonable assumptions and approaches, which were described before, along with reliable experimental test data. Figure 7.12 compares predicted numerical results with the experimental results at -30°C and -10°C . The predicted pre-peak trend, peak load and post-peak trend are found to be in excellent agreement with the experimental results.

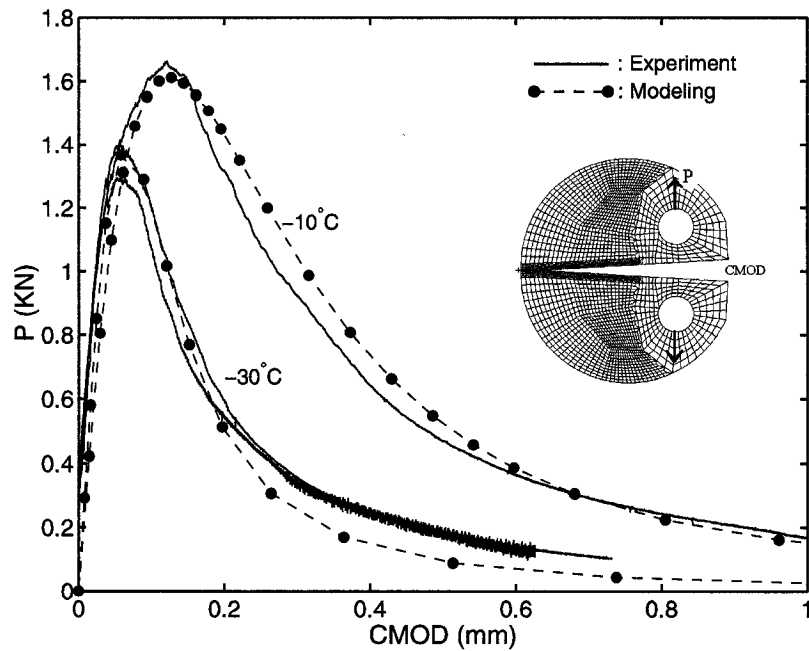


Figure 7.12: Comparison of P versus CMOD curves between numerical and experimental results.

7.7.2 Case II: IOWA-MAT-B

In this section, asphalt concrete IOWA-MAT-B, whose fracture behavior is found to be different from that of asphalt concrete IOWA-MAT-A, is utilized to further validate the proposed viscoelastic CZM and procedures further. The same geometry and boundary conditions used in Section 7.1 are employed. Fracture energy and material strength at three different temperatures are shown in Table 7.6 along with the thickness of the test samples. Because the samples are cored from actual field pavement, the thickness varies a little bit.

Constant $1.0\text{mm}/\text{min}$ CMOD rate is adopted for the DC(T) test at three temperatures. Material strength at -20°C is obtained from the experimental test, i.e. IDT test, and material strength at -10°C and -30°C is assumed as 79 percent and 82 percent, respectively, of material strength at -20°C . Model parameters (see Table 7.2) and shift factors (see Table 7.3) evaluated from the IDT test are adopted for viscoelastic analysis of bulk materials. The geometry and material and cohesive parameters are based on the cored pavement material, in which PG58-34 performance graded asphalt binder is used, located in northeast Iowa. In this analysis, -20°C is chosen as reference temperature, T_0 . The power-law CZM with $\alpha = 10$ is used (as before).

Table 7.6: Fracture energy of the two replicates and material strength at -10°C , -20°C and -30°C .

Temperature	Thickness	Replicate	Fracture energy (J/m^2)		Material strength (MPa)
			face 1	face 2	
-10°C	25	1	463	394	2.85
		2	359	422	
		Average	410		
-20°C	30	1	238	217	3.6
		2	176	185	
		Average	204		
-30°C	30	1	121	162	2.95
		2	192	175	
		Average	163		

In Figure 7.13 (a), predicted numerical results at the reference temperature $T = -20^\circ\text{C}$ are compared with experimental results in terms of P versus CMOD. The solid line and solid circle denote experimental and numerical results, respectively. The numerical results with $\eta = 0.6$ are found to be in good agreement with experimental results. Using the same procedures explained above, the parameters (γ and η) evaluated for -30°C and -10°C are shown in Table 7.7. Figures 7.13 (b) and (c) show a comparison of P versus CMOD curves between numerical and experimental results for -30°C and -10°C , respectively. Notice that the numerical and experimental results illustrated in Figure 7.13 (c) are for the thickness 30 rather than 25. In other words, the force (P) of numerical and experimental results at

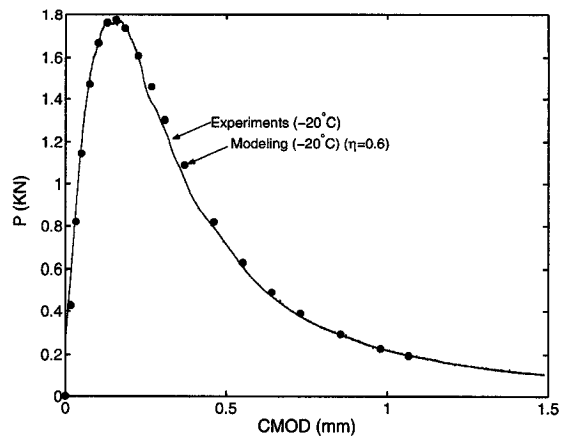
$-10^{\circ}C$ is multiplied by the factor 1.2. The predicted pre-peak trend, peak load and post-peak trend match favorably with experimental results, demonstrating that the proposed viscoelastic CZM with reasonable procedures can be applicable in viscoelastic fracture modeling in asphalt concrete. For comparison with Figure 7.2, predicted numerical results using the proposed viscoelastic CZM are compared with experimental results for $-30^{\circ}C$ and $-10^{\circ}C$ in Figure 7.14. For the lower temperature $-30^{\circ}C$ in which viscoelastic effects are minor, there is little difference in predicted results between that with the viscoelastic CZM and that with the rate-independent CZM. However, as temperature increases the rate-independent CZM modeling underestimates the peak load and the area of the curve, whereas reasonable numerical results are predicted using the proposed viscoelastic CZM. Thus, when viscoelastic effects are considerable, we need to account for time and temperature dependent fracture properly to obtain reasonable viscoelastic fracture responses.

Table 7.7: Magnitudes of parameters of the viscoelastic CZM for three temperatures with $1mm/min$ CMOD rate.

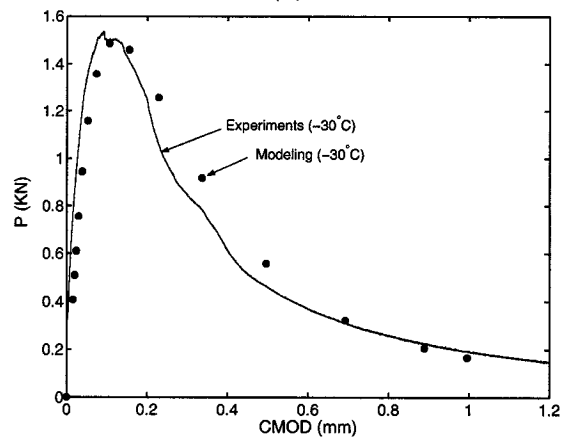
Temperature	α	δ_{cc}	G_c	σ_c	δ_c	ζ	δ_0	η	γ
$-10^{\circ}C$	10	0.00113 mm	$204J/m^2$	$3.6MPa$	0.593	0.6	0.68mm/min	0.3	0.79
$-20^{\circ}C$								0.6	1
$-30^{\circ}C$								0.76	0.82

7.8 Concluding remarks

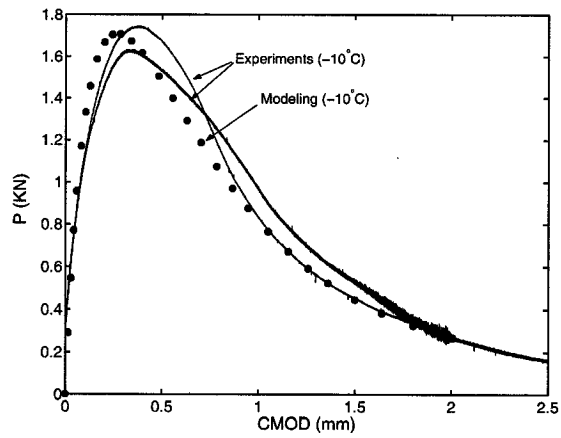
Asphalt concrete shows varied viscoelastic fracture behavior for different temperatures and loading rates due to asphalt binders displaying different viscoelastic properties. As a result, it is difficult to accurately capture viscoelastic fracture behavior in asphalt concrete using either rate-independent CZMs or conventional viscoelastic CZMs. In this work, we employed the activation energy theory of the rate-process of bond rupture to derive a separate material function which can deal with time and temperature dependent fracture, in conjunction with reasonable assumptions and simplifications. The final forms of the proposed viscoelastic CZM has a nice feature, i.e. Eq. (7.21) is almost identical with Eq. (3.26) except that



(a)



(b)



(c)

Figure 7.13: Comparison of P versus $CMOD$ curves between numerical and experimental results at: (a) $T = T_0 = -20^\circ C$; (b) $T = -30^\circ C$; and (c) $T = -10^\circ C$.

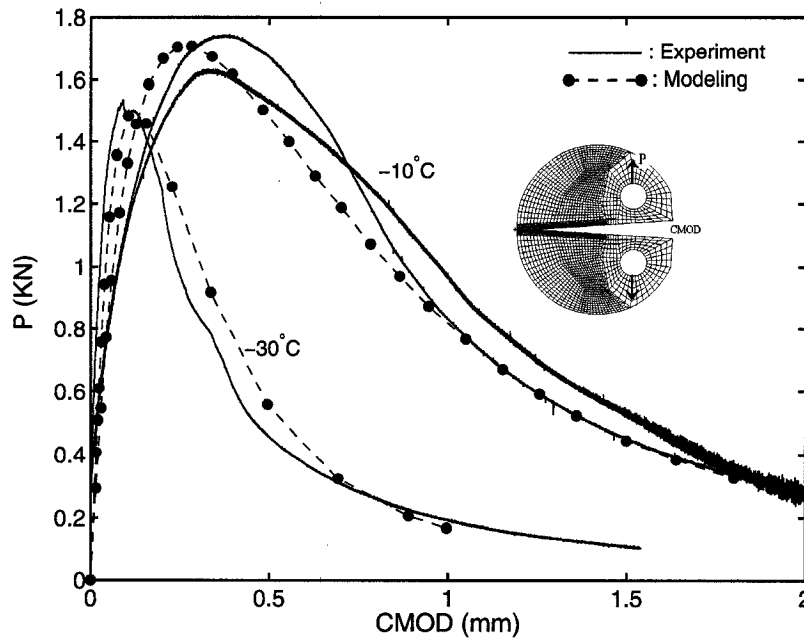


Figure 7.14: Comparison of P versus $CMOD$ curves between numerical and experimental results [135].

σ_c and δ_c in Eq. (3.26) are replaced with σ_{vc} and δ_{vc} , respectively. Moreover, appropriate procedures to evaluate several parameters accounting for time and temperature effects are adopted. The proposed viscoelastic CZMs and procedures as shown in Eqs. (7.21) through (7.24) are able to represent various situations which are relevant to asphalt concrete, due to the idea of controlling two important parameters, i.e. material strength and cohesive fracture energy, independently, considering viscoelastic effects explicitly and implicitly.

Asphalt concretes IOWA-MAT-A and IOWA-MAT-B are used to validate the novel viscoelastic CZM and procedures proposed in this study. For both materials, $-20^\circ C$ and $1mm/min$ $CMOD$ rate are chosen as reference temperature and loading rate, respectively. At the reference condition, γ equals 1 and η is calibrated to create a reasonable agreement between numerical and experimental results. Once the parameter η is calibrated at the reference condition, the parameter γ and η are evaluated at current temperatures and loading rates using the procedures explained above. For $-30^\circ C$ and $-10^\circ C$, the predicted numerical results are found to be in good agreement with experimental results. This demonstrates that

the proposed viscoelastic CZM with reasonable procedures can be applicable to viscoelastic fracture modeling in asphalt concrete.

Chapter 8

Pavement fracture using cohesive zone modeling

In asphalt concrete overlay systems, reflective cracking has been a major cause of distress. It is crucial to understand fracture mechanism in pavement well and to develop a procedure to minimize crack occurrence. Recently, a cohesive zone modeling technique has been developed and used widely to explore fracture behavior in various materials. In this chapter, a CZM is employed to simulate crack initiation and propagation, and to study fracture behavior in the actual pavement section (see Figure 8.1), located in northern IOWA, under temperature and tire loadings. Further detailed investigations of field modeling, (e.g. Iowa and Missouri) can be found in Dave's Ph.D. thesis [31]



Figure 8.1: Actual pavement section in IOWA.

8.1 Field description

The pavement of length 12200mm with thickness of surface 42mm , binder 43mm , leveling 75mm , portland cement concrete (PCC) 253mm , and soil 6100mm is analyzed using a cohesive zone modeling technique. Asphalt concrete pavement consists of surface, binder, and leveling courses. The performance graded asphalt binder PG64-22 is used for the three courses. The PCC, placed between the asphalt concrete and the soil, has a joint. The thickness of the pavement is 4572mm . A schematic drawing of the pavement section is illustrated in Figure 8.2.

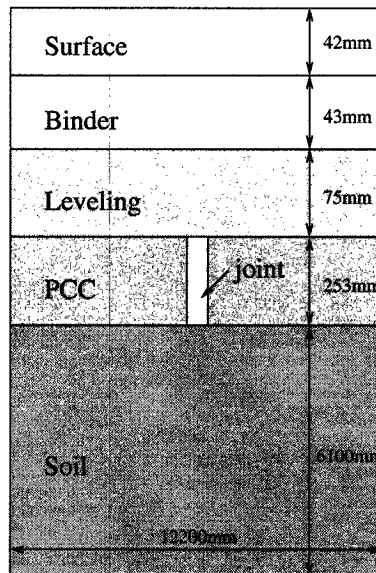


Figure 8.2: Schematic drawing of the pavement section in IOWA.

Figure 8.3 (a) shows the geometry and boundary conditions. Cohesive elements are inserted along the middle of the asphalt concrete, which is located above the PCC joint, to represent typical crack initiation and propagation, i.e. reflective cracking, in pavement. Interfaces among the asphalt concrete, the PCC, and the soil are assumed to be fully bonded. Displacement boundary conditions of $u_y = 0$ for the bottom edge and $u_x = 0$ for the left bottom node are prescribed. The temperature profile provided by Dave [31, 32] is employed as temperature loading for the asphalt concrete and the PCC. Enhanced integrated climatic

model [71] is used to obtain temperature profile through the depth of the pavement using the data such as air temperatures, precipitation, wind speed, pavement layer thicknesses, thermal properties and heat capacity. Figure 8.4 illustrates temperature profile between 4 and 5 p.m. on January 29, 2006 along the depth of the pavement. After temperature loading for one hour, tire loading is imposed for 0.1 second. Figures 8.3 (b) and (c) show mesh details for the whole geometry and the region where cohesive elements are inserted. The geometry is constructed using 12133 four-noded quadrilateral plane strain elements for the bulk material and 41 four-noded linear element for the cohesive material. Viscoelastic effects are considered in the asphalt concrete. Model parameters of relaxation modulus and shift factor for the asphalt concrete three layers are shown in Tables 8.1 and 8.2. Young's modulus for the PCC and the soil is $31GPa$ and $35MPa$, respectively. Table 8.3 shows Poisson's ratio for each layer. Fracture energy and material strength for the asphalt concrete layers are illustrated in Table 8.4. Fracture energy is obtained from the DC(T) test under $1mm/min$. CMOD rate and $-20^{\circ}C$ in conjunction with the δ_{25} measurement. Material strength is obtained from the IDT test based on AASHTO specification [1]. The power-law CZM with $\alpha = 10$ is employed in this simulation. The parameter δ_{cc} , which influences artificial compliance, is defined as $0.01\delta_c^{\alpha=1}$. Note that although magnitudes of material strength and fracture energy, i.e. cohesive parameters, vary depending on temperature and local rate, in this simulation we employ the same fracture energy and material strength regardless of temperature and local rate, which leads to qualitative conclusions.

Table 8.1: Model parameters for three different layers [131].

i	Surface		Binder		Leveling	
	$E_i(GPa)$	$\tau_i(sec)$	$E_i(GPa)$	$\tau_i(sec)$	$E_i(GPa)$	$\tau_i(sec)$
1	3.5	15	3.7	17	4.0	17
2	4.4	249	5.2	319	4.2	342
3	1.7	4817	2.3	7085	3.1	7160
4	7.2	57378	7.1	98891	6.6	104485
5	11.9	2605452	11.6	6082416	9.7	5467244

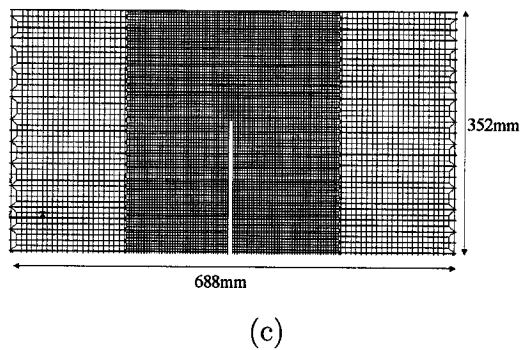
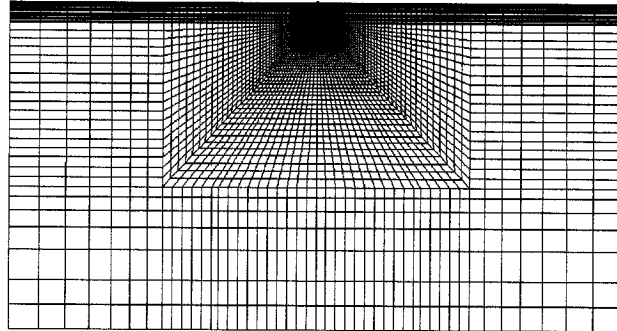
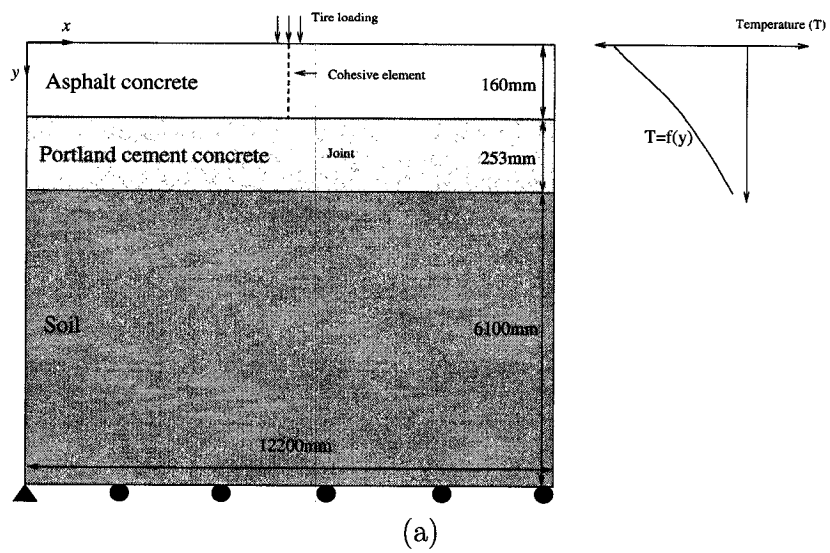


Figure 8.3: Pavement modeling: (a) geometry and boundary conditions; (b) mesh configuration for the whole geometry; and (c) mesh details for the regions where cohesive elements are inserted.

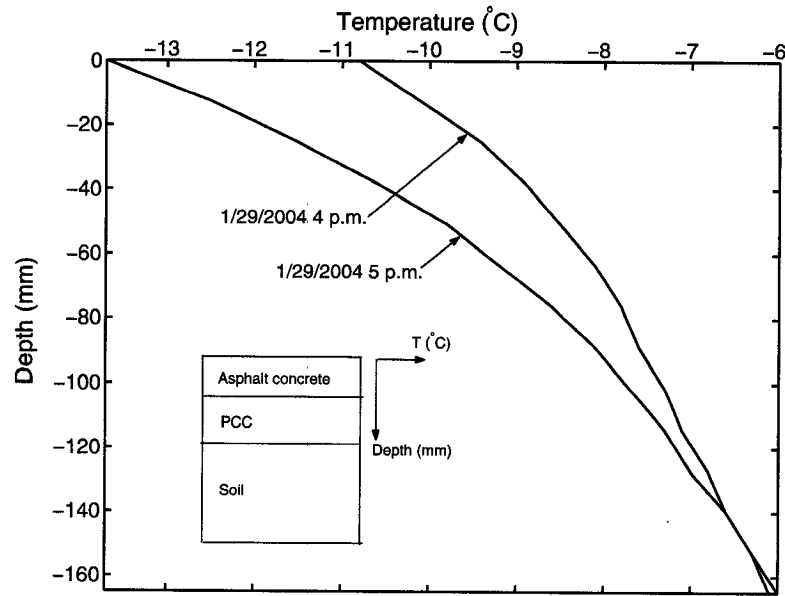


Figure 8.4: Temperature profile along the depth of the pavement.

Table 8.2: Temperature shift factors ($\log(1/a_T)$) [131].

Temperature	Surface	Binder	Leveling
$-30^{\circ}C$	0	0	0
$-20^{\circ}C$	1.95	1.9	1.8
$-10^{\circ}C$	3.2	3.5	3.55

Table 8.3: Poisson's ratio for each layer [131].

Layer	ν
Surface	0.37
Binder	0.37
Leveling	0.25
PCC	0.15
Soil	0.3

Table 8.4: Fracture energy and material strength for the three layers ($1mm/min$. CMOD rate and $-20^{\circ}C$) [131].

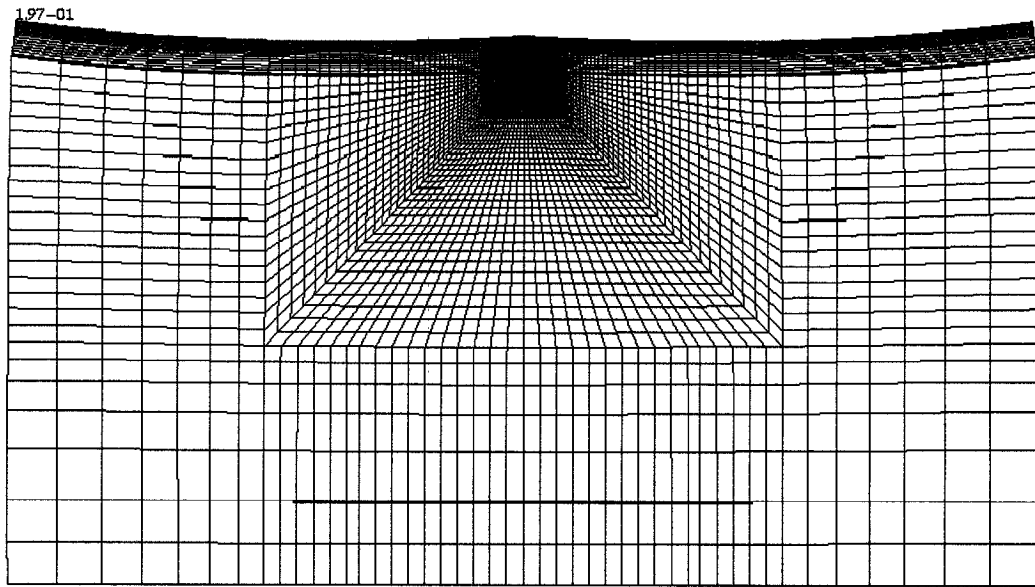
	Surface	Binder	Leveling
Fracture energy (G_c) (J/m^2)	120	123	110
Material strength (σ_c) (MPa)	2.9	2.79	3.07

8.2 Numerical results

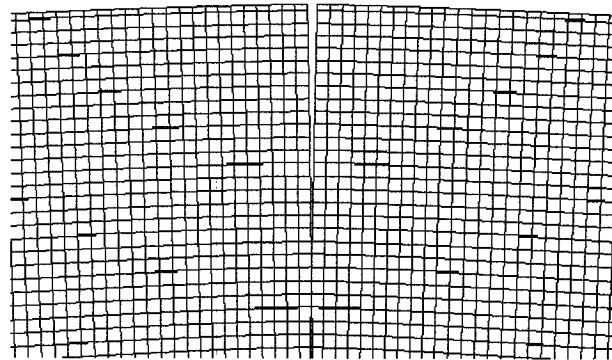
Figures 8.5 (a) and (b) show a deformed shape of the whole geometry and the regions where cohesive elements are inserted, respectively, due to the temperature loading. It induces tension on the top of the pavement structure and as a result, causes top-down cracking. Figures 8.6 illustrates the deformed shape of the pavement structure under the tire loading. Compression is induced on the top of the structure, while tension is generated around the region right above the PCC joint. As expected, temperature induces top-down cracking, while tire loading causes reflective cracking in this particular example.

8.3 Discussion

When an overlay is placed on an existing pavement, physical tearing of the overlay takes place as a result of movement at the joints and cracks in the underlying pavement layer. Reflective cracking has occurred in nearly all types of asphalt overlays, whether placed on existing asphalt or concrete pavements. This cracking in the overlay allows water to percolate into the pavement structure thereby weakening the roadbed foundation and contributing to increased roughness and joint deterioration. A number of studies have been conducted in an effort to minimize or delay the occurrence of reflective cracking. For example, geotextile interlayers (paving fabrics) have been placed over existing pavements before overlay construction in an attempt to isolate movements in the underlying layer and/or to act as an overlay reinforcement [76]. Early treatment methods (pre-1995) were not successful in mitigating reflective crack occurrence nor did they provide a significant economic benefit [18, 76, 82]. In this work, a truly integrated study involving laboratory experiments, analysis, simulations, and field observations is performed (see Figure 8.7). Experiments on the bulk materials are performed to extract bulk properties, e.g. relaxation modulus, and fracture testing is conducted to evaluate fracture quantities, e.g. fracture energy. These experiments provide data for a cohesive zone model, which is tailored for fracture of asphalt concrete. Then,



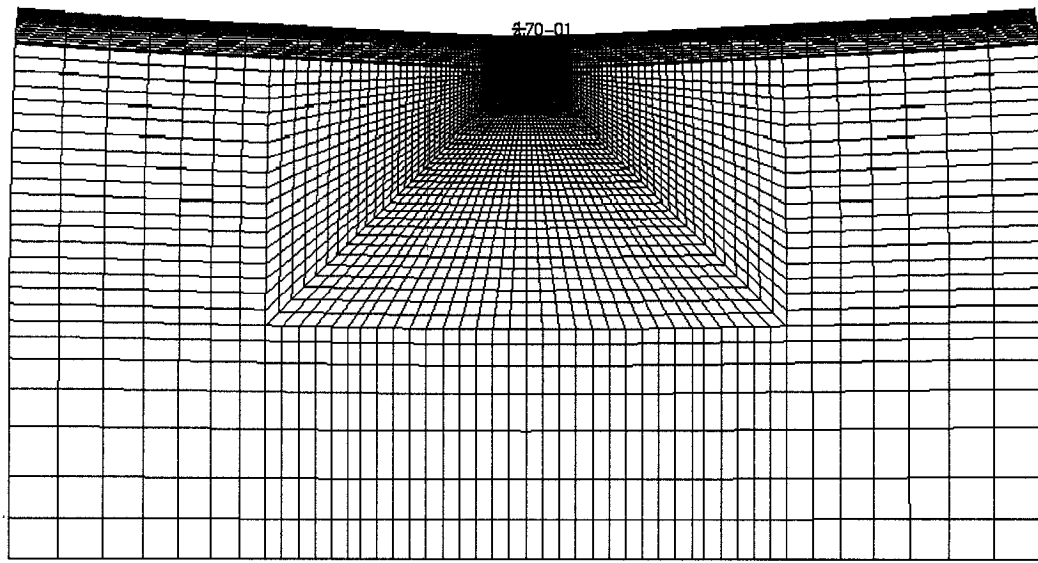
(a)



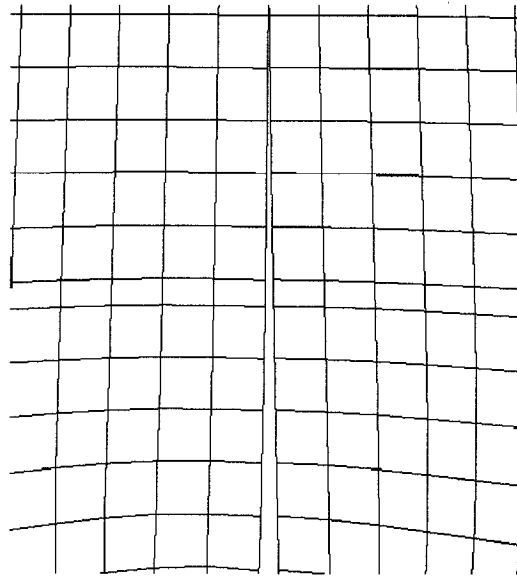
(b)

Figure 8.5: Deformed shape of the pavement structure under the temperature loading: (a) whole geometry; and (b) regions where cohesive element are inserted.

a CZM is used to investigate fracture behavior in asphalt concrete and pavement. In this chapter, as a result of the integrated approach, the ability of a cohesive zone modeling technique to simulate crack propagation in pavement under temperature and loading conditions is demonstrated. Temperature loading induces top-down cracking, while tire loading causes reflective-cracking in this example. A nice feature of computational modeling is that vari-



(a)



(b)

Figure 8.6: Deformed shape of the pavement structure under the tire loading: (a) whole geometry; and (b) regions right above the PCC joint where cohesive element are inserted.

ous geometries, boundary conditions, and constitutive models can be taken into account to evaluate pavement performance. Parametric studies considering several different conditions

can help to develop a procedure to prevent or minimize crack occurrence in pavement.

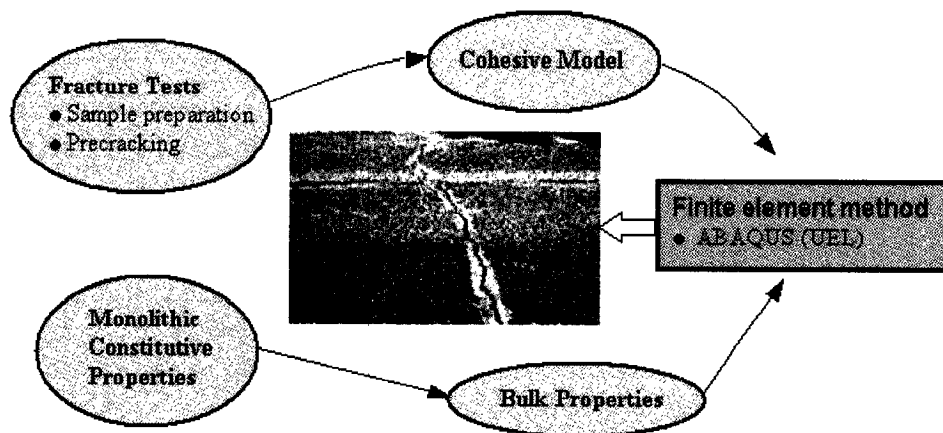


Figure 8.7: Integrated approach involving experiment, modeling and field.

Chapter 9

Concluding remarks

In this study, a cohesive zone model is employed to investigate viscoelastic fracture behavior in asphalt concrete. The various CZMs, such as the power-law CZM, are implemented by means of ABAQUS user element (UEL) capability. Cohesive parameters are experimentally evaluated. Artificial compliance and numerical non-convergence are addressed in detail. New rate-independent and dependent CZMs tailored for fracture of asphalt concrete are proposed. A new operational definition of crack tip opening displacement (CTOD) is employed to considerably minimize the contribution of bulk material in measuring fracture energy. Simulations of various two- and three-dimensional mode I fracture tests, e.g. disk-shaped compact tension (DC(T)), are performed considering viscoelastic effects. Numerical results match reasonably well with experimental results. The mixed-mode single-edge notched beam (SE(B)) test is simulated with cohesive elements inserted over an area to allow cracks to propagate in any general direction. The predicted mixed-mode crack trajectory is found to be in close agreement with experimental results. Crack competition phenomenon between initiation and nucleation is explored and the reasonable γ_{cr} is obtained. The ability to investigate fracture behavior in pavement is demonstrated. In this chapter, the summary and conclusions are presented and suggestions for future work are provided.

9.1 Summary

Chapter 1 of the present work provides a thorough literature review of theoretical, numerical, and experimental work related to cohesive zone modeling and fracture in asphalt concrete. Chapter 1 introduces crucial aspects in modeling asphalt concrete and pavement in context of bulk material and fracture characterizations, and also provides research objectives of this study. Chapter 1 concludes with the organization of the thesis.

Chapter 2 presents the development and application of graded finite elements for pavement analysis and a theoretical formulation for the graded finite element method is provided. The implementation of the UMAT is verified by comparing the numerical results with the analytical solutions by means of the isotropic graded materials where Young's modulus varies perpendicular to the loading direction. The graded element is applied for the asphalt pavement study to consider the aging effect more efficiently and accurately compared to conventional approach.

Chapter 3 provides theoretical and numerical aspects of three cohesive zone models adopted in this study: the potential based exponential model [144], the bilinear CZM [39] and the improved power-law CZM [35, 124]. For each model, both traction vector and tangent modulus matrix are evaluated. A description on how the cohesive element is incorporated into a finite element framework follows. Experimental procedures to evaluate bulk properties and cohesive parameters, e.g. relaxation modulus, fracture energy and material strength, are presented as well.

Chapter 4 describes fracture modeling using the exponential model. Verification of the CZM implementation into ABAQUS user element (UEL) is presented using double cantilever beam (DCB) test simulation and sensitivity analysis to cohesive parameters is performed. Additionally, Chapter 4 discusses the selection of cohesive element sizes for asphalt concrete fracture modeling. Mixed-mode crack propagation simulation is carried out in conjunction with SE(B) test in which mesh discretizations of cohesive elements are tailored to the crack

trajectory predicted by I-Franc2D [61]. Finally, a complete crack trajectory of the present numerical simulation using the Riks method [30] is compared with that of experimental results.

Chapter 5 investigates asphalt concrete fracture behavior considering viscoelastic bulk material in conjunction with the bilinear CZM, and numerically quantifies effects of CZM compliance on asphalt concrete fracture. Chapter 5 also presents the motivation for using the bilinear CZM. SE(B) mixed-mode crack propagation simulation is performed and the predicted crack trajectory is compared with experimental results. The influence of finite element discretizations on numerical convergence is explored in conjunction with mixed-mode fracture simulation. Crack competition and interaction phenomena between initiation and nucleation are studied in conjunction with a SE(B) test simulation.

Chapter 6 improves the previous power-law CZM and examines the usage of δ_{25} for asphalt concrete fracture modeling. The influence of CZM softening shapes on fracture behavior of asphalt concrete is studied and a suitable softening shape for asphalt concrete fracture modeling is proposed. Experimental investigations illustrate that δ_{25} -measurement is more appropriate in evaluating cohesive fracture energy than the *CMOD*-measurement in asphalt concrete. Three dimensional DC(T) test simulation is performed using the power-law CZM and the δ_{25} .

Chapter 7 develops a novel viscoelastic CZM from the activation energy theory of the rate process of bond rupture in conjunction with reasonable assumptions and simplifications, and proposes appropriate procedures to evaluate several parameters accounting for time and temperature effects. Sensitivity analysis to the new parameters introduced into the proposed CZM is carried out. Asphalt concretes IOWA-MAT-A and IOWA-MAT-B are used to validate the novel viscoelastic CZM and procedures proposed in this study.

Finally, Chapter 8 demonstrates the ability of cohesive zone modeling in simulating crack initiation and propagation and in exploring fracture behavior of pavement under tire and temperature loading. An actual pavement section located in northern Iowa is employed. All

material properties and cohesive parameters used in the simulation are obtained from the experiments.

9.2 Conclusions

The major contributions of this study can be summarized as follows:

- A graded element is implemented via user material (UMAT) capability of ABAQUS. The implementation of the UMAT is verified using a benchmark problem. The graded finite element method used here provides superior results over the conventional finite element solution, which involves assigning mixture properties in layers. More importantly, the differences are most pronounced when evaluating near-surface pavement responses, where severe material gradients are present due to environmental exposure.
- A cohesive zone model is implemented by means of ABAQUS user element (UEL) capability. Its implementation is verified using a double cantilever beam test. The numerical results show good agreement with the analytical solution even for both initial and final stages of crack propagation, which are influenced by boundary conditions.
- Mixed-mode crack propagation simulation is carried out using SE(B) test in which cohesive elements with a regular pattern are inserted over an area to allow cracks to propagate in any general direction. The predicted mixed-mode crack trajectory is found to be in close agreement with experimental results.
- Numerical convergence problems associated with a cohesive zone model is explored. Simulation of mixed-mode SE(B) test constructed with various finite element discretizations is performed using Riks and Newton-Raphson methods. Several important observations from this analysis are obtained. First of all, for the meshes constructed in a regular pattern, the Riks method yields better performance than the Newton-Raphson method with varying degrees of success depending on the mesh discretization. Secondly, for the mesh tailored to the crack trajectory predicted from I-Franc2D,

both nonlinear solvers perform very well, demonstrating that the degree of convergence depends highly upon the finite element discretizations, Thirdly, once crack branching occurs, numerical solutions are rarely converged. Finally, if the crack propagation angle of finite element discretization is similar with that of either analytical or experimental results, i.e. an optimal crack trajectory, the numerical solution converges relatively well.

- Crack competition phenomenon is studied numerically in conjunction with SE(B) test in which cohesive elements are inserted in advance to simulate either crack initiation or nucleation, and propagation. The predicted γ_{cr} is found to be in excellent agreement with the experimental results.
- A power-law cohesive zone model [35] is revisited and improved firstly to reduce artificial compliance, secondly to model general cases, e.g. mixed-mode and three-dimensional, and thirdly to have various choices in terms of CZM softening shapes.
- The influence of a pre-peak slope and a post-peak shape of a CZM is examined thoroughly. The pre-peak slope is a major source of artificial compliance, while the post-peak shape affects progressive softening phenomena occurring along the fracture process zone. It is clearly observed that as the number of cohesive elements increases, the compliance likewise increases. Moreover, as the pre-peak slope becomes stiff, the compliance decreases considerably. This study suggests minimizing the number of cohesive elements, if possible, and adopting a cohesive zone model which can control a pre-peak slope. For brittle and ductile materials, material strength and cohesive fracture energy, i.e. cohesive parameters, are considered to be more important than a CZM shape. However, the author demonstrates that the influence of a CZM softening shape becomes significant as the relative size of the fracture process zone compared to the structure size increases, which is relevant for asphalt concrete and other quasi-brittle materials. It is found that a nonlinear softening curve represented by the power-law

CZM with $\alpha = 10$ captures fracture behavior of asphalt concrete reasonably well.

- Simulation of various two dimensional and three dimensional laboratory fracture tests, such as SE(B), is performed considering bulk (background) viscoelasticity.
- δ_{25} parameter is proposed as an operational definition of crack tip opening displacement (CTOD) in asphalt concrete. The usage of the δ_{25} parameter in evaluating fracture energy leads to more reasonable numerical results due to the fact that the δ_{25} is more close to local quantity than the CMOD.
- A combination of δ_{25} measurement and the improved power-law CZM which can control the pre-peak slope and the softening shape can lead to reasonable numerical results without any calibration.
- A novel viscoelastic CZM is derived from the activation energy theory of the rate process of bond rupture in conjunction with reasonable assumptions, simplifications and procedures. The proposed viscoelastic CZM improves numerical results significantly, leading to a reasonable comparison with experimental results when viscoelastic effects are considerable. The predicted numerical results for $-30^{\circ}C$, $-20^{\circ}C$ and $-10^{\circ}C$ are found to be in good agreement with experimental results. The peak load and the post-peak trend match especially well with experimental results. Therefore, it can be concluded that the proposed viscoelastic CZM and procedures can be applicable for asphalt concrete viscoelastic fracture study.
- A CZM is employed to investigate fracture behavior in asphalt concrete pavement located in northern Iowa under various loading conditions. Temperature induces top-down cracking, while tire loading causes reflective cracking in this particular example.

9.3 Suggestions for future work

- In pavement, fatigue is one of the major sources of distress caused by incessant repetition of tire loads and temperature cycles. The Paris equation [92] has been widely used to explore fatigue phenomena in various materials. However, a few researchers pointed out that it provides a data correlation scheme rather than a predictive capability [6, 104, 125]. More importantly, its applicability to asphalt mixture is limited, because asphalt mixture generally behaves nonlinearly [81]. In addition, if the fracture process zone size is large compared to the structure size, which is relevant to asphalt concrete and other quasi-brittle materials, the Paris equation may not be applicable [104]. Thus, a CZM is a promising technique to explore fatigue in asphalt concrete and pavement, because material nonlinearity associated to fracture occurring along the large cohesive zone can be considered properly in terms of displacement and traction. However, the current CZMs used in this study need to be modified to implement the degradation of the cohesive properties due to cyclic loading. One approach is to introduce a damage variable which decreases with the increase of the number of cycles into the CZMs [77, 104].
- Cohesive parameters in asphalt concrete, i.e. fracture energy and material strength, depend on temperature and local rate. In the pavement modeling the same fracture energy and material strength are assumed, regardless of local rate, because of the lack of information regarding the relationship between the cohesive parameters and local rate. For example, current fracture tests, e.g. the DC(T), generate different local rates along the fracture process zone, and as a result, may not be well-suited to find the relationship between the cohesive fracture energy and local rate. Consideration of the different fracture energy and material strength for different local rates in the modeling will lead to better numerical results. Thus, either a new experiment inducing constant local rate along the fracture process zone needs to be proposed or analyses efforts need

to be made to find the relationship using current data.

- Asphalt paving layers, particularly the surface course, exhibit vertically graded material properties, which are most pronounced at the surface of the pavement and decrease rapidly with depth from the surface. This grading is caused primarily by temperature gradients and aging related stiffness gradients. The overall ideas applied to gradation of bulk materials (see Chapter 2) can be extended to viscoelastic materials. Considering correspondence principle in viscoelastic graded materials [83, 95], a functionally graded generalized Maxwell model can be developed to consider aging and temperature gradients in asphalt concrete.

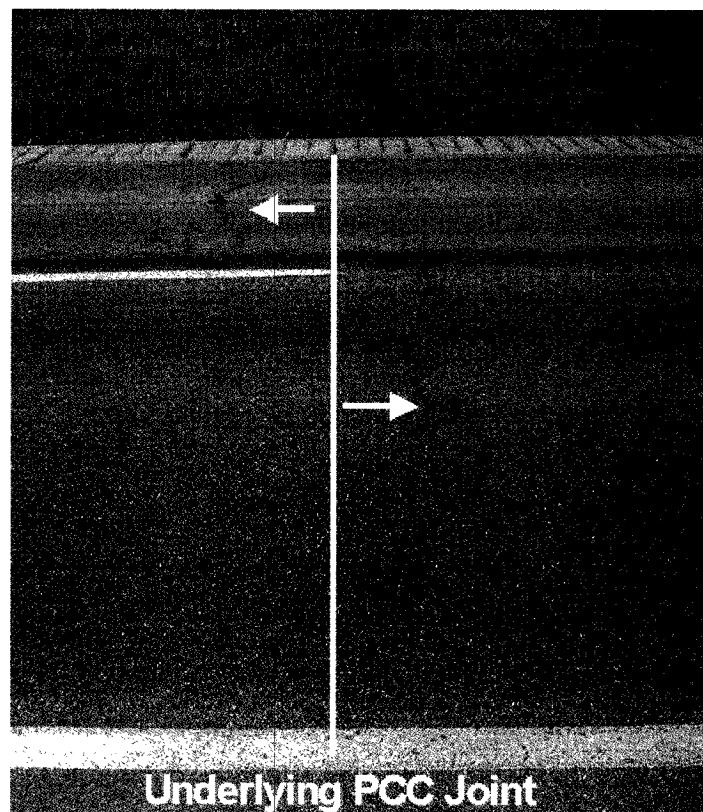


Figure 9.1: Pavement with crack offset.

- Typically, when an overlay is placed on an existing pavement, physical tearing of the overlay takes place as a result of movement at the joints. Thus, cracks generally initiate

at the joints and propagate. However, a crack offset phenomenon is observed when STRATA RCRS is placed between the PCC and the surface course (see Figure 9.1). The author speculates that an understanding crack competition phenomenon between initiation and nucleation is important in this particular problem. In this study, numerical investigations on crack competition phenomenon between initiation and nucleation are carried out and presented in Section 5.5 in conjunction with a laboratory fracture test simulation. In order to investigate the crack offset mechanism in pavement, seamless integration of experiment, modeling, and field needs to be undertaken along with the extension of the current numerical study on the crack competition phenomenon.

- A benefit of a computational approach is that it can be used as a tool for performing design or material optimization where various parameters are adjusted until the simulations yield desirable responses. For instance, material strength and fracture energy are important parameters related to fracture. Material strength governs an onset of material damage, while fracture energy describes the amount of total energy used until a material experiences a complete separation. So, parametric studies with different magnitudes of cohesive parameters can help to optimize the material which shows the best performance for a given condition [33].

Appendix A

ABAQUS user subroutine for the three-dimensional power-law CZM

```
C*****
c   The main purpose of UEL is to determine rhs and amatrx
c   where rhs is an array containing the contribution of this element
c   to the r.h.s vector of the overall system of equations and
c   amatrx is an array containing the contribution of this element
c   to the stiffness matrix of the overall system of
c   equations.
C*****
c
c   THE SAVED VARIABLES REQUIREMENT FOR VARAIOUS ELEMENT TYPES
c   AS FOLLOWS:
c
c   STATIC
c   -----
c
c   8-node 3D element                TYPE=U3
c
C*****
c
c Power-law cohesive zone model
c
c Song, S.H., Paulino, G.H. and Buttlar, W.G.
c Ref : Three-dimensional power-law cohesive zone model for fracture
c       modeling of asphalt concrete(to be submitted for journal
c       publication)
c
c   3D elements : (4 real properties + 1 integer properties)
c   -----
```

```

c
c   props(1) = G_c (cohesive fracture energy)
c   props(2) = Sigma_c (material strength)
c   props(3) = alpha (parameter influencing CZM softening shapes)
c   props(4) = del_cc/del_c (del_c: displacment at zero traction)
c                   (del_cc: displacement at peak traction)
c
c   jprops(1)
c
c       1 = Power-law CZM
c
c*****
c
c   DESCRIPTION OF SUBROUTINE
c
c   k_element_3d_8node : determine "rhs" and "amatrx" of 3d-8node element
c   k_B_matrix_3D      : determine B matrix which will be used for
c                       determining "amatrx"(K) matrix, i.e. int ([B]'[D][B])
c   K_gauss_shape_function_3D : determine the shape function
c   k_compute_traction_jacobian_3D: determine the traction vector "rhs" and
c                       the tangent modulus matrix
c   k_compute_del_c : compute new critical displacement
c   k_transformation_matrix_3D : determine the transformation matrix
c   k_matrix_transpose : transpose a matrix
c   k_matrix_zero: initialize a matrix
c   k_matrix_add : add two matrices
c   k_vector_zero: initialize a vector
c   k_matrix_multiplication: perform the matrix multiplication
c   k_matrix_multiplied_scalar: matrix is multiplied by scalar
c
c*****
c
c=====
c       subroutine uel(rhs,amatrx,svars,energy,ndofel,nrhs,nsvars,
c       x props,nprops,coords,mcrd,nnode,u,du,v,a,jtype,time,dtime,
c       x kstep,kinc,jelem,params,ndload,jdltyp,adlmag,predef,npredf,
c       x lflags,mlvarx,ddlmag,mdload,pnewdt,jprops,njprop,period)
c=====
c
c       include 'ABA_PARAM.INC'
c
c       dimension
c       x rhs(mlvarx,*),amatrx(ndofel,ndofel),props(*),
c       x svars(nsvars),energy(8),coords(mcrd,nnode),u(ndofel),

```

```

x du(mlvarx,*),v(ndofel),a(ndofel),time(2),params(*),
x jdltyp(mdload,*),adlmag(mdload,*),ddlmag(mdload,*),
x predef(2,npredf,nnode),lflags(*),jprops(*)
c
c --- Find the element type
c   jtype : the value of n from inputdata Un. Un is the type=Un.
c
c   if (jtype .eq. 3) then
c       call k_element_3d_8node (rhs, amatrix, props, coords,u,
c   &                               jprops, ndofel, mcrd, nnode, mlvarx,
c   &                               jtype, jelem, nrhs)
c   endif
c
c   return
c   end
c
c
c =====
c   subroutine k_element_3d_8node (rhs, amatrix, props, coords,
c   &                               u, jprops, ndofel, mcrd, nnode, mlvarx,
c   &                               jtype, jelem, nrhs)
c =====
c
c   - Important convention on node numbering
c
c       8       7       4       3
c       +-----+   +-----+
c       | side 2 |   | side 1 |
c       | (btm) |   | (top)  |
c       +-----+   +-----+
c       5       6       1       2
c
c
c   include 'ABA_PARAM.INC'
c
c-----UEL subroutine variable
c
c   dimension
c   & rhs(mlvarx, *),amatrix(ndofel,ndofel),props(*),
c   & coords(mcrd,nnode),u(ndofel), jprops(*)
c
c-----Local Variables
c
c   dimension

```

```

& cur_coord(3,8), aJacob_M(2,3), Rot_M(3,3),
& SFD(2,4), delta_u_l_gp(3), Bmat(3,24), shape_f(4),
& residual_global(ndofel,nrhs), stiff_global(24,24),
& dummy_mat(3,24), cur_coord_mid(3,4), Trac_Jacob(3,3),
& Trac(mcrd,nrhs), Transformation_M(24,24),
& stiff_local(24,24), trans_dummy(24,24),
& residual_local(ndofel,nrhs), cur_coord_local(3,8),
& delta_s1(4), delta_s2(4), delta_n(4), Bmat_T(24,3),
& Transformation_M_T(24,24)
c
c-----Initialize
c
call k_matrix_zero(amatrix, ndofel, ndofel)
call k_matrix_zero(rhs, ndofel, nrhs)
call k_matrix_zero(aJacob_M, 2, 3)
call k_matrix_zero(Trac,mcrd,nrhs)
call k_matrix_zero(Trac_Jacob, mcrd, mcrd)
call k_matrix_zero(B_mat, mcrd, ndofel)
call k_matrix_zero(B_mat_T, ndofel, mcrd)
call k_matrix_zero(Transformation_M, ndofel,ndofel)
call k_matrix_zero(Transformation_M_T, ndofel,ndofel)
call k_vector_zero(delta_u_l_gp,mcrd)
call k_matrix_zero(residual_local,ndofel,nrhs)
call k_matrix_zero(residual_global,ndofel,nrhs)
c
c-----Update current coordinates considering displacements
c
do i = 1, mcrd
  do j = 1, nnode
    cur_coord(i,j) = coords(i,j) + u(3*(j-1)+i)
  enddo
enddo
c
c-----Evaluate a mid-surface of the element
c
do i = 1, 3
  cur_coord_mid(i,1) = 0.5d0*(cur_coord(i,1) + cur_coord(i,5))
  cur_coord_mid(i,2) = 0.5d0*(cur_coord(i,2) + cur_coord(i,6))
  cur_coord_mid(i,3) = 0.5d0*(cur_coord(i,3) + cur_coord(i,7))
  cur_coord_mid(i,4) = 0.5d0*(cur_coord(i,4) + cur_coord(i,8))
enddo
c
c-----Determine the rotation matrix, Rot_M, which is based on the center
c point of the mid plane between side 1 and side 2.

```

```

c-----Compute the Jacobian matrix using Jacob_M=[S.D] (2x4)*[cur_coord
c   _mid] (4x3)
c-----Notice that the row of the Jacobian matrix define vectors on the
c-----tangent plane. For the normal vector, just take cross product.
c
      SFD(1,1)=-0.25d0
      SFD(1,2)=0.25d0
      SFD(1,3)=0.25d0
      SFD(1,4)=-0.25d0
      SFD(2,1)=-0.25d0
      SFD(2,2)=-0.25d0
      SFD(2,3)=0.25d0
      SFD(2,4)=0.25d0
c
      do i=1, 2
        do j=1,3
          do k=1,4
            aJacob_M(i,j)=aJacob_M(i,j)+SFD(i,k)*cur_coord_mid(j,k)
          enddo
        enddo
      enddo
c
c-----Measure the usual Jacobian of the transformation between the
c   referent and current coordinates which is used for computing
c   element stiffness matrix and the force vector.
c
      dum1=aJacob_M(1,2)*aJacob_M(2,3)-aJacob_M(1,3)*aJacob_M(2,2)
      dum2=aJacob_M(1,3)*aJacob_M(2,1)-aJacob_M(1,1)*aJacob_M(2,3)
      dum3=aJacob_M(1,1)*aJacob_M(2,2)-aJacob_M(1,2)*aJacob_M(2,1)
      a_Jacob=sqrt(dum1**2+dum2**2+dum3**2)
c
      aLen=(aJacob_M(1,1)**2+aJacob_M(1,2)**2+aJacob_M(1,3)**2)**0.5
      Rot_M(1,1)=aJacob_M(1,1)/aLen
      Rot_M(1,2)=aJacob_M(1,2)/aLen
      Rot_M(1,3)=aJacob_M(1,3)/aLen
c
      aLen1=(aJacob_M(2,1)**2+aJacob_M(2,2)**2+aJacob_M(2,3)**2)**0.5
      Rot_M(2,1)=aJacob_M(2,1)/aLen1
      Rot_M(2,2)=aJacob_M(2,2)/aLen1
      Rot_M(2,3)=aJacob_M(2,3)/aLen1
c
      Rot_M(3,1)=Rot_M(1,2)*Rot_M(2,3)-Rot_M(1,3)*Rot_M(2,2)
      Rot_M(3,2)=Rot_M(1,3)*Rot_M(2,1)-Rot_M(1,1)*Rot_M(2,3)
      Rot_M(3,3)=Rot_M(1,1)*Rot_M(2,2)-Rot_M(1,2)*Rot_M(2,1)

```

```

c
c-----Compute the transformation matrix
c
      call k_transformation_matrix_3D (Rot_M, Transformation_M, jtype,
&                                     ndofel)
      call k_matrix_transpose(Transformation_M, Transformation_M_T,
&                             ndofel, ndofel)
c
c-----Measure the local coordinates
c      cur_coord_local=Rot_M*cur_coord
c
      do i=1, nnode
          cur_coord_local(1,i)=Rot_M(1,1)*cur_coord(1,i)+
&      Rot_M(1,2)*cur_coord(2,i)+Rot_M(1,3)*cur_coord(3,i)
          cur_coord_local(2,i)=Rot_M(2,1)*cur_coord(1,i)+
&      Rot_M(2,2)*cur_coord(2,i)+Rot_M(2,3)*cur_coord(3,i)
          cur_coord_local(3,i)=Rot_M(3,1)*cur_coord(1,i)+
&      Rot_M(3,2)*cur_coord(2,i)+Rot_M(3,3)*cur_coord(3,i)
      enddo
c
c-----Compute the local opening (normal opening and shear sliding)
c
      do i=1, 4
          delta_s1(i)=cur_coord_local(1,i+4)-cur_coord_local(1,i)
          delta_s2(i)=cur_coord_local(2,i+4)-cur_coord_local(2,i)
          delta_n(i)=cur_coord_local(3,i+4)-cur_coord_local(3,i)
      enddo

      do i = 1, 4
c
c-----Determine shape functions
c
          call K_gauss_shape_function_3D (i, shape_f)
c
c-----determine one normal opening displacement and two
c      shear sliding displacements at Gauss points
c
          call k_vector_zero(delta_u_l_gp,mcrd)
          do j=1, 4 ! 4 means 4 different shape function
              delta_u_l_gp(1) = delta_u_l_gp(1)+delta_s1(j)*shape_f(j)
              delta_u_l_gp(2) = delta_u_l_gp(2)+delta_s2(j)*shape_f(j)
              delta_u_l_gp(3) = delta_u_l_gp(3)+ delta_n(j)*shape_f(j)
          enddo
c

```

```

c-----Compute traction vector (Trac) and
c          tangent modulus matrix (Trac_Jacob)
c
c          call k_compute_traction_jacobian_3D (props, delta_u_l_gp,
&          &          jprops,Trac,Trac_Jacob, nrhs,
&          &          jelem,mcrd)
c
c-----Determine B matrix and so on
c
c          call k_B_matrix_3D (shape_f, Bmat, jtype, mcrd, ndofel)
c          call k_matrix_transpose (Bmat, Bmat_T, ndofel, mcrd)
c
c-----Compute the stiffness matrix
c          Perform [Bmat]_t*[Trac_Tacob]*[Bmat]
c          mcrd is the dimension 3d -> 3
c          ndofel is total dofs in each element. i.e. 3d 8node -> 24
c
c          call k_matrix_multiplication(Trac_Jacob, Bmat, dummy_mat,
&          &          mcrd, ndofel, mcrd)
c          call k_matrix_multiplication(Bmat_T,dummy_mat,stiff_local,
&          &          ndofel,ndofel,mcrd)
c
c-----Transform local stiffness matrix to global stiffness matrix
c          K_global=transformation_m'*local_stiff*transformation_m
c
c          call k_matrix_multiplication(Transformation_M_T, stiff_local,
&          &          trans_dummy, ndofel, ndofel,
&          &          ndofel)
c          call k_matrix_multiplication(trans_dummy, Transformation_M,
&          &          stiff_global, ndofel, ndofel,
&          &          ndofel)
c
c-----Multiply Jacobian to local stiffness matrix and add each Gauss
c          point contribution to the stiffness matrix of each element.
c
c          call k_matrix_multiplied_scalar (stiff_global,ndofel,ndofel,
&          &          a_Jacob)
c          call k_matrix_add(stiff_global, amatrx, ndofel, ndofel)
c
c-----Similar procedure used in evaluating amatrx is employed.
c
c          call k_matrix_multiplication(Bmat_T,Trac,residual_local,
&          &          ndofel,nrhs,mcrd)
c          call k_matrix_multiplication(Transformation_M_T,

```



```

& residual_local,residual_global,ndofel,nrhs,ndofel)
  call k_matrix_multiplied_scalar (residual_global,ndofel,nrhs,
&                                a_Jacob)
  call k_matrix_add(residual_global, rhs, ndofel, nrhs)
c
  enddo
c
  return
  end
c
c=====
  subroutine k_transformation_matrix_3D (Rot_M,Transformation_M,
&                                     jtype,ndofel)
c=====
c
  include 'ABA_PARAM.INC'
c
  dimension Transformation_M (ndofel, ndofel), Rot_M(3,3)
c
  if (jtype.eq.3) then
    num=8
  endif
  do i = 1, num
    dum = 3*(i-1)
    Transformation_M(dum+1,dum+1) = Rot_M(1,1)
    Transformation_M(dum+1,dum+2) = Rot_M(1,2)
    Transformation_M(dum+1,dum+3) = Rot_M(1,3)
    Transformation_M(dum+2,dum+1) = Rot_M(2,1)
    Transformation_M(dum+2,dum+2) = Rot_M(2,2)
    Transformation_M(dum+2,dum+3) = Rot_M(2,3)
    Transformation_M(dum+3,dum+1) = Rot_M(3,1)
    Transformation_M(dum+3,dum+2) = Rot_M(3,2)
    Transformation_M(dum+3,dum+3) = Rot_M(3,3)
  enddo
c
  return
  end
c
c=====
  subroutine K_gauss_shape_function_3D (i, shape_f)
c=====
c
  include 'ABA_PARAM.INC'
c

```

```

dimension
& GP_coord(2), shape_f(4)
c
  if (i.eq.1) then
    GP_coord(1)=-sqrt(1.0d0/3.0d0)
    GP_coord(2)=-sqrt(1.0d0/3.0d0)
  elseif (i.eq. 2) then
    GP_coord(1)=sqrt(1.0d0/3.0d0)
    GP_coord(2)=-sqrt(1.0d0/3.0d0)
  elseif (i.eq. 3) then
    GP_coord(1)=sqrt(1.0d0/3.0d0)
    GP_coord(2)=sqrt(1.0d0/3.0d0)
  elseif (i.eq. 4) then
    GP_coord(1)=-sqrt(1.0d0/3.0d0)
    GP_coord(2)=sqrt(1.0d0/3.0d0)
  endif
c
  shape_f(1)=0.25d0*(1-GP_coord(1))*(1-GP_coord(2))
  shape_f(2)=0.25d0*(1+GP_coord(1))*(1-GP_coord(2))
  shape_f(3)=0.25d0*(1+GP_coord(1))*(1+GP_coord(2))
  shape_f(4)=0.25d0*(1-GP_coord(1))*(1+GP_coord(2))
c
  return
c
  end
c
c=====
  subroutine k_B_matrix_3D (Shape_F, Bmat, jtype, mcrd, ndofel)
c=====
c
  include 'ABA_PARAM.INC'
c
  dimension Shape_F(*),Bmat(mcrd,ndofel)
c
  call k_matrix_zero(Bmat, mcrd, ndofel)
c
  if (jtype.eq.3) then
    Bmat(1,1) = Shape_F(1)
    Bmat(1,4) = Shape_F(2)
    Bmat(1,7) = Shape_F(3)
    Bmat(1,10) = Shape_F(4)
    Bmat(1,13) = -Shape_F(1)
    Bmat(1,16) = -Shape_F(2)
    Bmat(1,19) = -Shape_F(3)

```

```

      Bmat(1,22) = -Shape_F(4)
      Bmat(2,2)  = Shape_F(1)
      Bmat(2,5)  = Shape_F(2)
      Bmat(2,8)  = Shape_F(3)
      Bmat(2,11) = Shape_F(4)
      Bmat(2,14) = -Shape_F(1)
      Bmat(2,17) = -Shape_F(2)
      Bmat(2,20) = -Shape_F(3)
      Bmat(2,23) = -Shape_F(4)
      Bmat(3,3)  = Shape_F(1)
      Bmat(3,6)  = Shape_F(2)
      Bmat(3,9)  = Shape_F(3)
      Bmat(3,12) = Shape_F(4)
      Bmat(3,15) = -Shape_F(1)
      Bmat(3,18) = -Shape_F(2)
      Bmat(3,21) = -Shape_F(3)
      Bmat(3,24) = -Shape_F(4)
    endif
  c
  return
  c
  end
  c
  c=====
  subroutine k_compute_traction_jacobian_3D (props,
    &      delta_u_l_gp ,jprops, Trac, Trac_Jacob, nrhs,
    &      jelem, mcrd)
  c=====
  c
  include 'ABA_PARAM.INC'
  c
  dimension
  & Trac(mcrd, nrhs),Trac_Jacob(mcrd,mcrd), props(*), jprops(*)
  c
  dimension
  & delta_u_l_gp(3)
  c
  if (jprops(1).eq.1) then ! this is power-law CZM
  c-----number of integer variables: 4
    Fracture_e = props(1)
    T_max      = props(2)
    alpha= props(3) ! t=tc*(1-eff_del/del_c)^alpha
    lambda_cr= props(4) ! delta_cc/del_c

```

```

        delta_t1_gp=delta_u_l_gp(1)
        delta_t2_gp=delta_u_l_gp(2)
        delta_n_gp =delta_u_l_gp(3)
c----- this is displacement in which traction becomes zero
        del_c=props(1)/props(2)*(props(3)+1.0d0)
c----- this is displacement in which traction becomes a peak
        del_cc=del_c*ambda_cr
c
        del_eff=sqrt(delta_n_gp**2+delta_t1_gp**2+delta_t2_gp**2)
c
c-----Calculate new del_c
c
        anew_del_c=del_c
        if (alpha.gt.1.0d0) then
            call k_compute_del_c (alpha,del_c,del_cc,T_max,Fracture_e,
&                                del_c_new, ambda_cr)
            del_c=del_c_new
            del_cc=del_c*ambda_cr
        endif

        if (del_eff .le. del_cc) then
            Trac(1,1)=T_max*delta_t1_gp/del_cc
            Trac(2,1)=T_max*delta_t2_gp/del_cc
            Trac(3,1)=T_max*delta_n_gp/del_cc
            Trac_Jacob(1,1)=T_max/del_cc
            Trac_Jacob(2,2)=T_max/del_cc
            Trac_Jacob(3,3)=T_max/del_cc
            Trac_Jacob(1,2)=0.0d0
            Trac_Jacob(1,3)=0.0d0
            Trac_Jacob(2,1)=0.0d0
            Trac_Jacob(2,3)=0.0d0
            Trac_Jacob(3,1)=0.0d0
            Trac_Jacob(3,2)=0.0d0
        elseif ((del_eff .gt. del_cc).and.(del_eff .lt. del_c)) then
            Trac(1,1)= T_max*(1-sqrt(delta_t1_gp**2+delta_t2_gp**2+delta_n_gp*
**2)/del_c)**alpha*delta_t1_gp/sqrt(delta_t1_gp**2+delta_t2_gp**2+d
#elta_n_gp**2)/(1-ambda_cr)**alpha
            Trac(2,1)= T_max*(1-sqrt(delta_t1_gp**2+delta_t2_gp**2+delta_n_gp*
**2)/del_c)**alpha*delta_t2_gp/sqrt(delta_t1_gp**2+delta_t2_gp**2+d
#elta_n_gp**2)/(1-ambda_cr)**alpha
            Trac(3,1)= T_max*(1-sqrt(delta_t1_gp**2+delta_t2_gp**2+delta_n_gp*
**2)/del_c)**alpha*delta_n_gp/sqrt(delta_t1_gp**2+delta_t2_gp**2+d
#lta_n_gp**2)/(1-ambda_cr)**alpha
            a1      = -T_max*(1-sqrt(delta_t1_gp**2+delta_t2_gp**2+delta_n_gp**

```

```

#2)/del_c)**alpha*alpha/(delta_t1_gp**2+delta_t2_gp**2+delta_n_gp**
#2)/del_c*delta_t1_gp**2/(1-sqrt(delta_t1_gp**2+delta_t2_gp**2+delt
#a_n_gp**2)/del_c)/(1-ambda_cr)**alpha+T_max*(1-sqrt(delta_t1_gp**2
#+delta_t2_gp**2+delta_n_gp**2)/del_c)**alpha/sqrt(delta_t1_gp**2+d
#elta_t2_gp**2+delta_n_gp**2)/(1-ambda_cr)**alpha-T_max*(1-sqrt(del
#ta_t1_gp**2+delta_t2_gp**2+delta_n_gp**2)/del_c)**alpha*delta_t1_g
#p**2/sqrt(delta_t1_gp**2+delta_t2_gp**2+delta_n_gp**2)**3/(1-ambda
#_cr)**alpha
a2      = -T_max*(1-sqrt(delta_t1_gp**2+delta_t2_gp**2+delta_n_gp**
#2)/del_c)**alpha*alpha/(delta_t1_gp**2+delta_t2_gp**2+delta_n_gp**
#2)/del_c*delta_t2_gp/(1-sqrt(delta_t1_gp**2+delta_t2_gp**2+delta_n
#_gp**2)/del_c)*delta_t1_gp/(1-ambda_cr)**alpha-T_max*(1-sqrt(delta
#_t1_gp**2+delta_t2_gp**2+delta_n_gp**2)/del_c)**alpha*delta_t1_gp/
#sqrt(delta_t1_gp**2+delta_t2_gp**2+delta_n_gp**2)**3/(1-ambda_cr)*
**alpha*delta_t2_gp
a3      = -T_max*(1-sqrt(delta_t1_gp**2+delta_t2_gp**2+delta_n_gp**
#2)/del_c)**alpha*alpha/(delta_t1_gp**2+delta_t2_gp**2+delta_n_gp**
#2)/del_c*delta_n_gp/(1-sqrt(delta_t1_gp**2+delta_t2_gp**2+delta_n_
#gp**2)/del_c)*delta_t1_gp/(1-ambda_cr)**alpha-T_max*(1-sqrt(delta_
#t1_gp**2+delta_t2_gp**2+delta_n_gp**2)/del_c)**alpha*delta_t1_gp/s
#qrt(delta_t1_gp**2+delta_t2_gp**2+delta_n_gp**2)**3/(1-ambda_cr)**
#alpha*delta_n_gp
a4      = -T_max*(1-sqrt(delta_t1_gp**2+delta_t2_gp**2+delta_n_gp**
#2)/del_c)**alpha*alpha/(delta_t1_gp**2+delta_t2_gp**2+delta_n_gp**
#2)/del_c*delta_t2_gp**2/(1-sqrt(delta_t1_gp**2+delta_t2_gp**2+delt
#a_n_gp**2)/del_c)/(1-ambda_cr)**alpha+T_max*(1-sqrt(delta_t1_gp**2
#+delta_t2_gp**2+delta_n_gp**2)/del_c)**alpha/sqrt(delta_t1_gp**2+d
#elta_t2_gp**2+delta_n_gp**2)/(1-ambda_cr)**alpha-T_max*(1-sqrt(del
#ta_t1_gp**2+delta_t2_gp**2+delta_n_gp**2)/del_c)**alpha*delta_t2_g
#p**2/sqrt(delta_t1_gp**2+delta_t2_gp**2+delta_n_gp**2)**3/(1-ambda
#_cr)**alpha
a5      = -T_max*(1-sqrt(delta_t1_gp**2+delta_t2_gp**2+delta_n_gp**
#2)/del_c)**alpha*alpha/(delta_t1_gp**2+delta_t2_gp**2+delta_n_gp**
#2)/del_c*delta_n_gp/(1-sqrt(delta_t1_gp**2+delta_t2_gp**2+delta_n_
#gp**2)/del_c)*delta_t2_gp/(1-ambda_cr)**alpha-T_max*(1-sqrt(delta_
#t1_gp**2+delta_t2_gp**2+delta_n_gp**2)/del_c)**alpha*delta_t2_gp/s
#qrt(delta_t1_gp**2+delta_t2_gp**2+delta_n_gp**2)**3/(1-ambda_cr)**
#alpha*delta_n_gp
a6      = -T_max*(1-sqrt(delta_t1_gp**2+delta_t2_gp**2+delta_n_gp**
#2)/del_c)**alpha*alpha/(delta_t1_gp**2+delta_t2_gp**2+delta_n_gp**
#2)/del_c*delta_n_gp**2/(1-sqrt(delta_t1_gp**2+delta_t2_gp**2+delta
#_n_gp**2)/del_c)/(1-ambda_cr)**alpha+T_max*(1-sqrt(delta_t1_gp**2+
#delta_t2_gp**2+delta_n_gp**2)/del_c)**alpha/sqrt(delta_t1_gp**2+de
#lta_t2_gp**2+delta_n_gp**2)/(1-ambda_cr)**alpha-T_max*(1-sqrt(delt

```

```

#a_t1_gp**2+delta_t2_gp**2+delta_n_gp**2)/del_c)**alpha*delta_n_gp*
**2/sqrt(delta_t1_gp**2+delta_t2_gp**2+delta_n_gp**2)**3/(1-ambda_c
#r)**alpha
      Trac_Jacob(1,1)=a1
      Trac_Jacob(1,2)=a2
      Trac_Jacob(1,3)=a3
      Trac_Jacob(2,2)=a4
      Trac_Jacob(2,3)=a5
      Trac_Jacob(3,3)=a6
      Trac_Jacob(2,1)=a2
      Trac_Jacob(3,1)=a3
      Trac_Jacob(3,2)=a5
elseif (del_eff.gt.del_c) then
      Trac(1,1)=0.0d0
      Trac(2,1)=0.0d0
      Trac(3,1)=0.0d0
      Trac_Jacob(1,1)=0.0d0
      Trac_Jacob(2,2)=0.0d0
      Trac_Jacob(3,3)=0.0d0
      Trac_Jacob(1,2)=0.0d0
      Trac_Jacob(1,3)=0.0d0
      Trac_Jacob(2,1)=0.0d0
      Trac_Jacob(2,3)=0.0d0
      Trac_Jacob(3,1)=0.0d0
      Trac_Jacob(3,2)=0.0d0
endif
c
      endif
c
      return
      end
c
c=====
      subroutine k_compute_del_c (alpha, del_c, del_cc,
&          T_max, Fracture_e, del_c_new, ambda_cr)
c=====
c
      include 'ABA_PARAM.INC'

      anew_del_c=del_c
      if (alpha. gt. 1.0d0) then
          anew_del_c=-1.*exp(log(-.5000000000*(-2.*T_max*((del_c-1.
&          *del_cc)/del_c)**(alpha+1.)*del_c+2.*Fracture_e
&          *(1.-1.*ambda_cr)**alpha*alpha+2.*Fracture_e

```

```

&          *(1.-1.*ambda_cr)**alpha-1.*del_cc*T_max
&          *(1.-1.*ambda_cr)**alpha*alpha-1.*del_cc*T_max
&          *(1.-1.*ambda_cr)**alpha)/T_max/del_c)/
&          (alpha+1.))*del_c+del_c
a_right=del_c
a_left=new_del_c
aa=0.5*(a_left+a_right)
a_center=aa
del_cc=ambda_cr*aa
do jj=1, 100000
  sum=0.0d0
  do kk=1, 10000
    ainterval=(aa-del_cc)/10000
    a1=del_cc+(kk-1)*ainterval
    a2=del_cc+kk*ainterval
    a_mean=(a1+a2)/2.0d0
    sum=sum+T_max*(1-a_mean/aa)**(alpha)
&          /((1-ambda_cr)**(alpha))*ainterval
  enddo
  sum=sum+0.5d0*del_cc*T_max
  if (Fracture_e. ge. 1.00001d0*sum) then
    a_left=a_center
    aa=0.5*(a_left+a_right)
    a_center=aa
    del_cc=ambda_cr*aa
  elseif (Fracture_e .le. 0.99999d0*sum) then
    a_right=a_center
    aa=0.5*(a_left+a_right)
    a_center=aa
    del_cc=ambda_cr*aa
  else
    del_c=aa
    del_cc=ambda_cr*aa
    goto 1000
  endif
enddo
endif
c
1000    del_c_new=del_c
c
      return
      end
c
c=====

```

```

      subroutine k_matrix_transpose (A,B,n1,n2)
C=====
C
      include 'ABA_PARAM.INC'
C
      dimension A(n2,n1), B(n1,n2)
C
      do i=1,n1
        do j=1, n2
          B(i,j)=A(j,i)
        enddo
      enddo
C
      return
      end

C=====
      subroutine k_matrix_zero (A,n1,n2)
C=====
C
      include 'ABA_PARAM.INC'
C
      dimension A(n1,n2)
C
      do i=1,n1
        do j=1, n2
          A(i,j)=0.0d0
        enddo
      enddo
C
      return
      end

C
C=====
      subroutine k_matrix_add (A,B,n1,n2)
C=====
C
      include 'ABA_PARAM.INC'
C
      dimension A(n1,n2), B(n1,n2)
C
      do i=1,n1
        do j=1, n2
          B(i,j)=B(i,j)+A(i,j)
        enddo

```



```

        enddo
c
        return
        end
c
c
c=====
        subroutine k_vector_zero (A,n1)
c=====
        include 'ABA_PARAM.INC'
c
        dimension A(n1)
c
        do i=1,n1
            A(i)=0.0d0
        enddo
c
        return
        end
c
c=====
        subroutine k_matrix_multiplication (A,B,C,n1,n2,n3)
c=====
c
        include 'ABA_PARAM.INC'
c
        dimension A(n1,n3), B(n3, n2), C(n1, n2)
c
        call k_matrix_zero (C,n1,n2)
c
        do i=1,n1
            do j=1, n2
                do k=1, n3
                    C(i,j)=C(i,j)+A(i,k)*B(k,j)
                enddo
            enddo
        enddo
c
        return
        end
c
c=====
        subroutine k_matrix_multiplied_scalar (A,n1,n2,fac)
c=====

```

```
c
  include 'ABA_PARAM.INC'
c
  dimension A(n1,n2)
c
  do i=1,n1
    do j=1, n2
      A(i,j)=A(i,j)*fac
    enddo
  enddo
c
  return
end
```

⋮

Appendix B

ABAQUS user subroutine for the two-dimensional power-law CZM

```
C*****
C
C   THE SAVED VARIABLES REQUIREMENT FOR VARAIIOUS ELEMENT TYPES
C   AS FOLLOWS:
C
C   STATIC
C   -----
C
C   4-node 2D element                TYPE=U1
C
C   props(1) = G_c (cohesive fracture energy)
C   props(2) = Sigma_c (material strength)
C   props(3) = alpha (parameter influencing CZM softening shapes)
C   props(4) = del_cc/del_c (del_c: displacment at zero traction)
C                   (del_cc: displacement at peak traction)
C   props(5) = thickness
C
C   jprops(1)
C
C       1 = Power-law CZM
C
C*****
C
C   DESCRIPTION OF SUBROUTINE
C
C   k_element_2d_4node : determine "rhs" and "amatrx" of 2d-4node element
C   k_B_matrix         : determine B matrix which will be used for
C                       determining "amatrx"(K) matrix, i.e. int ([B]' [D] [B])
```

```

c   K_gauss_shape_function : determine the shape function
c   k_gauss_point: obtain the information on Gauss points
c   k_compute_traction_jacobian: determine the traction the tangent modulus
c                                   matrix(D)
c   k_transformation_matrix : determine the transformation matrix
c   k_compute_del_c : see appendix 1
c   k_matrix_transpose : see appendix 1
c   k_matrix_zero: see appendix 1
c   k_matrix_add : see appendix 1
c   k_matrix_multiplication: see appendix 1
c   k_matrix_multiplied_scalar: see appendix 1
c
c=====
      subroutine uel(rhs,amatrx,svars,energy,ndofel,nrhs,nsvars,
x  props,nprops,coords,mcrd,nnode,u,du,v,a,jtype,time,dttime,
x  kstep,kinc,jelem,params,ndload,jdltyp,adlmag,predef,npredf,
x  lflags,mlvarx,ddlmag,mdload,pnewdt,jprops,njprop,period)
c=====
c
c   include 'ABA_PARAM.INC'
c
c   dimension
x  rhs(mlvarx,*),amatrx(ndofel,ndofel),props(*),
x  svars(nsvars),energy(8),coords(mcrd,nnode),u(ndofel),
x  du(mlvarx,*),v(ndofel),a(ndofel),time(2),params(*),
x  jdltyp(mdload,*),adlmag(mdload,*),ddlmag(mdload,*),
x  predef(2,npredf,nnode),lflags(*),jprops(*)
c
c   if (jtype .eq. 1) then
c       call k_element_2d_4node (rhs, amatrx, props, coords,
&                               u, jprops, ndofel, mcrd, nnode, mlvarx,
&                               jtype, jelem, nrhs)
c   endif
c
c   return
c   end
c
c=====
      subroutine k_element_2d_4node (rhs, amatrx, props, coords,
x                                   u, jprops, ndofel, mcrd, nnode, mlvarx,
x                                   jtype, jelem, nrhs)
c=====
c
c   4   side 2   3

```

```

c          +-----+
c          |         |
c          |         |
c          +-----+
c          1   side 1   2
c
c
c          include 'ABA_PARAM.INC'
c
c-----UEL subroutine variable
c
c          dimension
c          x rhs(mlvarx, *), amatrix(ndofel,ndofel), props(*),
c          x coords(mcrd, nnode), u(ndofel), jprops(*)
c
c-----Local Variables
c
c          dimension
c          x cur_coord(2,4),
c          x cur_coord_mid(2,2), Transformation_M(8,8), Shape_F(2),
c          x cur_coord_local(2,4), delta_n(2), delta_t(2),
c          x Bmat(2,8), Trac(2), Trac_Jacob(2,2),
c          x dummy_mat(2,8), residual_local(8), residual_global(8),
c          x trans_dummy(8,8), stiff_global(8,8), stiff_local(8,8),
c          x Bmat_T(8,2), Transformation_M_T(8,8)
c
c          call k_matrix_zero(amatrix, ndofel, ndofel)
c          call k_matrix_zero(rhs, ndofel, nrhs)
c          call k_matrix_zero(Trac, mcrd, nrhs)
c          call k_matrix_zero(Trac_Jacob, mcrd, mcrd)
c          call k_matrix_zero(B_mat, mcrd, ndofel)
c          call k_matrix_zero(B_mat_T, ndofel, mcrd)
c          call k_matrix_zero(Transformation_M, ndofel, ndofel)
c          call k_matrix_zero(Transformation_M_T, ndofel, ndofel)
c          call k_matrix_zero(residual_local, ndofel, nrhs)
c          call k_matrix_zero(residual_global, ndofel, nrhs)
c
c          do i = 1, mcrd
c            do j = 1, nnode
c              cur_coord(i,j) = coords(i,j) + u(2*(j-1)+i)
c            enddo
c          enddo
c          do i = 1, 2
c            cur_coord_mid(i,1) = 0.5d0*(cur_coord(i,1) + cur_coord(i,4))

```

⋮

```

        cur_coord_mid(i,2) = 0.5d0*(cur_coord(i,2) + cur_coord(i,3))
    enddo
c
    d_length = ((cur_coord_mid(1,1) - cur_coord_mid(1,2))**2 +
x             (cur_coord_mid(2,1) - cur_coord_mid(2,2))**2)**0.5
    o_length = ((coords(1,1)-coords(1,2))**2 +
x             (coords(2,1)-coords(2,2))**2)**0.5
c
    xx = (cur_coord_mid(1,2) - cur_coord_mid(1,1))/d_length
    yy = (cur_coord_mid(2,2) - cur_coord_mid(2,1))/d_length
c
    call k_transformation_matrix (xx,yy,Transformation_M, jtype,
&                                ndofel)
    call k_matrix_transpose(Transformation_M, Transformation_M_T,
&                                ndofel, ndofel)
c
    do i = 1, nnode
        cur_coord_local(1,i) = xx*cur_coord(1,i) + yy*cur_coord(2,i)
        cur_coord_local(2,i) = -yy*cur_coord(1,i) + xx*cur_coord(2,i)
    enddo
c
    delta_n(1) = cur_coord_local(2,4) - cur_coord_local(2,1)
    delta_n(2) = cur_coord_local(2,3) - cur_coord_local(2,2)
    delta_t(1) = cur_coord_local(1,4) - cur_coord_local(1,1)
    delta_t(2) = cur_coord_local(1,3) - cur_coord_local(1,2)
c
    do i = 1, 2
        num_iter=i
c
        call k_gauss_points (num_iter, GP_each, GPW_each)
        call k_shape_function (GP_each, Shape_f, jtype, 2)
c
        delta_t_gp = delta_t(1)*Shape_F(1) + delta_t(2)*Shape_F(2)
        delta_n_gp = delta_n(1)*Shape_F(1) + delta_n(2)*Shape_F(2)
c
        call k_compute_traction_jacobian (props,delta_n_gp,delta_t_gp
&                                         ,jprops,Trac,Trac_Jacob,d_length,o_length
&                                         ,jelem, num_iter, GPW_each,mcrd, nrhs)
c
        call k_B_matrix (Shape_F, Bmat, jtype, mcrd, ndofel)
        call k_matrix_transpose (Bmat, Bmat_T, ndofel, mcrd)
c
        a_Jacob=GPW_each*0.5*o_length*props(5)
        call k_matrix_multiplication(Trac_Jacob, Bmat, dummy_mat,

```

```

&          mcrd, ndofel, mcrd)
& call k_matrix_multiplication(Bmat_T,dummy_mat,stiff_local,
&          ndofel,ndofel,mcrd)
& call k_matrix_multiplication(Transformation_M_T, stiff_local,
&          trans_dummy, ndofel, ndofel,
&          ndofel)
& call k_matrix_multiplication(trans_dummy, Transformation_M,
&          stiff_global, ndofel, ndofel,
&          ndofel)
& call k_matrix_multiplied_scalar (stiff_global,ndofel,ndofel,
&          a_Jacob)
& call k_matrix_add(stiff_global, amatrix, ndofel, ndofel)
c
& call k_matrix_multiplication(Bmat_T,Trac,residual_local,
&          ndofel,nrhs,mcrd)
& call k_matrix_multiplication(Transformation_M_T,
&          residual_local,residual_global,ndofel,nrhs,ndofel)
& call k_matrix_multiplied_scalar (residual_global,ndofel,nrhs,
&          a_Jacob)
& call k_matrix_add(residual_global, rhs, ndofel, nrhs)
& enddo
c
& return
& end
c
c=====
c      subroutine k_B_matrix (Shape_F, Bmat, jtype, mcrd, ndofel)
c=====
c
c      include 'ABA_PARAM.INC'
c
c      dimension Shape_F(*),Bmat(mcrd,ndofel)
c
c      call k_matrix_zero (Bmat, mcrd, ndofel)
c
c      if (jtype.eq.1) then
c          Bmat(1,1) = Shape_F(1)
c          Bmat(1,3) = Shape_F(2)
c          Bmat(1,5) = -Shape_F(2)
c          Bmat(1,7) = -Shape_F(1)
c          Bmat(2,2) = Shape_F(1)
c          Bmat(2,4) = Shape_F(2)
c          Bmat(2,6) = -Shape_F(2)
c          Bmat(2,8) = -Shape_F(1)

```

```

endif
c
return
c
end
c
c=====
c      subroutine k_transformation_matrix(xx,yy,Transformation_M, jtype,
&                                     n_dim)
c=====
c
include 'ABA_PARAM.INC'
c
dimension Transformation_M(n_dim,n_dim)
c
if (jtype.eq.1) then
num=4
endif
do i = 1, num
dum = 2*(i-1)
Transformation_M(dum+1,dum+1) = xx
Transformation_M(dum+1,dum+2) = yy
Transformation_M(dum+2,dum+1) = -yy
Transformation_M(dum+2,dum+2) = xx
enddo
c
return
end
c
c=====
c      subroutine k_gauss_points (num_iter, GP_each, GPW_each)
c=====
c
include 'ABA_PARAM.INC'
c
if (num_iter.eq.1) then
GP_each = -0.5773502691896d0
GPW_each = 1.0d0
elseif (num_iter.eq.2) then
GP_each = 0.5773502691896d00
GPW_each = 1.0d0
endif
c
return

```



```

C
    end
C
C=====
    subroutine k_shape_function (GP_each,Shape_F, jtype, n_dim)
C=====
C
    include 'ABA_PARAM.INC'
C
    dimension Shape_F(n_dim)
C
C-----2d 4node element.
C
    If (jtype.eq.1) then
        Shape_F(1)=0.5d0*(1.d0-GP_each)
        Shape_F(2)=0.5d0*(1.d0+GP_each)
    endif
C
    return
    end
C
C=====
    subroutine k_compute_traction_jacobian (props,delta_n_gp,
    x delta_t_gp,jprops,Trac,Trac_Jacob, d_length, o_length,
    & jelem, num_iter, GPW_each,mcrd, nrhs)
C=====
C
    include 'ABA_PARAM.INC'
C
    dimension
    & Trac(mcrd, nrhs),Trac_Jacob(mcrd,mcrd), props(*), jprops(*)
C
    if(jprops(1).eq.1) then
C-----if alpha=0, rectangular cohesive model
C-----alpha=1, bilinear model
C-----alpha=2~inf exponentially decaying curve
        Fracture_e = props(1)
        T_max = props(2)
        alpha= props(3) ! t=tc*(1-eff_del/del_c)^alpha
        ambda_cr= props(4) ! same meaning with bilinear model
        thickness=props(5)
C
        del_c=props(1)/props(2)*(props(3)+1.0d0)
        del_cc=del_c*ambda_cr

```

```

del_eff=sqrt(delta_n_gp**2+delta_t_gp**2)
c
if (alpha.gt.1.0d0) then
call k_compute_del_c (alpha, del_c, del_cc, T_max, Fracture_e,
& del_c_new, ambda_cr)
del_c=del_c_new
del_cc=del_c*ambda_cr
endif
c
if (del_eff .le. del_cc) then
Trac(1,1)=T_max*delta_t_gp/del_cc
Trac(2,1)=T_max*delta_n_gp/del_cc
Trac_Jacob(1,1)=T_max/del_cc
Trac_Jacob(2,2)=T_max/del_cc
Trac_Jacob(1,2)=0.0d0
Trac_Jacob(2,1)=0.0d0
elseif ((del_eff .gt. del_cc).and.(del_eff .lt. del_c)) then
a1 = T_max*(1-sqrt(delta_t_gp**2+delta_n_gp**2)/del_c)**alpha*
#delta_t_gp/sqrt(delta_t_gp**2+delta_n_gp**2)/(1-ambda_cr)**alpha
a2 = T_max*(1-sqrt(delta_t_gp**2+delta_n_gp**2)/del_c)**alpha*
#delta_n_gp/sqrt(delta_t_gp**2+delta_n_gp**2)/(1-ambda_cr)**alpha
a3 = -T_max*(1-sqrt(delta_t_gp**2+delta_n_gp**2)/del_c)**alpha
**alpha/(delta_t_gp**2+delta_n_gp**2)/del_c*delta_t_gp**2/(1-sqrt(d
#elta_t_gp**2+delta_n_gp**2)/del_c)/(1-ambda_cr)**alpha+T_max*(1-sq
#rt(delta_t_gp**2+delta_n_gp**2)/del_c)**alpha/sqrt(delta_t_gp**2+d
#elta_n_gp**2)/(1-ambda_cr)**alpha-T_max*(1-sqrt(delta_t_gp**2+delt
#a_n_gp**2)/del_c)**alpha*delta_t_gp**2/sqrt(delta_t_gp**2+delta_n_
#gp**2)**3/(1-ambda_cr)**alpha
a4 = -T_max*(1-sqrt(delta_t_gp**2+delta_n_gp**2)/del_c)**alpha
**alpha/(delta_t_gp**2+delta_n_gp**2)/del_c*delta_n_gp/(1-sqrt(delt
#a_t_gp**2+delta_n_gp**2)/del_c)*delta_t_gp/(1-ambda_cr)**alpha-T_m
#ax*(1-sqrt(delta_t_gp**2+delta_n_gp**2)/del_c)**alpha*delta_t_gp/s
#qrt(delta_t_gp**2+delta_n_gp**2)**3/(1-ambda_cr)**alpha*delta_n_gp
a5 = -T_max*(1-sqrt(delta_t_gp**2+delta_n_gp**2)/del_c)**alpha
**alpha/(delta_t_gp**2+delta_n_gp**2)/del_c*delta_n_gp**2/(1-sqrt(d
#elta_t_gp**2+delta_n_gp**2)/del_c)/(1-ambda_cr)**alpha+T_max*(1-sq
#rt(delta_t_gp**2+delta_n_gp**2)/del_c)**alpha/sqrt(delta_t_gp**2+d
#elta_n_gp**2)/(1-ambda_cr)**alpha-T_max*(1-sqrt(delta_t_gp**2+delt
#a_n_gp**2)/del_c)**alpha*delta_n_gp**2/sqrt(delta_t_gp**2+delta_n_
#gp**2)**3/(1-ambda_cr)**alpha
Trac(1,1)=a1
Trac(2,1)=a2
Trac_Jacob(1,1)=a3
Trac_Jacob(1,2)=a4

```

```
        Trac_Jacob(2,2)=a5
        Trac_Jacob(2,1)=Trac_Jacob(1,2)
elseif (del_eff.gt.del_c) then
    Trac(1,1)=0.0d0
    Trac(2,1)=0.0d0
    Trac_Jacob(1,1)=0.0d0
    Trac_Jacob(1,2)=0.0d0
    Trac_Jacob(2,1)=0.0d0
    Trac_Jacob(2,2)=0.0d0
endif
endif
c
return
end
c
```

References

- [1] AASHTO. *Standard test method for determining the creep compliance and strength of hot mix asphalt (HMA) using the indirect tensile test device*. Standard Specifications for Transportation Materials and Methods of Sampling and Testing, 24th Edition, 2004.
- [2] ABAQUS. *User's manual-version 6.5*. Hibitt, Karlsson and Sorenson Inc., Pawtucket, R.I., 2006.
- [3] A.A. Abdulshafi and K. Majidzadeh. J-integral and cyclic plasticity approach to fatigue and fracture of asphalt mixtures. *Transportation Research Record*, 1034:112–123, 1985.
- [4] D.H. Allen and C.R. Searcy. A micromechanical model for a viscoelastic cohesive zone. *International Journal of Fracture*, 107(2):159–176, 2001.
- [5] T.L. Anderson. *Fracture Mechanics: Fundamentals and Applications*. CRC Press, Boca Raton, Florida, 1995.
- [6] J.P. Bailon and S.D. Antolovich. Effect of microstructure on fatigue crack propagation: a review of existing models and suggestions for further research. volume ASTM STP 811, pages 313–349, Philadelphia, 1983. American Society for Testing and Materials.
- [7] G.I. Barenblatt. The formation of equilibrium cracks during brittle fracture: General ideas and hypotheses, axially-symmetric cracks. *Journal of Applied Mathematics and Mechanics (PMM)*, 23(3):622–636, 1959.

- [8] G.I. Barenblatt. Mathematical theory of equilibrium cracks in brittle fracture. *Advances in Applied Mechanics*, 7:55–129, 1962.
- [9] Z.P. Bazant. Current status and advances in the theory of creep and interaction with fracture. In Z.P. Bazant and I. Carol, editors, *International RILEM symposium on creep and shrinkage of concrete*, pages 291–307, London, 1993. E and F Spon.
- [10] Z.P. Bazant. Concrete fracture models: testing and practice. *Engineering Fracture Mechanics*, 69(2):165–205, 2002.
- [11] Z.P. Bazant and R. Gettu. Rate effects and load relaxation in static fracture of concrete. *ACI Materials Journal*, 89(5):456–468, 1992.
- [12] Z.P. Bazant and Y.-N. Li. Cohesive crack with rate-dependent opening and viscoelasticity: I. mathematical model and scaling. *International Journal of Fracture*, 86(3):247–265, 1997.
- [13] Z.P. Bazant and J. Planas. *Fracture and Size Effect in Concrete and Other Quasi-brittle Materials*. CRC Press, Boca Raton, Florida, 1998.
- [14] A.S. Bhurke, E.E. Shih, and L.T. Drzal. Fracture morphology and fracture toughness measurement of polymer-modified asphalt concrete. *Transportation Research Record*, 1590:23–33, 1997.
- [15] T.W. Bjerke and J. Lambros. Theoretical development and experimental validation of a thermally dissipative cohesive zone model for dynamic fracture of amorphous polymers. *Journal of Mechanics and Physics of Solids*, 51(6):1147–1170, 2003.
- [16] D. Bozkurt and W.G. Buttlar. Three-dimensional finite element modeling to evaluate benefits of interlayer stress absorbing composite for reflective cracking mitigation. In *Proceedings of the Federal Aviation Administration Airport Technology Transfer Conference*, Atlantic City, NJ, May, 2002.

- [17] W.G. Buttlar and R. Roque. Development and evaluation of the new SHRP measurement and analysis system for indirect tensile testing of asphalt mixtures at low temperatures. *Transportation Research Record*, 1454:163–171, 1994.
- [18] J.W. Button. Overlay construction and performance using geotextiles. *Transportation Research Record*, 1248:24–33, 1989.
- [19] G.T. Camacho and Ortiz. M. Computational modeling of impact damage in brittle materials. *International Journal of Solids and Structures*, 33(20-22):2899–2938, 1996.
- [20] M.A. Castell, A.R. Ingraffea, and L.H. Irwin. Fatigue crack growth in pavements. *ASCE Journal of Transportation Engineering*, 126(4):283–290, 2000.
- [21] E.M. Castrodeza, J.E.P. Ipina, and F.L. Bastian. Fracture toughness evaluation of unidirectional fibre metal laminates using traditional CTOD (δ) and Schwalbe (δ_5) methodologies. *Engineering Fracture Mechanics*, 71(7-8):1107–1118, 2004.
- [22] W. Celes, G.H. Paulino, and R. Espinha. A compact adjacency-based topological data structure for finite element mesh representation. *International Journal for Numerical Methods in Engineering*, 64(11):1529–1556, 2005.
- [23] W. Celes, G.H. Paulino, and R. Espinha. Efficient handling of implicit entities in reduced mesh representations. *Journal of Computing and Information Science in Engineering*, 5(4):348–359, 2005.
- [24] N. Chandra. Evaluation of interfacial fracture toughness using cohesive zone model. *Composites Part A - Applied Science and Manufacturing*, 33(10):1433–1447, 2002.
- [25] K.P. Chong and M.D. Kuruppu. New specimens for mixed mode fracture investigations of geomaterials. *Engineering Fracture Mechanics*, 30(5):701–712, 1988.
- [26] R.M. Christensen. *Theory of Viscoelasticity*. Dover publications, Inc., New York, 2003.

- [27] RILEM committee on fracture mechanics of concrete test methods. Determination of the fracture energy of mortar and concrete by means of three-point bend test on notched beams. *Materials and Structures*, 18(106):285–290, 1985.
- [28] H.A.W. Cornelissen, D.A. Hordjik, and H.W. Reinhardt. Experiments and theory for the application of fracture mechanics to normal and lightweight concrete. In F.H. Wittmann, editor, *Fracture Toughness and Fracture Energy of Concrete*, pages 565–575, Amsterdam, 1986. Elsevier.
- [29] F. Costanzo and J.R. Walton. Steady growth of a crack with a rate and temperature sensitive cohesive zone. *Journal of Mechanics and Physics of Solids*, 50(8):1649–1679, 2002.
- [30] M.A. Crisfield. A fast incremental/iterative solution procedure that handles “snap-through”. *Computers & Structures*, 13(1-3):55–62, 1981.
- [31] E.V. Dave. Personal communication.
- [32] E.V. Dave, S.H. Song, W.G. Buttlar, and G.H. Paulino. Reflective and thermal cracking modeling of asphalt concrete overlays. In *3D FEM conference (accepted)*.
- [33] E.V. Dave, M.P. Wagoner, S.H. Song, P.H. Blankenship, W.G. Buttlar, and G.H. Paulino. Reflective cracking prediction in asphalt concrete overlays by an integrated testing and modeling approach. *Transportation Research Board (submitted)*.
- [34] A. de Andres, J.L. Perez, and M. Ortiz. Elastoplastic finite element analysis of three-dimensional fatigue crack growth in aluminum shafts subjected to axial loading. *International Journal of Solids and Structures*, 36(15):2231–2258, 1999.
- [35] J. Du, J.H. Yon, N.M. Hawkins, K. Arakawa, and A.S. Kobayashi. Fracture process zone for concrete for dynamic loading. *ACI Materials Journal*, 89(3):252–258, 1992.

- [36] D.S. Dugdale. Yielding of steel sheets containing slits. *Journal of Mechanics and Physics of Solids*, 8(2):100–104, 1960.
- [37] M. Elices, G.V. Guinea, J. Gomez, and J. Planas. The cohesive zone model: advantages, limitations and challenges. *Engineering Fracture Mechanics*, 69(2):137–163, 2002.
- [38] F. Erdogan and B.H. Wu. The surface crack problem for a plate with functionally graded properties. *ASME Journal of Applied Mechanics*, 64(3):449–456, 1997.
- [39] H.D. Espinosa and P.D. Zavattieri. A grain level model for the study of failure initiation and evolution in polycrystalline brittle materials. Part I: Theory and numerical implementation. *Mechanics of Materials*, 35(3-6):333–364, 2003.
- [40] A.G. Evans and Y. Fu. The mechanical behavior of alumina. In A.G. Evans, editor, *Fracture in Ceramic Materials: Toughening Mechanisms, Machining Damage, Shock*, pages 56–88, Park Ridge, N.J., 1984. Noyes Publications.
- [41] P.H. Geubelle and J.S. Baylor. Impact-induced delamination of composites: a 2D simulation. *Composites Part B - Engineering*, 29(5):589–602, 1998.
- [42] S. Glasstone, K.J. Laidler, and H. Eyring. *The Theory of Rate Processes*. McGraw-Hill Inc., New York, 1941.
- [43] F.J. Gomez, M. Elices, and J. Planas. The cohesive crack concept: application to PMMA at -60°C . *Engineering Fracture Mechanics*, 72(8):1268–1285, 2005.
- [44] V.S. Gopalaratnam and S.P. Shah. Softening response of plain concrete in direct tension. *Journal of the American Concrete Institute*, 82(3):310–323, 1985.
- [45] Z.K. Guo, A.S. Kobayashi, and N.M. Hawkins. Dynamic mixed-mode fracture of concrete. *International Journal of Solids and Structures*, 32(17-18):2591–2607, 1995.

- [46] T.-S. Han, A. Ural, C.-H. Chen, A.T. Zehnder, A.R. Ingraffea, and S.L. Billington. Delamination buckling and propagation analysis of honeycomb panels using a cohesive element approach. *International Journal of Fracture*, 115(2):101–123, 2002.
- [47] A. Hillerborg, M. Modeer, and P.-E. Peterson. Analysis of crack formulation and crack growth in concrete by means of fracture mechanics and finite elements. *Cement and Concrete Research*, 6(6):773–782, 1976.
- [48] D.R. Hiltunen and R. Roque. The use of time-temperature superposition to fundamentally characterize asphaltic concrete mixtures at low temperatures. In G.A. Huber and D.S. Decker, editors, *Engineering Properties of Asphalt Mixtures and the Relationship to Performance*, volume ASTM STP 1265, Philadelphia, 1994. American Society for Testing and Materials.
- [49] T. Hirano, J. Teraki, and T. Yamada. On the design of functionally gradient materials. In Yamanouchi M., Koizumi M., Harai T., and Shiota I., editors, *Proceedings of the First International Symposium on Functionally Gradient Materials*, pages 5–10, Sendai, Japan, 1990.
- [50] Y.H. Huang. *Pavement Analysis and Design*. Prentice Hall, New Jersey, 1993.
- [51] G. Huber and J.A. Scherocman. Investigations of premature distress: Highway us 36 and interstate highway 155. Illinois Department of Transportation, Final Project Report, October., 1994.
- [52] T.J.R. Hughes. *The Finite Element Method : Linear Static and Dynamic Finite Element Analysis*. Prentice Hall, New Jersey, 1987.

- [53] T. Igari, A. Notomi, H. Tsunoda, K. Hida, T. Koto, and S. Kunishima. Material properties of functionally gradient material for fast breed reactor. In Yamanouchi M., Koizumi M., Harai T., and Shiota I., editors, *Proceedings of the First International Symposium on Functionally Gradient Materials*, pages 209–214, Sendai, Japan, 1990.
- [54] M.M. Jacob, P.C. Hopman, and A.A.A. Molenaar. Application of fracture mechanics in principles to analyze cracking in asphalt concrete. *Journal of the Association of Asphalt Paving Technologists*, 65:1–39, 1996.
- [55] Z.-H. Jin, G.H. Paulino, and R.H. Dodds Jr. Finite element investigation of quasi-static crack growth in functionally graded materials using a novel cohesive zone fracture model. *ASME Journal of Applied Mechanics*, 69(3):370–379, 2002.
- [56] Z.-H. Jin, G.H. Paulino, and R.H. Dodds Jr. Cohesive fracture modeling of elastic-plastic crack growth in functionally graded materials. *Engineering Fracture Mechanics*, 70(14):1885–1912, 2003.
- [57] R. John and S.P. Shah. Mixed-mode fracture of concrete subjected to impact loading. *ASCE Journal of Structural Engineering*, 116(3):585–602, 1990.
- [58] K. Khan and N.A. Al-Shayea. Effect of specimen geometry and testing method on mixed mode I-II fracture toughness of a limestone rock from Saudi Arabia. *Rock Mechanics and Rock Engineering*, 33(3):179–206, 2000.
- [59] J. Kim. *Three-Dimensional Finite Element Analysis of Multi-Layered Systems*. PhD thesis, University of Illinois at Urbana-Champaign, 2000.
- [60] J. Kim and W.G. Buttlar. Analysis of reflective crack control system involving reinforcing grid over base-isolating interlayer mixture. *ASCE Journal of Transportation Engineering*, 128(4):375–384, 2002.

- [61] J.-H. Kim. *Mixed-mode crack propagation in functionally graded materials*. PhD thesis, University of Illinois at Urbana-Champaign, 2003.
- [62] J.-H. Kim and G.H. Paulino. Finite element evaluation of mixed-mode stress intensity factors in functionally graded materials. *International Journal for Numerical Methods in Engineering*, 53(8):1903–1935, 2002.
- [63] J.-H. Kim and G.H. Paulino. Isoparametric graded finite elements for nonhomogeneous isotropic and orthotropic materials. *ASME Journal of Applied Mechanics*, 69(4):502–514, 2002.
- [64] J.-H. Kim and G.H. Paulino. T-stress, mixed mode stress intensity factors, and crack initiation angles in functionally graded materials : a unified approach using the interaction integral method. *Computer Methods in Applied Mechanics and Engineering*, 192(11-12):1463–1494, 2003.
- [65] K.W. Kim and H.M. El Hussein. Effect of differential thermal contraction on fracture properties of asphalt materials at low temperatures. *Journal of the Association of Asphalt Paving Technologists*, 64:474–499, 1995.
- [66] P.A. Klein, J.W. Foulk, E.P. Chen, S.A. Wimmer, and H. Gao. *Physics-based modeling of brittle fracture: cohesive formulations and the applications of meshfree methods*. SAND 2001-8009, 2001.
- [67] W.G. Knauss. On the steady propagation of a crack in a viscoelastic sheet: experiments and analysis. In H.H. Kausch, J.A. Hassell, and R. Jaffee, editors, *Deformation and Fracture of High Polymers*, pages 501–541, New York, 1973. Plenum Press.
- [68] W.G. Knauss and G.U. Losi. Crack propagation in a nonlinearly viscoelastic solid with relevance to adhesive bond failure. *ASME Journal of Applied Mechanics*, 60(4):793–801, 1993.

- [69] L. Kogan, C.-Y. Hui, and A. Ruina. Theory of chain pull-out and stability of weak polymer interfaces. 1. *Macromolecules*, 29(11):4090–4100, 1996.
- [70] A.S. Krausz and K. Krausz. *Fracture Kinetics of Crack Growth*. Kluwer Academic Publishers, 1988.
- [71] G. Larson and B.J. Dempsey. Enhanced integrated climatic model, version 2.0. Minnesota Road Research Program, Minnesota Department of Transportation, Report No. DTFA MN/DOT 72114, Maplewood, MN., 1997.
- [72] X. Li and Marasteanu. M. Evaluation of the low temperature fracture resistance of asphalt mixtures using the semi-circular bend test. *Journal of the Association of Asphalt Paving Technologists*, 73:401–426, 2004.
- [73] Y.-N. Li and Z.P. Bazant. Cohesive crack model with rate-dependent opening and viscoelasticity: II. Numerical algorithm, behavior and size effect. *International Journal of Fracture*, 86(3):267–288, 1997.
- [74] G. Lin, A. Cornec, and K.-H. Schwalbe. Three-dimensional finite element simulation of crack extension in aluminium alloy 2024FC. *Fatigue & Fracture of Engineering Materials & Structures*, 21(10):1159–1173, 1998.
- [75] D.L. Lippert. A review of cracking on full-depth bituminous pavement (longitudinal cracking). Illinois Department of Transportation Internal Report, August, 1993.
- [76] R.L. Lytton. Use of geotextiles for reinforcement and strain relief in asphalt concrete. *Geotextiles and Geomembranes*, 8(3):217–237, 1989.
- [77] S. Maiti and P.H. Geubelle. Cohesive modeling of fatigue crack retardation in polymers: Crack closure effect. *Engineering Fracture Mechanics*, 73(1):22–41, 2006.

- [78] K. Majidzadeh, E.M. Kauffmann, and D.V. Ramsamooj. Application of fracture mechanics in the analysis of pavement fatigue. *Journal of the Association of Asphalt Paving Technologists*, 40:227–246, 1971.
- [79] M.W. Mirza and M.W. Witzak. Development of a global aging system for short and long term aging of asphalt cements. *Journal of the Association of Asphalt Paving Technologists*, 64:393–430, 1995.
- [80] B. Mobasher, M.S. Mamlouk, and H.-M. Lin. Evaluation of crack propagation properties of asphalt mixtures. *ASCE Journal of Transportation Engineering*, 123(5):405–413, 1997.
- [81] J. Molenaar, X. Liu, and A.A.A. Molenaar. Resistance to crack-growth and fracture of asphalt mixture. In *Proceedings of Sixth International RILEM Symposium on Performance Testing and Evaluation of Bituminous Materials*, Switzerland, 2003.
- [82] C.L. Monismith and N.F. Coetzee. Reflection cracking: analyses, laboratory studies and design considerations. *Journal of the Association of Asphalt Paving Technologists*, 49:268–313, 1980.
- [83] S. Mukherjee and G.H. Paulino. The elastic-viscoelastic correspondence principle for functionally graded materials, revisited. *ASME Journal of Engineering Mechanics*, 70(3):359–363, 2003.
- [84] L.A. Myers, R. Roque, B. Birgisson, and C. Drakos. Measurement of contact stresses for different truck tire types to evaluate their influence on near-surface cracking and rutting. *Transportation Research Board (CD-ROM)*, 1999.
- [85] NCHRP. *Guide for mechanistic-empirical design of new and rehabilitated pavement structures*. NCHRP Project 1-37A, Transportation Research Board, Washington D.C., 2004.

- [86] A. Needleman. A continuum model for void nucleation by inclusion debonding. *ASME Journal of Applied Mechanics*, 54(3):525–531, 1987.
- [87] T.D. Nguyen, S. Govindjee, P.A. Klein, and H. Gao. A rate-dependent cohesive continuum model for the study of crack dynamics. *Computer Methods in Applied Mechanics and Engineering*, 193(30-32):3239–3265, 2004.
- [88] H. Oonishi, T. Noda, S. Ito, A. Kohda, H. Ishimaru, M. Yamamoto, and E. Tsuji. Effect of hydroxyapatite coating on bone-growth into porous titanium-alloy implants under loaded conditions. *Journal of Applied Biomaterials*, 5(1):23–27, 1994.
- [89] M. Ortiz and A. Pandolfi. Finite deformation irreversible cohesive elements for the three dimensional crack propagation analysis. *International Journal for Numerical Methods in Engineering*, 44(9):1267–1282, 1999.
- [90] E.B. Owusu-Antwi, L. Khazanovich, and L. Titus-Glover. A mechanistic-based model for predicting reflective cracking in AC overlaid pavements. *Transportation Research Board (CD-ROM)*, 1998.
- [91] K.D. Papoulia, C.H. Sam, and S.A. Vavasis. Time continuity in cohesive finite element modeling. *International Journal for Numerical Methods in Engineering*, 58(5):679–701, 2003.
- [92] P.C. Paris and F. Erdogan. A critical analysis of crack propagation laws. *ASME Journal of Basic Engineering*, 85:528–534, 1963.
- [93] S.W. Park and Y.R. Kim. Interconversion between relaxation modulus and creep compliance for viscoelastic solids. *Journal of Materials in Civil Engineering*, 11(1):76–82, 1999.

- [94] G.H. Paulino, W.G. Buttlar, and P. Blankenship. GOALI: Reflective crack control treatment and design procedures: A new integrated approach. <http://www.nsf.gov/awardsearch/showAward.do?AwardNumber=0219566>.
- [95] G.H. Paulino and Z.-H. Jin. Correspondence principle in viscoelastic functionally graded materials. *ASME Journal of Engineering Mechanics*, 68(1):129–132, 2001.
- [96] G.H. Paulino, Z.-H. Jin, and R.H. Dodds Jr. Failure of functionally graded materials. In B. Karihaloo and W. G. Knauss, editors, *Comprehensive Structural Integrity*, volume 2, Chapter 13. Elsevier Science, 2002.
- [97] P.-E. Peterson. Crack growth and development of fracture zone in plain concrete and similar materials. Technical Report Report No. TVBM-1006, 1981.
- [98] J. Planas and M. Elices. Towards a measure of G_F : An analysis of experimental results. In F.H. Wittmann, editor, *Fracture Toughness and Fracture Energy of Concrete*, pages 381–390, Amsterdam, 1986. Elsevier.
- [99] P. Rahul-Kumar, A. Jagota, S.J. Bennison, and S. Saigal. Cohesive element modeling of viscoelastic fracture: application to peel testing of polymers. *International Journal of Solids and Structures*, 37(13):1873–1897, 2000.
- [100] P. Rahul-Kumar, A. Jagota, S.J. Bennison, S. Saigal, and S. Muralidhar. Polymer interfacial fracture simulations using cohesive elements. *Acta Materialia*, 47(15-16):4161–4169, 1999.
- [101] D.V. Ramsamooj. Prediction of fatigue life of asphalt concrete beams from fracture tests. *Journal of Testing and Evaluation*, 19(3):231–239, 1991.
- [102] J.R. Rice. Mathematical analysis in the mechanics of fracture. In Liebowitz H., editor, *Fracture: An Advanced Treatise*, pages 191–311, New York, 1968. Academic Press.

- [103] E. Riks. An incremental approach to the solution of snapping and buckling problems. *International Journal of Solids and Structures*, 15(7):529–551, 1979.
- [104] K.L. Roe and T. Siegmund. An irreversible cohesive zone model for interface fatigue crack growth simulation. *Engineering Fracture Mechanics*, 70(2):209–232, 2003.
- [105] K. Rokugo, M. Iwasa, T. Suzuki, and W. Koyanagi. Testing methods to determine tensile strain softening curve and fracture energy of concrete. In H. Mihashi, H. Takahashi, and F.H. Wittmann, editors, *Fracture Toughness and Fracture energy: Test Methods for Concrete and Rock*, pages 191–311. Balkema, Rotterdam, 1989.
- [106] P. Romero and E. Masad. Relationship between the representative volume element and mechanical properties of asphalt concrete. *Journal of Materials in Civil Engineering*, 13(1):77–84, 2001.
- [107] J.G. Rots and R. de Borst. Analysis of concrete fracture in direct tension. *International Journal of Solids and Structures*, 25(12):1381–1394, 1989.
- [108] Y.A. Roy and R.H. Dodds Jr. Simulation of ductile crack growth in thin aluminum panels using 3-D surface cohesive elements. *International Journal of Fracture*, 110(1):21–45, 2001.
- [109] G. Ruiz, A. Pandolfi, and M. Ortiz. Three-dimensional cohesive modeling of dynamic mixed-mode fracture. *International Journal for Numerical Methods in Engineering*, 52(1-2):97–120, 2001.
- [110] C.-H. Sam, K.D. Papoulia, and S.A. Vavasis. Obtaining initially rigid cohesive finite element models that are temporally convergent. *Engineering Fracture Mechanics*, 72(14):2247–2267, 2005.

- [111] B. Sangpetngam, B. Birgisson, and R. Roque. A multi-layer boundary element method for the evaluation of top-down cracking in hot mix asphalt pavements. *Transportation Research Board (CD-ROM)*, 2004.
- [112] M.H. Santare and J. Lambros. Use of graded finite elements to model the behavior of nonhomogeneous materials. *ASME Journal of Applied Mechanics*, 67(4):819–822, 2000.
- [113] R.A. Schapery. A theory of crack initiation and growth in viscoelastic media I. Theoretical development. *International Journal of Fracture*, 11(1):141–159, 1975.
- [114] K.-H. Schwalbe. Introduction of δ_5 as an operational definition of the CTOD and its practical use. In *Fracture Mechanics: 26th Volume*, volume ASTM STP 1256, pages 763–778, Philadelphia, 1995. American Society for Testing and Materials.
- [115] K.-H. Schwalbe, R.A. Ainsworth, A. Saxena, and T. Yokobori. Recommendations for a modification of ASTM E1457 to include creep-brittle materials. *Engineering Fracture Mechanics*, 62(1):123–142, 1999.
- [116] K.-H. Schwalbe and A. Cornec. The engineering treatment model (ETM) and its practical application. *Fatigue & Fracture of Engineering Materials & Structures*, 14(4):405–412, 1991.
- [117] K.-H. Schwalbe, J.C. Newman Jr., and J.L. Shannon Jr. Fracture mechanics testing on specimens with low constraint -standardisation activities within ISO and ASTM. *Engineering Fracture Mechanics*, 72(4):557–576, 2005.
- [118] S.P. Shah, S.E. Swartz, and C. Ouyang. *Fracture Mechanics of Concrete: Applications of Fracture Mechanics to Concrete, Rock, and Other Quasi-Brittle Materials*. John Wiley and Sons, New York, 1995.

- [119] W.X. Shen and Kirkner D.J. Distributed thermal cracking of AC pavement with frictional constraint. *ASCE Journal of Engineering Mechanics*, 125(5):554–560, 1999.
- [120] T. Siegmund and A. Needleman. A numerical study of dynamic crack growth in elastic-viscoplastic solids. *International Journal of Solids and Structures*, 34(7):769–787, 1997.
- [121] J.B. Soares, F.A. Colares de Freitas, and D.H. Allen. Crack modeling of asphaltic mixtures considering heterogeneity of the material. *Transportation Research Board (CD-ROM)*, 2003.
- [122] S.H. Song, G.H. Paulino, and W.G. Buttlar. A bilinear cohesive zone model tailored for fracture of asphalt concrete considering viscoelastic bulk material. *Engineering Fracture Mechanics (in press and available online)*.
- [123] S.H. Song, G.H. Paulino, and W.G. Buttlar. Simulation of crack propagation in asphalt concrete using an intrinsic cohesive zone model. *ASCE Journal of Engineering Mechanics (in press)*.
- [124] S.H. Song, G.H. Paulino, and W.G. Buttlar. Three-dimensional power-law cohesive zone model for fracture modeling of asphalt concrete (to be submitted).
- [125] S. Suresh. *Fatigue of Materials*. Cambridge University Press, Cambridge-New York, 1988.
- [126] J. Tani and G.R. Liu. Surface waves in functionally gradient piezoelectric plates. *JSME International Journal Series A: Mechanics and Material Engineering*, 36(2):152–155, 1993.
- [127] M.G.A. Tijssens, B.L.J. Sluys, and E. van der Giessen. Numerical simulation of quasi-brittle fracture using damaging cohesive surfaces. *European Journal of Mechanics A - Solids*, 19(5):761–779, 2000.

- [128] N.W. Tschoegl. *The Phenomenological Theory of Linear Viscoelastic Behavior: An Introduction*. Springer-Verlag, Germany, 1989.
- [129] V. Tvergaard. Effect of fiber debonding in a whisker-reinforced metal. *Materials Science and Engineering A*, 125(2):203–213, 1990.
- [130] M.J. van den Bosch, P.J.G. Schreurs, and M.G.D. Geers. An improved description of the exponential Xu and Needleman cohesive zone law for mixed-mode decohesion. *Engineering Fracture Mechanics*, 73(9):1220–1234, 2006.
- [131] M.P. Wagoner. Personal communication.
- [132] M.P. Wagoner, W.G. Buttlar, and G.H. Paulino. Development of a single-edge notched beam test for the study of asphalt concrete fracture. In *Geotechnical Special Publication No. 130: Advances in Pavement Engineering, Proceedings of Sessions of the GeoFrontiers 2005 Congress*, Austin, TX, 2005.
- [133] M.P. Wagoner, W.G. Buttlar, and G.H. Paulino. Development of a single-edge notched beam test for asphalt concrete mixtures. *ASTM Journal of Testing and Evaluation*, 33(6):452–460, 2005.
- [134] M.P. Wagoner, W.G. Buttlar, and G.H. Paulino. Disk-shaped compact tension test for asphalt concrete fracture. *Experimental Mechanics*, 45(3):270–277, 2005.
- [135] M.P. Wagoner, W.G. Buttlar, G.H. Paulino, and P. Blankenship. Investigation of the fracture resistance of hot-mix asphalt concrete using a disk-shaped compact tension test. *Transportation Research Record*, 1929:183–192, 2005.
- [136] B. Wang and T. Siegmund. Numerical simulation of constraint effects in fatigue crack growth. *International Journal of Fatigue*, 27(10-12):1328–1334, 2005.

- [137] F. Watari, A. Yokoyama, F. Saso, M. Uo, S. Ohkawa, and T. Kawasaki. EPMA elemental mapping of functionally graded dental implant in biocompatibility test. In *Proceedings of the Fourth International Symposium on Functionally Graded Materials*, Tsukuba City, Japan, 1996.
- [138] M.W. Witczak. Development of relationships between binder viscosity and stiffness. SUPERPAVE Support and Performance Models Contract, FHWA No. DTFH 61-94-R-00045, Team Technical Report, University of Maryland, 1998.
- [139] F.H. Wittmann, K. Rokugo, E. Bruhwiler, H. Mihashi, and P. Simonin. Fracture energy and strain softening of concrete as determined by means of compact tension specimens. *Materials and Structures*, 21(121):21–32, 1988.
- [140] Z.-S. Wu and Z.P. Bazant. Finite element modeling of rate effects in concrete fracture with influence of creep. In Z.P. Bazant and I. Carol, editors, *International RILEM symposium on creep and shrinkage of concrete*, pages 427–432, London, 1993. E and F Spon.
- [141] C. Xu, T. Siegmund, and K. Ramani. Rate-dependent crack growth in adhesives I. Modeling approach. *International Journal of Adhesion and Adhesives*, 23(1):9–13, 2003.
- [142] C. Xu, T. Siegmund, and K. Ramani. Rate-dependent crack growth in adhesives II. Experiments and analysis. *International Journal of Adhesion and Adhesives*, 23(1):15–22, 2003.
- [143] D.-B. Xu, C.-Y. Hui, and E.J. Kramer. Interface fracture and viscoelastic deformation in finite size specimens. *Journal of Applied Physics*, 72(8):3305–3316, 1992.
- [144] X.-P. Xu and A. Needleman. Numerical simulations of fast crack growth in brittle solids. *Journal of Mechanics and Physics of Solids*, 42(9):1397–1434, 1994.

- [145] P.D. Zavattieri and H.D. Espinosa. Grain level analysis of crack initiation and propagation in brittle materials. *Acta Materialia*, 49(20):4291–4311, 2001.
- [146] Z. Zhang and G.H. Paulino. Cohesive zone modeling of dynamic failure in homogeneous and functionally graded materials. *International Journal of Plasticity*, 21(6):1195–1254, 2005.
- [147] S.N. Zhurkov. Kinetic concept of the strength of solids. *International Journal of Fracture*, 26(4):295–307, 1984.

Author's biography

Seong Hyeok Song was born to Song, Seunghoo and Kim, Minsuk in Cheju, Korea on May 21, 1972. He earned his B.E. degree from the Department of Civil Engineering, University of Seoul, in February 2000. Graduate studies commenced at the Department of Civil and Environmental Engineering, University of Illinois at Urbana-Champaign (UIUC) from August 2000. He had worked for the Caterpillar Simulation Center from June 2001 to May 2002 as a graduate assistant. In January 2002, he joined Professor Paulino's research group and has worked for the Grant Opportunities for Academic Liaison with Industry (GOALI) project since June 2002. This is a three-way project involving the National Science Foundation (NSF), the University of Illinois at Urbana-Champaign, and the industry (SemMaterials, previously Koch Materials). He earned his M.S. degree with the thesis in December 2003. He finished the work necessary for a Ph.D. in August, 2006. After graduation, he will work for the California Department of Transportation as a structural/bridge engineer.